ISSUE NO. 285

बीएआरसी
न्यूज़लैटर

BARC
NEWSLETTER

OCTOBER 2007

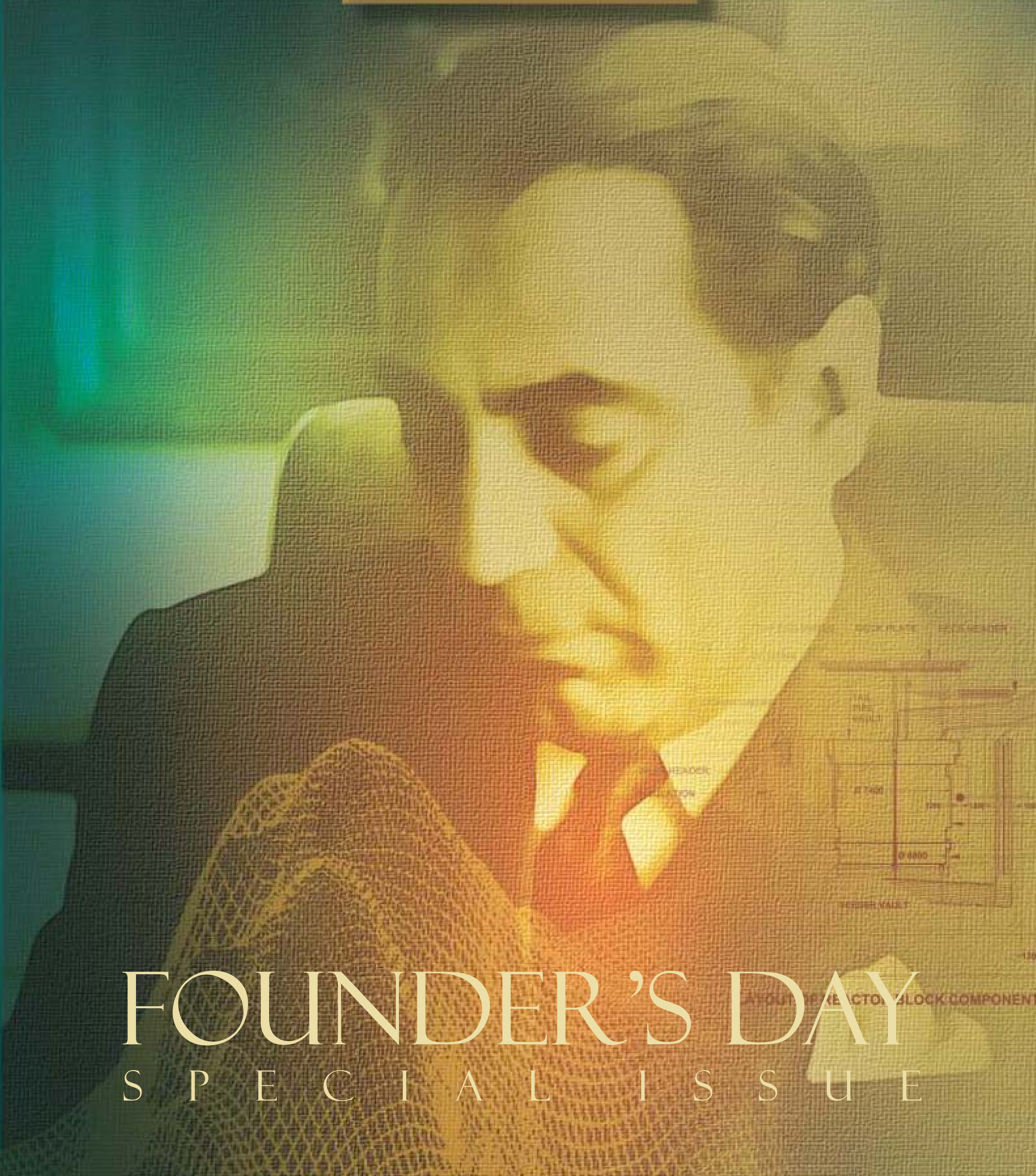

FOUNDER'S DAY
SPECIAL ISSUE

बीएआरसी
न्यूज़लैटर
BARC
NEWSLETTER

FOUNDER'S DAY
SPECIAL ISSUE

सत्यमेव जयते
Government of India

BHABHA ATOMIC RESEARCH CENTRE

DEDICATED TO THE MEMORY OF
HOMI JEHANGIR BHABHA
(1909 -1966)

Founder and Architect of the
Indian Atomic Energy Programme

CONTENTS

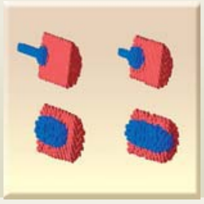

1 **Computer simulations for strategic applications** 1

Chaturvedi, S.
Recipient of the Homi Bhabha Science &
Technology Award for the year 2005

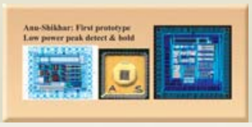

2. **An approach to modernizing nuclear instrumentation: Silicon-based sensors, ASIC and HMC** 8

Chandratre, V.B. et al
Recipients of the DAE Technical Excellence Award
for the year 2005

3. **Advances in x-ray neutron imaging and its applications** 17

Sinha, A.
Recipient of DAE Technical Excellence Award
for the year 2005 for his work on X-ray and
Neutron Imaging

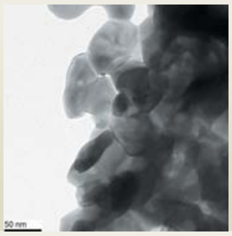

4. **Combustion synthesis : a soft-chemical route for functional nano-ceramics** 39

Tyagi, A.K.
Recipient of the CRSI Medal by the
Chemical Research Society of India in
February 2006

5. **Development and applications of C-scan ultrasonic facility** 49

Anish Kumar et al
Recipients of the Best Journal Paper at the National Seminar
NDE2006 held at Hyderabad, during December 7-9, 2006

6. **Preparation and preliminary biological evaluation of ^{175}Yb labeled hydroxyapatite for possible use in radiation synovectomy of small joints** 58

Chakraborty, S. et al
Recipients of the Second Best oral presentation Award at the International Conference on Application of Radiotracers at Chemical, Environmental and Biological Sciences (arcebs-06), held at Kolkata during January 23-27, 2006

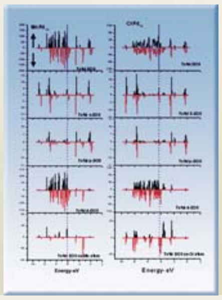

7. **Geometry, electronic and magnetic properties of MPd^{12} clusters (M=Ti, V, Cr, Mn, Fe, Co, Ni, Cu, Zn, Pd)** 62

Nigam, S. et al
Recipients of the Best Paper Award (Second Prize), presented at the International Symposium on Materials Chemistry (ISMC-2006) held at BARC, Mumbai during December 4-8, 2006

8. **Studies on sulfur-iodine thermochemical cycle for hydrogen production** 67

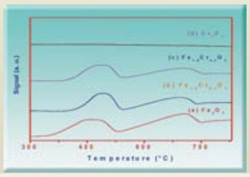

Banerjee, A.M. et al
Recipients of the best Paper Award (Third Prize), presented at the International Symposium on Materials Chemistry (ISMC-2006) held at BARC, Mumbai during December 4-8, 2006

9. **Studies of material issues, science and technology for immobilization of sulphate-bearing high-level radioactive liquid waste** 73

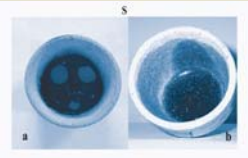

Kaushik, C.P. et al
Recipients of the Best Paper Award at the International Symposium on Materials Chemistry (ISMC-2006) held at BARC, Mumbai, during December 4-8, 2006

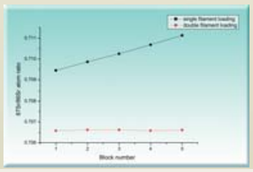

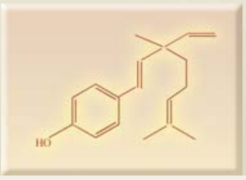
HO

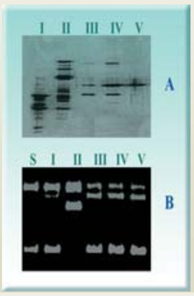
I II III IV V
A
S I II III IV V
B

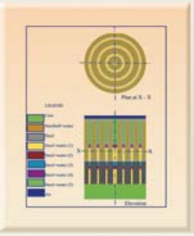

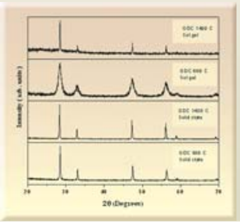
2θ (Degrees)
Intensity (arb. units)

18. **Selective preconcentration of molecular iodine by complexation with poly (vinylpyrrolidone) in membrane and its determination by NAA** 121

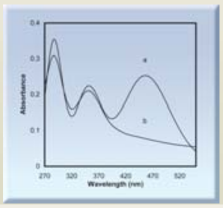

Bhagat, P. et al
Recipients of the Best Paper Presentation Award at the DAE-BRNS Symposium on "Emerging Trends in Separation Science and Technology (SESTEC 2006) held during September 29-October 1, 2006 at BARC, Mumbai

19. **Studies on electrical properties of $Cr_{2-x}Ti_xO_{3+\delta}$ by impedance spectroscopy** 125

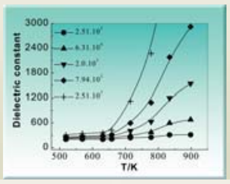

Pai, R.V. et al
Recipients of the Third Prize for Oral for Presentation at Thermans 2006 held in Jaipur during February 6-8, 2006

20. **Distribution of technetium in PUREX process streams** 130

Dileep, C.S. et al
Recipients of the Best Paper Award at the DAE-BRNS Symposium on "Emerging Trends in Separation Science and Technology (SESTEC-2006) held at BARC, Mumbai, during September 29-October 1, 2006.

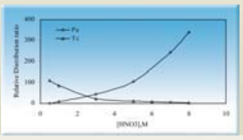

21. **Third phase formation in the extraction of U(VI), Th(IV) and Pu(IV) byN, N-Dialkyl aliphatic amides** 135

Jha, R.K. et al
Recipients of the the Best Paper Award in the Poster Catagory at the DAE-BRNS Symposium on "Emerging Trends in Separation Science and Technology (SESTEC-2006) held at BARC, Mumbai, during September 29-October 1, 2006.

22. **Beam dynamics for the 1 GeV proton Linac for ADS** 140

Pande, R. et al
Recipients of the Oral Presentation Prize at the DAE-BRNS Indian Particle Accelerator Conference (InPAC-2006) held at BARC Mumbai, during Nov. 1-4, 2006.

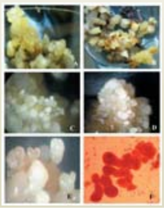

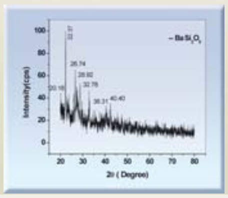
Intensity(cps)
100
80
60
40
20
0
20.16
22.91
26.74
28.92
32.78
36.31
40.40
– $BaSi_2O_5$
20
30
40
50
60
70
80
2θ (Degree)

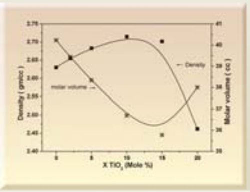
Density (gm/cc)
Molar volume (cc)
Density
Molar volume
X TiO_2 (Mole %)
0
5
10
15
20

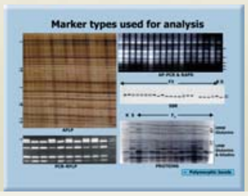
Marker types used for analysis
AFLP
PCR-RFLP
PROTEIN

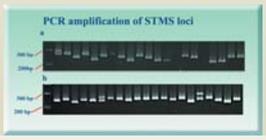
PCR amplification of STMS loci
a
b

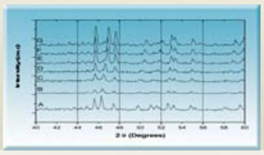
2 θ (Degrees)

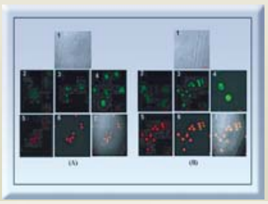
(A)
(B)

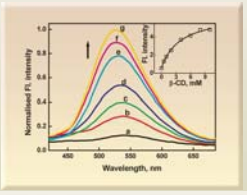
Normalised Fl. intensity
Wavelength, nm
Fl. intensity
β-CD, mM

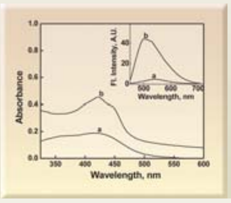
Absorbance
Wavelength, nm
Fl. Intensity, A.U.
Wavelength, nm
a
b

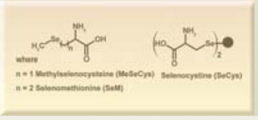
NH₂
OH
H₃C
Se
n
O
HO
Se
2
where
n = 1 Methylselenocysteine (MeSeCys)
n = 2 Selenomethionine (SeM)
Selenocystine (SeCys)

COMPUTER SIMULATIONS FOR STRATEGIC APPLICATIONS

S. Chaturvedi
Beam Technology Development Group
Bhabha Atomic Research Centre

**Dr S. Chaturvedi is the recipient
of the Homi Bhabha Science & Technology Award
for the year 2005**

Abstract

We have developed advanced capability in computer simulations, for a variety of problems of strategic interest. These include : hypervelocity impact and fracture involving solids, shock waves, reactive flows, radiation-hydrodynamics, pulsed electromagnetics and compact sources of powerful electrical pulses. Two and three-dimensional simulations are performed using parallelized computer codes that make use of parallel computers. The capability also includes the generation of materials data, such as, the equation of state and opacity for use in these simulations. Data generation is based on a variety of techniques, including density functional theory and ab-initio molecular dynamics. Validation of this capability is an ongoing process and includes extensive checking against experimental results obtained in several Indian laboratories.

This paper presents an overview of some of these capabilities and our plans for the future. Our goal over the next ten years, is the development of predictive, validated simulation capability in these areas, that is superior to what is available elsewhere in the world. This effort will be facilitated, by the development of powerful parallel computers by BARC, reaching a speed of 20-50 Teraflops during the 11th Plan and even higher during the 12th Plan period. We also plan to take up a systematic, long-term experimental programme for in-house generation of materials data under extreme conditions of pressure, temperature and strain-rates. This experimental programme will help validate the theoretical models, yielding a national database of materials properties under extreme conditions.

We have built an advanced capability in computer simulations for a variety of problems of strategic interest. These include hypervelocity impact and fracture involving solids, shock waves, reactive flows, radiation-hydrodynamics, pulsed electromagnetics and compact sources of powerful electrical pulses. Two and three-dimensional simulations are performed using parallelized computer codes that make efficient use of parallel computers. The capability also includes the generation of materials data, such as the equation of state and radiation opacity, for use in these simulations. Materials data generation is based on a variety of techniques, including density functional theory and *ab-initio* molecular dynamics. Validation of this capability is an ongoing process and includes extensive checking against experimental results obtained in several Indian laboratories.

In this paper, we describe the focus areas of this programme and our plans over the next ten years.

Need for computer simulations

Computer simulations help in the development and optimization of experimental systems at three levels. Firstly, while an experiment is being planned, it is usually necessary to choose reasonable values of a number of parameters. Simulations, even fairly simple ones, can help identify useful regions in "parameter space" where experiments can be focused. Secondly, once an actual system starts working, detailed simulations can help interpret experimental data, identify the most critical parameters and suggests changes for optimization. This can substantially reduce the time and cost associated with system optimization. Around the world, complex and expensive experiments are now being preceded by advanced simulations. Thirdly, once simulations are validated against experimental data, they can provide information which is difficult to measure through experiments. For example, conditions in the interiors of systems producing ultra-high-pressure shock waves can only be revealed by simulations.

All this does not mean that simulations can replace experiments – the two are complementary.

Focus areas

Our simulations are intended to support experimental programmes in a variety of areas. While the capability is fairly broad-based, the focus areas are as follows:

1. High-velocity impact and the resulting shock wave, fracture and penetration.
2. Shock waves and the flow of energy by thermal radiation in hot, dense plasmas.
3. Shock waves in energetic materials, where the shock waves are supported by chemical reactions that release large amounts of energy.
4. Powerful, short-duration pulses of electromagnetic waves, e.g. high-power microwaves.
5. Compact sources of powerful electrical pulses.

In the next section, we present a few examples of simulations for real-life systems.

Capabilities in focus areas

Hydrocodes for shock waves and fracture

Many strategic systems of interest involve shock waves in materials ranging from condensed phases (solids and liquids) to gases and plasmas. These shock waves can be produced in many ways, for e.g., by the high-velocity impact of a projectile on a target, by the detonation of energetic materials or by dumping a large amount of electrical energy into the target in a short time. The durations of these events typically range from nanoseconds to microseconds. The shocks are usually associated with high pressures (0.1 - 50 million atmospheres). These pressures could either be the result of high temperatures (tens of thousand or even millions of degrees) or high densities (several times the normal density of solids) or a combination of both. In pulsed electrical systems, there could also be high magnetic fields of several millions of gauss.

Simulating matter under such conditions requires several things. The first is the ability to predict the evolution of the system under these conditions – this is done using "hydrocodes", which model the system as a kind of "fluid". Such codes require, as an input, the equation of state of the material (solid, liquid, gas or plasma), i.e., the dependence of its pressure and internal energy on its temperature and density. In the case of solids, the models must also take into account the material strength (*yield strength and shear modulus*) and its dependence upon the temperature (*thermal softening*), pressure, plastic strain (strain hardening) and the strain-rate. In addition to this, if the solid undergoes fracture during the event, it is also necessary to incorporate fracture mechanics models which describe how voids are created (*nucleation*), grow and coalesce, finally leading to fracture of the material. The material strength and fracture models, since they are required for fast phenomena (*high strain-rates*) are different from those used to describe these phenomena at low strain-rates.

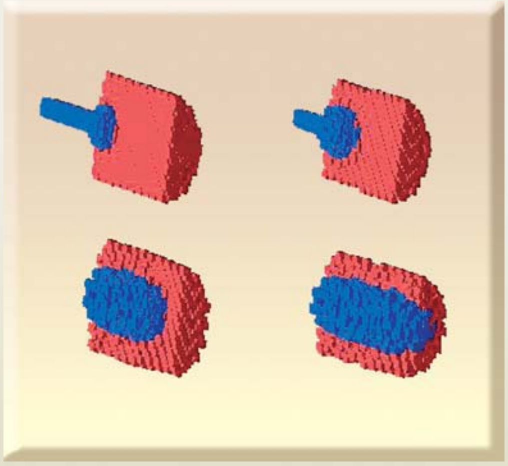

Fig. 1: High-velocity impact and penetration of tungsten projectile on armour plate

Our hydrodynamic simulations are performed using locally-developed codes that can describe the two- and three-dimensional, time-dependent evolution of such systems. The dynamic strength models include the Steinberg-Guinan, Johnson-Cook and Zerilli-Armstrong models. They can use either tabulated or analytical EOS data, including the effect of phase transformations. Several fracture models have been incorporated, such as the Void-Growth, Nucleation and Growth and Johnson-Cook models. These codes have been parallelized, in order to make efficient use of powerful parallel computers available with BARC.

Fig. 1 shows the high-velocity impact and penetration of a tungsten projectile on armour plate, obtained using Smoothed Particle Hydrodynamics (SPH) simulations. Fig. 2 shows the evolution to a final stabilized shape, of an explosively formed projectile. These simulations have been validated against experimental data available in the literature and elsewhere. Fig. 3 shows the interaction of three detonation waves in an energetic material.

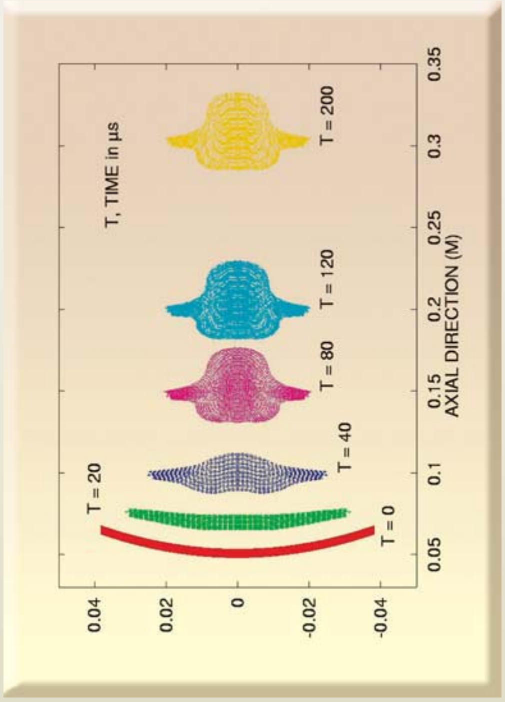

Fig. 2: Evolution of an explosively formed projectile into a final stabilized shape

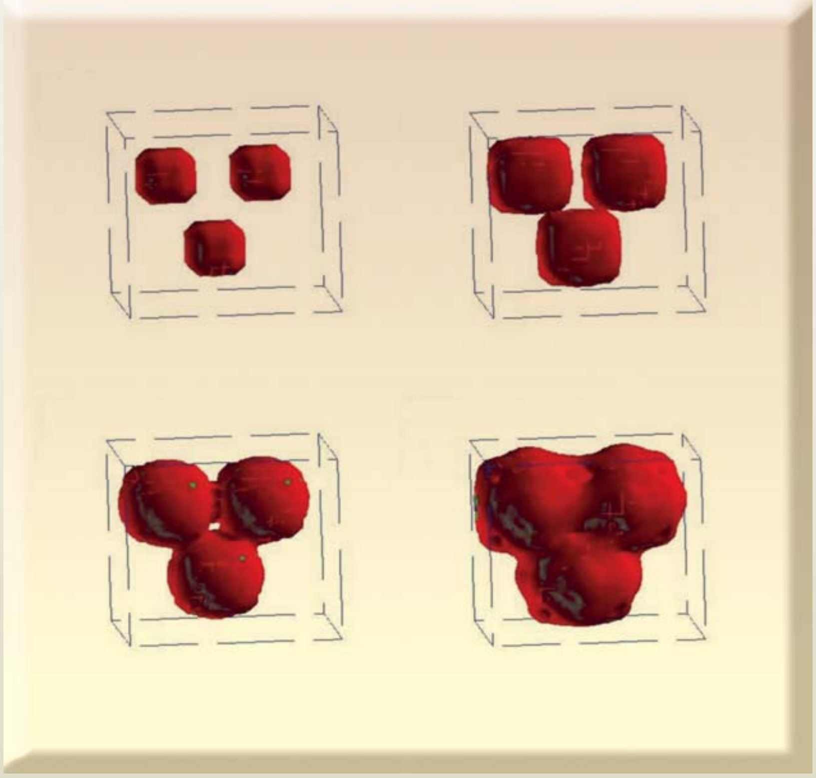

Fig. 3: Interaction of three detonation waves in an energetic material

Electromagnetic implosion and compact pulsed power generators

Ultra high-pressure shocks can be produced by the electromagnetic implosion of hollow metallic shells. Such implosions can yield pressures as high as 50 million atmospheres and compressions of upto 6 times the normal solid density. Such systems are being modeled using a locally-developed 2-D Magneto-Hydro Dynamic (MHD) code. Fig. 4 shows the cross-section of one such system, involving nearly spherical (quasi-spherical) implosion of an aluminium shell, driven by a current pulse having a peak value of 12 million amperes.

The same codes are also being used for modeling Magnetized Target Fusion (MTF) systems, which is a new promising approach to Nuclear Fusion.

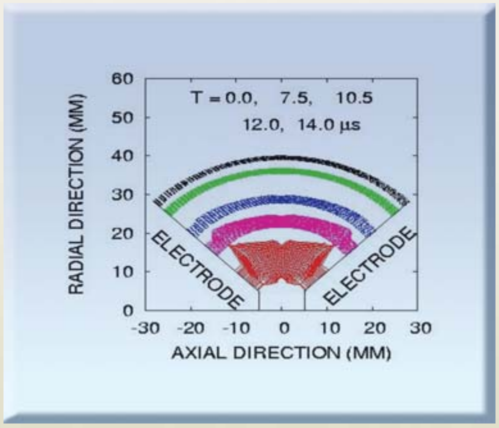

Fig. 4: Electromagnetic implosion of aluminium shell in quasi-spherical geometry

Electromagnetic implosion and MTF require powerful electrical sources, delivering currents of several millions of amperes for a few microseconds. One such source, called an FCG, converts the chemical energy of energetic materials into powerful, short-duration electrical pulses. Codes have been developed for modeling different types of FCGs and their predictions show good agreement with experimental results.

Generation of materials data

Many hydrocodes and radiation-hydrocodes require, as input, materials data such as the Equation Of State (EOS) and the radiation opacity of materials *under extreme conditions of temperature, pressure and strain-rate*. The results of simulations are only as good as the materials data used. Most countries with advanced strategic research programmes have produced their own databases of such properties, but they are not accessible to Indian researchers. Even when data is available in the literature, its accuracy is often questionable. Hence it is necessary to have a systematic, long-term programme for developing our own databases.

No single model is applicable for calculating the EOS, given that the densities and temperatures can vary over orders of magnitude. We have a suite of codes, combining in-house codes with publicly-available ones, for generating tables of EOS data. The full potential-LAPW method and pseudopotential-based approaches are used for determining the pressure in cold crystalline materials up to high compressions. The EOS for dense plasmas is generated using first-principles (quantum-mechanics based) molecular dynamics calculations. Fig. 5 shows the shock hugoniot of Aluminium and its comparison with published data.

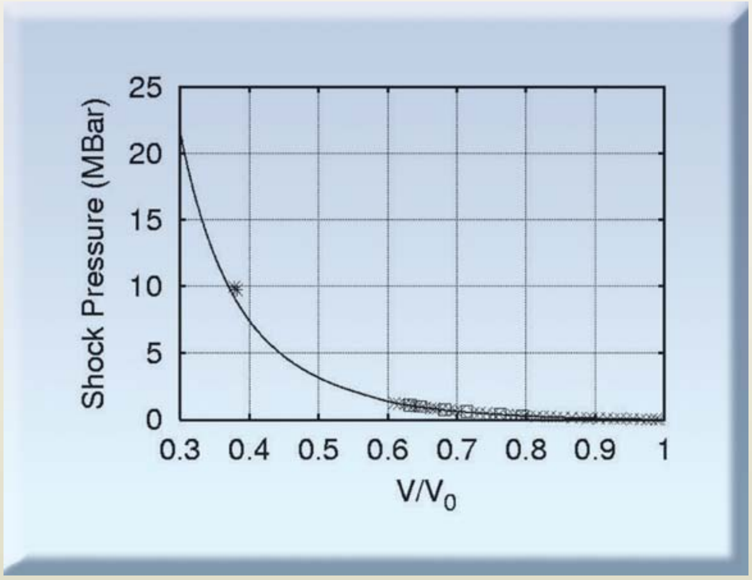

Fig. 5: Computed shock hugoniot for aluminium (solid line) and a comparison with published experimental and theoretical data

Some simulations involve modeling of energetic materials. In such materials, shocks lead to rapid energy release by chemical reactions which, in turn, maintain the shock. The reaction rates are sensitively dependent upon density and pressure and this dependence varies with the composition and initial density of the energetic material. Such data is rarely available in the literature. An effort has thus been started, to generate the properties of energetic materials, including their reaction rates, using Molecular Dynamics based on reactive potentials, that permit the formation and breaking of bonds.

Pulsed Electromagnetics

Sources of High-Power Microwaves (HPM), such as virtual cathode oscillators (Vircators), involve the conversion of the kinetic energy of an electron beam into microwaves. Fig. 6 shows a schematic of a vircator.

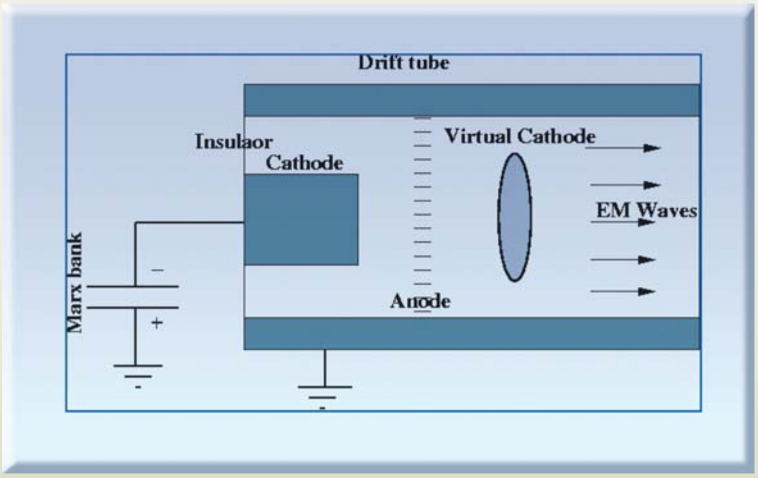

Fig. 6: Schematic of an axially-extracted virtual cathode oscillator (vircator)

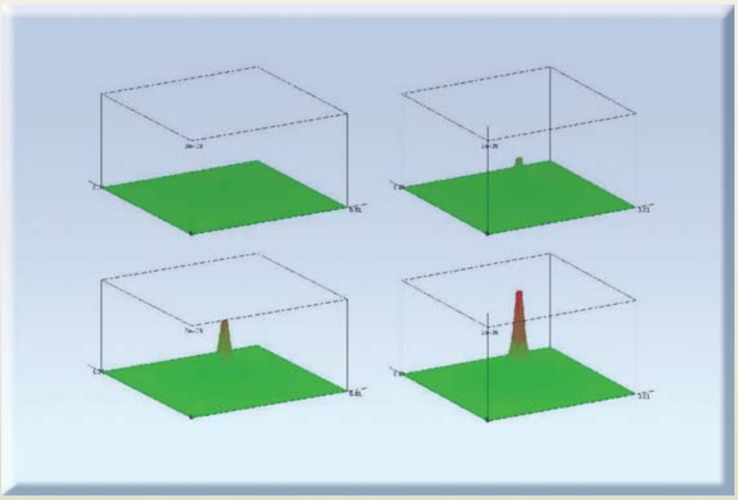

Fig. 7: Spatial variation of microwave power at the exit window of a vircator. Each frame represents a snapshot at the specified time

Such systems are being modeled using a locally-developed Particle-In-Cell (PIC) code. This model yields the complete three-dimensional evolution of electric and magnetic fields within the device, as also the self-consistent motion of electrons. Fig. 7 shows the time-evolution of the spatial distribution of output microwave power. This code will be of great help in designing and optimizing vircators for BARC's programmes.

An Electro Magnetic Pulse (EMP) consists of a powerful, short-duration burst of electromagnetic waves. Such pulses can be produced in various ways, one of which is a high-altitude nuclear detonation. The large electric fields so produced can damage sensitive electronic equipment over a wide area. EMP simulators are used for testing the susceptibility of electronic equipment to such pulses. Three-dimensional simulations have been performed, for a bounded-wave EMP simulator, using the Finite Difference Time Domain (FDTD) technique. These simulations have provided insight into

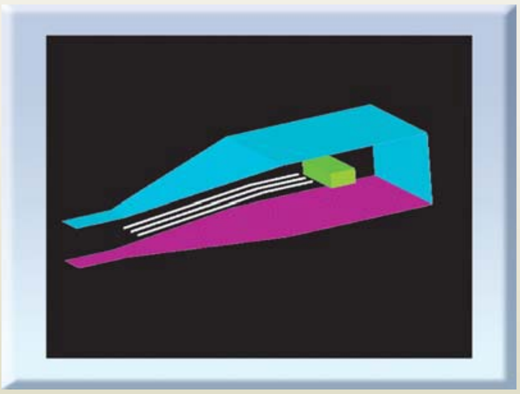

Fig. 8: Schematic of a bounded-wave EMP simulator with a spatial mode filter

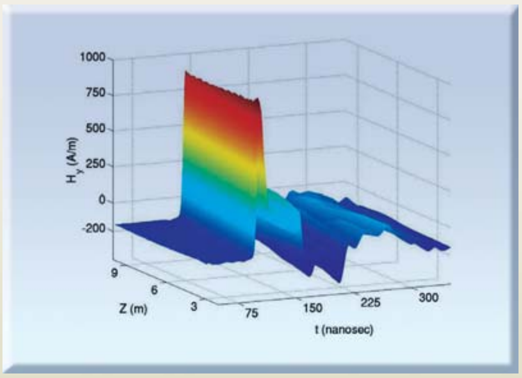

Fig. 9: One component of the magnetic field within the bounded volume of an EMP simulator

the previse fields "seen" by the test object, as also the effect of the test object on the pulse to which it is exposed. Since EMP simulators operate at very high power levels, leakage of electromagnetic power into surrounding areas is a major safety concern. The simulations have suggested ways of minimizing this leakage. Fig. 8 shows the schematic of an EMP simulator and Fig. 9 shows one component of the magnetic field within the bounded volume.

Future plans

Our goal, over the next ten years, is the development of predictive, validated simulation capability in these areas that is superior to that available anywhere in the world. This effort will be facilitated by the development of powerful parallel computers by BARC, reaching a speed of 20-50 Teraflops in the 11th Plan and considerably higher during the 12th Plan period.

The computational programme will be complemented by a systematic, long-term, experimental programme for in-house generation of materials data under extreme conditions of pressure, temperature and strain-rates. This experimental programme will help validate the theoretical models, yielding a National Database of materials properties under extreme conditions.

About the Author

Dr S. Chaturvedi obtained his B.Tech. in Chemical Engineering from IIT Delhi in 1985 and his Ph.D. in Chemical Engineering from Princeton University in 1989. He is currently part of the Beam Technology Development Group at BARC. His research interests include computer simulations of shock waves, pulsed electromagnetics, compact pulsed-power sources, hypervelocity impact and fracture, high strain-rate deformation, chemically reactive flows, plasma stealth systems and Magnetized Target Fusion.His interests also include the theoretical generation of materials data such as the Equation Of State and radiation opacity.

AN APPROACH TO MODERNIZING NUCLEAR INSTRUMENTATION: SILICON-BASED SENSORS, ASIC AND HMC

V.B. Chandratre, Menka Tewani, R.S. Shastrakar, V. Shedam,
S. K. Kataria and P. K. Mukhopadhyay
Electronics Division,
Bhabha Atomic Research Centre

Mr. V.B. Chandratre is the recipient of the Technical Excellence Award for the year 2005

Abstract

Modernization of nuclear instrumentation is pursued for realizing the goal of compact portable nuclear instruments, detector mount electronics and related instrumentation that can be designed, developed and manufactured, to mitigate contemporary instrumentation challenges. The activity aims at indigenous design and development of crucial components of nuclear instrumentation. Efforts are also undertaken to develop the critical microelectronics technologies to fulfill the gaps in nuclear instruments " end to end". The activity's objective has been fulfilled by working in close collaboration with semiconductor foundries and HMC (Hybrid Micro Circuits) facilities. Various ASIC, sensors, IP cores, HMC, display devices and critical instrumentation modules developed, are discussed.

Preamble

The design and development of nuclear instruments require a variety of high performance components and sensors. Till recently these components were available and activity based on this approach has grown mature, with good expertise in related areas but has availability and obsolescence issues. As the technologies have moved up, various competing devices, techniques and technologies are available today. It's important and as well prudent to catch up with these cutting edge developments, for a very strong reason that we have not been able to catch up with previous technology movements. Technology updates are difficult and have higher lead times with steeper learning curve. The Electronics Division has taken a modest initiative in fulfilling the gap in this area. Care has been taken to develop critical instrumentation by an approach of "mix and match", integrating the newer development in the existing instrumentation on the basis of merit and requirements.

Introduction

Nuclear instrumentation has been a strong driver for technology developments worldwide. The low / medium energy instrumentation requirements we meet fairly with combination of NIM, CAMAC, FASTBUS and VME-based instrumentation. With use of the sensors of higher granularity, higher event rate, imaging and tracking requirements coupled with complex trigger mechanism, the approach has changed to low power detector mount electronics or monolithic sensor with electronics. Rapid developments in semiconductor technology have aided in realizing this concept.

The CMOS technology is usually chosen for designing readout and signal processing integrated circuits on the merits of low power, high impedance for handling small charge, ability to build high gain amplifiers, availability of passive components (i.e. Capacitors resistors), bipolar transistors and analog and digital memories. Further, there is good support of digital /analog standard cells with low power advantage. With the same technology we can fabricate silicon detectors of type micro/macro strip, pixel, silicon drift detector SDD, DPFET, photodiode, Avalanche photodiode etc.

The Approach

Basically, nuclear detectors produce charge impulses in response to radiation. The readout electronics has to accurately measure this weak charge impulse. The objective is to measure this charge accurately for spectroscopy purpose and also get timely information. Other requirement is to detect event, corresponding to charge generated. On the other extreme is to measure the detector DC current when the rate of events is high. The typical configuration of the readout instrumentation is charge /current preamps, pulse shapers (filters), peak detectors and data conversion acquisition blocks. The modern detectors for position detection have higher granularity, this constrains the design of discrete readout electronics. The low power, low noise solution to higher channel density detector electronics with reduced readout latency, is the integration of detector with pulse processing and data conversion electronics. This integration can be achieved by development of ASICs (Application Specific Integrated Circuits). This however requires the designers to adapt integrated circuit design methodology by understating the process technology used and build skill sets to design up to transistor level. This also requires the proficiency to use EDA tools and design techniques.

Microelectronics is an expensive and unforgiving technology. CAD tools play an important role in reducing the time of design and development and reducing the risks associated, provided, design kits match with the tools. Therefore, a good CAD facility is augmented with state CAD golden tools for IC design, Semiconductor technology development and modeling. Besides the CAD tools a good computing cluster for supporting the tools, is also established. This facility is being further augmented with testing, packaging, Technology CAD (TCAD) and modeling tools. The CAD-FAB technology interface activity is a central activity to design and development.

Silicon Sensor Development

The solid-state radiation detectors are also important elements in the portable radiation monitoring instruments. Under the BARC-CERN-CMS collaboration, large area (6 cm / 6 cm) silicon strip detectors are developed. The detectors have low leakage and high breakdown voltage. The development of detectors was done using TCAD tools and the process was normalized with foundry parameters. These detectors are part of silicon pre-shower detector assembly of CMS experiment. Besides the strip detectors array, different types of detectors were designed and fabricated for in-house use. The detectors developed are Silicon strip detector, PN detector and Photo-diodes, pseudo pixel array. These detectors can also be used for neutron detection after boron/ gadolinium lining. Further more the photo and

UV-enhanced detectors can be interfaced with scintillators. The Small Area PIN diodes (3mm x 3mm x 300 microns) shown in Fig. 1 can be used for measuring gamma ray doses (30 KeV energy) over a dynamic range of 10^6 by pulse counting method. These PIN diodes are used in personnel dosimeters as well as in area-monitors.

Front-end Signal Processing ASICs

CMOS readout ASICs were developed using the 1-micron technology available at SCL Ltd. for optimally using these detectors. These ASICS are **OCTPREM, SPAIR, CODA & MICON (Fig. 1)**. They are **full custom analog / mixed designs** for Silicon detectors in various dynamic energy ranges.

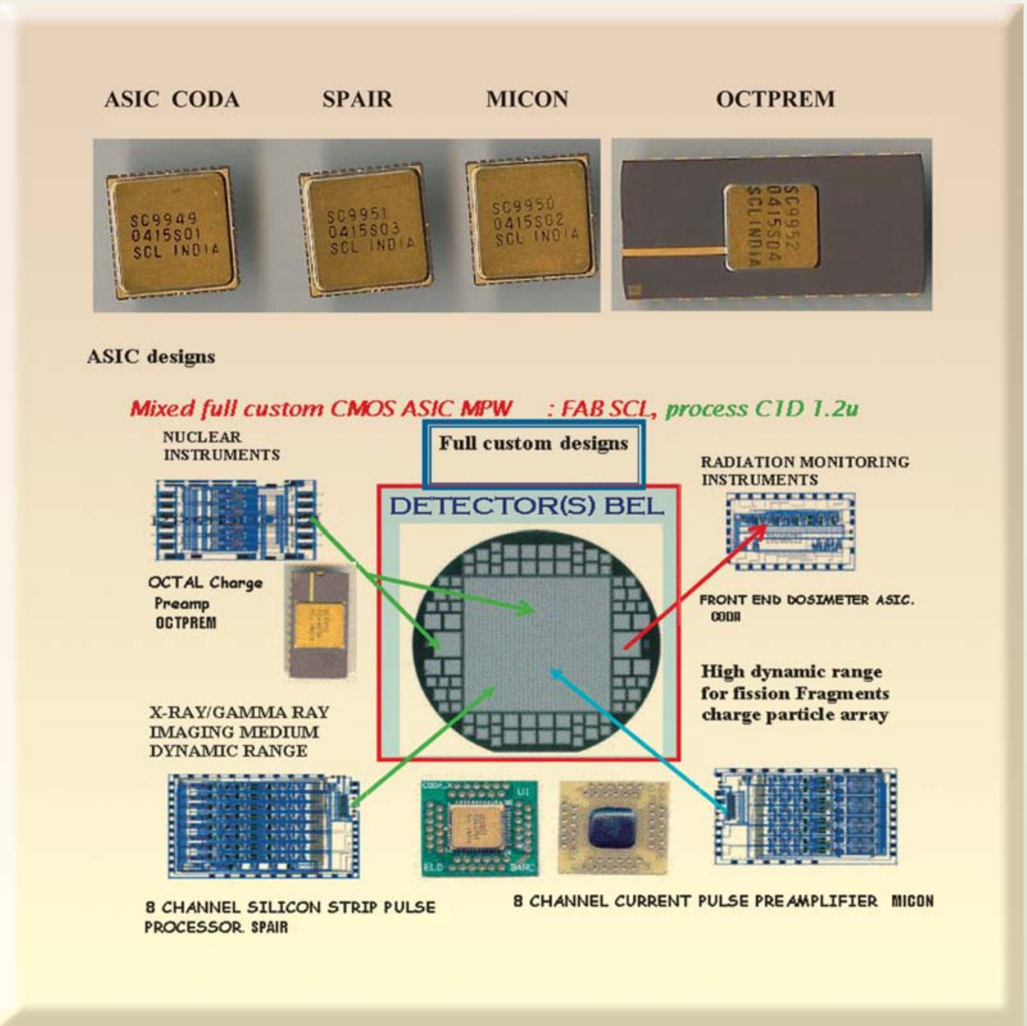

Fig.1 : ASIC and target detectors and applications

OCTPREM ASIC

This is an eight channel low-noise charge preamplifier in a modified folded cascode topology. The ASIC low noise is archived by careful design and sizing of the front end device optimized to 50pf detector load. The noise is reduced by increasing the feedback resistor to 100M ohms, this is achieved by using active devices, eliminating high meg resistors and related problems. The main feature of the preamplifier is that it can drive 50 ohms load. The charge gain is 2v/pC. The CSA is packaged in Ceramic DIP and Chip on board. Fig. 2 shows the typical response of CSA with 50 ohms load.

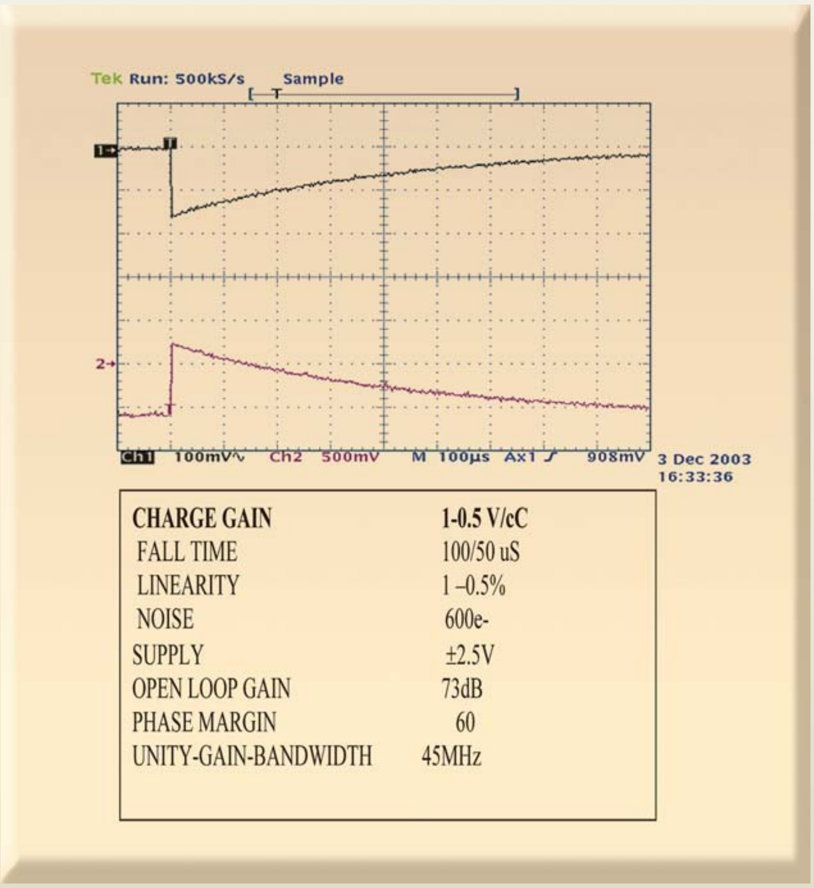

CHARGE GAIN	1-0.5 V/eC
FALL TIME	100/50 uS
LINEARITY	1 -0.5%
NOISE	600e-
SUPPLY	±2.5V
OPEN LOOP GAIN	73dB
PHASE MARGIN	60
UNITY-GAIN-BANDWIDTH	45MHz

Fig. 2 : Shaped output and type specification obtained

ASIC CODA (CO-chip for Dosimeter Application)

CODA stands for CO-chip for Dosimeter Application. It is a CMOS low-noise charge-sensitive amplifier, with semi-gaussian shapers followed by a general-purpose comparator. The gain, peaking time are digitally programmable. 'CODA' is best suited as a front-end chip for detectors with capacitance up to 50pf with input dynamic range of 120KeV to 8 MeV, targeted both for counting (e.g. dosimeter) and low energy spectroscopy applications. It can take either polarity inputs and output polarity can be fixed using polarity control. Preamplifier output fall time can be controlled externally to optimize noise and count rates. Additional In-built trigger channel with smaller peaking time is also available, for generating trigger input for track and hold in spectroscopy applications.

ASIC SPAIR

SPAIR stands for ***Silicon-strip Pulse Analog Integrated Readout.*** This ASIC is a typical nuclear instrumentation pulse-processing channel. The chip comprises of 8 pulse processing channels. Each channel comprises of a charge amplifier, shaper and track & hold. Also an analog multiplexer is included for multiplexed output. 'SPAIR' is best suited as a front-end chip for detectors with capacitance up to 50pf with input dynamic range of 660KeV to 10 MeV, targeted for spectroscopy applications in multi-channel environment e.g. Si-stripes detectors. It is equipped with both direct output and serial read-out at a rate externally clocked which can be given to analog-to-digital converter for processing. Additional trigger channel is also available for generating trigger input for track and hold in spectroscopy applications. Preamplifier output fall time can be controlled externally to optimize noise and count rates. The Gain, Output Polarity, Shaping time are adjustable by digital controls. The die size is 5.5 by 4.5 mm.

ASIC MICON' – Modified Current Conveyer

The chip comprises of 8 independent pulse-processing channels. Each channel comprises of a current pulse amplifier, shaper and track and hold. Also an analog multiplexer is included for multiplexed output. 'MICON' is best suited as a front-end chip for detectors with capacitance upto 50pf with very large input dynamic range of 10MeV to 150 MeV, targeted for both counting (with high counting rates) and spectroscopy applications in multi-channel environment e.g. fission detectors. It is equipped with both direct output and serial read-out at a rate externally clocked which can be given to analog-to-digital converter for processing. It can take either polarity inputs and output polarity can be fixed using polarity control. It can be directly connected with the detector (without ac coupling) and can handle leakage current of the order of 100uA.

AISC INDIPLEX and SINGLEPLEX

Continuing the development, using the 0.7 micron technology two more ASICs namely **INDIPLEX & SINGLEPLEX** were developed indigenously for CERN ALICE experiment pad detectors for VECC. Singleplex is single channel and INDIPLEX is 16 channel design. Fig. 3 shows the block diagram.

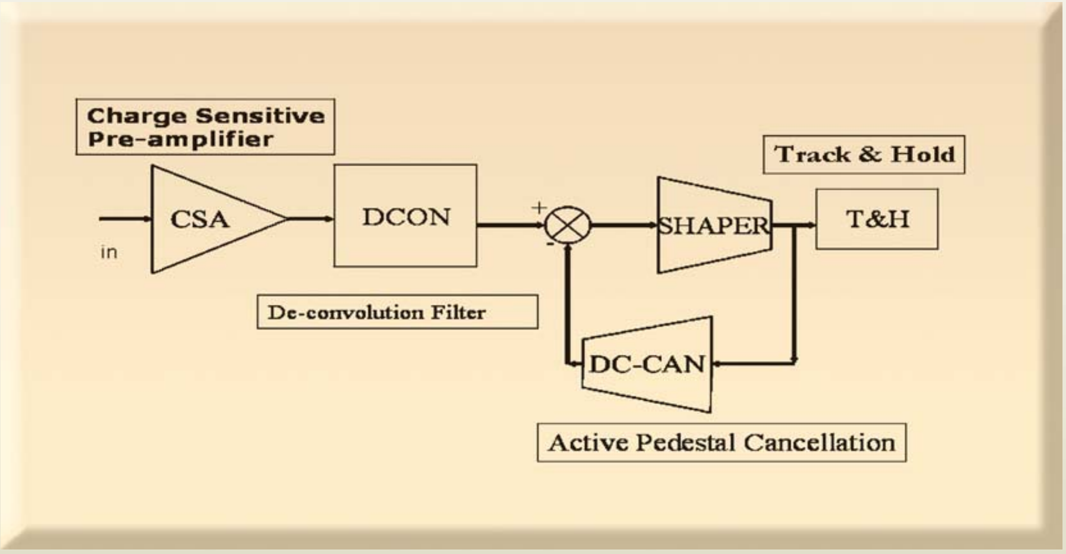

Fig. 3 : Block diagram of INDIPLEX and SINGLEPLEX ASIC

The ASIC is targeted for gas proportional counters / Si strip detectors. The design is optimized for the dynamic range of +500 fC to –500 fC, with provision for externally adjusted pole-zero cancellation. A dedicated filter, based on the de-convolution principle, is used for cancellation of the long hyperbolic signal tail, produced by the slow drift of ions, typical in gas proportional with the filter time constants, derived from the actual detector input signal shape. The pole-zero adjustment can be done by external DC voltage to achieve perfect base-line recovery to 1% after 5 µs. The ASIC's 0pf noise is 500e$^-$- rms for the peaking time of 1.2 µs with noise slope of 7e$^-$/pf. The gain is 3.4 mv/fC over the entire linear dynamic range with power dissipation of 14mW. This features equal gain over the dynamic range on both polarities and swing. The Singlepex ASIC serves as diagnostic chip for Indiplex. The chip can be used for radiation monitoring instruments. The design contains many unique circuit concepts. The feedback resistor greater than 100 MΩ is implemented by using current conveyer. Being a low power, low noise ASIC it has been integrated in the front end modules of radiation monitoring instruments. Fig. 4 is an output of Singlepex ASIC coupled to BF3 counter.

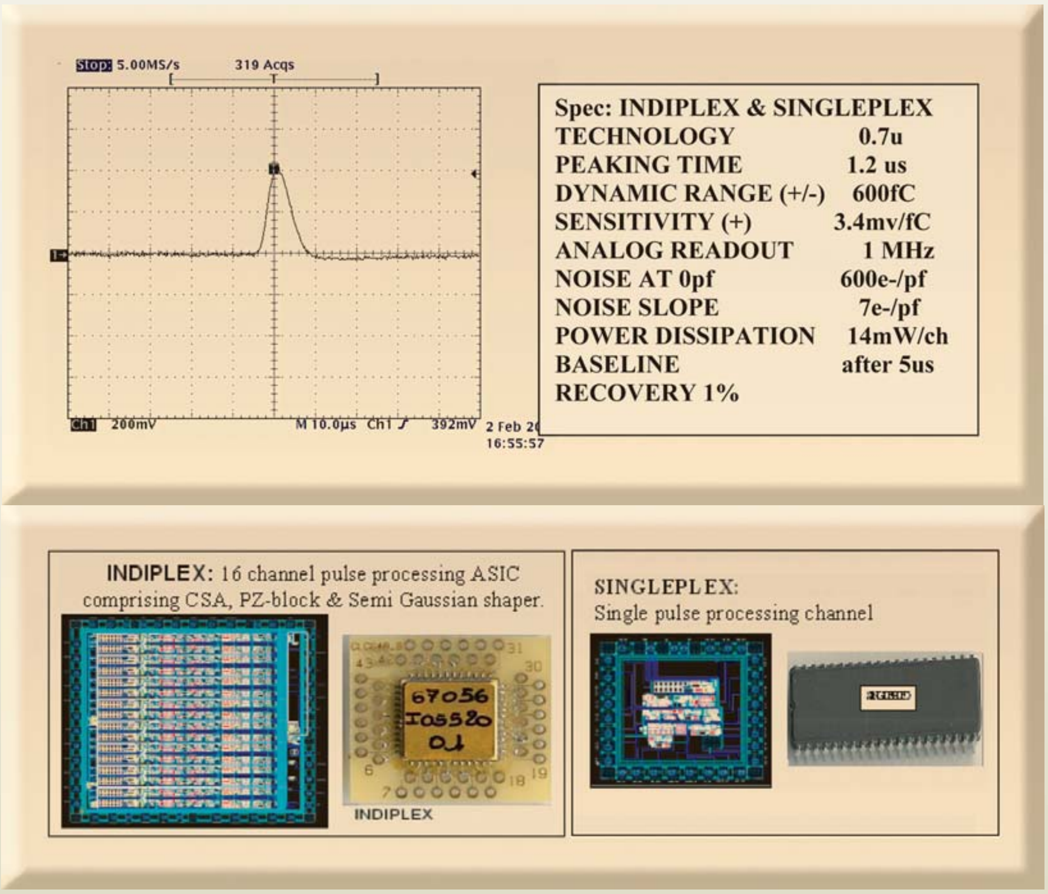

Spec: INDIPLEX & SINGLEPLEX	
TECHNOLOGY	0.7u
PEAKING TIME	1.2 us
DYNAMIC RANGE (+/-)	600fC
SENSITIVITY (+)	3.4mv/fC
ANALOG READOUT	1 MHz
NOISE AT 0pf	600e-/pf
NOISE SLOPE	7e-/pf
POWER DISSIPATION	14mW/ch
BASELINE RECOVERY 1%	after 5us

Fig. 4 : Output of Indiplex ASIC and Die photo

Data Conversion ASICs:ASIC ANUSHIKHAR and NuCAPS

In nuclear radiation monitoring instruments there is a need to have portable instruments. In order to cater to this requirement, low power data conversion ASICs like Anushikar, (Low-power pulse peak detector) is designed in 0.7u technology. The design is fabricated and tested. It features a peak detector using rectifying current mirrors with dynamic bias control and can be used with commercial ADC. (Fig. 5a).

NuCaps (Nuclear CMOS ADC for portable spectrometer) ASIC is a 12-bit low power nuclear ADC based upon Wilkinson ADC principle. It is designed around the Anushikhar ASIC, linear current source and gray counter. (Fig. 5b).

ASIC ANUSMRITI

ASIC ANUSMRITI (Fig. 6) is an Analog **Memory for transient digitization at 500MHZ** being developed to reduce the power consumption and cost of

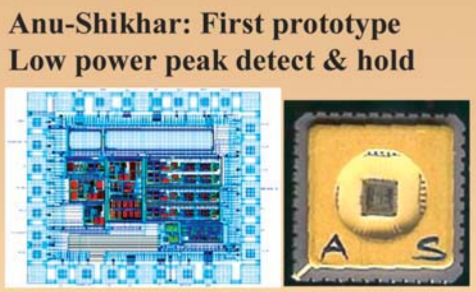

Fig. 5a : Anushikhar : First protype low power peak detect and hold

Fig. 5b : NuCAPS ASIC

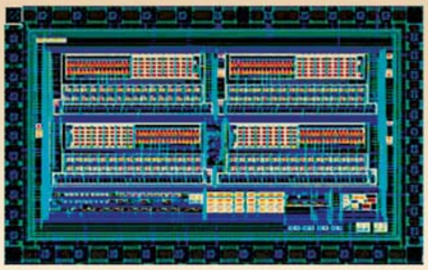

Fig 6 : Analog memory (AnuSmriti)

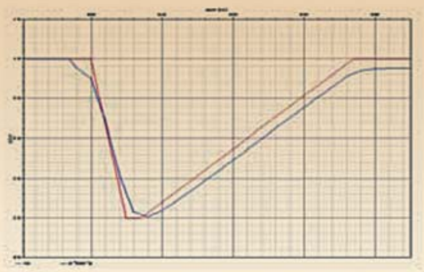

Fast signal recovery (simulation)

applications where continuous high-speed digitization is not required. The NuCAPS and Analog Memory ASIC designs are in the pipeline for fabrication.

In development of instruments, digital blocks area is also required. The first digital ASIC design and fabricated was **ADAM**. (ASIC for Dose Accumulation and measurement) developed in 1u Digital process of SITAR. The ASIC is designed to count total dose accumulated with in- built two phase LCD display driver. The ASIC features gain /unit section for a wide variety of detectors with alarm setup and data read/write vis serial port. This ASIC design is the precursor to all microelectronics development. The development is further complemented with development of IP cores for 8051 microprocessor, TMS9914GPIB controller, triplex LCD Display controller for developed triplex LCD display. The displays were developed at BEL.

Hybrid Micro Circuits

Design of ASIC is also complemented by the development of Hybrid Micro Circuits (HMC) (Fig. 7). These are specifically devoted to ultra fast signal processing or very high timing accuracy. Some of these hybrids like TAC (time to amplitude hybrid) having resolution of 50 ps and low power fast pulse amplifiers with rise time of 1.2-2 nsec for INO (Indian Neutrino Observatory), are in production. Notably there still exists a place for HMC in the arena of system on chip.

HMC incorporating the ASICs provides a very unique functionality.

Acknowledgements

The authors wish to thank Dr B. Bhattacharjee, former Director, BARC, Dr Banerjee, Director, BARC, Dr V.C. Sahni, Director Physics Grp. and RRCAT, Indore, Mr. G Govindarajan former Director E&I, Mr G. P. Srivastava Director E &I, Dr Nayak, Director Anurag DRDO, Mr. P.S. Dhekne, Associate Director, E&I, Dr, D.N. Singh, Dr Prabhakarao. BEL C N Noronha ZM (W) ECIL, Mr. N K Metha ECIL, Prof. Dr D.N. Sharma. IITB, Mumbai, Mr. M D Ghodgaonkar for support, guidance and encouragement. Authors also wish to thank Sammit Sardesi, Soumen Sarkar, Routray, Neeta, Rakesh Mall, Kori, Sudheer, Nidhi Gupta, V.D. Srivastava and S. Khole for their association and help.

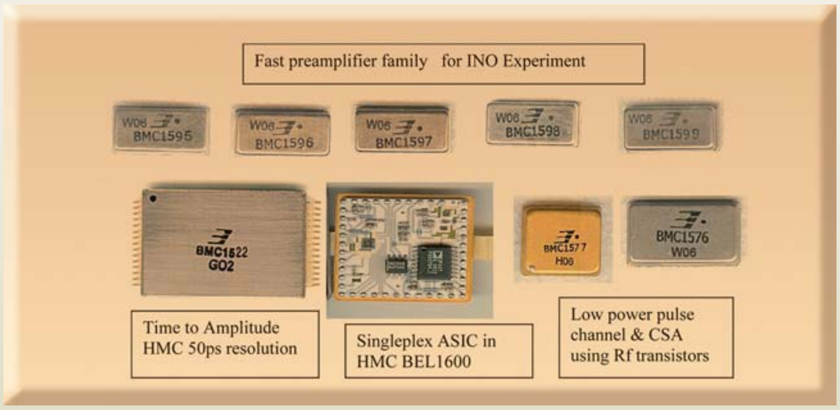

Fig. 7 : HMC developed

About the Authors

Mr. V.B. Chandratre did his post graduation in Physics from University of Poona. He joined the 31st batch of BARC training school in 1988. He has been working in design and development of nuclear and laser instrumentation. He is presently working in the area of micro electronics for development of ASIC, HMC, and sensors. At present he is leading the Micro Electronics Section of the Electronics Division.

Ms. Menka Tewani did her BE (Electronics & Communication) from the University of Rajasthan, in 2003. She joined the 47th batch of BARC training school. She has been working in the area of micro electronics for design and development of CMOS ASICs for nuclear instrumentation. Her areas of interest are design of mixed signal, high-speed data conversion ASICs and development of CAD tools and techniques.

Mr. R.S.Shastrakar joined BARC in 1985. He has been involved in the development and testing of various types of nuclear instrumentation. He is also involved in design and development of HMC for INO experiment. He has been involved in testing of various types of ASIC and HMCs. His area of interest is development of high speed, low noise instrumentation.

Ms. Vaishali Shedam joined BARC in 1998. Since then she has been actively involved in development and testing of nuclear instrumentation. She has been involved in testing of various types of ASIC and Hybrids. Her area of interest is development of high speed instrumentation.

Mr. P.K.Mukhopadhyay M Tech (Electronics) graduate, is from 14TH Batch of BARC training school. At present he is Head Electronics Division, BARC. His areas of expertise are Nuclear instrumentation, Hybrid Microcircuits and ASICs . His fields of interest include Nuclear pulse processing, data conversion and analysis, design of bipolar integrated circuits. Currently he is involved in the development of FBTR instrumentation, ASICs, HMC design. He has made significant contributions to various DAE/ E&I programmes.

Dr Sushil Kumar Kataria Joined BARC training school in 1966. For three decades, he worked in the area of experimental nuclear studies and nuclear instrumentation. He has zealously pursued the mission of modernization of Electronics and Radiation Detectors and related instrumentation at BARC. He has spearheaded the development of new radiation detectors, Hybrid Micro Circuits and ASICs (CMOS and BIPOLAR) for nuclear electronics, bio-medical and reactor instrumentation. To his credit he has 120 research papers in journals of international repute and over 200 in national and international symposia. He retired as Associate Director, Electronics and Instrumentation Group of BARC and is at present Raja Ramanna Fellow at the Electrical Engineering Department at IIT Mumbai, working towards the promotion of collaborative development programs in these areas between DAE Institutes and IIT

ADVANCES IN X-RAY AND NEUTRON IMAGING AND ITS APPLICATIONS

Amar Sinha
Laser And Neutron Physics Section
Bhabha Atomic Research Centre

Dr Amar Sinha is the recipient of the DAE Technical Excellence Award for the year 2005, for his work on X-ray and Neutron Imaging

Neutrons and X-rays provide a means to peer into the interior of objects, which are otherwise not optically visible. With the development of detector technology and new radiation sources, several new imaging technologies using x-rays and neutrons have emerged and have found widespread applications in industry, material science and medical imaging. The last two decades have seen the development of numerous new radiation-based imaging techniques and applications. The conventional film-based radiography using either x-rays or neutrons, has been replaced with digital imaging technique which has revolutionized the way images are acquired and analyzed. Imaging has expanded its scope from conventional qualitative radiography to quantitative imaging techniques such as image reconstruction for tomography and real time analysis of void fraction in two-phase flow. We have been engaged in the development of several new techniques using neutrons and x-rays and their application from basic to applied research. Some of these have been brought to the level where these technologies have been transferred for commercial production. This paper gives an overview of various techniques, which have been developed by us in the field of x-ray and neutron imaging.

X-ray Phase contrast imaging

The conventional approach in x-ray imaging, relies on absorption as a sole source of contrast in the image. It has remained unchanged for over a century despite many limitations. Though this approach works well in distinguishing between hard and soft substances, its major limitation lies in its inability to distinguish between different kinds of soft materials (low atomic mass), such as carbon composites or small carbon coatings or between tumors and surrounding normal tissues. This is an inherent limitation of absorption based imaging techniques. However the information regarding the details of these objects is still contained in the phase of the propagating radiation. As radiation (for example, x-ray) passes through a specimen, the phase gradients are developed between boundaries of materials having different densities. The effects of propagation of the x-ray wave can be conveniently described by the refractive index n, which is a complex quantity and is given by,

$$n = 1 - \delta - i\beta$$

The real part d corresponds to the phase shift due to scattering and the imaginary part β corresponds to the absorption of the wave.

At the typical energies used for such imaging of soft materials (~10-100 kV), the phase shift term in the index of refraction of x-rays is 1000 times greater than absorption term. Hence the images based on the phase contrast effect are still visible for such materials even though absorption contrast is poor and it shows much greater detail, particularly of boundaries or edges. In the last few years, this imaging technique named *Phase Sensitive Imaging* is being explored to remove the limitations of convention absorption based imaging. This new technique promises to revolutionize the way, materials with low atomic mass or medical imaging of soft tissues have been conducted till now. Experiments conducted using this new approach have shown unprecedented clarity in imaging of composite materials or soft tissues[1-2].

This technique could not be utilized till now due to the special requirement of coherent x-ray source. However with the availability of microfocus x-ray source and synchrotron-based x-ray sources, this technique has been used for both industrial and medical applications. The synchrotron sources are able to provide x-rays, which meet the criteria of both temporal and spatial coherence and hence these are ideal sources for these imaging applications. A large number of techniques have been developed, to obtain phase-enhanced x-ray images. We shall describe here one such technique called "In-line x-ray phase contrast imaging" where edge enhancement in images occur as a result of interference between diffracted rays and direct rays at the boundaries of the objects. Moreover for formation of images using this technique, the requirements of spatial coherence is more important than temporal coherence and hence this technique can to some extent be implemented using microfocus X-ray sources which have only spatial coherence and not temporal coherence.

We have set up an experimental facility, to evaluate the x-ray phase contrast imaging technique for industrial and medical applications (Fig. 1). The x-ray detector consists of Gd_2O_2S:Tb phosphor layer deposited on an entrance window of 4:1 glass fibre-optic taper. The taper is bonded to front-illuminated CCD with active pixel pitch of 13.5μm X 13.5μm and having 1024 X 1024 pixels. Hence, the effective area of the detector is 55μm X 55μm with pixel size of 54 μm X54 μm. The thick fiber-optic taper not only serves to increase the detector area, but it also helps to protect the CCD chip from the direct impact of X-rays. The image readout frequency is 1 MHz. The CCD can be cooled down up to –35 °C using a combination of thermoelectric and chilled water-cooling. We have used 160kV 1mA, microfocus X-ray source for these experiments. It has a tungsten target and nominal focal spot size of 5μm. Figs. 2-5 show the images of various objects taken with this set-up in phase contrast radiography mode.

Fig .1 : Experimental set-up for phase-sensitive imaging experiments

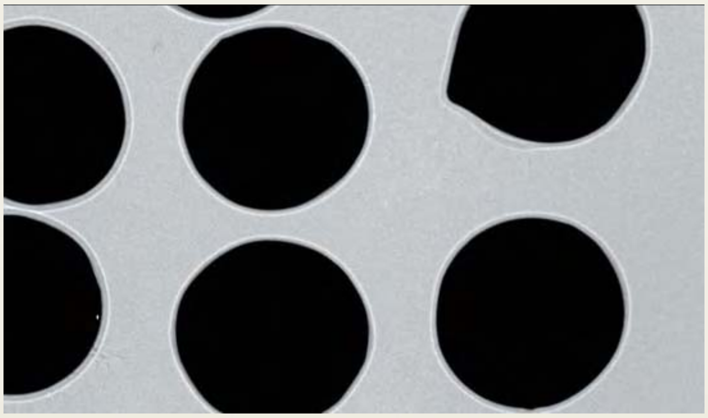

Fig. 2 :Phase contrast image of a zirconia micro-sphere (500 μm) coated with pyrocarbon (40 μm) using microfocus source

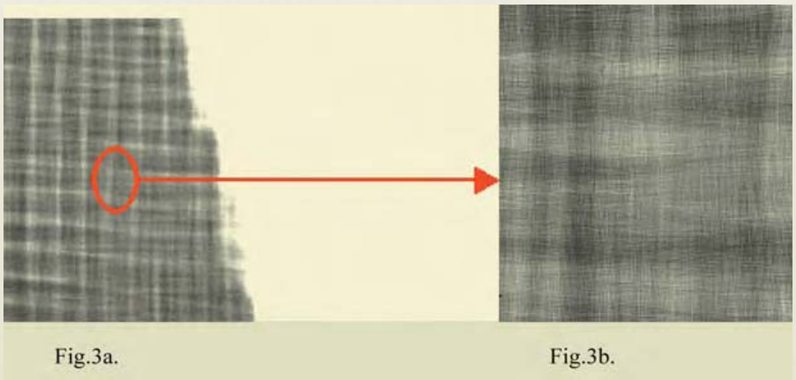

Fig.3a.

Fig.3b.

Fig.3. (a) Shows the magnified x-ray radiograph of a carbon composite sample used in aircraft industry and (b) shows the phase contrast image of the red-circled portion revealing individual fibres (microfocus source is used in the experiment)

Fig. 4 : Image of a bee taken in phase radiography mode (microfocus source)

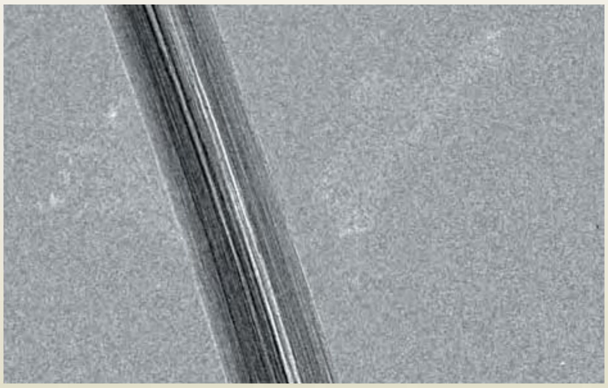

Fig. 5 : Phase contrast image of carbon fibre using microfocus x-ray source and x-ray CCD

In India, Indus-II synchrotron source is under construction at RRCAT, Indore. In collaboration with Tata Memorial Hospital of Cancer Research, Mumbai, we are developing a phase-sensitive imaging beam line at INDUS-II. Design of this beam line is in progress. This will be used for phase contrast imaging, diffraction enhanced imaging, phase contrast tomography and for the development of other advanced imaging applications.

Three dimension (3D) cone beam tomography

Computed x-ray tomography (CT) permits retrieval of three-dimensional information from inside an object. To make a CT measurement, several radiographic images (or projections) of an object are acquired at different angles and the information collected by the detector is processed in a computer. The final reconstructed image, generated by mathematically combining the radiographic images, provides the tomography image which gives the exact locations and dimensions of the internal features of the object. Conventional third generation x-ray tomographic systems produce two-dimensional sectional images, using either fan beam or parallel beam geometry. Fig. 6 shows schematic diagram of such a system used in medical as well as in industrial applications. An x-ray fan from an x-ray source penetrates the object and the attenuation is measured by a linear detector. In medical tomographs, the source and detector rotate around the object (patient). However in industrial applications, it is advantageous to rotate the object. During the rotation, a set of one dimensional projection is measured and reconstructed. The result is a two dimensional image.

To get a three-dimensional image with such a conventional tomography setup, the object has to be moved along the direction of the axis of rotation and several scans have to be performed. A stack of slices are mounted to get a three-dimensional image. This procedure is very time-consuming. Keeping this in mind, we have developed a tomography system which allows the reconstruction of three-dimensional structures, using only rotation along one axis with no horizontal or vertical translation of the sample. A conical beam from an X-ray source penetrates the object. The attenuated radiation is measured by an area detector. In order to irradiate the

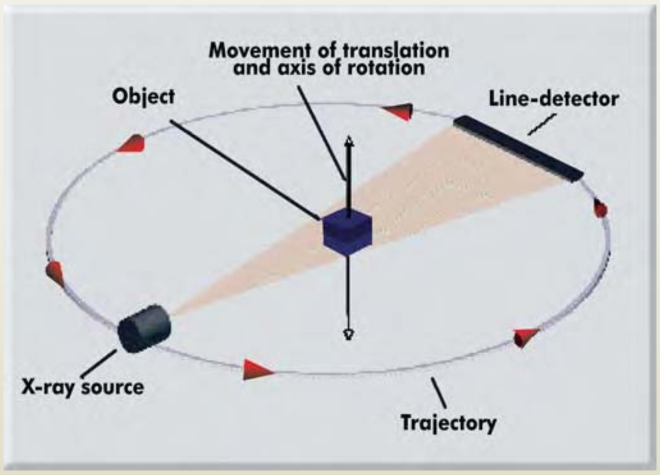

Fig. 6 : Schematic diagram of 2D fan beam tomography setup

object from all sides, the X-ray source and the detector are either rotated around the object (for medical applications), or the object rotates in the X-ray cone (for industrial applications). During rotation, a set of projections are measured and stored. These set of projections are then used to reconstruct the 3D structure of the object. This method known as Cone-beam Computed Tomography (CT) is an emerging imaging technology (Fig. 7). It provides all projections needed for three-dimensional (3D) reconstruction in a single spin of the object. However, the algorithm for reconstruction of 3D images becomes much more complex and computationally involved as compared to 2D reconstruction algorithm. Two main families of reconstruction algorithms have been developed for cone beam x-ray tomography with circular source trajectories: the generalized filtered backprojection methods and the 3D Radon transform inversion. Both methods have their own advantages and limitations. We have implemented Feldkamp algorithm for our cone beam tomography setup. This algorithm has been numerically checked using simulated phantoms.

Fig. 8 : Experimental set-up for cone beam tomography experiments at L&NPS, Purnima Labs, BARC

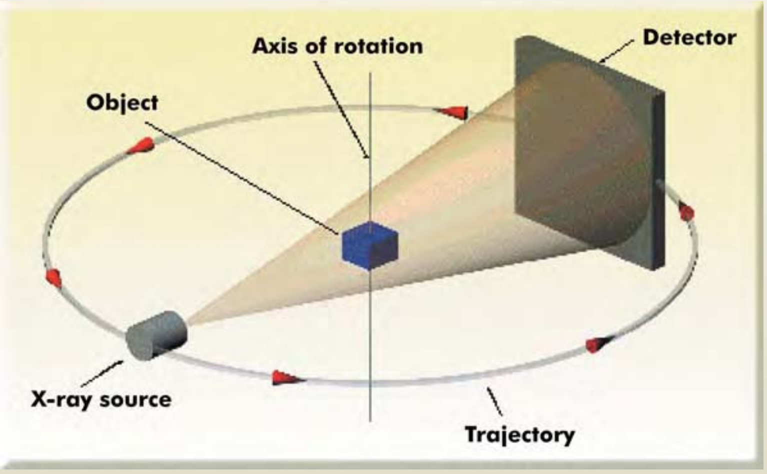

Fig. 7 : Schematic diagram of 3D cone beam tomography setup

Fig. 8 shows the experimental setup used for cone beam tomography experiments. The data is collected using a cooled CCD detector, which is coupled to a large area x-ray scintillator through a lens and a 45° oriented mirror. The CCD can be cooled to below -45 °C to minimize noise and has 16 bit dynamic range. Some initial experiments have been conducted using this setup to analyze its performance[3-5].

Fig. 9 shows an actual sample used for 3D reconstruction. This is the end cap of reactor fuel bundle made up of aluminum. Fig. 10 shows 3D reconstruction of the above sample, by taking 200 projections in full 360°. The second image of this figure, shows sectioning of this reconstructed object on computer, to reveal its interior. This technique provides a means to dimensionally measure the internal structure and make an stl file for rapid prototyping. Thus it can be used as a tool for reverse engineering.

To demonstrate the usefulness of this technique we have carried out tomography on a sample having Zircaloy-Zircaloy weld. Fig. 10a shows reconstructed the image.

Fig. 9 : Experimental test phantom

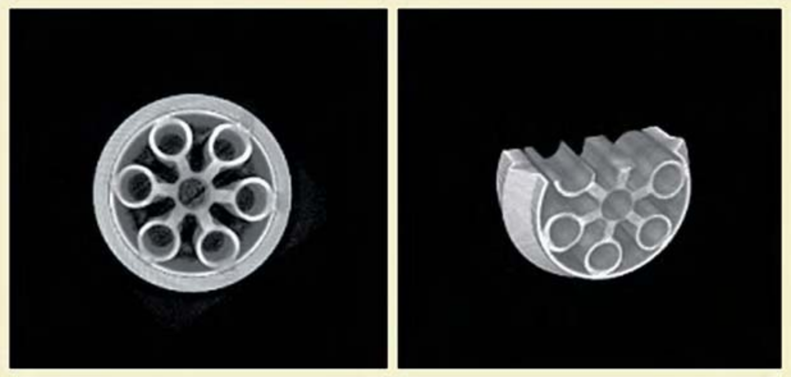

Fig. 10 : Reconstructed volume of experimental test phantom (cull image and cut-way view)

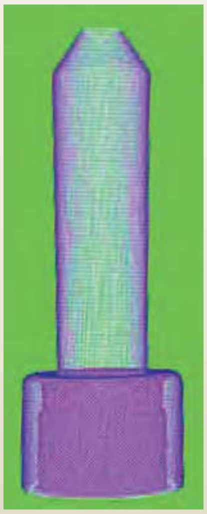

Fig. 10a : Reconstructed image of a sample with zircaloy-zircaloy weld.

Three dimensional microtomography

We have developed x-ray tomography using conventional x-ray sources. However with x-ray tubes of mm size focal spot, we could obtain only mm size resolution. For many applications such as miniature electronic circuits, small biological samples such as human tooth, defects within a diamond etc. such a millimeter size resolution was insufficient. With the availability of small focal spot (a few micron) x-ray tubes, we have set up a microtomography facility. This set up was used, for interesting applications such as mapping of defects and cracks within raw diamond for its optimum cutting, finding the distribution of cavities in a human tooth etc.

We describe below one such application carried out by us on the microtomography of unpolished diamonds and obtained distribution of impurities and cracks within the object. The experiments were conducted in collaboration with IIT, Mumbai. These experiments were conducted to determine volume distribution of impurities within diamond and then this data was fitted to another program which generates the maximum permissible volume of polished diamond that can be obtained from it, by avoiding the impurities (Fig. 11). This can be a valuable tool for diamond cutting industries and many other such applications.

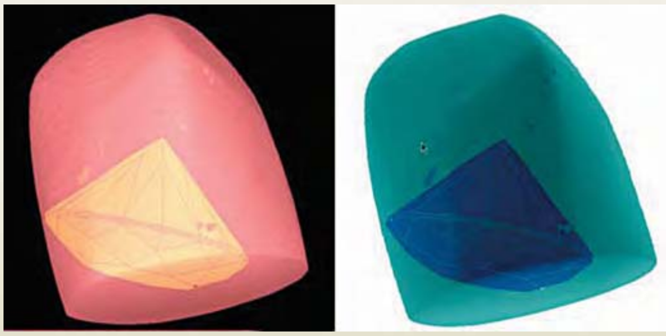

Fig. 11 : Reconstructed image of unpolished diamond along with the computer generated volume of polished diamond which can be cut from this diamond piece

Development of CCD-based area detector for X-ray diffraction studies

X-ray diffraction is a widely used tool in material science, for structural characterization of substances. In particular, real time x-ray diffraction imaging is useful for a variety of applications such as : to orient single crystals, to study crystal lattice rotation accompanying plastic deformation, to measure the rate of grain boundary migration during re-crystallization annealing of cold-worked metals, to monitor the amorphous to crystalline phase transformation of rapidly solidified metals, to rapidly measure residual stress and quick scan of pressure-induced phase transitions in materials. In particular, X-ray diffraction under high pressure is normally recorded using Imaging Plate (IP) detector. The sample size under Diamond Anvil Cell (DAC) used for high pressure experiments is very small and due to this, the time taken for data collection using IP detector, is quite large. In order to mitigate such a problem, we have developed a real time x-ray diffraction setup which shows x-ray diffraction images on real time basis or in an online manner[7-9].

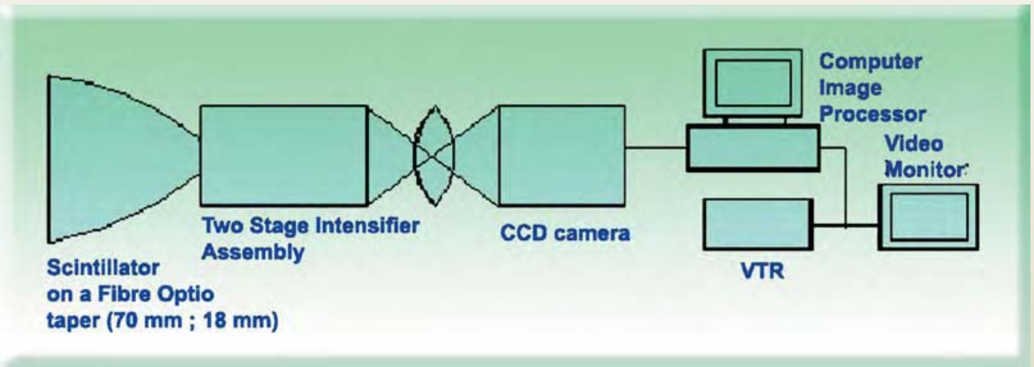

Fig. 12 : Schematic diagram of ICCD-based area detector for online diffraction imaging

The system has been developed using an intensified CCD (ICCD) based detector system. This system can record data in a few seconds. This is particularly useful in high pressure research as well as for dynamic x-ray diffraction studies such as those indicated above.

Fig. 12 shows schematic diagram of the ICCD-based XRD setup. Fig. 13 shows XRD pattern and their one dimensional radially integrated pattern of $AuGa_2$ powder sample recorded using this detector. The recording time is in seconds.

In Fig.14, application of this setup for diffraction pattern under DAC at ambient pressure for $In_{0.25}Sn_{0.75}$ is shown

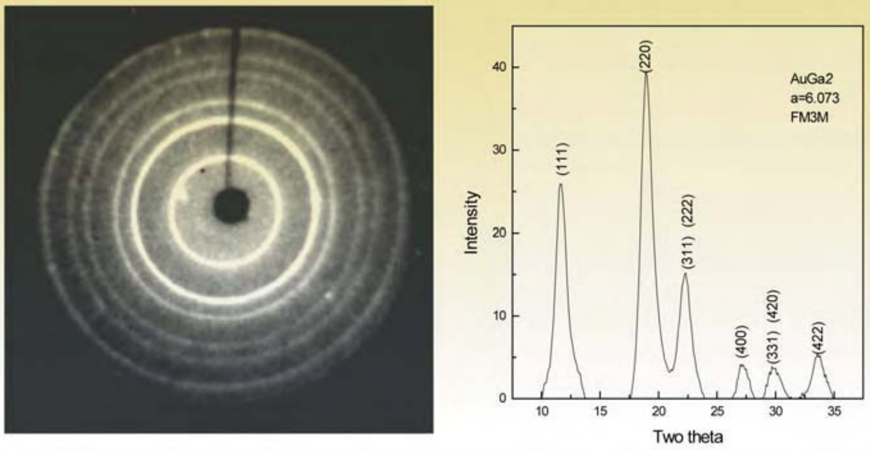

Fig. 13 : Intensity pattern of $AuGa_2$ powder sample and its 1D radially integrated pattern

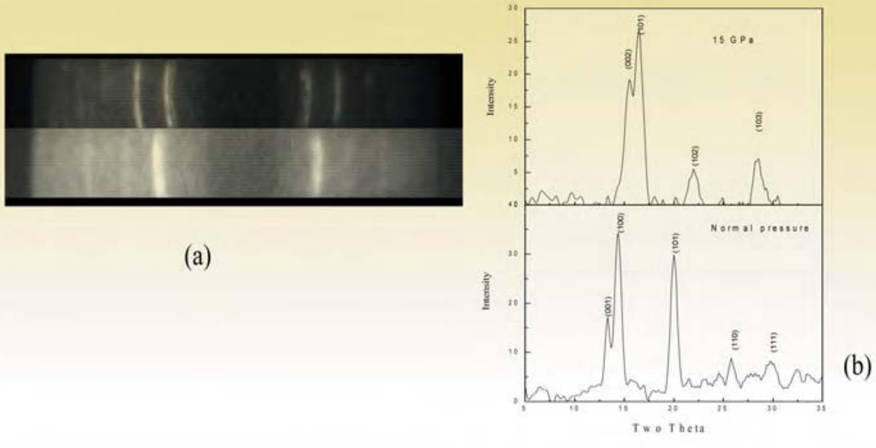

Fig. 14. (a) Diffraction pattern under DAC at ambient pressure for $In_{0.25}Sn_{0.75}$ is shown at the top and at 15 Gpa is shown at the bottom (b) 1D radially integrated plot of the same pattern

at the top and at 15 Gpa at the bottom. The phase transition can be clearly seen. This is also clear from the 1D pattern shown in Fig. 13(b).

Digital Medical Imaging System

As a part our efforts to bring the benifits of basic research to practical applications, we have developed a digital medical imaging system which can be used in the most demanding environments of hospitals, for day-to-day diagnostic applications.

Conventional medical imaging technique, of using screen film has remained unchanged ever since its inception, despite tremendous progress made by digital imaging technology. Besides possibility of reduced doses due to improvement in sensor technology and image acquisition methodology, digital medical imaging can substantially improve the throughput of radiological units of hospitals. Though the basic elements of the technique of digital imaging are known, there has been little attempt to make an indigenous system, which will be on par with similar imported systems. We have made an effort to design such a digital medical imaging system, which can be used in multipurpose roles. The system has been designed using high resolution, high dynamic range CCD and intensifier, interfaced with a locally available x-ray generator. The design of such a medical system involves a variety of multidisciplinary tasks ranging from development of computer controlled x-ray generator manipulation, interface with imaging system, synchronization of imaging system with x-ray generator for millisecond snaps, development of procedures for fluoroscopy, radiography and angiography, database management system and a easy-to-use user interface[10].

Since the x-ray generators available in local market are designed for film-based radiography, the first task was to make such a generator, computer controlled. This was done using a series of relays. For imaging side, a digital 12 bit CCD with 1 K x 1K pixels was optically coupled to a high dynamic range 12 inch image intensifier. The CCD chosen was such that, it can operate at the rate of 30 frames per second to single or multi millisecond pulsed exposure mode, with external trigger. This was necessary to make the system suitable for both radiography and continuous or pulsed fluoroscopy applications. For synchronization of CCD and x-ray generator, a high sensitivity photodiode was used. A control system interfacing all the sub components was designed and interfaced through a user PC. Some of the characteristic features of this system are: simultaneous analog and digital images, multi-monitor display of different images using a special graphics card. The system was tested with international grade anthropomorphic phantoms and scientific contrast and resolution phantoms, for validating the quality of image. The system has been designed for multipurpose applications such as digital fluoroscopy, digital radiography. The digital subtraction angiography has also been incorporated to take care of online subtraction of mask and live picture. Several modalities especially designed for angiography such as overlapping of mask and live images, pixel shifting, image rotation, simultaneous display of movies and images for easy comparison have been included, for angiography purpose.

The system has its own database management and can be easily interfaced with existing hospital data base management system. One of the features of this system is off-line study mode where all the images and movies are stored in digital format and can be referred to anytime later. For data storage and its management a special scheme has been designed, where one can take daily, incremental or selected data backup, on any type of media or on a separate PC server.

One of the highlights of the system is its very powerful user interface. The system is designed such that, it can do quantitative radiography such as gray value mapping or measurement of anatomical distances or microradiography. Besides a standard image processing function, online averaging and recursive filtering to improve signal-to-noise ratio has been incorporated. All the images are linked to its data besides having the provision for separate annotation of patient detail and exposure condition and marking function on the image. The provision for data archival, linking to central server, has also been incorporated. We have also developed a stand-alone user interface, so that, the images can be viewed directly in different departments of the hospital. Fig. 15 shows the schematic and actual setup at the BARC hospital.

The system and its software were tested for its ruggedness, for several months before installation at

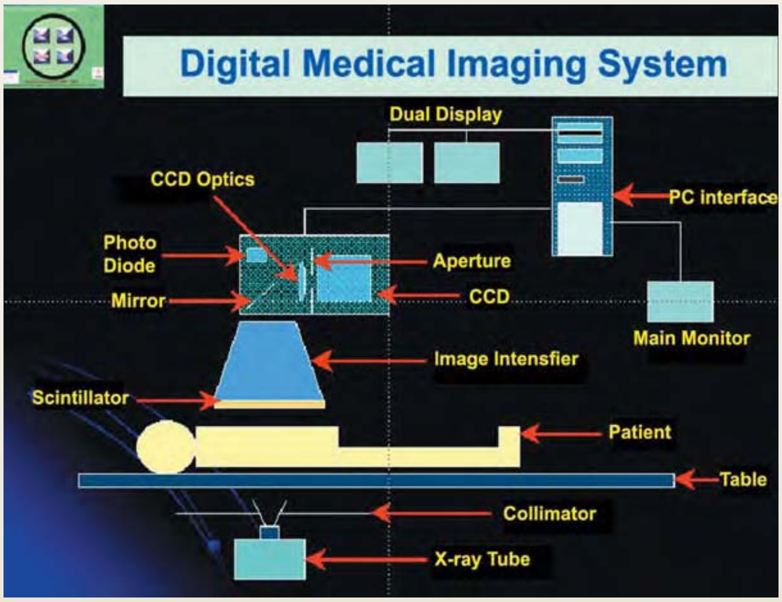

Fig. 15 (a) : Schematic layout of the Digital Medical Imaging System

Fig .15 (b) : Photograph of Digital Medical Imaging System at BARC hospital

Fig. 16 : Results of investigation done at BARC hospital

BARC hospital. At BARC hospital about 1500 patients have been diagnosed using this system (Fig. 16) and it has provided valuable inputs for knowing the strengths and shortcomings of the system. Presently the system at BARC hospital is being used for special investigative purposes, mostly for real time applications such as barium meal etc. This being the first design, there have been some shortcomings, which are constantly being improved upon.

The technology of medical imaging is continuously being upgraded and in order to keep pace with technological developments, we have initiated programs to improve our technology using flat panel detector and only CCD based systems.

Portable unclaimed baggage inspection system

A number of technologies have been developed in order to counter the threat of terrorism. X-ray based inspection systems are used by security agencies at airports, high security buildings for investigation of suspected objects. However most of these X-ray systems are fixed type and the object to be inspected has to be carried to the X-ray imaging system. However, in recent years there has been an increase in explosives being left in suitcases at public places where X-ray machines cannot be easily accessible. Therefore, there is a need for a portable lightweight X-ray inspection system, which works on battery and can be used wherever an unidentified object is located. We have developed a portable battery-based

Fig. 17 : Photograph of portable baggage inspection system

x-ray imaging system (Fig. 17). This system can be used by security agencies for on the site bomb disposal, checking of parcels, unidentified packets and bags etc. Some of the main feature of this system are: complete wireless operation of the system including x-ray generator and imaging system from a distance of about 150 ft and the availability of the images on operator's laptop with in seconds. Thus, the operator using this system need not be near the object being detected. Very sophisticated user interface has been provided (Fig. 18) for analysis of the images and for quick decision making[11]. The whole system can be carried in a suitcase. X-ray Image of the simulated baggage containing battery, wires, knife and X-ray image of electronic circuit board are shown in Fig. 19. This system has been tested for at least 18mm steel penetration and 42 SWG wire resolution (Fig. 20).

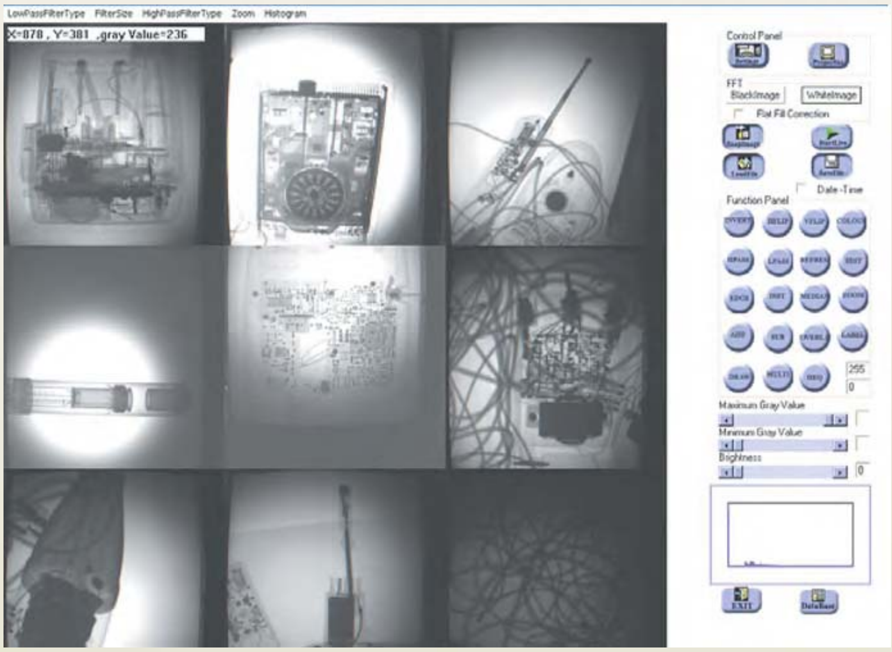

Fig. 18 : GUI of imaging software for acquisition and enhancement

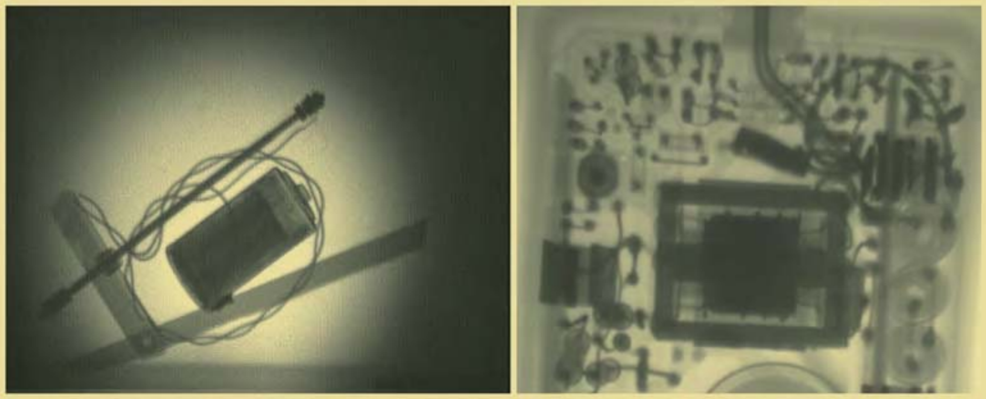

Fig. 19 : Images of various test objects taken using the portable baggage inspection system

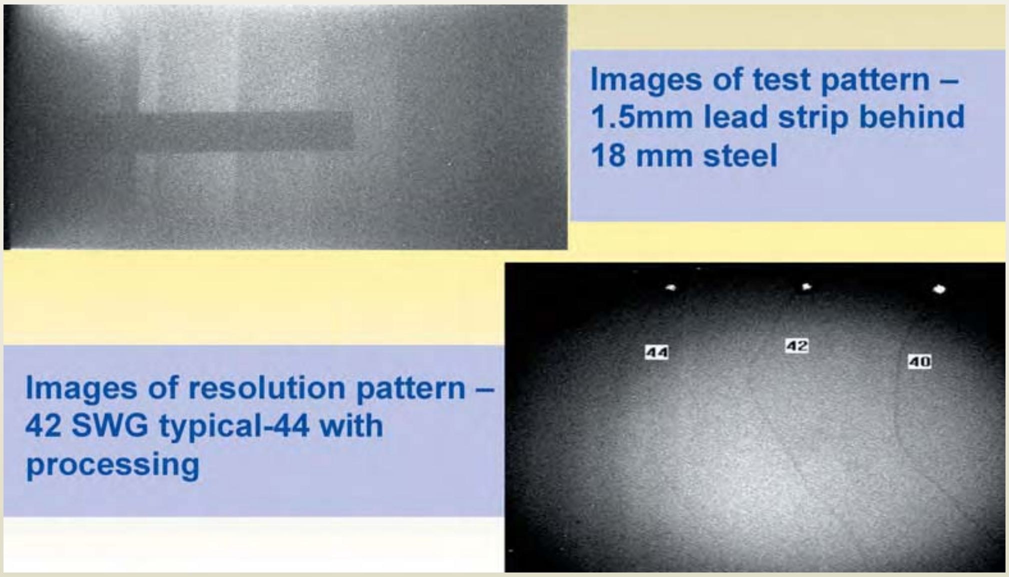

Images of test pattern – 1.5mm lead strip behind 18 mm steel

Images of resolution pattern – 42 SWG typical-44 with processing

Fig. 20 : Image of lead strips and resolution pattern

Microtron-based neutron source

In our country, neutron research has been confined mostly to nuclear research centers like BARC or IGCAR. The unavailability of accelerator-based neutron sources has been one of the major handicaps for popularization of neutron-based research within the country. With this view in mind, we have collaborated with the Mangalore University in setting up an accelerator-based photoneutron source. This design has led to the development of a neutron source with source strength which is $2x10^{9}$ n/s which is the highest within the country, outside nuclear establishments. Mangalore University has a Microtron Centre which is being used as a national facility. The microtron at Mangalore University can produce an electron beam of 9 MeV with 50 to 250 pulses per second of 2 micro-sec and 30mA peak current. Bremsstrahlung photons of peak energy corresponding to incident electron energy are produced, using tantalum target. The bremsstrahlung radiation from microtron is used to produce neutrons. Neutrons are produced through interaction of photons with the beryllium nucleus in photoneutron production reaction ^{9}Be (γ, n) ^{8}Be. Its cross section from threshold $E_o = 1.667$ up to 20 MeV has been measured by several investigators. The bremsstrahlung spectrum at 9 MeV has a large soft component of around 78% below 1.67 MeV which is useless for neutron production. Around 13% of this spectrum is between 1.67 MeV and 3.1 MeV, around 6% between 3.1 and 4.7 MeV and balance 3% upto 9 MeV. The choice of target is decided by this crucial data. For 9 MeV electron, only two targets could have been chosen, (a) ^{9}Be and (b) deuterium. We have chosen ^{9}Be as target so as to take advantage of large flux of photon between 1.67 MeV and 3.1 MeV. Though a composite target of beryllium deuteride could have given a higher source strength, the production of tritium with a deuterium based target may pose a health hazard.

A typical design of microtron-based neutron source and target-moderator assembly is shown in Fig. 21. In this figure, the region mentioned as "Target" is the position where the electron beam from Microtron impinges on a high Z metallic target such as tantalum and produces photons by bremsstrahlung radiation. These photons then interact with beryllium to produce neutrons by photo-neutron reaction[12-13].

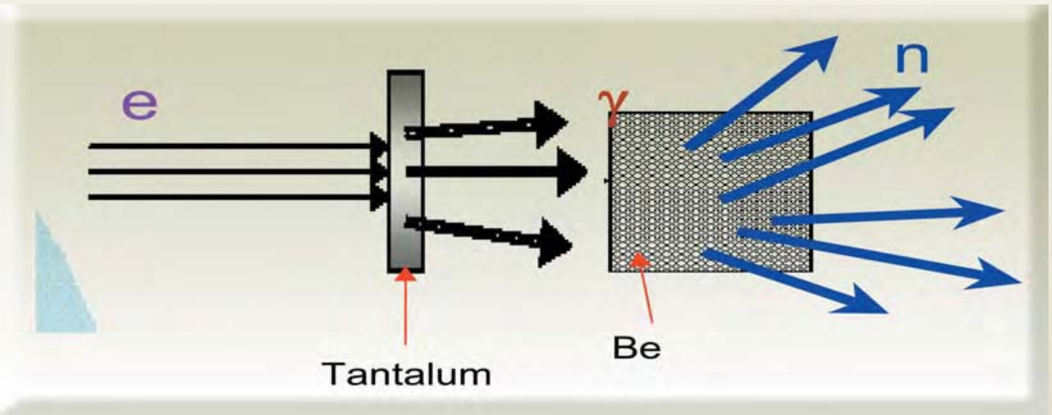

Fig. 21 : Schematic of neutron converter assembly

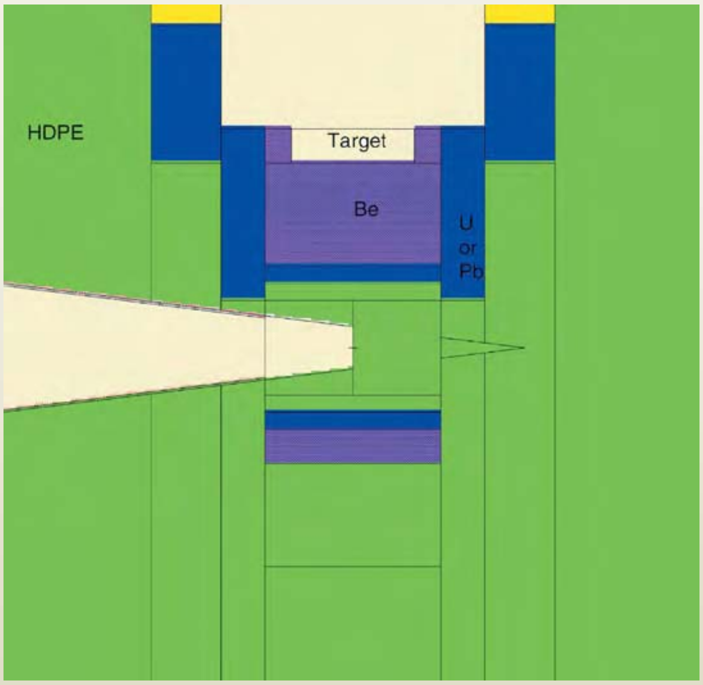

Fig. 22 : Schematic of microtron-based neutron radiography assembly

The first step in the designing of this neutron source, was the carrying out of a detailed monte-carlo simulation study to design a neutron converter assembly. The main parameters estimated through simulations were: electron to x-ray conversion, its spectrum, angular distribution, x-ray interaction within the target and its transport, neutron production and its leakage spectrum. The particular design of this converter assembly was optimized for providing an in-house radiography facility to the university. A special design of radiography assembly (see Fig. 22) was also made in order to strike a balance between quality of image, image acquisition time and resolution. A number of applications of this neutron source have been worked out ranging from radiography using electronic imaging technique to elemental characterization of bulk sample using gated counting to simple activation. Each of these applications requires special detectors and methodology to be adopted. For example, as the source strength is very less, conventional radiography imaging techniques don't work. Similarly counting of capture gammas in the presence of large incoming gamma flux from the microtron source is a challenge and special methodology will be needed to count such captured gammas for bulk sample elemental characterization.

Flow visualization inside metallic pipes using neutrons for AHWR studies

Visualization and analysis of water/air or water/vapour two-phase flow inside metallic pipes under high temperature and pressure is of considerable importance in thermal hydraulics design of nuclear reactors[14-20]. Conventionally, visualization experiments on two-phase flow are conducted using transparent glass sections which do not permit simulation of high pressure and temperature conditions. Similarly, other methods like conductance probe or gamma ray based techniques, do not permit real time visualization of flow pattern. Neutrons have the unique property of penetrating dense material such as steel but they get easily attenuated by water. This makes them a unique probe to visualize water/air flow or water/vapour flow condition inside metallic pipes. This property of neutrons has been utilized for developing an electronic imaging setup for real time two-phase flow visualization and void fraction measurement, inside SS or aluminum pipe (optically opaque channels).

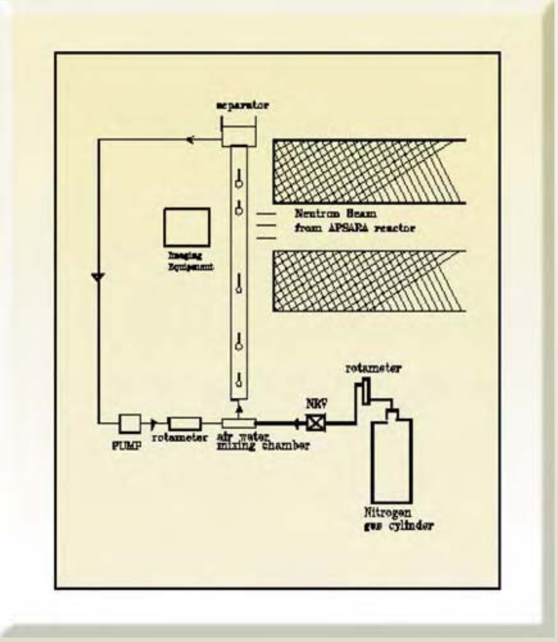

Fig. 23: Calibration test loop for study of two phase flow at APSARA reactor

This system has been designed to compute online void fraction for air/water two-phase flow, using neutron radiography technique. The accuracy of this method of void fraction estimation has been tested using several test pieces of perspex having a number of holes. A test loop to simulate various flow conditions like annular, slug or bubbly inside aluminum/SS pipe has been fabricated. The schematic diagram of this test loop is shown in Fig.23. Fig. 24 shows images of different flow patterns of water/air flow inside the aluminum pipe. The imaging system for two-phase flow visualization has been successfully tested at the APSARA reactor for a test loop designed by the Reactor Engineering Division to simulate AHWR convection driven flow (Fig. 25). Fig. 26 shows result of online computer plot of void fraction measured over a small section of pipe.

Fig. 24: Images of mixture of air and of water inside metal tube (dark shades indicate water)

The dashed curve shows instantaneous values of measured void fraction over this small section of pipe. We have also plotted moving time averaged void fraction values which are shown in the plot as solid lines.

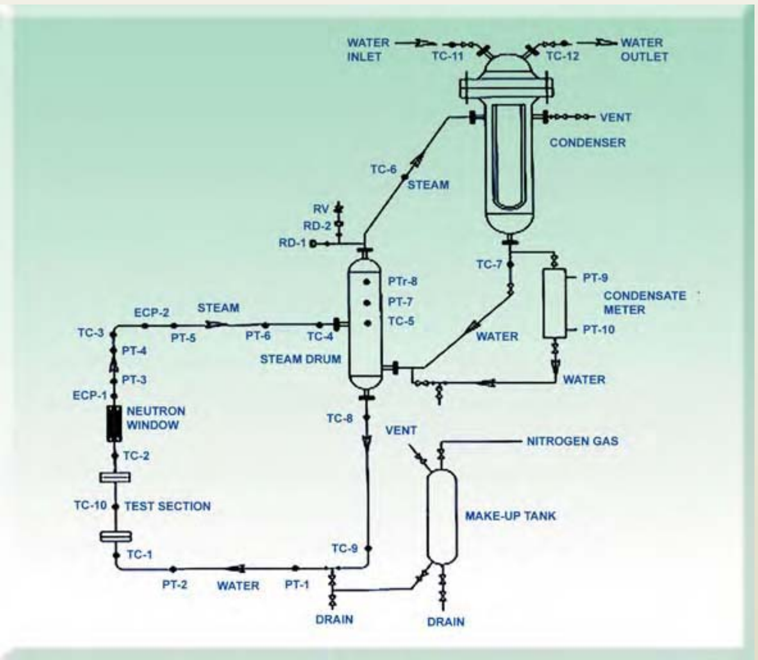

Fig. 25 : Schematic of test loop for AHWR used by RED at APSARA

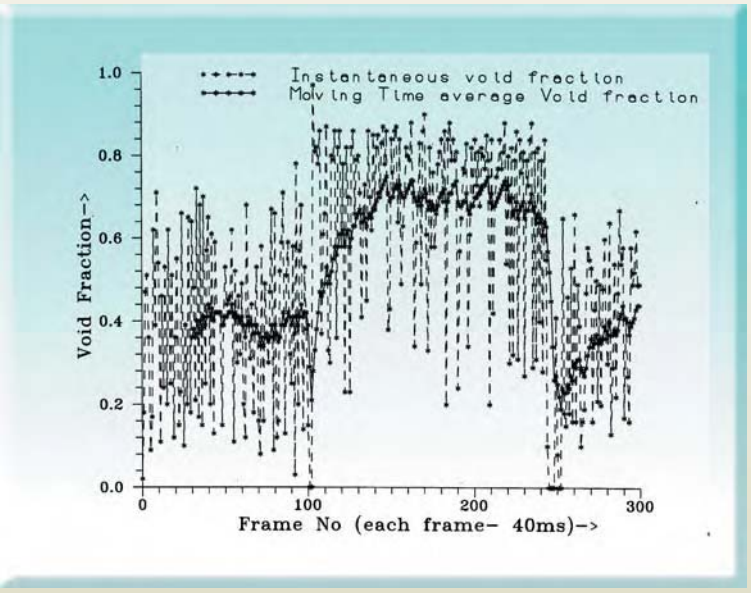

Fig. 26 : Graph of on-line plot of void fraction of two phase water/air flow inside the test loop

Real time X-ray system for the study of fluidization process for coal gasification project of BHEL

Two-phase flow study can also be done, using x-ray generators and real time x-ray imaging technique for specific applications. It can be used in cases where test samples to be examined are denser than the material used for cladding it, or in other words, the attenuation of x-ray from the container is much less, than the material flowing inside it. The study of fluidization process in coal bed, inside a simulated gasifier made up of perspex, represents a typical problem which can be solved by this technique. This experiment was proposed by BHEL and NTPC and conducted at Purnima Labs, BARC. The experiment was conducted on a small scale perspex model of coal gasifier being used at BHEL. A real time x-ray imaging system was designed especially for this purpose. The flow visualization and analysis was carried out under different conditions. Even though this experiment was preliminary in nature and had a limited purpose, it provided very valuable insight

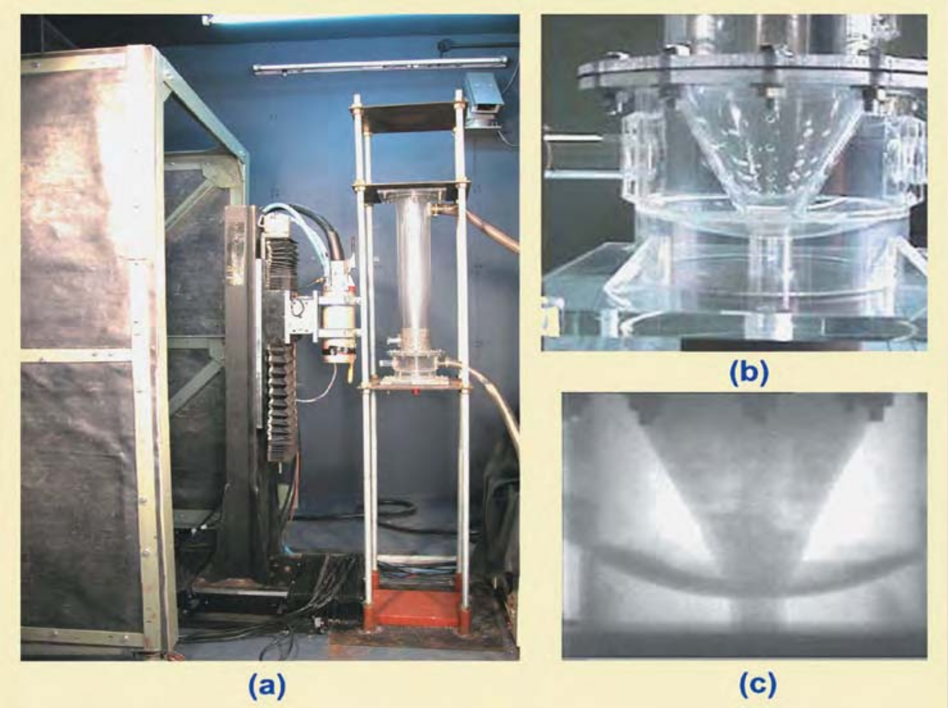

Fig. 27 : (a) Photograph of the experimental set (b) photograph of gasifier assembly (c) Radiograph of the two-phase flow pattern

into the fluidization process. The following Figs. (27(a)-(c), shows pictures of the gasifier and the Figs. 27(c) shows x-ray images of the fluidization process at the initial mixing stage.

2D and 3D Neutron tomography

Though neutron-radiography is being routinely used for nondestructive evaluations, neutron-computed tomography is a relatively recent addition to NDE. It overcomes many of the limitations of radiography and makes possible visualization of physical structures in their relative spatial positions and orientations. We have developed a neutron tomography system, based on CCD area detector [21-22] and successfully tested at APSARA reactor for obtaining neutron CT scan of several test specimens and industrial samples. The neutron tomography system developed for this purpose is fully automated, with integrated image acquisition and stepper motor control.

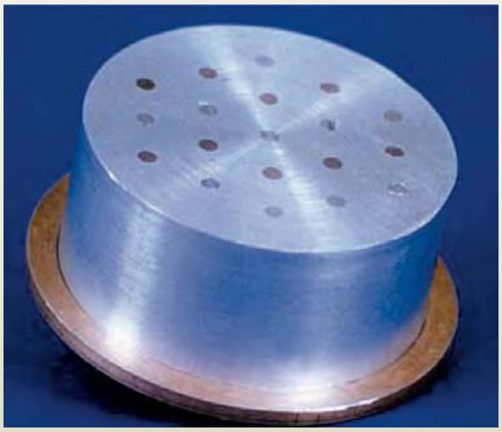

Fig. 28 : Aluminum test piece containing 9 SS rods and 10 brass rods

These images are preprocessed and subjected to reconstruction algorithm developed in-house, for obtaining CT scan images. Fig. 28 shows picture of

Fig. 29 : Radiograph of the object

an object made up of aluminum of 60mm diameter and containing 9 SS rods of 3mm diameter and 10 brass rods of 3mm diameter. One of the rods is broken halfway. Fig. 29 shows radiograph of the object placed on stepper motor. Figs. 30(a)-(c) shows CT scan of this object. We have been able to distinguish between SS and brass rods. This is shown in Fig. 30c by adjusting the contrast and suitably thresholding the CT scan image[24-25].

The spatial resolution obtained with this CT system is better than 1mm (8). Test samples made up of different materials and containing holes and rods

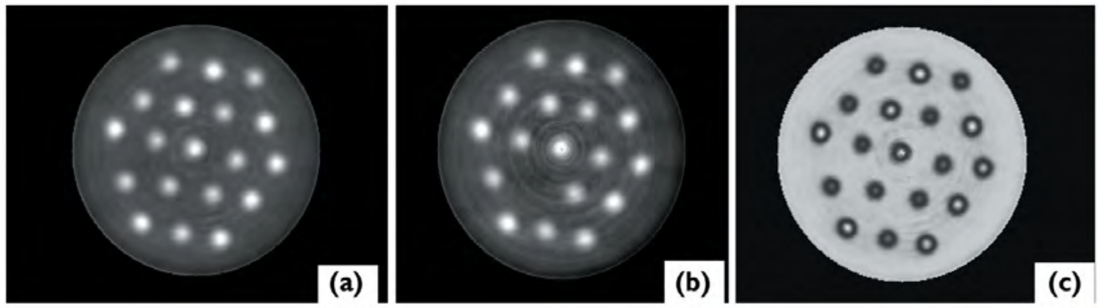

Fig. 30 : (a) CT Scan of the object showing 9 SS and 10 brass rods (b) CT scan of the object at different heights showing one broken rod (c) Processed CT scan image to highlight differences of attenuation coefficient between SS and brass rods

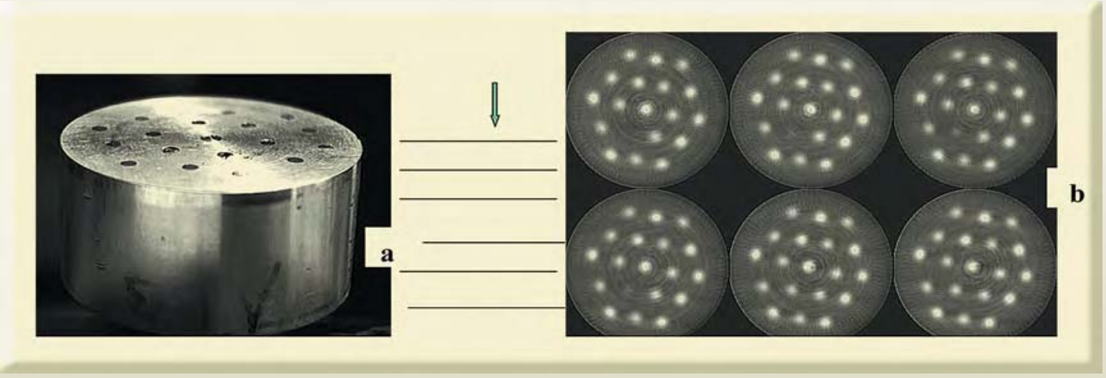

Fig. 31 : (a) Aluminum test object containing rods of SS and brass and (b) its multiple CT scan slice images

of various sizes as low as 300 micron in diameter, have been used for characterization of this tomography system. The resolution of this technique is limited by characteristics of CCD and demagnification used and can be further improved by using high resolution cooled CCD. Special care has to be taken to minimize the effects of scattering which results in cross correlation of different imaging elements.

As this technique gives multiple CT scans in a single experiment, we have combined these multiple 2D CT images into 3D volume data using volume rendering technique. This enables three-dimensional visualization of the interior of industrial objects. We describe below the procedure used for such 3D volume visualization.

Fig. 32 : Volume rendered image obtained using stacking of multiple slices

Multiple CT scans of the object shown in Fig. 27 were obtained, by reconstruction of projection data at various heights. Fig. 31(a) shows the object and the horizontal lines show the representative slices at which image reconstruction is done. We have shown only a few such reconstructed CT images in Fig. 31 (b). Fig. 32 shows stacking of these slices using volume rendering technique. The volume rendered images are shown in figure with the opacity of aluminum changed, so that it looks almost transparent. Fig. 33 shows cutaway view of the same object, using cut plane to highlight the broken rod.

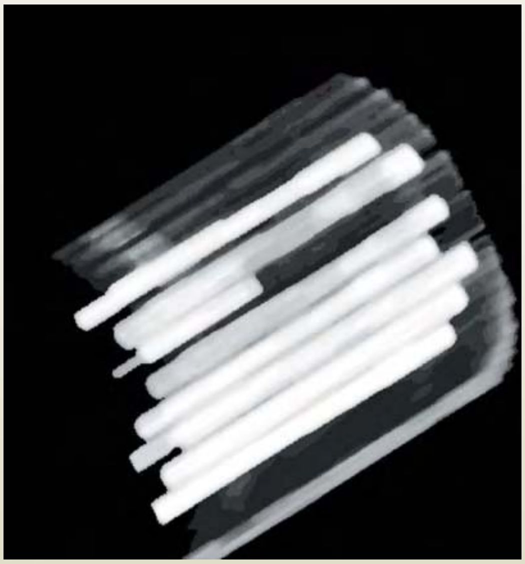

Fig. 33 : Cut away view to show broken rod

Thus 3D tomography helps in examining the interior of the object such as position and dimension of the broken rod. The object can be opened layer by layer or cut at any angle, using such a visualization technique, without physically cutting the material. This is like performing reverse engineering on an object. The example shown here is only a representative one to demonstrate the powerful features of the 3D tomography technique.

Conclusions

We have described several new developments in the field of neutron and x-ray imaging techniques and used these for a variety of applications. Phase contrast imaging has got tremendous applications for imaging in material and medical science. Techniques of cone beam tomography has the potential to provide a means of reverse engineering and visualization on

3D scale. Digital medical imaging is an attempt to design within the country, a state-of-the-art digital medical imaging system. Real time two-phase flow system can provide valuable input for better thermal hydraulics design and understanding of the fluidization process. Design of non reactor based sources is a key to spreading of neutron-based technique to industry and to universities. Similarly we have also discussed design of real time x-ray diffraction imaging system for basic research purposes and portable unclaimed baggage inspection system which has got tremendous security applications.

Acknowledgements

I would like to acknowledge the valuable contributions made by my colleagues Mr. P.S. Sarkar, Mr. Yogesh Kashyap, Dr Mayank Shukla, Ms V. Jilju and Mr. M.R. More during various stages of this work. I would like to thank Mr. P.K. Vijyan (RED) for collaboration on two-phase flow studies. I would like to thank Dr D. Sathiyamoorthy (Head, PMD) for collaboration on phase imaging of carbon coated samples, Dr P.R. Vaidya (AFD) for valuable consultation on tomography work, Prof. K. Siddappa (ex Vice Chancellor, Bangalore University) and Mr K. Eshwrappa (Mangalore University) for Microtron based neutron source design, Dr B.K Godwal (ex head, HPPD) and Dr S.K. Sikka (Ex Director, SSPG and Scientific Secretary to the office of Principal Scientific Officer) for constant encouragement and Dr S. Kailas, Associate Director, Physics Group for valuable suggestions.

References

1. Characterization of pyrocarbon coated materials using laboratory based x-ray phase contrast imaging technique, Y.Kashyap, T.Roy, P.S.Sarkar, P.S.Yadav, M.Shukla, A.Sinha, K.Dasgupta, D.Sathiyamoorthy, *Rev. Sci. Intru.,*78,083703 (2007).
2. Study of Phase Contrast Imaging for carbon fiber, polystyrene and lung tissue using monochromatic and polychromatic X-ray sources., P.S.Yadav, Y.Kashyap, P.S.Sarkar, Amar Sinha & B.K.Godwal, *Nucl. Instr. Meth* – A 564 (2006) 496-505.
3. Development of a 3D Cone Beam Tomography System:A Tool for Reverse Engineering, Amar Sinha, P.S. Sarkar, Yogesh Kashyap, M.R. More, presented at the NDE-2002 held at Chennai, Dec 2002.
4. Development and Characterization of a 3D Cone Beam Tomography System, P.S.Sarkar, A.Sinha, Y.kashyap, M.R.More, B.K.Godwal, *Nucl. Instr. Meth.* A 524, pp377-384 (2004)
5. Developments in radiation imaging techniques, A.Sinha, P.S.Sarkar, Y.Kashyap, B.K.Godwal, Published in *British NDT journal "INSIGHT"*, Jan 2003, vol (45) No.1.
6. X-ray Imaging using CCD based area detector, Amar Sinha, Invited talk at The SSPS-98 Kurukshetra Univ., 1998.
7. Performance of a CCD detector using rotating anode generator for x-ray diffraction studies at ambient & high pressure conditions , Alka B. Garg, Amar sinha, V.Vijay Kumar, B. K. Godwal and S.K.Sikka, Presented at the SSPS-98 Kurukshetra Univ., 1998.
8. A CCD-based detector for quick detection of pressure induced phase transition, Amar Sinha, Alka B. Garg, V. Vijaykumar , B.K. Godwal and S.K. Sikka, *High Pressure Research* vol 21, pp 51-64, 2001.
9. A CCD area detector for X-ray diffraction under high pressure for rotating anode generator, Amar Sinha, A.B. Garg, V. VijayKumar, B.K. Godwal and S.K. Sikka, *Bul. Mater. Sci.* Vol. 23 No.2, April 2000.
10. CCD based digital imaging technique for medical applications, Amar Sinha, Paper presented at the symposium on BioMedical Engineering and Nuclear Medicine and workshop on medical imaging, BARC, Bombay, 24-29 Jan 2000.

11. Development of battery based portable x-ray baggage inspection systems, P.S.Sarkar, Y.Kashyap, Jilju.V, M.Shukla, M.R.More, A.Sinha, B.K.Godwal, Presented at DAE-BRNS National Symposium Compact Nuclear Instruments and Radiation Detectors, Jodhpur, March 2-4, 2005.
12. Estimation of photoneutron yield from beryllium target irradiated by variable energy microtron based bremsstrahlung radiation, K.M. Eshwarappa*, Ganesh*, .Siddappa*, Yogesh Kashyap, Amar Sinha, P.S. Sarkar B.K. Godwal, Dept. of Studies in Physics, Microtron Centre, Mangalore University, Mangalore, INDIA, *Nucl. Instr. Meth.* A 540 (2005) 412-418.
13. Comparison of photoneutron yield from beryllium irradiated with bremsstrahlung radiation of different peak energy, .M. Eshwarappa*, Ganesh*, K.Siddappa*, Yogesh Kashyap, Amar Sinha, P.S.Sarkar, B.K.Godwal, Microtron Centre, Mangalore University, Mangalore, INDIA, Accepted for publication in *Annals of Nuclear Energy* 2007.
14. Digital imaging of neutrons and its application, Amar Sinha, *BARC NewsLetter # 183,* April 1999.
15. Applications of real time neutron radiography for convection driven flow pattern transition studies, P.S. Sarkar, Y. Kashyap, Amar Sinha, P.K. Vijyan, G.S.S. PrasadRao *IEEE-TNS* Vol 52, Number 1, Pp 290 – 294, Feb 2005.
16. Applications of digital neutron imaging at BARC (India) using reactor and non reactor sources, Amar Sinha, P.S. Sarkar, Y. Kashyap, *IEEE - TNS* Vol 52, Number 1, Pp 305 – 312, Feb 2005.
17. Applications of digital neutron imaging at BARC (India) using reactor and non reactor sources, Amar Sinha, P.S. Sarkar, Y. Kashyap, Presented at the 7th World Conference on Neutron Radiography held at Rome, Italy on Sept. 2002.
18. Applications of real time neutron radiography for convection driven flow pattern transition studies, P.S. Sarkar, Y. Kashyap, Amar Sinha, [1]P.K. Vijyan, [1]G.S.S. Prasad Rao, Presented at the 7th World Conference on Neutron Radiography held at Rome, Italy on Sept. 2002.
19. Visualization and analysis of two phase flow by neutron radiography and its applications in the thermal hydraulics studies of advanced reactors, Amar Sinha, P.K. Vijyan, A.M. Shaikh, Presented at the 6th World Conference on neutron radiography held at OSAKA, Japan, May17-21,1999.
20. An Experimental Investigation of Boiling Crisis in a Two Phase Natural Circulation Loop Under Oscillatory Conditions, GSSP Rao, PKVijayan, R.Rajlakshmi, DS Bisht, AK Nayak, D.Saha, R.K.Sinha, A.Sinha and P.S.Sarkar, Presented at the 1st National Conference on Nuclear Reactor Safety, November 25-27, 2002, Mumbai, India.
21. Experiments with electronic imaging system at APSARA reactor, Amar Sinha, A.M. Shaikh Presented at the 6th World conference on neutron radiography held at OSAKA, Japan, May17-21, 1999.
22. Advances in Neutron Radiography Applications, A.Sinha, *Journal of Nondestructive Evaluation,* Vol.19, No.4, Dec. 1999.
23. Development of three dimensional neutron tomography system and its applications Amar Sinha *Rev. Sci. Instrum.,* Vol. 71 No. 3, March 2000.
24. High sensitivity neutron imaging system for neutron radiography with a small neutron source, Amar Sinha, B.D.Bhawe, C.G.Panchal, A.Shyam, M.Srinivasan & V.M.Joshi, *Nuclear Instrument and Methods.* B 108 ,1996.
25. Development and characterization of a neutron tomography system based on image intensifier/ CCD system, Amar Sinha, A.M. Shaikh, A. Shyam *Nuclear Instrum. Method. B.* 142 (1998) 425.

About the Author

Dr Amar Sinha graduated from the 20th Batch of BARC training school. He has worked extensively on the neutron and x-ray imaging research in particular on the development of x-ray phase imaging, 3D x-ray and neutron tomography, real time imaging systems for basic and applied research etc. He and his team have been responsible for designing a digital medical imaging system and a Microtron based neutron source at Mangalore University. He obtained his Ph.D in 1990 on the design of spallation neutron source for the simulation of radiation damage in fusion materials. He has been a Visiting Scientist for a year at the Joint Research Centre of European Communities, Ispra, Italy and worked on the design of a spallation neutron source for fusion material studies. Dr Sinha has been the principal investigator of several of IAEA coordinated research programs on advanced neutron sources and neutron- based explosive detection. He has published more than 60 papers in international and national journals. He has been awarded the DAE-Technical Excellence Award -2005 for his work on X-ray and neutron imaging.

COMBUSTION SYNTHESIS: A SOFT-CHEMICAL ROUTE FOR FUNCTIONAL NANO-CERAMICS

A. K. Tyagi
Chemistry Division
Bhabha Atomic Research Centre

The author was conferred the CRSI Medal by
the Chemical Research Society of India, in February 2006

Abstract

Ceramic nanopowders are potential materials for many advanced applications. Soft-chemical routes play an important role in preparation of nano-materials. In particular, combustion synthesis has emerged as a promising solution-chemistry route, for synthesizing a variety of oxide ceramics, in nano-crystalline form. A variety of nanopowders have been prepared by this route and characterized by X-ray diffraction, surface area analysis, electron microscopy. These combustion-synthesized sinter-active powders, result in near theoretical density, while retaining fine grain microstructure. In this article, the potential of this technique, for preparation of a few selected rare-earth based oxide ceramics, will be discussed.

Introduction

Nanomaterials (1-100 nm in size) are potential candidates for a variety of technological applications and hence, their commercial value is increasing tremendously. Nano-ceramics exhibit improved properties as compared to conventional bulk ceramic materials. In particular, the combination of a relatively large portion of interfacial or grain boundary atoms along with the interactions of electrons or dislocations can lead to unusual mechanical and electrical behavior. Nano-ceramics can be utilized, for various applications concerning electronic, ionic, thermal, optical and catalytic properties [1]. Depending upon the final application, oxide ceramics are used in the form of sintered body, having the required shape, size and microstructure. The characteristics of a sintered body, fabricated through the powder metallurgy route, are highly dependent on the starting powder characteristics. The size, extent of agglomeration and purity are important characteristics for governing the powder quality. Another important aspect concerning nano-crystalline ceramics, is to prepare different crystallographic modifications of a given material, by tailoring the processing conditions. In fact, there are a number of investigations wherein the metastable phases were obtained, by converting a given material into its nano-state [2].

There are a number of physical methods for preparing nano-crystalline materials viz. inert gas condensation, physical vapor deposition, laser ablation, chemical vapor deposition, sputtering, Molecular Beam Epitaxy etc. Among the available solution-chemistry routes, combustion technique is capable of producing nano-crystalline powders of oxide ceramics, at a lower calcination temperature in a surprisingly short time

[3-5]. The solution-combustion is a two-step process viz. (i) formation of a precursor and (ii) auto-ignition. The formation of the precursor (viscous liquid or gel), is a primary condition for an intimate blending of the starting constituents and preventing the random redox reaction between a fuel and an oxidizer. The very high exothermicity generated during combustion manifests in the form of either a flame or a fire and hence, the process is termed as auto-ignition process. The nature of the fuel and its amount, are some of the important process parameters, for getting the transparent viscous gel without any phase separation or precipitation [6]. Thus, the basic characteristics of the fuel are that it should be able to maintain the compositional homogeneity among the constituents and also under go combustion with an oxidizer at a low ignition temperature. The commonly used fuels are: glycine, citric acid, urea, ascorbic acid etc.

The two events, which occur during combustion, are (i) generation of heat of combustion, and (ii) gas evolution. Heat of combustion (or flame temperature) helps in crystallization and formation of the desired phase. However, a very high flame temperature can adversely affect powder characteristics like increase in the crystallite size, formation of hard agglomerates and thereby reduction in the surface area and sinterability. The evolution of gaseous products during combustion, dissipates the heat of combustion and limits the rise of temperature, thus reducing the possibility of premature local partial sintering among the primary particles. The powder characteristics are primarily governed by heat of combustion and gas evolution, which themselves are dependent on nature of the fuel and oxidant-to-fuel ratio [7].

Experimental

Various rare-earth oxides were prepared, using the corresponding metal nitrates and a suitable fuel. Different combinations of fuel and oxidant were used, so as to tailor the powder properties. In order to prepare $SrCeO_3$ and Sr_2CeO_4, the appropriate amounts of cerium nitrate $[Ce(NO_3)_3 \times 6H_2O]$, $[Sr(NO_3)_2 \times 6H_2O]$ and glycine (NH_2CH_2COOH) were used. Three different molar ratios of oxidants-to-fuel were chosen for $SrCeO_3$ viz. the stoichiometric ratio (1:1.38), fuel-deficient ratio (1:0.5) and fuel-excess ratio (1:2.76). In case of Sr_2CeO_4 also, three different molar ratios of oxidant-to-fuel were chosen: viz. the stoichiometric ratio (1:1.29), fuel-deficient ratio (1:0.5) and fuel-excess ratio (1:2.0). In case of fuel-excess ratios, appropriate amount of NH_4NO_3 was added as an external oxidant. Nano-crystalline Eu_2O_3, Gd_2O_3, Dy_2O_3 were prepared, using corresponding metal nitrates and two fuels viz., glycine and citric acid $(C_6H_8O_7 \times H_2O)$ in different oxidant-to-fuel ratios. In the nano-crystalline neodymia-doped ceria system, about 8 compositions of $Ce_{1-x}Nd_xO_{2-x/2}$ (0.0 d" x d" 0.50) were prepared by the combustion process, using $[Ce(NO_3)_3 \times 6H_2O]$, $[Nd(NO_3)_3 \times 6H_2O]$ as the oxidants and glycine as a fuel in 1:1.0 ratio. Nano-crystalline $YCrO_3$ was prepared starting from $Y(NO_3)_3 \times 6H_2O$, $Cr(NO_3)_3 \times 9H_2O$ and glycine (NH_2CH_2COOH). In this case, two different oxidants-to-fuel ratios i.e. stoichiometric ratio (1:1.66) and fuel-deficient ratio (1:0.5) were chosen. $Fe(NO_3)_3 9H_2O$, $Gd(NO_3)_3 \times 6H_2O$ and glycine were used as starting materials, to synthesize nano-crystalline $GdFeO_3$. The oxidants and the fuels were mixed in the required molar ratios in a minimum volume of de-ionized water to obtain transparent aqueous solutions. These solutions after thermal dehydration (at ≈ 80 °C on a hot plate to remove the excess solvent) gave highly viscous liquids. As soon as the viscous liquids were formed, the temperature of the hot plate was increased to ≈ 250 °C. At this stage, the viscous liquid swelled and auto-ignited, with the rapid evolution of large volume of gases, to produce voluminous powders. The powders obtained after auto-ignition were calcined at 600 °C for 30 minutes to obtain pure and well crystalline powders.

X-ray diffraction measurements were carried out on the combustion-synthesized powder for phase identification and crystallite size estimation, using monochromatized Cu-K radiation on a Philips X-ray diffractometer, Model PW 1927, Netherlands. Silicon was used as an external standard for correction, due to instrumental broadening. The surface area analysis was carried out, by the standard BET technique with N_2 adsorption using a Sorptomatic 1990 CE instrument. The extent and nature of agglomeration was studied, by a particle size analyzer. The equipment used was Horiba, Model LA-500 (Japan), particle size analyzer based on laser diffraction, which covers the particle size range of 0.20-200 μm. A non-ionic dispersant (Triton X 100) was also added initially, for facilitating the dispersion of these powders. These nano-crystalline powders were cold pressed to 8 mm diameter pellets, at a compaction pressure of 200 MPa, using a uni-axial hydraulic press. Stearic acid was used as a lubricant. Sintering was performed at 1200°C for 2 hours with a heating rate of 8°C/min and a cooling rate 6°C/min. The sintered densities were determined using the Archimedes' principle. The microstructure of the sintered pellets was studied by Scanning Electron Microscopy (SEM). The sintered pellets were carbon coated before conducting SEM studies. TEM investigations were carried out using a Philips CM30/ Super TWIN Electron Microscope, to study the morphology of the powders. The flame temperatures were measured by a two-color optical pyrometer (Reytek) covering a temperature range of 1000°C to 3000°C.

Results and discussion

The salient results of these systems are discussed as follows:

Combustion synthesis of $SrCeO_3$ and Sr_2CeO_4

These two line compositions in the CeO_2-SrO system, have many promising applications, viz. $SrCeO_3$ is a potential material as a high temperature protonic conductor, apart from exhibiting electronic as well as oxygen ion conductivity [8]. Sr_2CeO_4, on the other hand, shows excellent blue-white luminescence [9]. The phase diagram in CeO_2-SrO system reveals that, the line compositions $SrCeO_3$ and Sr_2CeO_4 coexist at 50 mol % to 66 mol % of SrO in CeO_2 [10]. It may be noted that, different heating conditions were required for the preparation of these compositions by the solid state route. $SrCeO_3$ could be prepared by heating the appropriate mixture at 1400°C for 36 h. However, Sr_2CeO_4 could not be prepared under similar heating conditions as it led to the formation of $SrCeO_3$ phase. It could be prepared only at 1050°C with prolonged soaking for 60 h, with three intermittent grindings [11]. To avoid prolonged heat treatment, it was felt worthwhile to develop a suitable combustion process, to prepare these technologically important materials. It was found that a precise control of oxidant-to-fuel ratios was necessary, to prepare phase-pure $SrCeO_3$ and Sr_2CeO_4.

In the case of $SrCeO_3$ it was observed that the fuel-deficient ratio (1:0.5) as well as the stoichiometric ratio (1:1.38) resulted in an impurity phase of Sr_2CeO_4. This was because, the exothermicity and the associated flame temperature for these two oxidant-to-fuel ratios, were not sufficiently high enough, thus resulting in some Sr_2CeO_4 phase, which is stable up to 1400°C. Therefore, it was necessary to further increase the exothermicity and in turn the flame temperature involved in the combustion process, so as to result in temperatures above the stability range of the Sr_2CeO_4 impurity phase. Subsequently, large amount of fuel was used, but to compensate for the extra-reducing valency thus incorporated, appropriate amount of NH_4NO_3, as an additional oxidizer was also added. Out of the several molar ratios, the final molar ratio of metal-nitrates:fuel:additional-oxidizer of 1:2.76:6.21, was found to give the phase pure $SrCeO_3$. In fact, the actual flame temperature associated in this case, was found to be about 1850°C, (as measured by an optical pyrometer) which is well above that of the stability range of Sr_2CeO_4 phase, thus resulting in phase-pure $SrCeO_3$.

In the case of Sr_2CeO_4, however, it was observed that a low exothermicity was needed to maintain the flame temperature within the stability range of the Sr_2CeO_4 phase. Thus it was observed, that the stoichiometric ratio (1:1.29) and fuel-excess ratio (1:2.0) resulted in the impurity phase of $SrCeO_3$ along with the Sr_2CeO_4 phase.

It was found that phase pure Sr_2CeO_4 could be prepared only in the case of a fuel deficient ratio of 1:0.5. This was because, this combustion reaction resulted in low exothermicity without any flame, suggesting the temperature was well below 1400°C and therefore no $SrCeO_3$ impurity was obtained. The XRD patterns of phase-pure $SrCeO_3$ and Sr_2CeO_4 are given in Figs. 1 (a) and (b), respectively.

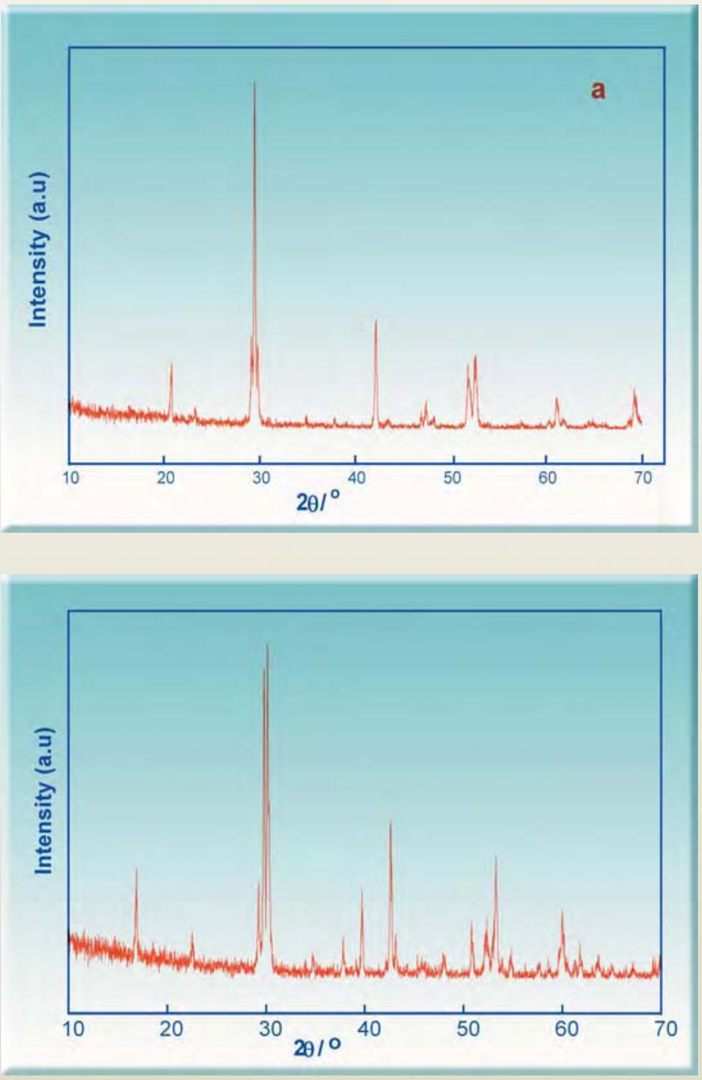

Fig. 1: XRD patterns of (a) $SrCeO_3$ and (b) Sr_2CeO_4 powders calcined at 950°C

Nano-crystalline RE_2O_3 (RE = Gd, Eu, Dy) by combustion process: role of oxidant-to-fuel ratio

Rare-earth sesqui-oxides have a wide range of applications as refractory materials, phosphors, catalysts etc. [12]. Rare-earth oxides like Eu_2O_3, Gd_2O_3 and Dy_2O_3 are common neutron absorbers and are used as burnable poisons in nuclear reactors. Eu_2O_3, Gd_2O_3 and Dy_2O_3 exist in C-type cubic modification at ambient temperature and are known to undergo an irreversible phase transition to B-type monoclinic modification i.e., the B-type at about 1000°C, 1200°C and 1750°C, respectively. In order to explore the possibility of preparing high temperature crystallographic phases of these rare-earth oxides and also to obtain corresponding oxide powders with improved powder characteristics, two different fuels viz. glycine and citric acid with varying fuel contents were used. The combustion reaction performed between $Eu(NO_3)_3$ and glycine in the stoichiometric ratio (1:1.66) stabilized the high temperature monoclinic modification of Eu_2O_3. However, the product obtained by europium nitrate-glycine in fuel deficient ratio (1:1.0) was found to be cubic. The XRD patterns of the nano-crystalline monoclinic and cubic phase of Eu_2O_3 are shown in Figs. 2 (a) and (b), respectively. This observation can be attributed to the fact that in the europium nitrate-glycine stoichiometric combustion reaction, the flame temperature was about 1420°C. This was higher than the temperature required for the C to B phase transition of Eu_2O_3 (at ≈ 1000), which led to the formation of B-type Eu_2O_3 phase. A similar observation was made in case of Gd_2O_3. However, the monoclinic phase could not be obtained for Dy_2O_3, irrespective of the fuel-to-oxidant ratio used. This could be attributed to a very high C to B phase transition temperature (about 1750°C) in the case of Dy_2O_3, which could not be achieved by a combustion reaction.

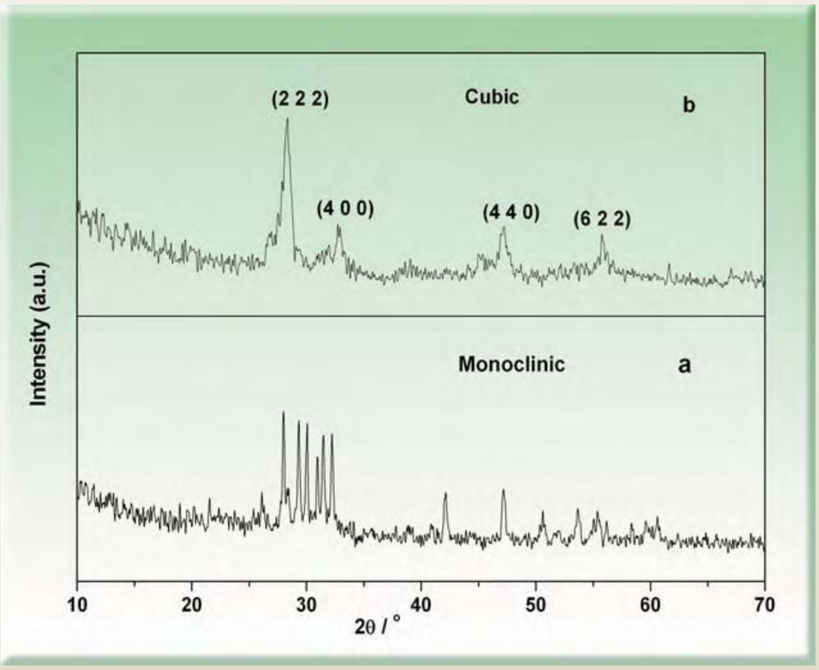

Fig. 2: XRD patterns of Eu_2O_3 using glycine as the fuel (a) stoichiometric ratio (1:1.66) and (b) fuel deficient (1:1.0)

In order to understand the role of oxidant-to-fuel ratio, the powder properties obtained using glycine and citric acid as fuels, were compared (Table 1). It was observed that in case of combustion using glycine as the fuel, in fuel-deficient ratio, finest crystallites for Eu_2O_3, Gd_2O_3 and Dy_2O_3 were obtained, whereas the glycine-stoichiometric ratio yielded the largest crystallite sizes. This observation can be explained based on the flame temperatures associated with combustion reactions, as calculated in case of Eu_2O_3. The flame temperature associated with stoichiometric combustion is around 1420°C, whereas the fuel-deficient combustion reaction gave rise to temperature as low as 650°C. Thus, higher the flame temperature, higher the crystallite size and smaller is the surface area. It can be inferred, that higher flame temperatures can affect powder properties adversely. However, in the case of citric acid as fuel, it was observed that the stoichiometric ratio (1:0.83) resulted in the finest crystallites of these rare-earth oxides as compared to that obtained by the fuel-deficient ratio (1:0.5). This observation can be attributed to the fact that in case of citric acid taken in the stoichiometric ratio, there are more number of gaseous products, which fragment the product while escaping, to give finer particles. It appears that the superior powder properties in case of stoichiometric ratio of citric acid are due to the dominant effect of number of gas molecules over the flame temperature.

The sintering studies in case of RE_2O_3 oxides were performed at 1200°C for two hours and the results are given in Table 1. The fuel-deficient ratio (1:1.0) of glycine fuel resulted in powders consisting of smallest crystals and largest surface areas, which in turn gave very high sintered densities. A stoichiometric ratio on the other hand, yielded much coarser powders thereby resulting in much poorer densities. Thus, it shows that highly sinter-active rare earth oxide nanopowders can be prepared by suitably varying the oxidant-to-fuel ratio. Fig. 3 is a typical representative SEM micrograph. It shows a compact microstructure with a negligible porosity and high sintered density (98% of theoretical density). The grains were well developed but appeared to be of variable sizes ranging from <1 µm to some as large as 5 µm.

Table 1: Powder properties of RE_2O_3 (RE = Eu, Gd, Dy)

Sample	Glycine						Citric acid					
	Stoichiometric ratio (1:1.66)			Fuel Deficient (1:1.0)			Stoichiometric ratio (1:0.83)			Fuel Deficient (1:0.5)		
	Cryst. size (nm)	Surface Area (m^2/g)	Density (%Th.D)	Cryst. size (nm)	Surface Area (m^2/g)	Density (%Th.D)	Cryst. size (nm)	Surface Area (m^2/g)	Density (%Th.D)	Cryst. size (nm)	Surface Area (m^2/g)	Density (%Th.D)
Eu_2O_3	86	9	87	11	51	95	11	20	95	25	37	93
Gd_2O_3	78	12	89	17	43	95	15	24	92	18	26	91
Dy_2O_3	43	14	89	11	37	92	14	16	90	14	28	89

Fig. 3: SEM micrograph of RE_2O_3 pellet sintered at 1200°C for 2 h.

Nano-crystalline neodymia doped ceria by the combustion route

Doped ceria (CeO_2) is an important material, in view of its potential application as a solid electrolyte for use in oxygen concentration cells and in solid oxide fuel cells. The high ionic conductivity coupled with low activation energy for ionic conduction, makes the doped CeO_2 an attractive material for use at temperatures below 800°C, which would allow greater flexibility in design of the electrode and inter-connectors [13]. About 8 compositions in the system $Ce_{1-x}Nd_xO_{2-x/2}$ $(0.0 \leq x \leq 0.50)$ were prepared by the gel combustion process. The various powder properties of the nano powders are compiled in Table 2. The crystallite size of powders, as obtained by the line broadening method, was typically in the range of 7 to 16 nm. The agglomeration studies showed, that the average agglomerate size of these powders, increased with increasing content of Nd in CeO_2. The powders were sintered at 1200°C for 2 h, to yield densities in the range of 80-95 % of theoretical densities. An interesting observation was that, the nature and size of the agglomerates, plays an important role in governing properties such as sintered density and in turn ionic conductivity of nano-ceramics.

Table 2 : Powder properties in $Ce_{1-x}Nd_xO_{2-x/2}$

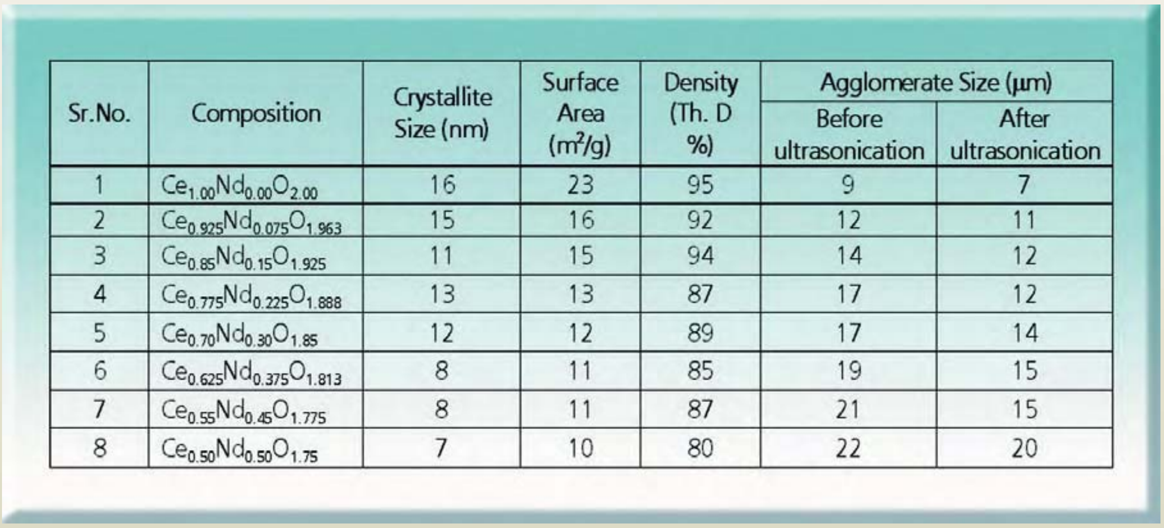

Sr.No.	Composition	Crystallite Size (nm)	Surface Area (m^2/g)	Density (Th. D %)	Agglomerate Size (μm)	
					Before ultrasonication	After ultrasonication
1	$Ce_{1.00}Nd_{0.00}O_{2.00}$	16	23	95	9	7
2	$Ce_{0.925}Nd_{0.075}O_{1.963}$	15	16	92	12	11
3	$Ce_{0.85}Nd_{0.15}O_{1.925}$	11	15	94	14	12
4	$Ce_{0.775}Nd_{0.225}O_{1.888}$	13	13	87	17	12
5	$Ce_{0.70}Nd_{0.30}O_{1.85}$	12	12	89	17	14
6	$Ce_{0.625}Nd_{0.375}O_{1.813}$	8	11	85	19	15
7	$Ce_{0.55}Nd_{0.45}O_{1.775}$	8	11	87	21	15
8	$Ce_{0.50}Nd_{0.50}O_{1.75}$	7	10	80	22	20

In the present case, the nano-powders were agglomerated in nature. There was no significant change in the agglomerate size before and after the ultrasonic treatment. Therefore, the agglomerates were hard in nature, which is detrimental for achieving high sintered density and hence, result in poor micro structural characteristics. It can be seen from Table 2, that the sintered densities varied significantly from that of the undoped ceria sample. With successive increase of the Nd concentration in the ceria matrix, the particle size and surface area decreased but the agglomerate size increased systematically. In the case of 50 mol% Nd-doped ceria, the powder showed smallest crystallite size (7 nm), smallest surface area (10 m^2/g), largest agglomerate size (22 μm) and poor sintered density (80 % th. d). This can be attributed to the presence of large and hard agglomerates. Although the primary particles were smaller in size, they were strongly coalesced to each other resulting in large agglomerated particles. These results indicate that sintering is governed not only by particle size and surface area but also by agglomerate size.

The ionic conductivity measurements were carried out on a few samples in the temperature range of 300 – 700°C. It was observed, that for pure ceria, the ionic conductivity was contributed by the grain and the grain boundary. The conductivity values corresponding to grain and grain boundary were found to be 1.5563 x 10^{-4} Scm^{-1} and 0.1265 x 10^{-4} Scm^{-1} at 650°C, respectively. The activation energy (E_a) values of ceria were 0.76 eVand 1.25 eV for grain and grain boundary, respectively, which are in agreement with available data [14]. However, on introducing neodymia into the ceria matrix, distinct semi-circles for the grain and grain boundary were not observed. In the case of 50 mol% doped ceria, total conductivity was calculated as the frequency response for the grain and grain boundary were too close to resolve. The conductivity of this sample was found to be 1.3672 x 10^{-4} Scm^{-1} and the activation energy was 1 eV.

Nano-crystalline $YCrO_3$ with onion-like structure

Refractory ABO_3 perovskite ceramics are generally used as high-temperature electrodes and thermoelectric materials. Recently the rare-earth chromates such as $YCrO_3$ joined the illustrious class of biferroic materials [15]. $YCrO_3$ is an antiferromagnet T_N =141 K with weak ferromagnetism [16]. Therefore, the synthesis of such an important material in single-phasic form is of prime significance. The conventional solid state synthesis of $YCrO_3$ requires high temperatures and long annealing duration [17]. Therefore, a facile low temperature synthesis of $YCrO_3$ was attempted, using the solution glycine-nitrate combustion in the stoichiometric ratio (1:1.66) and fuel-deficient ratio (1:0.50). The product obtained in each of the combustion reactions was calcined at 600°C for 1 h, to obtain chemically pure and crystalline powder. It was observed that the phase pure orthorhombic $YCrO_3$ could be obtained using stoichiometric ratio, whereas, the combustion reaction performed in the fuel-deficient ratio resulted in the formation of zircon-type $YCrO_4$. The XRD patterns of phase-pure $YCrO_3$ and $YCrO_4$ are given in Figs. 4 (a) and (b), respectively. The formation of phase pure $YCrO_3$ in the stoichiometric ratio, can be attributed to the high exothermicity generated during the combustion reaction. The flame temperature observed in the stoichiometric combustion was about 1675°C; while the fuel-deficient combustion was flame-less. It was also found that the product of the fuel-deficient combustion reaction, i.e. $YCrO_4$ on further external heat treatment (800°C) gave $YCrO_3$. Therefore, it can be inferred that because of the high exothermicity, $YCrO_3$ could be synthesized in a single step in the phase-pure form using glycine fuel in stoichiometric ratio.

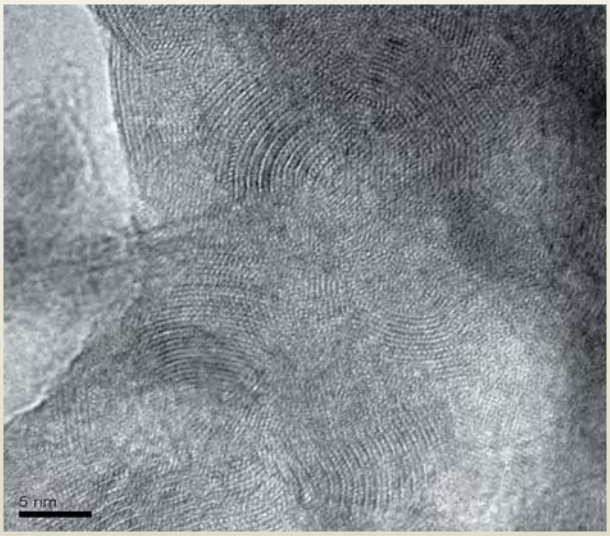

Fig. 5: HR-TEM micrograph of $YCrO_3$

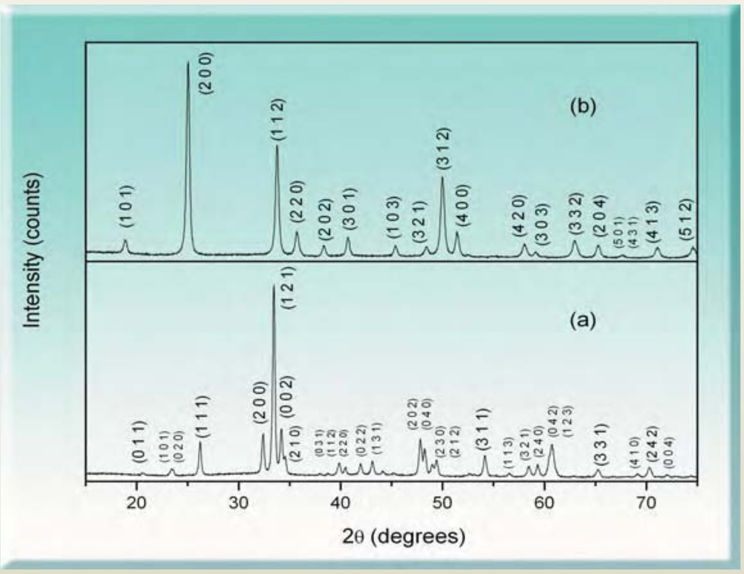

Fig. 4: XRD patterns of (a) $YCrO_3$ and (b) $YCrO_4$

The average crystallite size of nano-crystalline $YCrO_3$, as found by Scherrer's formula, was found to be 36 nm. The HRTEM micrographs of nano-crystalline $YCrO_3$ are shown in Fig. 5. An unusual observation in the TEM microstructure was the presence of onion-like structure made of concentric rings. Nano-crystalline $YCrO_3$ powder was also studied for its magnetic behavior. Magnetization measurement was carried out on the sample between 5K to 300 K at 10 kOe. It was observed, that there is an increase in magnetization around 140 K. The presence of hysteresis in magnetization curve (M vs H) clearly reveals the weak ferromagnetic nature of $YCrO_3$ nano particles. Hence, nano-crystalline $YCrO_3$ exhibits features similar to those of canted antiferromagnetic system which may be attributed to the nano-structured nature of the material.

Nano-crysytalline $GdFeO_3$

$GdFeO_3$ belongs to the perovskite rare-earth ortho-ferrites. These materials form an important class with a wide range of applications such as catalysts, as ferroelectric and semiconductors, magnetic and magneto-optical materials [18]. The synthesis of such ferrite materials is quite challenging because of the formation of garnet phase which is thermodynamically more stable than the desired ferrite. Of late, the preparation of garnet-free ferrite material has received tremendous renewed interest.

Nano-crystalline $GdFeO_3$ powder was synthesized by a gel combustion technique, using glycine as the fuel and the corresponding metal nitrates as oxidants. The oxidant-to-fuel ratios were varied from 1:1.0 to 1:2.5. It was observed that phase pure $GdFeO_3$ was obtained only when the fuel content is increased to 1:1.20 as observed in without any impurity phase. The phase pure $GdFeO_3$ was also *in situ* obtained after combustion with higher fuel contents viz, 1.40 and 1.66. Thus, it appears that there is a minimum fuel content and in turn exothermicity, that is necessary for the formation of the $GdFeO_3$ phase by the combustion route, which was found to be 1:1.20. Any fuel content below this, probably doesn't provide sufficient exothermicity for the formation of single phasic $GdFeO_3$ phase. The crystallite sizes for the phase pure products after calcination at 600°C, were in the range 40 to 65 nm. The TEM micrographs of the powders prepared from the stoichiometric ratio (1:1.66) are shown in Fig. 6. The particles have a size in the range of about 60-80 nm, which is in agreement with that calculated by X-ray line broadening. The magnetic properties of nanocrystalline $GdFeO_3$ were also investigated.

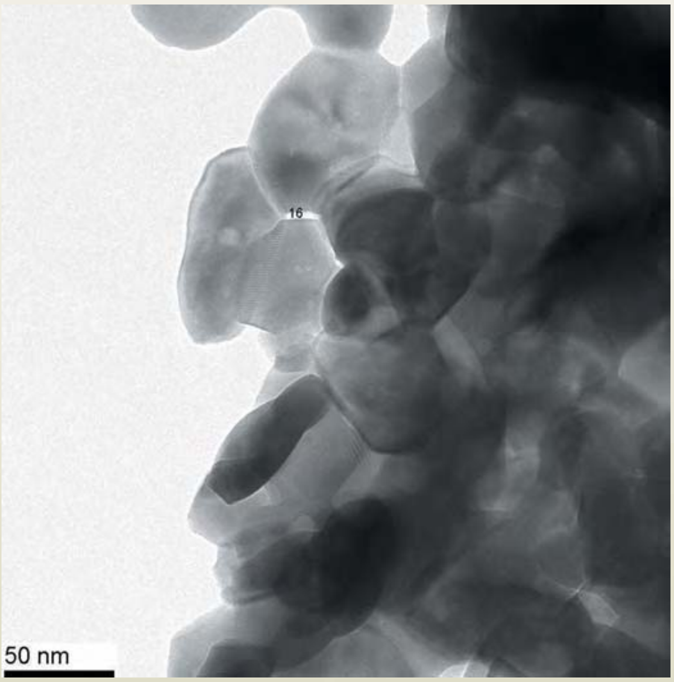

Fig. 6: TEM micrograph of $GdFeO_3$

Conclusions

From the foregoing study it can be concluded, that solution combustion process is a potential technique for preparation of a variety of phase-pure nano-crystalline powders of oxide ceramics. The combustion-synthesized powders have high surface area and can be sintered to high densities at lower sintering temperatures. The various powder properties can be systematically tuned, by altering the oxidant-to-fuel ratio. It is also possible to prepare metastable phases by the combustion technique. Thus, the preparation of nano-crystalline oxide ceramics by a simple and cost-effective solution combustion process, for the powder property-functionality correlation, is a wide area of interest and further research.

Acknowledgement

Dr D. Das, Head, Chemistry Division and Dr T. Mukherjee, Director, Chemistry Group are thanked for their support and encouragement. I would like to thank all my colleagues and PhD students.

References

1. H. S. Nalwa, Encyclopedia of Nanoscience and Nanotechnology (American Scientific publishers) 2004, p. 727.
2. R. C Garvie, *J. Phys. Chem.* 82, (1978) 218.
3. J. J. Kingsle, K. Suresh and K. C. Patil, *J. Mater. Sci.* 25 (1990)1305.
4. V. M. Ferreira, F. Azough, J. L. Baptista and R. Freer, *Ferroelectrics,* 133 (1992) 127.
5. S. Bhaduri, S. B. Bhaduri and E. J. Zhou, *J. Mater. Res.* 13 (1998) 156.
6. R. D. Purohit and A. K. Tyagi, *J. Mater. Chem.* 2 (2002) 312.
7. S. V. Chavan and A. K. Tyagi, *J. Mater. Res.,* 19 (2004) 3181.
8. N. Bonanos, B. Ellisand M. N. Mahmood, *Solid State Ionics,* 28-30 (1988) 579.
9. L. V. Pieterson, S. Soverna and A. J. *Meijerink Electrochem. Soc.,* 147 (2000) 4688.
10. V. Longo, D. Minichelli and F. Ricciardiello, *Sci. Ceram.* 11 (1981) 171.
11. R. Sankar and G. V. Subbarao, *J Electrochem. Soc.* 147 (2000) 2773.
12. Kirk-Othmer, J. I. Kroshwitz, M. H. Grant "Encyclopedia of Chemical Technology", John Wiley & Sons, New York 12 (1994) 417.
13. G. B. Jung, T. J. Huang, C. L. Chang, *J. Mater. Sci.* 36 (2001) 5839.
14. L. Aneflous, J. A. Musso, S. Villain, J. Gavarri, H. Benyaich, *J. Solid State Chem.* 177 (2004) 856.

About the Author

Dr A. K. Tyagi joined BARC in 1986 after completing one year orientation course from BARC-Training school. He has done extensive work in the field of nuclear materials, nano-materials and functional materials. He was a postdoctoral fellow at Max-Planck Institute, Stuttgart, Germany (1995-96). He has to his credit a large number of publications in internationally reputed journals and several review articles. He is on the reviewing panel of 25 international journals. He is a recognized PhD guide of Mumbai University and of Homi Bhabha National Institute. He is a recipient of several prestigious awards like Max-Planck Fellowship, Gold Medal of Indian Nuclear Society, MRSI Medal, CRSI Medal, Rheometric Scientific ITAS Award, Dr. Laxmi Award of ISCAS and IANCAS-Dr. Tarun Dutta Memorial Award. He is a Fellow of National Academy of Sciences, India and also a Fellow of Maharashtra Academy of Sciences. Presently, he is heading the Solid State Chemistry Section of Chemistry Division, BARC.

DEVELOPMENT AND APPLICATIONS OF C-SCAN ULTRASONIC FACILITY

Anish Kumar, K. V. Rajkumar, P. Palanichamy, T. Jayakumar, R. Chellapandian, K.V. Kasiviswanathan and Baldev Raj
Indira Gandhi Centre for Atomic Research
Kalpakkam

V.H.Patankar and V.M.Joshi
Electronics Division
Bhabha Atomic Research Centre

and

B.K.Lande
Electrical Department, V.J.T.I., Mumbai

This paper was adjudged Best Journal Paper at the National Seminar "NDE2006" held at Hyderabad, during December 7-9, 2006

Abstract

This paper presents the in-house development and application of a C-scan ultrasonic facility ULTIMA 200M2 at the Indira Gandhi Centre for Atomic Research (IGCAR), Kalpakkam, carried out in collaboration with the Electronics Division, Bhabha Atomic Research Centre (BARC), Mumbai. The paper describes various constituents of the system developed and also highlights the typical results obtained using this system, including bond integrity assessment of explosive welds and imaging of fuel sub-assembly heads of the Fast Breeder Test Reactor. The system has also been used for imaging both the sides of a one rupee Indian coin. All the finer details of the coin could be extracted, demonstrating the resolution capabilities of the system.

Introduction

Conventional ultrasonic testing is generally a contact test and is subject to the operator's ability to efficiently hand-scan a component. Further, the results need to be analyzed by reading a scope-type display or listening for an audio alarm. The most commonly used form of presentation of the ultrasonic testing is known as A-scan presentation. In this presentation, the horizontal line on the screen indicates the elapsed time (distance traveled) and the vertical deflection shows the echo amplitude. From the location and amplitude of the echo on the screen, the depth of the flaw in the component and an estimate of the size of the flaw can be made respectively. Ultrasonic test results can also be presented in the form of images providing the details of the component and two of these presentations are known as B-scan and C-scan presentations. B-scans are generated by scanning the probe in a straight line across the surface of the test piece at a uniform speed and acquiring all the A-scans at predetermined distance intervals. One axis of the display, usually the horizontal axis, represents the distance traveled along this line and the axis orthogonal to the probe position axis, usually measured top to bottom on the screen, indicates the depth of the echo within the component. Echo amplitudes are indicated in the gray scale. The principal advantage of B-scan presentation is the ability to display cross sectional view of the component and the flaws within it.

In an ultrasonic C-scan presentation, the transducer scans the part and initially displays the A-scan in which radio frequency (RF) waveforms show the ultrasonic signals reflected from the component. This display is used to set up the data collection gates, which are individual areas on the A-scan that correspond to specific depth ranges. The peak amplitude of the signal, within this gate, is then converted to a color or grayscale image called a C-scan, which shows the variations within the component. The data gates can either be placed along a single timeline (depth) to detect defects in the full volume of the component, or they can be located at various depths within the thickness of the component. Each data gate produces a separate C-scan image, which allows the component to be profiled through a top view (like an X-ray) or through individual layers. The results of the scan are provided as an image, showing the sectional view of the component and the flaws within it. Fig. 1 shows the schematic setup of a C-scan ultrasonic testing system. It consists of a computer (containing ultrasonic pulse-receiver card, analog-to-digital converter card and system operating software), mechanical scanner, motion control subsystem, ultrasonic transducer and an immersion tank.

The multi-channel C-scan ultrasonic imaging system ULTIMA with 100 MHz digitization was originally

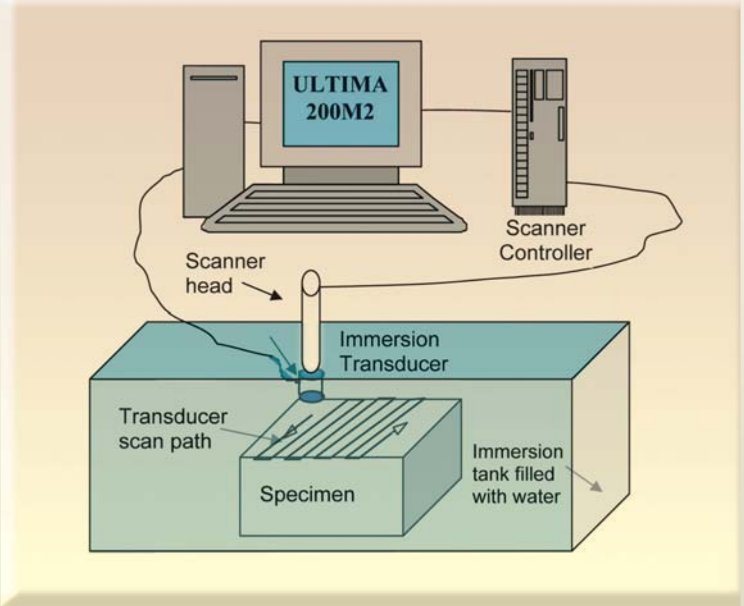

Fig. 1 : Schematic setup for ultrasonic C-scan imaging system

developed at Electronics Division, BARC, for various specific routine applications [1-5]. The details of various components of the two channel ULTIMA 200M2, with higher digitization capabilities and enhanced versatility, developed and established at IGCAR in collaboration with BARC are dealt first in the paper, followed by a few typical results obtained using this system.

ULTIMA 200M2 : Two-Channel Ultrasonic C-scan Imaging System

Hardware

ULTIMA 200 M2 is a two channel ultrasonic system which can excite two ultrasonic transducers in a sequence and digitize the data (acquired by both the transducers) at a maximum sampling rate of 200 MHz. Fig. 2 shows the schematic block diagram of the ULTIMA 200M2. The Pulser / Receiver units (one for each transducer), 200 MHz Digitizer and the channel sequencer are configured in the form of PC add-on cards, which are mounted in an Industrial Personal Computer. An additional amplifier card (PC-plug-in type) provides additional amplification for the received signals and the rectifier card carries out envelope detection of these signals so that either the rectified or un-rectified (i.e. RF) echo data can be digitized. Thus, the basic hardware for ultrasonic data acquisition consists of the following PC plug-in boards:

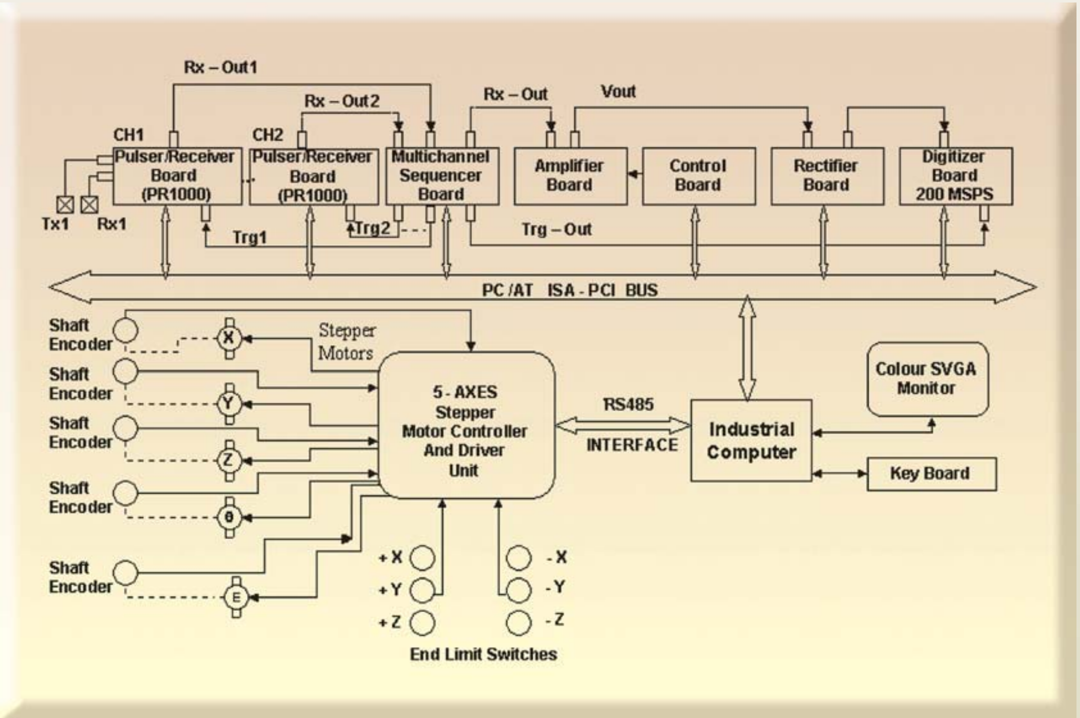

Fig. 2 : Schematic block diagram of ULTIMA 200M2 system

- Multi-channel Sequencer Board (Programmable channel-to-channel duration; Sequencing of respective triggers and multiplexing of echo signals for max. 8 channels; On board programmable 26 dB gain amplifier with 30 MHz Bandwidth)
- Wideband, Programmable Gain Amplifier Board *(RF amplifier with a Programmable gain of 40 dB; Bandwidth: 30 MHz)*
- Envelope detector Board *(Full wave precision Rectification and envelope detection)*
- 200 MHz, 8 Bits (ISA Bus) RF Digitizer Board *(Sampling rate: 200 MHz @ 8 bits resolution; RF Digitization; On board 8 Kbytes FIFO memory; Internal/External Trigger facility)*

This setup enables one to obtain digitized A-Scan information received by the transducer from the test object. For generating B-scan (i.e. a vertical cross section) and C-scan (horizontal cross section) images, controlled movement of the transducers is necessary. This is achieved with the help of PC-controlled multi axes mechanical scanner with a provision for mounting the transducers. A 5 axes (X, Y, Z, q and f axes respectively) stepper-motor-driven scanner, developed earlier [6], has been coupled with ULTIMA 200M2. Each axis imparts a controlled movement to the transducer holders in the specified direction with defined rate and increment. Each axis has a stepper motor, driver electronics and motion controller. The controller is interfaced to PC via an industry standard RS-485 interface. This interface permits cascading of multiple interfaces and hence it has been employed for the ULTIMA 100 M2 System.

Thus the PC plug-in cards mentioned above and RS-485 interface along with the 5 stepper motor controllers, 5 motor drives and associated power supply unit constitute the complete electronics hardware of the system. The hardware design of the ULTIMA100M2 system is modular in nature and all the function-specific PC Add-on boards are interfaced to PC via ISA or PCI Bus. Function-specific units/boards have an advantage that they can be independently upgraded without changing the rest of the system.

Software

A comprehensive Windows 98/ME compatible System software has been developed for ULTIMA 200M2 using Microsoft Visual Basic (VB) and Visual C++ (Version 6.0). The required Graphical User Interface (GUI) has been provided using VB, whereas controls for all the hardware boards/units have been established in the form of Dynamically Linked Libraries (DLLs) using VC++.

The system software has the following major features:

- Selection and calibration of transmitter/receiver transducer in terms of probe delay and angle of incidence.
- Selection and calibration of material in terms of velocity of propagation.
- Selection of digitizer parameters viz. sampling rate, depth range and initial delay for delayed data acquisition (DAQ) for thick objects and immersion scanning method.
- DAQ, storage/retrieval and display for A-Scan waveforms or B-Scan (cross-sectional front view) and C-Scan (cross-sectional top view) images for all the channels.
- Storage and retrieval of A-Scan data in Binary or ASCII format and B/C-Scan images in Binary or BMP format.
- Measurements of amplitude, flaw depth, linear distance, material velocity, transducer delay, transducer angle etc.
- Storage and retrieval of setup (*.INI) files for repeating the test using the same setup, if so desired.
- 4-Axis mechanical scanner control and test software.
- Return-On-Defect for C-Scan mode for confirmation of the defect and quantitative evaluation of the defect.

A 'project file' is generated for storing the multi-channel A-Scan data. This contains the header-information that includes all the major data acquisition parameters followed by the actual digitized data. The data from each channel is stored in separate files. The data retrieval and view feature enables to perform measurements like flaw depth, amplitude, linear distance / depth for angle beam probes, probe angle, velocity of propagation, two probe delay value etc.

In B-Scan mode, probe can be moved either manually or under the control of the scanning mechanism. While acquiring and displaying the B-Scan image on-line for a selected channel, the current A-Scan waveforms for the channels are also displayed. The B-Scan image can be displayed either in pseudo colors or gray shades.

In C-Scan mode, an on-line C-Scan image (in pseudo colour/grayscale) corresponding to the selected channel along with current A-Scan waveforms for both the channels is displayed. In the C-Scan retrieve mode, the software provides display of a B-Scan (cross-sectional front view) or a D-Scan (cross-sectional side view) image also along with the A and C-scans.

Return On Defect (ROD) command can be employed for repositioning the transducer at the desired location on the job for careful scrutiny of suspected regions and quantitative evaluation of the defects.

Further details of the development of hardware and software for the system can be obtained from the earlier publications [2-6].

Results of the Application of Ultima 200M2 C-Scan Imaging System

Fig. 3 shows the photograph of the C-scan test facility established at IGCAR. This system has been used for various applications such as imaging of weld profiles in ferritic and austenitic steel weldments; interface characterization of braze joints, explosive welds of different metals, various cladded specimens and imaging of dummy fuel sub-assembly heads of the Fast Breeder Test Reactor (FBTR). Some of the typical results obtained are presented in the following sub-sections.

Fig. 3 : C-scan ultrasonic facility at IGCAR

Bond integrity of weld and braze joints

Ultrasonic testing is one of the most popular nondestructive testing techniques for the evaluation of bond quality and defects, such as delaminations. The amplitude of the interface echo is dependent upon the acoustic impedance ($Z = \rho V$, where ρ is density and V is velocity of ultrasonic wave) of the two media on both sides of the interface. The reflection coefficient is given as:

$$R=(Z_2-Z_1)/(Z_2+Z_1)$$

where, Z_1 and Z_2 are the acoustic impedances of the first and the second media respectively. In the case of a good bond, the amplitude of the interface echo is less, because of the small difference between the acoustic impedances of the two metals. Whereas, in the case of any debond, because of the presence of metal-air interface, all the energy gets reflected back due to the large difference in acoustic impedance between the metal and the air and hence a signal with large amplitude is observed. This is indicated as a gray or black area in the C-scan.

C-Scan imaging has been carried out for evaluation of bond integrity of a titanium-carbon steel explosive weld joint [7] and a titanium-aluminum braze joint using aluminum foils as the brazing material. C-scan ultrasonic studies were carried out, using a 6 MHz point focused immersion transducer, focused at the interface. Figs. 4 a and b show the photograph and C-scan image of the titanium-carbon steel explosive weld joint. The ultrasonic inspection was carried out from the carbon steel side of the weld joint. The gray area in the C-scan image depicts the good weld joint leading to lower reflection from the interface, whereas, the black area indicates the delamination at the interface.

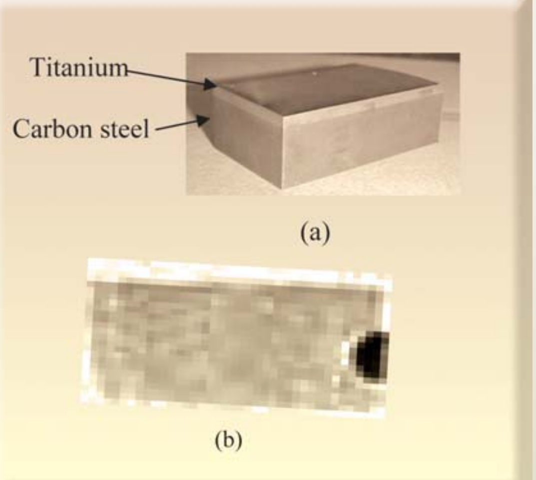

(a)

(b)

Fig. 4 : (a) Photograph and (b) C-scan image of the titanium–carbon steel explosive weld joint. (Gray area shows good weld and black area shows the delamination)

Fig. 5 shows the C-scan of the titanium-aluminum braze joint. The ultrasonic inspection was carried out from the titanium side of the braze plate. Two black areas in the C-scan indicate the delaminations at the interface. The observed delaminations are attributed to the improper thermal distribution due to clamping of the fixture at these locations.

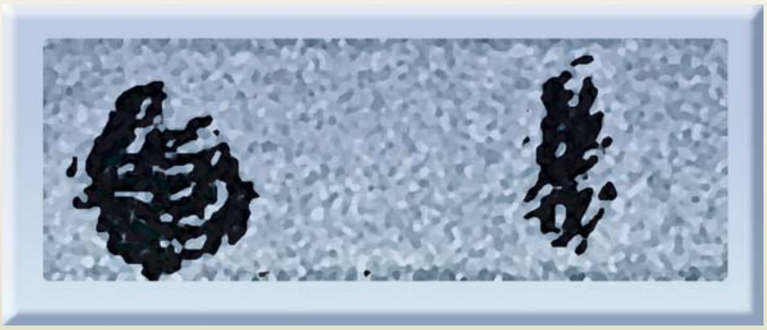

Fig. 5 : C-Scan image of the titanium-aluminum brazed plate indicating lack of bond (Black patches).

Imaging of fuel sub-assembly heads of Fast Breeder Test Reactor (FBTR)

The distance between the centers of the adjacent fuel subassembly heads, is often required to be measured in FBTR, in order to assess the degree of bowing/deflection of the fuel subassemblies due to irradiation damage. C-scan ultrasonic imaging has been attempted on dummy fuel sub-assembly heads in the laboratory, in order to examine the feasibility of using the C-scan based approach for the above purpose. Both focused and unfocused transducers have been used for the C-scan imaging. Figs. 6 a and b show the photograph and the C-scan image of

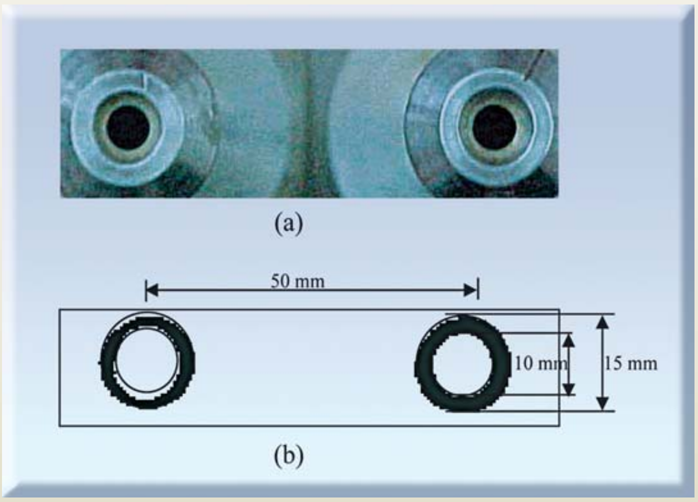

Fig. 6 : (a) Photograph of the top portion of the fuel subassembly head and (b) C-scan image obtained using the reflection from the top surface

the fuel sub-assembly heads respectively, obtained by using a 6 MHz point focused ultrasonic transducer, at a scan step of 0.5 mm. The reflection from the top surface of the sub-assembly heads has been used for the imaging. It was found that the center to center distance between the two heads can be measured from the C-scan image with an accuracy of ~2% and ~3% by using focused and unfocused transducers respectively. The outer and inner diameters of the top reflector of the sub-assembly head can be measured with an accuracy of ±0.5 mm with focused transducer, whereas the unfocused transducer overestimates the outer diameter by about 2 mm.

Imaging of one rupee Indian coin

In order to demonstrate the capabilities of the C-scan ultrasonic system, imaging of an Indian coin of one rupee denomination was carried out, using 20 MHz point focused transducer at a scan step of 0.2 mm. Figs. 7 a and b show the photographs and ultrasonic C-scan images of the two sides of the one rupee Indian coin, for direct comparison. The C-scan images (Fig. 7b) represent in gray scale, the amplitude of the echo obtained from the water-coin interface. The flat area in the coin reflected more energy and seen as light area in the C-scan image. At the edges (peripheries) of the protrusions in the coin, the ultrasonic wave gets deflected in different directions and hence the received amplitude is less, leading to the dark area in the C-scan image. All the finer details of the coin could be revealed, demonstrating the resolution capabilities of the C-scan ultrasonic system established at IGCAR.

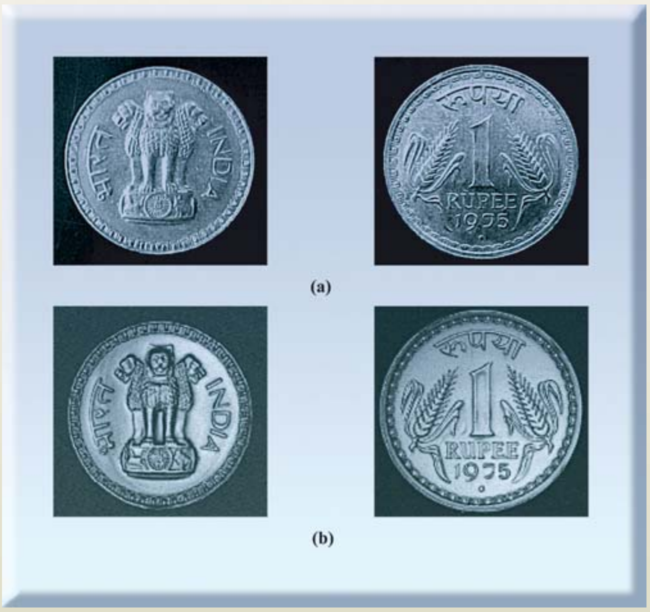

Fig. 7 : (a) Digital photo and (b) Ultrasonic C-scan image of an Indian coin

Future developments in the ULTIMA 200M2 system

Further developments in ULTIMA 200M2 are in progress at BARC with respect to both the hardware and the software. In the hardware, efforts are being made to upgrade the system to have 500 MHz digitization in order to improve the time resolution. Various modifications and additions in the software, such as facilities to get time-of-flight and spectral content based C-scan imaging are in progress, for microstructural characterization applications.

Conclusions

A C-scan ultrasonic facility ULTIMA 200M2 has been developed and installed at the Indira Gandhi Centre for Atomic Research, Kalpakkam, in collaboration with the Electronics Division, Bhabha Atomic Research Centre, Mumbai. This paper provides the details of various modules of this system and also a few results of applications, such as bond integrity assessment of explosive weld joints and imaging of dummy fuel sub-assembly heads of the Fast Breeder Test Reactor. The sensitivity and resolution of the system has been demonstrated by imaging both sides of the one rupee Indian coin. All the finer details of the coin could be extracted very clearly.

Acknowledgements

We are thankful to Mr. K. Swaminathan, Head, Instrumentation Division and Mr N. Raghu, PIRD, Indira Gandhi Centre for Atomic Research, Kalpakkam for providing the specimens. We are also thankful to Dr S.L. Mannan, Director, Metallurgy and Materials Group and Mr. P. Kalyanasundaram, Associate Director, Inspection Technology Group, Indira Gandhi Centre for Atomic Research, Kalpakkam, and Dr. S.K. Kataria, Associate Director, Electronics & Instrumentation Group (E), Bhabha Atomic Research Centre, Mumbai for their encouragement and support.

References

1. Patankar V.H., Agashe A.A., P. Jyothi, Joshi V.M. " ULTIMA 100M8 – Multichannel Ultrasonic Imaging System for NDE of Tubes/Pipes ", Xth National Conference On Ultrasonics, Osmania University, Hyderabad, March 15-16, 2001.
2. Patankar V.H., Joshi V.M., Kataria S.K. "Multichannel - Ultrasonic C-Scan Imaging System For NDE of Metallic Tubular Objects", National Seminar and Exhibition NDE 2001, Lonavala, December 7-9, 2001.
3. Patankar V.H., V.M.Joshi "Design and Development of an Ultrasonic Pulser-Receiver For Non-Destructive Testing of Materials", BARC External Report No. BARC/2002/E/034, November 2002.
4. S.P.Srivastava, B.N.Lahiri, A. Manjunatha, V.H.Patankar, V.M.Joshi and S.K.Kataria "Ultrasonic C-Scan Imaging of End Fitting Forgings for 500 MWe PHWR using Automated Scanner and ULTIMA-100M4 System", *BARC Newsletter* No.233, June 2003.
5. V.H.Patankar, V.M.Joshi, S.P.Srivastava, "Development of a 4-channel ultrasonic imaging system for volumetric inspection of solid cylindrical Forgings", NDE-2003 - National Seminar on Non-Destructive Evaluation, Thiruvananthapuram, Kerala, December 11-13, 2003.
6. Development of 5-Axis manipulator.
7. N.Raghu, Sanjay K.Rai, Anish Kumar, T. Jayakumar and K. V. Kasiviswanathan "Characterization of Explosive Weld Interfaces", To appear in the *Proc. of International Symposium of Research Students (ISRS) on Material Science and Engineering*, IIT Chennai, 20-22 December 2004.

About the Authors

Dr V.H. Patankar joined Electronics Division, BARC in June 1988, after graduating in Electronics Engineering from Shivaji University, Kolhapur. He completed his Ph.D. in Electrical Engg. from VJTI, Mumbai University in 2006. He is an Assistant professor at HBNI. Initially, he developed microprocessor-based EMG system, for investigation of neural disorders. Since 1991, he is working on the design and development of PC-based, Automated, Ultrasonic Imaging Systems for NDT of mechanical components, tubes, pipes, etc. He received the prestigious National NDT Award 2003 in the System Innovation and Development category, from Indian Society For Non-Destructive Testing (ISNT). Recently, he received the Best Journal Paper Award 2006 by ISNT for the technical paper he published in JNDE, March 2005 issue, jointly with scientists from BARC, IGCAR and a faculty from VJTI. Currently, he is engaged in the design and development of Automated - Under Sodium Ultrasonic Inspection System intended for detection of growth in fuel subassemblies of 500MWe Fast Breeder Reactor. He has more than 25 technical papers on ultrasonics, published in journals and seminars.

Mr. V.M.Joshi joined the Electronics Division of BARC in 1976 after completing his M.Tech. from I.I.T. Bombay in Instrumentation, Controls and Computers (Elect. Engg.). He initially worked on the development of Bio-medical instruments such as Electromyograph and Medical Ultrasonic Scanner (B-Scan system). He then worked on the development of Video Frame Grabbers. Since late eighties, he concentrated his developmental efforts on Ultrasonic Imaging systems for Nondestructive Testing/Evaluation (NDT/E) of materials. Under his leadership, several Ultrasonic Testing systems have been developed and supplied to NDT experts in BARC and IGCAR. Mr. Joshi heads the Ultrasonic Instrumentation Section of Electronics Division and is the recipient of the "NDE AchivementAward" for contributions to R&D in NDT. This award was given to him by the Mumbai chapter of I.S.N.T. Mr. Joshi has more than thirty scientific publications - including journal and conference papers and BARC reports - to his credit. Mr. Joshi is a life member of " The Biomedical Engineering Society of India" and the "Indian Society for Nondestructive Testing" (I.S.N.T.).

बीएआरसी न्यूज़लैटर
BARC NEWSLETTER

PREPARATION AND PRELIMINARY BIOLOGICAL EVALUATION OF ^{175}Yb LABELED HYDROXYAPATITE FOR POSSIBLE USE IN RADIATION SYNOVECTOMY OF SMALL JOINTS

Sudipta Chakraborty, Tapas Das, Sharmila Banerjee and Meera Venkatesh
Radiopharmaceuticals Division
Bhabha Atomic Research Centre

and

H.D. Sarma
Radiation Biology and Health Sciences Division
Bhabha Atomic Research Centre

This paper received the second best oral presentation award at the International Conference on Application of Radiotracers in Chemical Environmental and Biological Sciences (arcebs-06), held at Kolkata, during January 23-27, 2006

Introduction

Radiation synovectomy, which involves local intraarticular injection of suitable β^- emitting radionuclides in the form of radiocolloids or radiolabeled particulates into the affected synovial joints, has been successfully employed in the treatment of rheumatoid arthritis and other types of inflammatory arthropathies [1,2]. Owing to its suitable nuclear decay properties [$E_{\beta(max)}$ = 480 keV, E_γ = 113 keV (1.9%), 282 keV (3.1%), 396 keV (6.5%)] and feasibility of production in adequate specific activity by thermal neutron irradiation in a nuclear reactor, ^{175}Yb could be considered as a promising radionuclide for developing potential agents for radiosynoviorthesis of small-size joints. Hydroxyapatite (HA) [$Ca_{10}(PO_4)_6(OH)_2$] is one of the preferred particulates for effective management of synovial inflammation, owing to its excellent biocompatibility [2,3]. The present paper describes the preparation and preliminary biological studies of ^{175}Yb labeled hydroxyapatite (HA) particles, for use as a potential agent, for radiosynoviorthesis of small-size joints.

Experimental

Production and radiochemical processing of ^{175}Yb

^{175}Yb was produced, by thermal neutron bombardment on enriched (98.6% ^{174}Yb) Yb_2O_3 target in the CIRUS reactor, at a flux of ~3 x 10^{13} n/cm^2/s for 7 days. The irradiated target was dissolved in 0.1 M HCl by gentle warming. Radionuclidic purity as well as the yield of ^{175}Yb activity produced was ascertained by recording the γ ray spectra using a HPGe detector coupled to a 4 K Multi Channel Analyzer (MCA) system.

Synthesis of HA

Hydroxyapatite particles (particle size range 1-20 µ particle) was synthesized and characterized by following the procedure already reported earlier [2].

Preparation of ^{175}Yb-HA

Preparation of ^{175}Yb labeled HA was carried out, by adding 50 µL of $^{175}YbCl_3$ solution (~10 MBq ^{175}Yb) containing 250 mg of Yb carrier to a suspension of 10 mg HA in 850 µL of normal saline after the addition of 100 mL of 0.5 M $NaHCO_3$ buffer (pH ~9). The reaction mixture was vortexed thoroughly and was kept mixing at room temperature for 30 min, in a rotary shaker after adjusting the pH to ~7.

Biological studies

The biological efficacy of ^{175}Yb labeled HA particles thus prepared, was studied, by injecting the preparation (~7.4 MBq) in one of the knee joints in normal Wistar rats and recording scintigraphic images at 30 min, 3 h, 24h, 48 h, 72 h and 7 days time intervals, using a single head digital SPECT gamma camera. Blood samples were drawn at the same time intervals from tail vein.

Results and Discussion

Production of ^{175}Yb

About 5.5 GBq/mg (150 mCi/mg) of ^{175}Yb activity was obtained at 24 h post EOB, after 7 d irradiation at a flux of 3 x 10^{13} n/cm^2/s, using enriched (98.6% ^{174}Yb) Yb_2O_3 target. The radionuclidic purity of ^{175}Yb produced was ~100% as obtained from the analysis of the gamma ray spectrum.

Optimization studies

In order to obtain the optimum protocol for maximum radiolabeling yield, several experiments were carried out, by varying reaction parameters such as, HA concentration (1-40 µg/mL), pH (2-11), carrier Yb concentration (20-500 µg/mL) and incubation time (5 - 60 min). A maximum complexation yield of ~99% was obtained, when 10 mg/mL of HA was used and the reaction was carried out for 30 min at room temperature at pH ~7. The ^{175}Yb-HA complex, prepared under optimized reaction conditions, showed excellent stability even after 14 days at room temperature.

Biological studies

The scintigraphic images of Wistar rats (Fig. 1), recorded after injecting ^{175}Yb-HA in knee joints, indicate near-complete retention of the activity in the synovium even

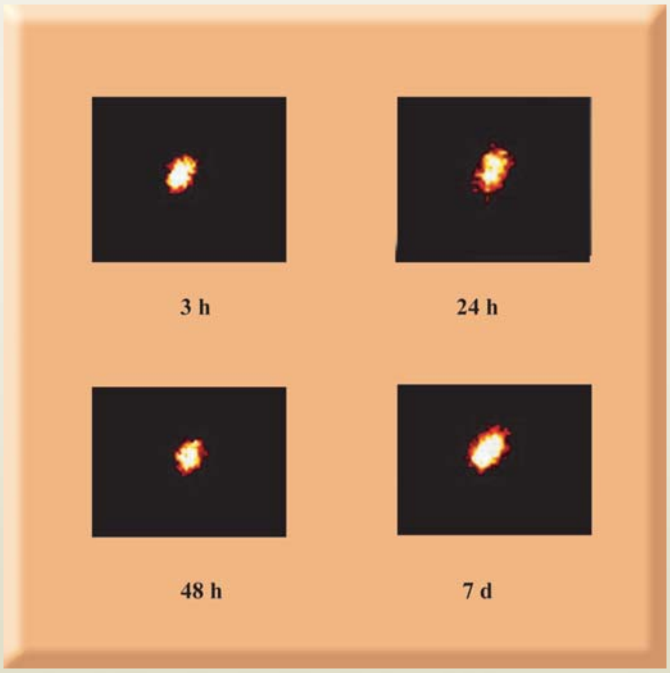

Fig. 1 : Scintigraphic images of normal Wistar rat injected with ^{175}Yb-HA in knee joint at various time points post-injection

after 7 d post-injection. No detectable activity was observable in any other organs. This is further confirmed by measuring the blood activity which did not show any radioactivity.

Conclusion

The radiolabeling of HA particles with ^{175}Yb was carried out in high yield and the labeled particles showed excellent stability. The scintigraphic images of ^{175}Yb-HA revealed no leaching of the activity from the synovial joints of the knee in Wistar rats, thereby indicating its potential as a therapeutic agent in the management of arthritis.

References

1. E. Deutsch, J. W. K. Brodack, F. Duetsch. *Eur. J. Nucl. Med.* 20 (1993), 1113.
2. P.R. Unni, P.R. Chaudhari, M. Venkatesh, N. Ramamoorthy, M.R.A. Pillai. *Nucl. Med. Biol.,* 29 (2002), 199.
3. M. Chinol, S. Vallabhajosula, J. Goldsmith. *J. Nucl. Med.,* 34 (1993), 1536.

About the Authors

Dr Sudipta Chakraborty is a gold medalist of Jadavpur University, Kolkata and obtained M.Sc. (Chemistry) degree in 1997. He joined the Radiopharmaceuticals Division, BARC, after graduating from BARC Training School in 1999 (42nd Batch, Chemistry discipline). Since then he has been actively involved in research and development work on therapeutic radiopharmaceuticals. He obtained Ph.D. degree in Chemistry from Mumbai University in 2006. Dr Chakraborty has to his credit about 20 publications in international journals and 35 papers in various national and international symposia/conferences.

Dr Tapas Das obtained M.Sc. (Chemistry) degree from Kalyani University (West Bengal) in 1997. After graduating from BARC Training School in 1998 (41st Batch, Chemistry discipline), he joined the Radiopharmaceuticals Division, BARC. Since then he has been actively involved in research and development work on diagnostic and therapeutic radiopharmaceuticals. He obtained Ph.D. degree in Chemistry, from University of Mumbai in 2005. He was awarded the 'Prof. H.J. Arnikar - Best Thesis Award' by IANCAS in 2006. Dr Das has to his credit about 25 publications in international journals and 40 papers in various national and international symposia/conferences.

Dr (Mrs.) Sharmila Banerjee joined the Radiopharmaceuticals Division, BARC in 1996. Prior to that, she obtained her M.Sc. degree in Organic Chemistry from the University of Calcutta and Ph.D. degree from Indian Institute of Technology, Mumbai in 1992. She is currently heading the Radiopharmaceutical Chemistry Section of the Radiopharmaceuticals Division. Her current areas of interest include research in the field of radiopharmaceuticals chemistry aiming at the development of new diagnostic and therapeutic radiopharmaceuticals. She is a recognized guide for M.Sc. and Ph.D. under the University of Mumbai. She has about 100 publications in international journals including review articles.

Dr (Mrs.) Meera Venkatesh joined the Training School of Bhabha Atomic Research Centre in the year 1976 after completing Bachelors Degree in Chemistry from Bombay University. She joined the Radiopharmaceuticals Division in 1977 and has been engaged in research and development of Radiopharmaceuticals and radiometric assays since then. Dr. Meera obtained her doctorate degree from Bombay University in 1986 for her work in the field of Radioimmunoassays. She did her post-doctoral fellowship at the University of Missouri, USA during 1992-94 in the field of therapeutic radiopharmaceuticals and later in 1999 served as a visiting professor at the same university. Currently, Dr. Meera is heading the Radiopharmaceuticals Division, BARC and concurrently serves in the capacity of General Manager of Quality Control at the Board of Radiation and Isotope Technology. She has published over 150 papers in international journals, international and national symposia/conferences and has authored a few invited articles. She has served as an expert in the field of Radiopharmaceuticals and Radiometric assays for the International Atomic Energy Agency.

Dr Haladhar D. Sarma is Head of Laboratory Animal Facility and Radioisotope Laboratory in Radiation Biology and Health sciences Division. He obtained M.V.Sc. with distinction from Assam Agricultural University, Guwahati in 1989. His major research interest concerns radiation carcinogenesis and application of nuclear technology in human and animal health. Prior to joining BARC in 1994, Dr. Sarma was Assistant Professor in the faculty of Veterinary Sciences, Assam Agricultural University. He has published more than 50 publications in various national and international journals.

बीएआरसी न्यूज़लैटर
BARC NEWSLETTER

GEOMETRY, ELECTRONIC AND MAGNETIC PROPERTIES OF MPd_{12} CLUSTERS (M = Ti, V, Cr, Mn, Fe, Co, Ni, Cu, Zn, Pd)

Sandeep Nigam, Chiranjib Majumder and S. K. Kulshreshtha
Chemistry Division
Bhabha Atomic Research Centre

This paper won the Best Paper Award (second prize), at the International Symposium on Materials Chemistry (ISMC-2006) held at BARC, Mumbai during December 4-8, 2006

Abstract

In this communication, we report the equilibrium geometry, electronic and magnetic characteristics of MPd_{12} clusters, obtained by using the density functional theory formalism, under spin-polarized generalized gradient approximation method. Unlike, bulk Pd metal, the Pd_{13} cluster in its lowest energy structure, shows a magnetic moment of 8 μB with close packed icosahedral geometry. The substitution of one Pd atom with different 3d elements, leads to similar atomic configuration, with 3d transition metal element occupying the central position in the icosahedral structure. However, the magnetic characteristics of these clusters are significantly affected by the electronic configuration of the substituent element. The substitution of one Pd atom with Ti, V, Cr, Cu and Zn atom, reduces the total magnetic moment due to antiferromagnetic coupling between the moments of Pd atoms and 3d transition metal atom. For $CrPd_{12}$, the calculated value of the magnetic moment of 2μB, is the lowest. Unlike this, the substitution of Pd atom by Mn, Fe and Co enhances the magnetic moment of the cluster due to the ferromagnetic coupling of all the moments, the effect being most pronounced for Mn substitution as the $MnPd_{12}$ cluster carries a magnetic moment of 11μB. Substitution of Ni, which is isoelectronic with Pd, does not affect the magnetic moment of the cluster.

Introduction

During the last decade, a large number of investigations have been carried out for doped clusters [1] with a view to understanding their atomic and electronic structure. Based on these studies it is found, that the impurity atom can influence the geometry, electronic and bonding properties of the host clusters. One of the important questions in the study of transition metal clusters, is the estimation of the size of the cluster, when it shows the cooperative phenomenon as shown by the corresponding bulk materials like appearance of magnetism. In this connection, we have investigated the atomic and electronic structure of Pd_{13} and $Pd_{12}M$ (where M is the 3d transition metal element) clusters, with a view to understanding the location of the transition metal atom in these clusters and its influence on the magnetic characteristics of these clusters. Although bulk Pd metal is diamagnetic in nature, its clusters of finite size are found to show significant magnetic moment. The choice of Pd_{13} as the host cluster has been driven by its high stability and icosahedral symmetry.

Computational Details

The total energy calculation and geometry optimization of clusters were performed, using the density functional theory with Projector Augmented Wave (PAW) pseudopotential and plane wave basis set. The spin-polarized Generalized Gradient Approximation (GGA) [2] has been used to calculate the exchange-correlation energy. In order to check the reliability of the pseudo-potential used in the present work, test calculations were performed for bulk Pd. The cohesive energy and lattice constant thus calculated is found to be 3.718 eV/atom and 3.96 Å, which is in good agreement with the experimental values of 3.89 eV/atom and 3.89 Å, respectively.

Results And Discussion

Fig. 1(a) shows the ground state geometry of the Pd_{13} cluster, which favors slightly distorted icosahedron structure. The Pd-Pd distance between the center and apex atom is found to be 2.59 Å. The separation between other Pd atoms varies between 2.71 Å to 2.79 Å. Most importantly, the Pd_{13} cluster shows a total magnetic moment of $8\mu_B$. This is interesting as the bulk Pd metal is non-magnetic. The distortion in the symmetry of Pd_{13} icosahedron is attributed to the John-Teller effect, which in turn causes the spin polarization in the Pd_{13} icosahedron. The average binding energy of Pd_{13} cluster is estimated to be 2.31 eV/atom. The removal of one atom from Pd_{13} cluster and optimization of its structure, resulted in a similar skeleton for Pd_{12} cluster with the same value of magnetic moment of $8\mu b$ implying an increase in the local magnetic moment of each Pd atom. The structure of Pd_{12} cluster is shown in Fig.1 (b), which is almost similar to that of Pd_{13} less the central atom.

The search for ground state geometry of MPd_{12} clusters has been derived from the icosahedron configuration obtained for Pd_{12}. The interaction of an impurity atom with such a homo-atomic cluster can lead to three different possibilities viz., (a) the impurity atom can occupy the center of the cage formed by the host cluster (endohedral), (b) the impurity atom can replace one atom from the network of the host cluster (substitutional) and (c) the impurity atom can adsorb on the surface of the host cluster (exohedral). In all cases we found, that for the lowest energy structure, the 3d transition atom

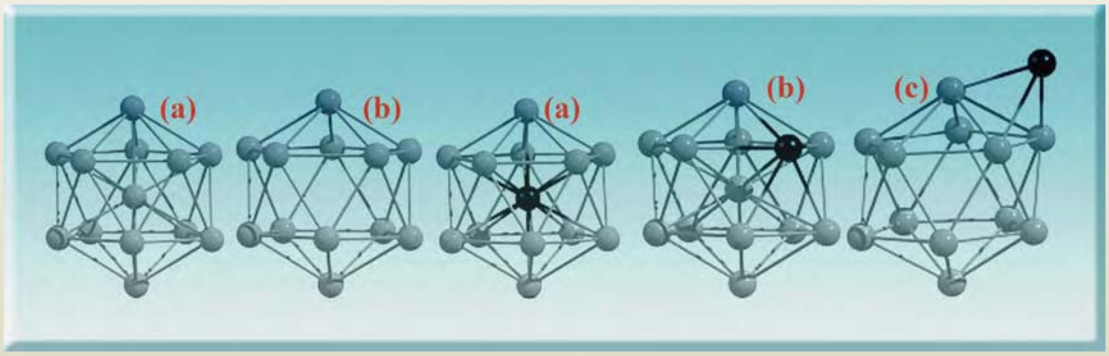

Fig. 1 : Structure of Pd_{13} and Pd_{12} and different structural isomers of MPd_{12}.

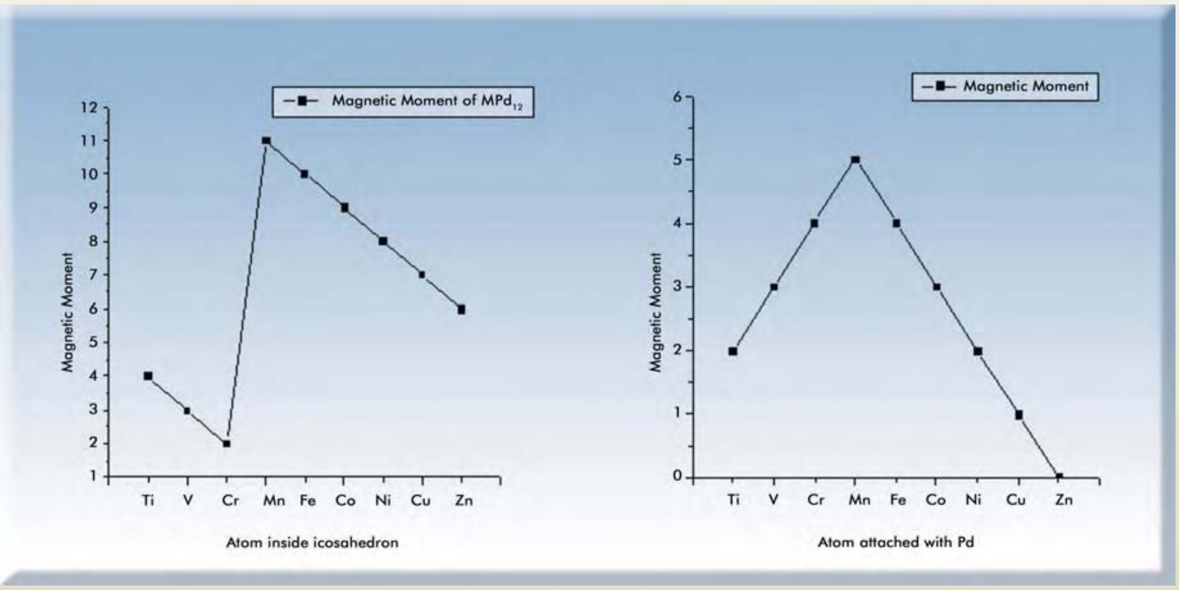

Fig. 2: Magnetic moment of MPd$_{12}$ cluster and M-Pd dimer

is occupying the central position in the icosahedron. However, there are interesting differences in the magnetic behavior of these clusters, depending on the location of the M atom. For example, in case of CrPd$_{12}$ cluster we find that all three isomers, which differ in their energy, have also got different magnetic moments.

In fig. 2, we have plotted the variation in the magnetic moment of MPd$_{12}$ clusters with different transition metal atoms and compared them with the M-Pd dimers, From this figure it can be seen that both M-Pd dimer and MPd$_{12}$ cluster show maximum magnetic moment. For M-Pd, the magnetic moment increases linearly upto Mn and then decreases in the same way. However, in case of MPd$_{12}$ clusters the magnetic moment shows a decrease up to Cr and then there is a sharp increase for MPd$_{12}$ after which the magnetic moment decreases linearly. While M-Pd clusters show lowest magnetic moment for Zn-Pd, the MPd$_{12}$ shows a minimum at CrPd$_{12}$, which has a magnetic moment of 2μB. The major difference in the variation of the magnetic moments of MPd and MPd$_{12}$ clusters is observed for Ti, V and Cr.

The local spin moments of MPd$_{12}$ clusters have been obtained by expanding the wave function into angular momentum components within a sphere of radius. For Pd$_{13}$ cluster, the average magnetic moment on each site is 0.61μB. This average magnetic moment decreases significantly on substitution of central atom with V, Ti, and Cr which are coupled to the Pd$_{12}$ antiferromagnetically. Unlike this trend, the substitution by Mn, Fe, Co, results in the enhancement of the moment through ferromagnetic coupling.

From the charge distribution analysis it is found, that for M-Pd dimer, there is a transfer of charge to the 5s orbital of Palladium from the 4s- orbital of the heteroatom and the 4d-orbital of Pd itself. Similar trend was found in case of MPd$_{12}$, the central heteroatom gives the charge to Pd$_{12}$ super atom. In Fig. 3 we have plotted the decomposed density of states for MnPd$_{12}$ and CrPd$_{12}$ clusters. The dashed vertical line is representing the HOMO level. It is clear from this figure, that at the HOMO energy level, while the Mn impurity atom interacts through up-spin, the Cr interacts

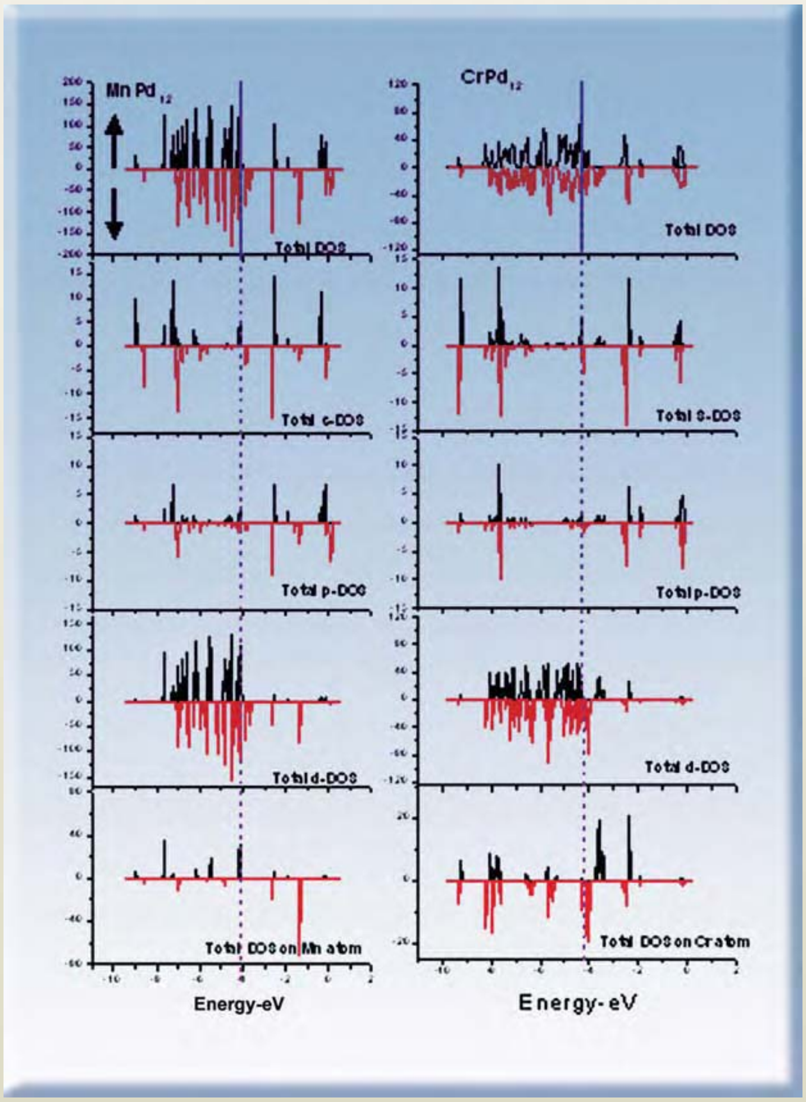

Fig. 3 : DOS of $MnPd_{12}$ and $CrPd_{12}$ clusters

through down-spin. This feature directly corroborates the ferro- and antiferro-coupling of $MnPd_{12}$ and $CrPd_{12}$ clusters, respectively as predicted above.

Conclusion

Based on these results, we infer that, although Pd metal as bulk is non-magnetic, it can show large Magnetic Moment for finite size clusters. The reason for such behavior could be due to the hybridization of atomic s and d states. During cluster formation there is significant de-localization of 5s and 4d electrons, which leads to depletion of local d contribution around each atom and an open-shell-like behavior. Doping of Pd_{12} cluster with 3d- elements can lead to decrease or increase in the magnetic moments of MPd_{12} cluster depending on, the electronic configuration of M - element. The magnetic moment present at Ti, V and Cr atoms interacts anti-ferromagnetically with Pd_{12} magnetic moment. Unlike this the magnetic moment of Mn, Fe, Co, Ni, interacts ferromagnetically. While $MnPd_{12}$ shows the highest magnetic moment of 11μB, Cr doping leads to the quenching of the magnetic moment down to 2μB.

References

1. V. Kumar et al.: in Clusters and Nanomaterials, Springer Series in Cluster Physics, Springer-Verlag, Heidelberg, 2002, p. 9.
2. J. P. Perdew et al.: *Phys. Rev. Lett.* 77, 3865 (1996).

About the Authors

Mr. Sandeep Nigam joined Bhabha Atomic Research Centre in 2003 after graduating through 46th batch of training school. Since then, he has been working on theoretical study of small atomic and mixed clusters using first principal calculations. At present he is working on magnetic properties of metal encapsulated cage like clusters.

Dr Chiranjib Majumder joined Chemistry Division, Bhabha Atomic Research Centre in 1992 after graduating through 35th batch of training school. He has developed an in-house experimental facility to generate supersonic molecular beams in tandem with a time-of-flight mass spectrometer. He received his Ph.D. degree in 2000 for experimental and theoretical studies of metal clusters. During 2000-2002, he was at the Institute for Materials Research, Tohoku University, Japan to carry out post doctoral work with Prof. Y. Kawazoe, where he worked on the theoretical aspects of molecular electronics. Subsequently, he visited laboratory of Prof. P. Jena, at the Physics department of Virginia Commonwealth University, USA to work on the electronic and atomic structures of clusters. His current research interest is to design novel materials for catalysis by tuning the electronic properties of nano-materials and to underscore the mechanism of cluster-molecule interactions on a support matrix.

Dr S. K. Kulshreshtha graduated from Agra University in 1966 and joined chemistry division, BARC through 10th batch of training school. He started his research career with the study of diamagnetically substituted spinel ferrites using Mossbauer spectroscopy for which he was awarded Ph.D. by Bombay University in 1974. He did his postdoctoral work in Germany at the University of Erlangen-Nurnberg on the nature of low and high spin state transition in Fe(II) complexes. He superannuated in Dec.2006 as Associate Director Chemistry Group and Head Chemistry Division of BARC and as Outstanding Scientist. During the past 40 years, he was mainly associated with a variety of research, developmental and academic activities pertaining to the Department of Atomic Energy. Currently, Dr Kulshreshtha is working as the Adjunct Professor, Applied Chemistry Department, University Institute of Chemical Technology, Mumbai University. His current research interests are centered around material science, catalysis and structural science.

STUDIES ON SULFUR-IODINE THERMOCHEMICAL CYCLE FOR HYDROGEN PRODUCTION

A.M. Banerjee, K. Bhattacharyya, M.R. Pai, A.K. Tripathi,
V.S. Kamble, S.R. Bharadwaj and S.K. Kulshreshtha
Chemistry Division,
Bhabha Atomic Research Centre

This paper won the Best Paper Award (third prize), presented at the International Symposium on Materials Chemistry (ISMC-2006) held at BARC, Mumbai during December 4-8, 2006

Abstract

We report here the work that has been initiated at the Chemistry Division, on Sulfur-Iodine thermochemical cycle, which deals with the development of catalyst systems for decomposition of sulfuric acid, the most energy intensive step involved in this cycle towards decomposition of water for hydrogen production. Chromium substituted Fe_2O_3 catalysts were synthesized via solid-state route and characterized by XRD, N_2 sorption and Temperature Programmed Reduction/Oxidation (TPR/O) techniques. Catalytic activity for decomposition of sulfuric acid in temperature range of 400 - 800°C has shown, that onset temperature for SO_2 formation in all samples was ~600°C. Successive TPR/O studies on these samples have revealed better sintering characteristics as compared to a pure Fe_2O_3 sample and thereby suggested a better performance of chromium substituted catalyst, during prolonged use for sulfuric acid decomposition.

Introduction

In the light of depleting fossil resources and limitation on release of greenhouse gases, hydrogen is emerging as a prospective energy carrier, to meet the increasing global energy demands in the 21st century. In this connection, water is being looked at as a natural choice for the raw material. Presently, the large-scale production of hydrogen involves steam reforming of hydrocarbons, mostly natural gas. One major drawback of this process is the formation of CO_2 as an undesirable by-product. To augment and sustain the hydrogen economy on a long-term basis, decomposition of water has been suggested and in this regard, two processes, namely, thermochemical cycle and high-temperature electrolysis have shown great potential towards efficient production of hydrogen on an industrial scale.

In a thermochemical cycle, water is decomposed into hydrogen and oxygen through series of chemical reactions with some occurring at rather high temperatures and involving intermediates that are fully recyclable. Though, after initial reports on hydrogen production from water by thermochemical route by

Funk and Reinstrom [1], numerous thermochemical cycles (almost 200) were investigated from the point of view of their efficiency, number of reactions/steps involved, corrosion issues etc., the focus remained on few processes namely, Sulfur-Iodine (SI) cycle, hybrid sulfur cycle, UT-3 cycle and the Ispra Hybrid cycle [2-4]. Out of these cycles, Sulfur-Iodine (SI) cycle, originally proposed by General Atomics [5], is being looked at, as a promising process for hydrogen production, due to its higher efficiency (~56%). It involves the following chemical reactions:

I_2 (l) + SO_2 (g) + $2H_2O$ (l) →
2HI (l) + H_2SO_4 (l) (70 - 120°C) ....(1)

H_2SO_4 (l) → SO_2(g) + H_2O(l) +
$1/2O_2$(g) (800- 900°C) ....(2)

2HI (l) → I_2(g) + H_2(g) (300 – 450°C) ....(3)

The whole process takes place in water and high-temperature heat, particularly, in the decomposition steps (Equation 2 and 3), and releases hydrogen and oxygen. High temperature requirements of these steps are normally met either by nuclear source (high temperature reactor) or by solar radiation. The first step (Eqn.1) also known as Bunsen reaction, proceeds exothermically in liquid phase and produces two immiscible aqueous acid phases. Kubo et al, at JAERI have recently demonstrated a closed cycle production of hydrogen using this cycle in a glass system where 20 h operation of S-I cycle was accomplished and hydrogen was produced at a rate of 31.5 l/h [6].

Recently, work on S-I cycle has been started at BARC in view of availability of high-grade heat from the proposed Compact High Temperature Reactor (CHTR). In the Chemistry Division, studies on the development of catalyst systems, which are active for decomposition of sulfuric acid in the temperature range of 873-1073 K have been initiated. In this paper, we present some of the preliminary results on the catalytic decomposition of sulphuric acid.

Experimental

Catalyst preparation and characterization

Chromium substituted iron oxide catalysts ($Cr_xFe_{2-x}O_3$: X = 0 - 0.4) were synthesized by solid-state route employing AR grade Fe_2O_3 and Cr_2O_3 as starting materials. Samples were calcined initially at 650°C for 72 h and finally at 750°C for 16 h. BET Surface area of these samples as evaluated by N_2 sorption technique was around 2 m^2g^{-1}. Powder XRD patterns recorded in 2-q range 10-70° (step width 0.02° and step time 1.25 s) using a Philips X-ray Diffractometer (model 1729) equipped with nickel filtered Cu-K_a radiation matched with those reported for iron chromium oxide (PCPDF Card No. 34-0412). Redox behavior of samples was studied by recording temperature programmed reduction/oxidation (TPR/TPO) profiles on a TPDRO-1100 analyzer (Thermo Quest, Italy) under the flow of H_2 (5%) + Ar, alternatively, O_2 (5%) + He gas mixtures at a flow rate of 20 ml min^{-1}, in temperature range of 25-1000°C for TPR and up to 800°C for TPO at a heating rate of 6°C min^{-1}. The samples were pretreated at 350°C for about 2.5 h in helium, prior to recording of the first TPR run.

Catalytic activity

Catalytic activities of the samples were evaluated for decomposition of sulfuric acid in temperature range of 400 – 800°C using 2 g of catalyst samples (40-80 mesh) in a flow through quartz reactor (30 cm long, 0.8 cm I.D.) at a space velocity of 1200 ml g^{-1} h^{-1}. High purity nitrogen bubbling through boiling sulfuric acid reservoir (~338°C) carried the acid vapors to the catalyst bed at a flow rate of 40 ml min^{-1}. A gas chromatograph (Netel, model-Michro 9100) equipped with Porapak-Q column and a thermal conductivity detector was used for the analysis of reaction products. IR and mass spectrometry techniques were also employed for analysis of various decomposition products. For comparison, data on catalytic activity was also collected on a pure iron oxide sample.

Results and Discussion

Temperature Programmed Reduction / Oxidation

The TPR profiles depicting the reduction behavior of $Fe_{2-x}Cr_xO_3$ samples are shown in Fig. 1. Data on pure Fe_2O_3 and Cr_2O_3 samples are also included in this figure. As seen in Fig. 1 a, the TPR profile of Fe_2O_3 sample comprises a prominent band with T_{max} at ~470°C and another broad band with onset of 530°C and having T_{max} at ~705°C. The reduction onset temperature of the main band is at 330°C. The presence of two bands suggests the two reduction steps. Since Cr^{3+} is stable towards H_2 atmosphere up to 1000°C, as evident from Fig. 1d, the reduction profile of the substituted samples is attributed to reduction of $Fe^{3+} \rightarrow Fe^0$ species. T_{max} value of the main band at ~ 470°C shifted to higher values by ~ 25°C upon chromium substitution.

The over all TPR profiles of these samples remained same during successive TPR/TPO cycles (Fig. 2). However, the T_{max} value for the main band in case of chromium substituted samples reduced by about 45°C during 2nd TPR run and remained unchanged during subsequent cycles. On the other hand, T_{max} for the main band was shifted to higher temperatures by ~30°C in case of Fe_2O_3 during subsequent TPR/TPO cycles and was attributed to sintering of the sample. Thus, Cr^{3+} substitution has not only eased the reduction of iron oxide but also enhanced the compositional stability towards multiple TPR/TPO cycles, as compared to unsubstituted sample.

Catalytic activity

Fig. 3 shows the catalytic activity of various samples prepared in this study. Both substituted and unsubstituted iron oxide samples were found to be active for decomposition of sulfuric acid in temperature range of 600-800°C. The SO_2 yield, as measured with gas

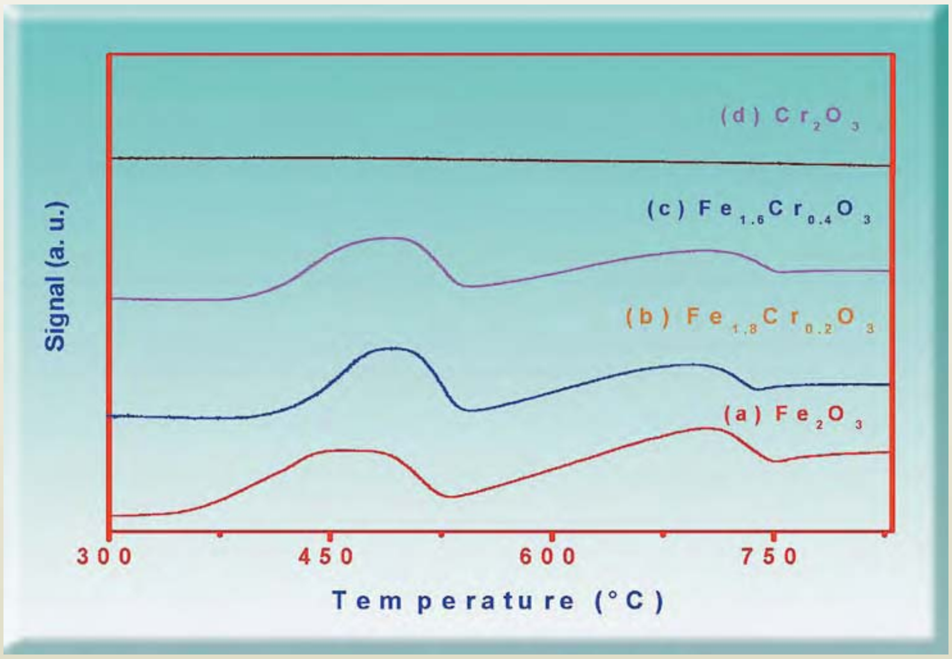

Fig. 1: TPR profile of various chromium substituted iron oxide and that of unsubstituted samples.

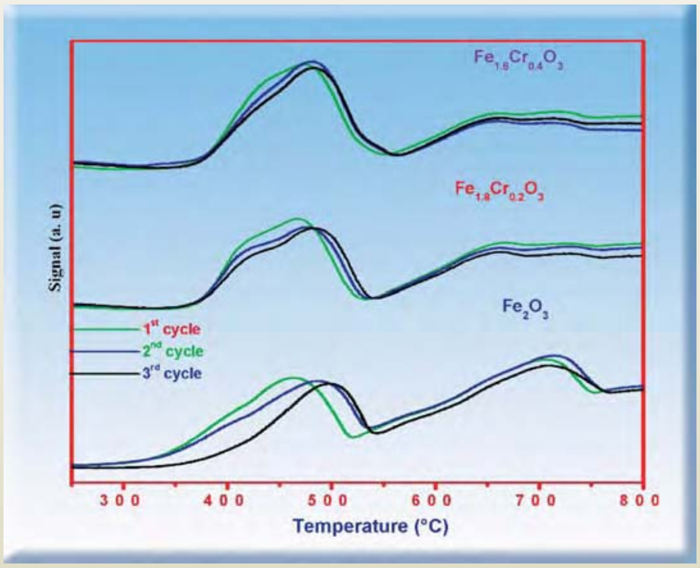

Fig. 2: Successive TPR profiles chromium substituted iron oxide and unsubstituted iron oxide.

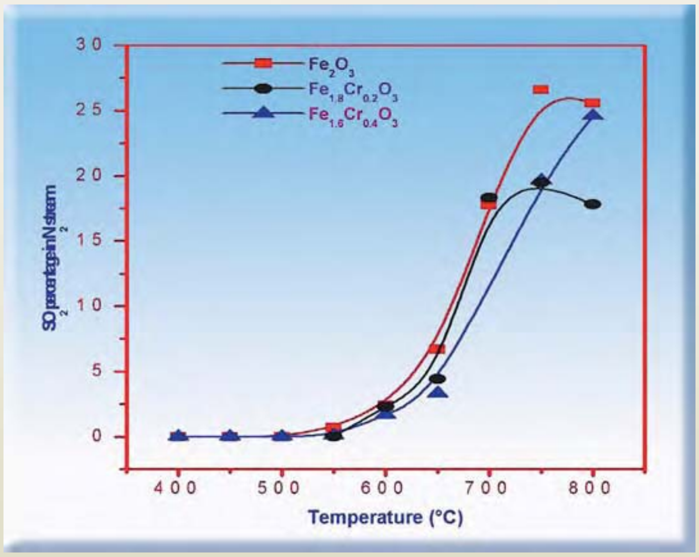

Fig. 3: Successive TPR profiles chromium substituted iron oxide and unsubstituted iron oxide

chromatograph increased gradually with rise in temperature; the reaction onset temperature in all samples was ~ 600°C. Mass spectrometry and IR spectroscopy data further substantiated the GC results. It is pertinent to mention here that no SO_2 was produced under identical conditions in the absence of a catalyst and formation of SO_3 was confirmed during IR analysis of the effluent stream.

Although chromium substitution has not much improved the catalyst performance of a Fe_2O_3 sample its role in improving sintering characteristics of the substituted samples, as revealed during successive temperature programmed reduction / oxidation cycles mentioned above, does hold a promise on their prolonged use for the titled reaction.

References

1. J. E. Funk and R. M. Remstrom, *Ind. Eng. Chem. Process Des. Dev.,* 5 (1966) 336.
2. L.C. Brown, J. F. Funk, S.K. Showalter, GA-A23373 Report, 2000.
3. J. E. Funk, *Int. J. Hydrogen Energy,* 26 (2001) 185.
4. B. Yildiz and M.S. Kazimi, *Int. J. Hydrogen Energy,* 31 (2006) 77.
5. J. H. Norman, G. E. Besenbruch, L. C. Brown, D. R. O'Keefe and C. L. Allen, General Atomic Company Report- GA-A16713 (1982).
6. S. Kubo, H. Nakajima, S. Kasahara, S. Higashi, T. Masaki, H. Abe and K. Onuki, *Nucl. Eng. Des.,* 233 (2004) 347.

About the Authors

Mr. Atindra Mohan Banerjee completed his Master of Science in Chemistry from Calcutta University in 2004. He completed a one year Orientation Course in Nuclear Science and Engineering from BARC Training School (OCES - 48 batch). Subsequently he joined Chemistry Division of BARC, Mumbai in Sept. 2005. He is involved in the development of catalysts for their application in generation of hydrogen by water splitting via photocatalysis and S-I thermochemical cycle.

Mr. K. Bhattacharyya joined BARC in 2003 after graduating from 46 th Batch OCES of BARC Training School. He is presently working in the field of Heterogeneous Photo-catalysis. His research interests include supported metal catalysts, host-guest chemistry in micro/mesoporous molecular sieves hosts, entrapment of nanosized oxides in mesoporous materials and evaluation of their catalytic/photo catalytic behavior towards reactions of environmental importance and efficient sun-light assisted photo catalytic oxidation of volatile organic compounds (VOC's) using Titania and doped Titania containing mesoporous molecular sieves. He is also engaged in studies related to catalyst development for various steps of S-I thermochemical cycle for hydrogen production.

Dr (Mrs.) Mrinal R. Pai joined BARC through Training School (40th Batch) after completing her post graduation in Chemistry from IIT Delhi in 1996. She initiated her research activities in the field of catalysis with development of H_2 mitigation catalyst during year 1999 in Chemistry Division. Also, she gained experience in synthesizing fine powders of nano-size mixed oxides and characterizing them by various techniques for their prospective applications in pollution abatement, water splitting by photocatalysis and sulfuric acid decomposition reaction in S-I thermochemical cycle. She was awarded Ph.D degree in Physical Chemistry from Mumbai University in year 2005'. There are fourteen publications in refereed international journals, several publications in symposia and conferences and invited talks to her credit.

Dr A.K. Tripathi joined BARC in 1984 after successful completion of one year Orientation course in Nuclear Science and Engineering of BARC Training School. He started his research activity in the area of heterogeneous catalysis and has contributed to the development of catalytic solution for the gas recovery problem in sealed off CW-CO_2 lasers. His research interests include supported metal catalysts, host-guest chemistry in micro/mesoporous molecular sieves hosts, entrapment of nanosized oxides in mesoporous materials and evaluation of their catalytic/photocatalytic behavior towards reactions of environmental importance. Presently, he is actively engaged in studies related to catalyst development for various steps of S-I thermochemical cycle for hydrogen production.

Dr V.S. Kamble joined Chemistry Division, BARC in 1974 after his M.Sc. from Nagpur University. He initiated his research career in the area of heterogeneous catalysis by studying the CO and CO_2 adsorption/methanation over supported metal catalyst and evaluated the role of gamma irradiation in enhancement of catalytic activity. He also investigated mode of adsorption and encapsulation of various molecules such as CO, CO_2, methanol, ethylene and benzene in micro/mesoporous molecular sieves using techniques such as, FTIR, TPD, ESR and microcalorimetry and established structure-activity relationship. He has successfully demonstrated an efficient sun-light assisted photocatalytic oxidation of volatile organic compounds (VOCs) using uranium containing mesoporous molecular sieves. His current interest lies in the S-I processes for hydrogen production specifically in development of catalyst for decomposition of H_2SO_4 and HI acids.

Dr (Ms) S. Bharadwaj, M.Sc. and Ph.D. from Mumbai University joined BARC in 1977 through 20th Batch Training School. She has been working in the area of high temperature thermo-dynamics of nuclear as well as other refractory materials for the past 30 years. During the year 2000-01, she worked as Guest Scientist at Juelich Research Centre, Juelich, Germany. Presently, she is heading the Fuel Cell Materials and Catalysis Section of Chemistry Division, BARC. She is a Ph.D guide of Mumbai University and professor of Homi Bhabha National Institute, Mumbai. She has been bestowed with NETSH-ITAS Award 2006 for her contribution in the field of thermodynamics and thermal analysis.

Dr S. K. Kulshreshtha graduated from Agra University in 1966 and joined Chemistry Division, BARC through 10th batch of training school. He started his research career with the study of diamagnetically substituted spinel ferrites using Mossbauer spectroscopy for which he was awarded Ph.D. by Mumbai University in 1974. He did his postdoctoral work in Germany at the University of Erlangen-Nurnberg on the nature of low and high spin state transition in Fe(II) complexes. He superannuated in Dec.2006 as Associate Director, Chemistry Group and Head Chemistry Division of BARC and as Outstanding Scientist. During the past 40 years, he was mainly associated with a variety of research, developmental and academic activities pertaining to the Department of Atomic Energy. Currently, Dr. Kulshreshtha is working as the Adjunct Professor, Applied Chemistry Department, University Institute of Chemical Technology, Mumbai University. His current research interests are centered around material science, catalysis and structural science.

STUDIES OF MATERIAL ISSUES, SCIENCE AND TECHNOLOGY FOR IMMOBILIZATION OF SULPHATE-BEARING HIGH-LEVEL RADIOACTIVE LIQUID WASTE

C. P. Kaushik, R. K. Mishra, Amar Kumar and Kanwar Raj
Waste Management Division,
Bhabha Atomic Research Centre

P. Sengupta and G. B. Kale
Materials Science Division
Bhabha Atomic Research Centre

and

D. Das
Chemistry Division
Bhabha Atomic Research Centre

This paper received the Best Paper Award at the International Symposium on Materials Chemistry (ISMC-2006) held at BARC, Mumbai, during December 4-8, 2006

Abstract

High level radioactive Liquid Waste (HLW), generated during reprocessing of spent fuel, contains most of the radioactivity present in the entire nuclear fuel cycle. The composition of HLW is site-specific and largely depends on off-reactor cooling of spent nuclear fuel, its type and burn up, and chemistry of reprocessing flow sheet. Development of matrices for conditioning of HLW, to ensure isolation of radioactivity from human environment, for extended period of time, is a scientific and technological challenge. Sodium borosilicate glass formulations, adopted worldwide for immobilization of waste, is not suitable for sulphate bearing HLW, because of its low solubility in such glass. Various compositions based on different glass formulations were made with simulated waste to examine compatibility with waste oxide and containing around 10% sulphate. Vitrified waste product obtained from barium borosilicate glass matrix, were extensively evaluated for its characteristic properties like homogeneity, glass transition temperature, thermal conductivity, impact strength etc. using appropriate techniques. Properties like melt viscosity, pour temperature were also determined. It was found that SB44 glass composition ($SiO_2+B_2O_3=50.5$wt%, $Na_2O+BaO= 28.5$ wt%), can be safely loaded with 21 wt% waste oxide, without any phase separation. The other product qualities of SB-44 glass were also found to be on par with internationally adopted glass matrices. This formulation has been successfully implemented in plant scale for immobilization of sulphate-bearing HLW.

Introduction

Material issues are important during the entire process of nuclear waste management. Performance of the materials used in nuclear waste management, determines its safety/hazards. Since the safety of nuclear waste management, relies mainly on the immobilization of radioactive constituents, issues pertaining to materials, immobilization science and its technological development are particularly important.

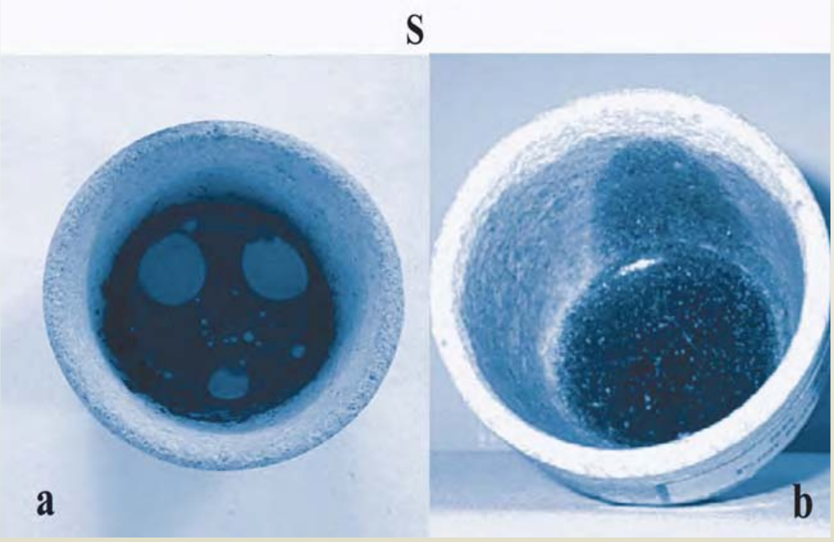

Fig. 1: (a) Separated yellow phase in the glass (b) Homogeneous product of SB-44 glass formulation

Borosilicate glass matrices have global acceptance in the containment of HLW [1]. Presently stored HLW at BARC, Trombay is characterized by significant concentrations of U, Na, Al, and SO4^{-2} in addition to fission products, corrosion products and small amounts of actinides. Vitrification of sulphate-bearing waste is associated with several difficulties. Earlier studies indicated that solubility of sulphate in borosilicate matrix is very poor (~1 wt%) [2]. At higher sulphate concentration, a separate yellow phase (Fig. 1a) of alkali sulphate predominantly comprising of Na_2SO_4 is formed. This yellow phase, behaves as a sink for ^{137}Cs and ^{90}Sr and being highly soluble in water may promote early release of these isotopes to human environment. A need therefore was felt to study and develop a glass matrix having good solubility for sulphate. The present paper briefly describes the details of the work carried out for development of glass formulation for immobilization of sulphate-bearing waste. Based on investigations, a barium borosilicate glass matrix was developed and characterized to meet the product acceptance criteria and it has been successfully deployed at WIP, Trombay for vitrification of sulphate-bearing high-level radioactive liquid waste.

Experimental

Characterization of Waste

Composition of waste plays a vital role in finalizing the glass matrix because of different solubilities of waste constituents in the glass forming system. Detailed radiochemical analysis of HLW was carried out, in one of the well ventilated fume hoods with adequate shielding arrangement. HLW has gross beta activity of 8.77Ci/L and 4.22 mCi/L of alpha activity. Waste is characterized by high amount of salts (≅ 317 g/L) resulting to waste oxide of 108 g/L. Uranium, sodium, aluminium, iron and sulphate are the main contributors. Salient properties of the waste are presented in Table 1.

Development of glass formulation and preparation of glass

In order to contain sulphate in glass, efforts were made to identify chemically stable phase, which can be used

Table 1: Salient properties of HLW

Property	Value
Molarity (free acid), HNO_3	1.34 M
Density	1.22 g/mL
Total solids (major elements as Na, U, Fe, Al, Ca, Cr, Ni, Mn in the form of nitrates)	317 g/L
Gross β, γ (major isotopes ^{137}Cs, ^{90}Sr, ^{106}Ru, ^{144}Ce)	8.77 Ci/L
Gross α	4.22 mCi/L
Sulphate	9.95 g/L

as one of the modifiers in glass formulations. The detailed literature survey in this context indicated that Barite i.e. $BaSO_4$ is one of the most stable phases. Barite bearing litho units, as old as 3500 million years have been reported. Considerations of these historical facts prompted the present authors to investigate into quaternary $BaO-Na_2O-B_2O_3-SiO_2$ system. Glass made up from this system is referred to as base glass. High SiO_2 and Na_2O were avoided as SiO_2 increases the pouring temperature and Na_2O decreases leach resistance. The base glass composition in the range of 30-40 wt% of SiO_2, 15-25 wt% of B_2O_3, 2-15 wt% of Na_2O and 2-25 wt% of BaO were selected in accordance with glass forming region. These base glasses were loaded with 15-30 wt% of waste oxides, to obtain waste glass using simulated waste. Out of various glass compositions that were tried, a barium borosilicate based glass formulation (SB-44: SiO_2= 30.5 wt%; B_2O_3=20.0 wt%; Na_2O=9.5 wt% BaO=19.0 wt% and waste oxide=21 wt%) was able to retain sulphate homogeneously (Fig.1b) without impairing the desired properties of the vitrified product. All glasses were prepared using melt quench method, which include weighing of stoichiometric amount of glass forming chemicals and known amount of simulated waste which is essentially a synthetic waste prepared having same chemical composition as that of HLW. The mix is charged in high temperature furnace. Glasses were made in 100gm batch size in fire clay crucibles.

Product Characterization

This selected composition (SB-44) was taken up for detailed evaluation with respect to various properties like chemical durability, viscosity, thermal conductivity, glass transition temperature, homogeneity, phase separation etc. using standard procedures. Salient properties of selected barium borosilicate glass are presented in Table 2.

Table 2 : Salient properties of vitrified waste product using SB-44 matrix

Properties	Value
Product melt temperature	925 °C
Density	3.0 – 3.2 g / mL
Waste loading	21 wt%
Phase separation (XRD, SEM/EDS, EPMA)	Not detectable
Nature	Amorphous
Softening temperature	496 °C
Leach rate (365 days) Na release basis, DM water, 100 °C	4.26×10^{-6} gm/cm^2/day
Viscosity (950 °C)	30 poise
Thermal conductivity (100°C)	0.92 W/M/°K
Impact strength	0.85 RIAJ

Results and Discussion

Addition of oxides of alkaline earth elements as modifier in sodium borosilicate glass matrix improves the solubility of sulphate in the matrix. Barium based glass formulation (SB44) is one of the optimum formulations in terms of waste loading, pour temperature of the product and the base glass as well as solubility of sulphate having no separated phase as the vitreous mass.

Summary

The aim of the present study was to develop a suitable matrix for vitrification of sulphate-bearing high-level radioactive waste. It was seen that barium borosilicate based formulation (SB-44) was able to retain sulphate without having phase separation and without affecting the desired properties of the conditioned product. The glass formulation has been successfully implemented in plant scale.

References

1. M. I. Ojovan and O. K. Karlina, *Radiochim. Acta.* 34 (1992) 97.
2. W. Lutze, R.C. Ewing (Eds.), Radioactive waste forms for the future ,North-Holland, Amsterdam, (1988) 31.

About the Authors

Mr. C. P. Kaushik, a Post Graduate in Chemistry, is responsible for development of matrices for treatment/conditioning of different types of radioactive wastes and its implementation in the plant scale. He is also actively involved in characterization of waste and waste forms. He is recipient of INS gold medal award for the year 2004 for his outstanding contribution in the field of nuclear waste management. He has around 70 papers in national/international symposia, conferences and journals

Mr. R. K. Mishra, a Post Graduate in Chemistry is engaged in development of vitreous matrices for different types of high level radioactive liquid waste. His main area of research includes preparation and characterization of different matrices with respect to homogeneity, thermal characterization, structural characterization and chemical characterization. He has published around 30 papers in national/international symposia, conferences and journals.

Dr Amar Kumar, a Post graduate in Chemistry is engaged in separation of actinides and fission products from HLW using selective extractants based on cyclic polyether compounds. He research work includes development and characterization of matrices for management of ILW and HLW. He has around 30 papers in national/international symposia, conferences and journals.

Mr. Kanwar Raj, Head, Waste Management Division, an engineering graduate from IIT, Roorkee in Chemical Engineering is responsible for safe management of different types of radioactive wastes generated from nuclear facilities and spent radiation sources all over the country. His field of research includes development of matrices and processing technology and evaluation of long term durability of waste forms under geological repository condition. He has to his credit 70 publications in national and international journals.

Dr P. Sengupta, joined BARC from the 3rd batch of Dr. K. S. Krishnan research fellows. His research field include geological disposal of high level nuclear waste, joining of dissimilar materials and characterization of nuclear fuels. He has published around 70 papers in national/international symposia, conferences and journals.

Dr G.B.Kale an engineering graduate in metallurgy from Visvesarayya Regional College of Engineering, Nagpur has vast experience of over three decades on the applications of Electron Probe Micro analyser (EPMA) to the field of materials science research. His main interest is in multi component multiphase diffusion in alloys, diffusion bonding of dissimilar materials and materials for disposal of nuclear waste. He has to his credit 135 publications in national and international journals.

Dr D. Das, Head, Chemistry Division, a Ph. D. in Science from University of Mumbai is responsible for studying thermodynamics of strategic materials, development of high temperature PIA facility for transport property measurement of gas and volatile fission products in fuel samples. He has made significant contribution in process chemistry development for immobilization of high level radioactive liquid waste. He has to his credit 70 publications in international journals.

बीएआरसी न्यूज़लैटर
BARC NEWSLETTER

ISOTOPE DILUTION THERMAL IONIZATION MASS SPECTROMETRY USING UO^+ FOR THE DETERMINATION OF TRACES OF U IN Pu CHEMICAL ASSAY REFERENCE MATERIAL*

D. Alamelu, P.S. Khodade, R. Govindan and S.K. Aggarwal
Mass Spectrometry Section, Fuel Chemistry Division
Bhabha Atomic Research Centre

This paper received the 1st prize in Nuclear Technology (NT) category, at the 10th Triennial International Symposium on Mass Spectrometry (ISMAS), held at Munnar, Kerala, during January 28 to February 1, 2006

Determination of trace amounts of uranium (U) in plutonium (Pu) is important in nuclear technology for different reasons. A few are (a) purity and fissile content of the purified Pu as part of chemical quality assurance of purified or recycled PuO_2 and (b) for characterization of chemical assay reference materials of Pu. Usually electrochemical techniques are employed for the determination of traces of U in Pu. But, the technique is not sensitive below 5000 ppm of U in Pu. Radiometric and other analytical techniques can also be employed to a limited extent but it is necessary to separate U from Pu matrix. Hence, these techniques do not have the capability to be applied for certification. In view of the high sensitivity of mass spectrometric techniques, it was considered interesting to exploit this technique in conjunction with isotope dilution and preferably without matrix separation, for determining traces of U in Pu matrix. It is known that U^+ and Pu^+ atomic ions are formed at nearly similar filament heating conditions. Also, in TIMS, Pu has a much higher ionization efficiency in comparison to U. In view of these, the conventional approach of carrying out measurements using U^+ ion cannot be employed for determining traces of U in Pu matrix due to the isobaric interference at m/q 238 ($^{238}Pu^+$ at $^{238}U^+$ peak). In our previous study with a synthetic mixture of Pu & U, with a Pu/U amount ratio ~ 5, it was found that, at suitable filament heating conditions, while UO^+ was significantly produced, no oxide ions for Pu were observed. Therefore, by monitoring UO^+ ions, traces of U in Pu matrix can be determined without the isobaric interference problem which is encountered when using atomic ions. This paper presents the results obtained for U determination at ppm levels, without separation from bulk of Pu, by monitoring UO^+ ions instead of commonly used U^+ ions, in chemical assay reference material potassium plutonium sulphate. Two independent samples were taken up for U determination. It was found that the amount of U in the chemical assay reference standard is around 80 ppm.

---

* This paper was published in the "Journal of Alloys & Compounds", Vol. 444-445, Feb. 2007, p. 640.

About the Authors

Ms D. Alamelu, obtained her M.Sc. Degree in Physics from Annamalai University. After graduating from 38th Batch of Training School, BARC, she joined Mass Spectrometry Section of the Fuel Chemistry Division in 1995. Since then, she has been actively involved in the indigenous development of Time of Flight Mass Spectrometer. Her other areas of interest include thermal ionization mass spectrometry and alpha spectrometry and laser based analytical techniques.

Mr. R. Govindan, obtained his M.Sc. Degree in Chemistry from Annamalai University. He joined Mass Spectrometry Section of Fuel Chemistry Division, BARC, Mumbai during November 2001 after working in Advanced Fuel Fabrication Facility, BARC, Tarapur for a period of 14 years, since 1987. He is currently working in the field of inorganic mass spectrometry for precise isotopic analysis and concentration determination of elements which are important in nuclear technology. He actively participated in the chemical characterization of Mixed Oxide fuel for BWR, Tarapur. His other areas of interest include Potentiometry, Electro-analytical chemistry involving ion selective electrodes.

Mr. P.S. Khodade is working as a Scientific Officer in Mass Spectrometry Section of the Fuel Chemistry Division, B.A.R.C, Trombay, Mumbai. Since 1975, he has been working in the field of inorganic Mass Spectrometry and Alpha Spectrometry for precise determination of isotopic composition and concentration of various elements which are of interest in nuclear technology. He is a coauthor of 50 scientific publications in various journals and symposia.

Dr S.K. Aggarwal, is currently, Head, Mass Spectrometry Section of the Fuel Chemistry Division, BARC, Trombay, Mumbai. He received his B.Sc. (Hons.) from Guru Nanak Dev University, Amritsar, in 1972 with two Gold Medals. He joined the 16th Batch of BARC Training School in 1972 and received Homi Bhabha Award. He did his Ph.D. from Mumbai University in 1980. He is a coauthor of 300 scientific publications, which include 100 articles published in reputed journals. Dr Aggarwal has participated in several international and national conferences and in different international intercomparison experiments. He is a specialist in the field of atomic mass spectrometry and alpha spectrometry and is interested in various mass spectrometric techniques. His other areas of interest include electrochemistry and solvent extraction. He represents India in the Executive Committee of International Mass Spectrometric conferences. He has visited several countries in America, Europe and Australia as an expert as well as for delivering lectures. He is a recognized Ph.D. Guide of Mumbai University.

बीएआरसी न्यूज़लैटर
BARC NEWSLETTER

A STUDY ON THE DETERMINATION OF STRONTIUM ISOTOPIC RATIO BY THERMAL IONIZATION MASS SPECTROMETRY USING SINGLE AS WELL AS MULTIPLE FILAMENT ASSEMBLY

R.M. Rao, A.R. Parab and S.K. Aggarwal
Mass Spectrometry Section, Fuel Chemistry Division
Bhabha Atomic Research Centre

This paper won the 2nd prize in the Isotope Composition and Concentration (ICC) Category at the 10th Triennial International Symposium on Mass Spectrometry (ISMAS), held at Munnar, Kerala, during January 28 to February 1, 2006

Introduction

Accurate and precise ^{87}Sr/^{86}Sr ratio is required, in isotope hydrology and also for forensic purposes. As ^{87}Sr is radiogenic, produced through the decay of ^{87}Rb, variations in ^{87}Sr/^{86}Sr atom ratio are found in nature. Determination of small variations in the ^{87}Sr/^{86}Sr atom ratio can be used to trace the source of salinity in groundwater samples and the origin of fossil or any other sample for forensic investigations. TIMS or ICPMS with multicollector is normally used, to obtain the isotopic composition of Sr. Variation in ^{87}Sr/^{86}Sr ratio is normally reported in absolute terms or it is expressed using the delta notation. As the strontium mass is low, isotope fractionation during analysis by TIMS is expected, resulting in variable systematic error. The use of ^{88}Sr/^{86}Sr ratio as an internal standard helps to correct for fractionation during measurement. Strontium is conventionally loaded from nitrate medium on Ta single filament assembly after a dried drop of 0.05M phosphoric acid [1]. In some labs, Sr isotopes are measured by TIMS from single W filaments using a Ta activator[2,3]. For elements that have low I.P. and high vapour pressures, single filament loading assembly is ideally suited due to high ionization efficiency achievable. Multiple filament analysis is required, for elements having high ionization potential and present as low vapor compound. Strontium is a group II element and has reasonably high ionization energy of 5.7 eV. The strontium oxide is a low vapor pressure compound, having a melting point of 2530°C. During heating step, strontium oxide decomposes to give the metal peak. In our laboratory, it was observed that for analysis of purified Sr using Ta single filament, the filament has to be heated to 3 amperes to get a good signal for Sr^+ ions. Changing fractionation pattern during the analysis was also observed. In the presence of impurities like Ca and Na which inhibit the Sr^+ signal, the temperatures required were higher, which at times resulted in melting of the filament.

The advantage of double/triple filament assembly is the ability to independently control vaporization and ionization. A comparison of the two filament assemblies single and multiple, was therefore undertaken, to understand the vaporization phenomenon during thermal ionization mass spectrometric analysis.

Experimental

NIST SRM 987 Sr isotopic reference material was used for the studies. The carbonate dissolved in nitric acid was loaded on two types of filament assemblies Ta single filament and Ta/Re double filament assemblies. For loading on single filament, 2μl of 0.05 M phosphoric acid was loaded on the centre of the filament prior to the sample. The solution was dried at 1 Ampere. 2μL of sample containing 2μg Sr was then loaded on the filament. The filament was slowly heated to 2 Amperes and maintained there for 2 minutes before putting off the current. For double filament, 2 μL solution containing Sr was directly loaded on the Ta filament and dried as above. The analysis was carried out using an thermal ionization multicollector mass spectrometer. For Sr isotopes, simultaneous ion collection was done, after adjusting the Faraday cups for different isotopes. The intensity for Sr was increased from 0.2 to around 8 X 10 $^{-11}$ Amperes during analysis. The temperature required for double filament was 1.9A/5.9A for the side and center filaments, respectively. In the case of single filament loading, the filament heating temperature of analysis was around 3.1 Amps. ^{87}Sr was corrected for isobaric interference, if any, due to ^{87}Rb by using the interfering element correction methodology of the software. Data was corrected for fractionation using ^{88}Sr/^{86}Sr = 8.3786,as normalizing ratio. The data was acquired in 5 blocks of 12 cycles each. The integration time for each cycle was 10 sec.

Results and discussion

The data for both single and double filament analysis of 60 cycles of separate loadings of 2μg Sr are given in Tables 1&2. Analysis 1a and 1b are ratios obtained from 60 cycles of same loading obtained at different temperatures. As can be observed, there is a wide variation in the ^{87}Sr/^{86}Sr uncorrected ratio for single filament analysis as compared to that obtained from double filament analysis. This variation is reflected on the mass bias (K-factor) obtained. It is observed that for single filament loading, as the current intensity is increased, the observed ^{87}Sr/^{86}Sr ratio also increases unlike in multiple filament loading where the ratio is not

Table 1 : Results of SRM-987 Strontium isotopic ratio determination from single filament assembly

Analysis no.	Filament heating current (Amp)	^{88}Sr intensity (V)	^{87}Sr/^{86}Sr observed	Mass bias factor	^{87}Sr/^{86}Sr * normalized
1a	3.23	2.6	0.71182 (±0.02%)	-0.20	0.71020 (±0.007%)
1b	3.37	8.8	0.71472 (±0.01%)	-0.55	0.71022 (±0.02%)
2	3.12	7.0	0.71493 (±0.02%)	-0.57	0.71020 (±0.01%)
3	3.22	3.4	0.71367 (±0.07%)	-0.41	0.71026 (±0.0082%)
4	3.12	9.3	0.71280 (±0.1%)	-0.30	0.71028 (±0.005%)
6	3.1	1.4	0.71039 (±0.27%)	-0.14	0.71015 (±0.02%)

Table 2 : Results of SRM-987 Strontium isotopic ratio determination from double filament assembly

Analysis no.	Filament heating current (Amp) VT/IT	^{88}Sr intensity (V)	^{87}Sr/^{86}Sr observed	Mass bias factor	^{87}Sr/^{86}Sr* normalized
1a	1.95/5.9	4.5	0.70696 (±0.01%)	0.39	0.71017 (±0.009%)
1b	1.98/5.92	7.6	0.70729(±0.01%)	0.35	0.71019(±0.005%)
2	1.86/5.9	4.2	0.70696 (±0.01%)	0.40	0.71026 (±0.008%)
3	1.98/6	7.2	0.70692 (±0.007%)	0.41	0.71034 (±0.006%)
4	1.95/5.9	4.5	0.70660(±0.006%)	0.45	0.71029 (±0.009%)
5	1.89/5.9	8.8	0.70668 (±0.006%)	0.44	0.71027 (±0.005%)

*Normalized w.r.t. ^{88}Sr/^{86}Sr = 8.3786

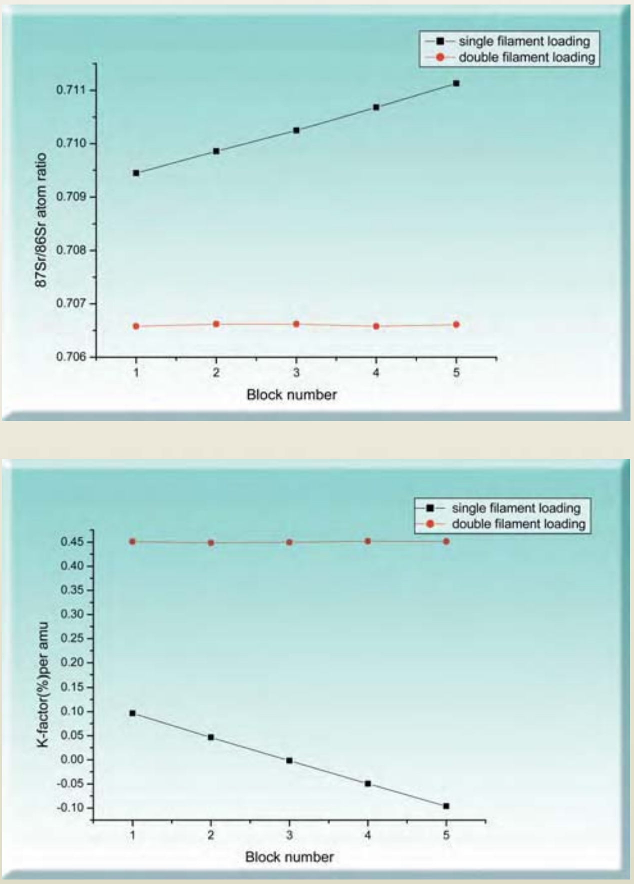

Figures showing graphical representation of the change in the ^{87}Sr/^{86}Sr observed ratio with time

affected. For the same signal intensity, the ^{87}Sr/^{86}Sr observed ratio is 1 to 2% higher for single filament analysis than that for double filament. This means that for the same signal intensity, more sample is consumed for single filament loading as compared to double filament. The figures give a graphical representation of the change in the ^{87}Sr/^{86}Sr observed ratio with time and its effect on the mass discrimination factor. It can be seen that there is a sharp change in the ratio for single filament analysis as compared to that from analysis by double filament. Fortunately the application of the normalization takes care of the fractionation effects. However, these corrections are based on assumptions about mass fractionation e.g. linear dependence on the difference in isotopes, or in recent years an exponential relationship is considered to be more accurate. This would put a limitation on the extent of correction that could be applied.

Conclusion

The experiments conducted were an effort to understand the vaporization and ionization phenomena using two loading assemblies. The two loading assemblies show different vaporization behaviour for strontium which is reflected in the mass discrimination factor. Multiple filament assembly gives more stable observed atom ratio than single filament, loading assemblies for strontium. Multiple filament loading assemblies is better suited than single filament for analysis in presence of impurities. The advantage of single filament, which is, lower cost of analysis cannot be overlooked, especially in the case of Sr where internal normalization takes care of fractionation effects. However, stringent analysis conditions are required for analysis of low amounts of Sr to avoid high fractionation.

References

1. Multiple Collection in Thermal Ionisation ratio Mass Spectrometry of Strontium, I. Platzner, *International Jounral of Mass Spectrometry and Ion Processes*, 67 (1985) 129-136.
2. J.L. Birck, *Chemical Geology* 56 (1986) 73.
3. High Sensitivity Measurements of Strontium Isotopes in Polar Ice, G.R. Burton, V.I. Morgan, C.F. Boutron, K.J.R. Rosman, *Analytica Chimica Acta*, 469 (2002) 225-233.

About the Authors

Mrs. R.M. Rao is working in the field of Inorganic Mass Spectrometry and HPLC, as analytical tools for nuclear fuel materials. She has developed an HPLC method for determination of subppm amount of boron in samples. Her other areas of interest are alpha spectrometry and Microwave assisted digestion.

Mr. A.R. Parab is currently working as a Scientific Officer in the Mass Spectrometry section of Fuel Chemistry Division, BARC, Mumbai. His scientific interest is in the area of thermal ionisation mass spectrometry for precise isotopic analysis of elements which are important in nuclear technology. He has more than 60 research publications in various journals and symposia.

Dr S.K. Aggarwal, is currently, Head, Mass Spectrometry Section of the Fuel Chemistry Division, BARC, Trombay, Mumbai. He received his B.Sc. (Hons.) from Guru Nanak Dev University, Amritsar, in 1972 with two Gold Medals. He joined the 16th Batch of BARC Training School in 1972 and received Homi Bhabha Award. He did his Ph.D. from Mumbai University in 1980. He is a coauthor of 300 scientific publications, which include 100 articles published in reputed journals. Dr Aggarwal has participated in several international and national conferences and in different international intercomparison experiments. He is a specialist in the field of atomic mass spectrometry and alpha spectrometry and is interested in various mass spectrometric techniques. His other areas of interest include electrochemistry and solvent extraction. He represents India in the Executive Committee of International Mass Spectrometric conferences. He has visited several countries in America, Europe and Australia as an expert as well as for delivering lectures. He is a recognized Ph.D. Guide of Mumbai University.

SELF-ASSEMBLY OF PEO-PPO-PEO TRIBLOCK COPOLYMERS IN AQUEOUS ELECTROLYTE SOLUTION

M.K. Sharma
Fuel Chemistry Division
Bhabha Atomic Research Centre

V.K. Aswal
Solid State Physics Division
Bhabha Atomic Research Centre

and

P.A. Hassan
Chemistry Division
Bhabha Atomic Research Centre

This paper won the third prize at the International Symposium on Materials Chemistry (ISMC-2006) held at BARC, Mumbai during December 4-8, 2006

Abstract

Self-assembly of a PEO-PPO-PEO triblock copolymer P85 [$(EO)_{26}(PO)_{39}(EO)_{26}$] has been examined in presence of NaCl in aqueous solution. The temperature range for solubility of block copolymer or cloud point decreases with increasing NaCl concentration. This effect has been explained in terms of the changes in the self-assembled structures of block copolymers to micelles as characterized by viscosity, Dynamic Light Scattering (DLS) and Small-Angle Neutron Scattering (SANS). These studies suggest that the enhanced propensity of sphere-to rodlike transition is related to an increase in micelle dehydration (decrease in solubility) on approaching the cloud point with increase in electrolyte concentration or temperature.

Introduction

Triblock copolymers PEO-PPO-PEO based on polyethylene oxide (PEO) and polypropylene oxide (PPO) are widely used due to their excellent amphiphilic behavior in aqueous solution [1]. These block copolymers self-assemble to micelles in aqueous solution composed of a core of PPO blocks and an outer shell consisting of PEO end blocks and water. The self-assembly can be induced by either increasing temperature and/or copolymer concentration. This makes temperature an important parameter to govern the self-assembling properties of block copolymers [2]. However, in recent studies it has been shown that addition of selective salts can give similar results to that of increasing temperature [3]. While the water dehydration from blocks of copolymer decides the structure of self-assembly, the stability of these structures is still decided by the delicate balance of hydrophilic repulsion to the hydrophobic attraction between the copolymer molecules. The dehydration beyond a limit makes the hydrophobic attraction dominating and the phase separation occurs at the cloud point. In this work, we show the phase diagram for the stability of P85 block copolymer in presence of varying concentration of NaCl. Viscosity, DLS and SANS techniques have been used, to characterize the evolution of self-assembled structures on approaching the cloud point.

Experimental and Data Analysis

The block copolymer P85 and NaCl were obtained from BASF and Fluka, respectively. The phase diagram for the stability of 1 wt% P85 solutions was examined in the NaCl concentration range of 0 – 4 M. The cloud point temperature was measured at the first appearance of the clouding (phase separation) observed. On one of these samples (1 wt% P85 + 3.75 M NaCl) viscosity, DLS and SANS measurements were performed at different temperatures approaching the cloud point. Viscosity was measured with Cannon-Ubbelohde Semi-Micro Viscometer. DLS measurements were performed using a Malvern 4800 Autosizer employing 7132 digital correlator. The light source was argon ion laser, operated at 514.5 nm with a maximum output power of 2 W. The average decay rate (*Ã*) of the electric field autocorrelation function g^1(ô) was estimated, using the method of cumulants. SANS measurements were performed using small-angle neutron diffractometer at the Dhruva reactor, BARC, Mumbai. The incident wavelength was 0.52 nm with wavelength resolution Δë/ë) about 15%. The measured SANS distributions were corrected for empty cell contribution and normalized to cross-sectional unit using standard procedure.

In SANS experiment, one measures differential scattering cross-section per unit volume (dΣ/dΩ) as a function of scattering vector Q and for a dilute system of micelles it can be expressed as

$$\frac{d\Sigma}{d\Omega}(Q) = nP(Q) + B$$

where *n* is the number density of the micelles and *B* is a constant term that represents the incoherent scattering background mainly from the hydrogen molecules present in the sample. The block copolymer micelles can be considered as a core-shell particle with different scattering length densities of the core and the shell. The structure of these micelles is described by following a model as proposed by Pederson [4]. The form factor *P*(*Q*) comprises of four terms: the self-correlation of the core, the self-correlation of the chains, the cross term between core and chains and the cross term between different chains.

Result and Discussion

Fig. 1 shows the phase diagram for the stability of 1 wt% P85 in presence of varying concentration of NaCl. It is seen that the cloud point of the block copolymer solution decreases as the NaCl concentration is increased. The block copolymer solution of 1 wt% P85 in presence

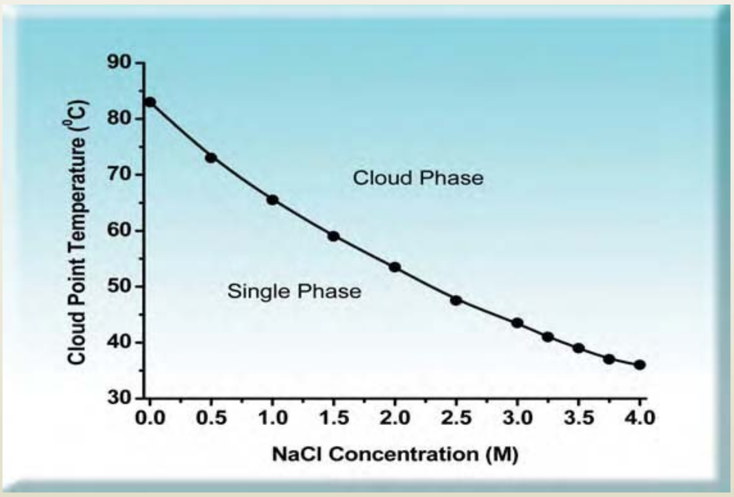

Fig. 1 : Phase diagram for stability of 1 wt% P85 in presence of varying NaCl

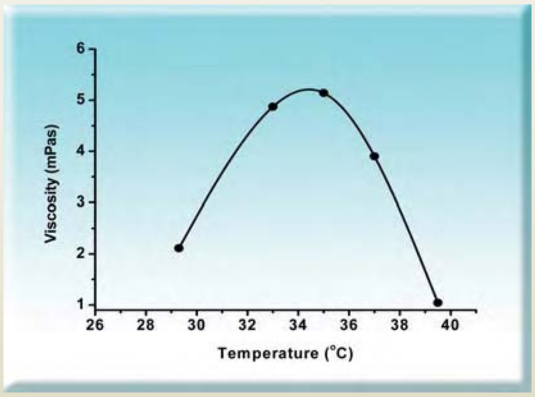

Fig. 2 : Viscosity of 1 wt% P85 in presence of 3.75 M NaCl with varying temperature

of 3.75 M NaCl has been characterized, using viscosity, DLS and SANS on approaching the cloud point. This sample has a cloud point at 37 °C.

Fig. 2 shows the variation of viscosity as a function of temperature near the cloud point. The viscosity curve shows a maximum. The viscosity increase prior to cloud point can be related to the structural transition of the self-assembled block copolymer micelles. The viscosity decrease after the cloud point is believed to be due to coalescing of micelles.

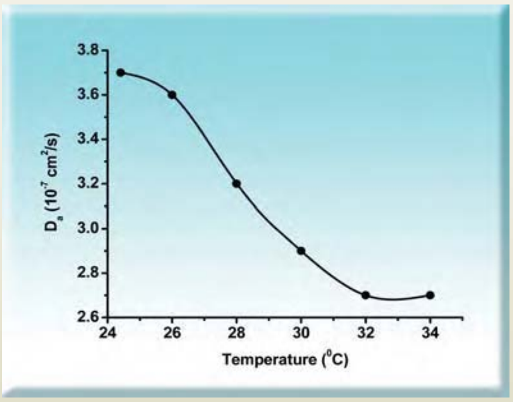

Fig. 3 : DLS results of 1 wt% P85 in presence of 3.75 M NaCl with varying temperature

Fig. 3 shows the variation of apparent diffusion coefficient ($D_a = \tilde{A}/Q^2$) as obtained from DLS data as a function of temperature. The value of D_a decreases with increase in temperature on approaching the cloud point. This suggests a possible transition from sphere to rodlike micelles with the increase in temperature.

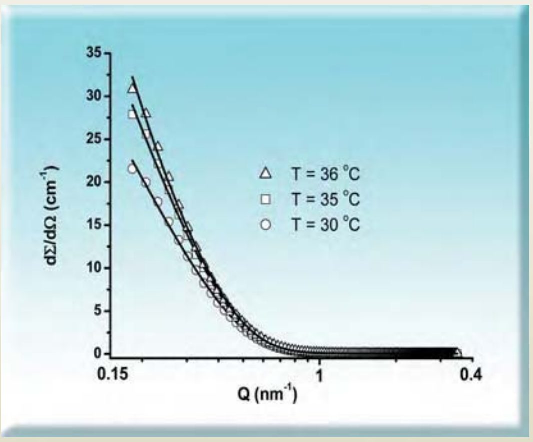

Fig. 4 : SANS data of 1 wt% P85 in presence of 3.75 M NaCl with varying temperature

SANS data as a function of temperature is shown in Fig. 4. The scattering intensity in the low Q region increases with increase in the temperature. It is found that the data is best fitted to the system, consisting of a mixture of spherical and rodlike micelles. The spherical micelles have a core radius 3.6 nm and rodlike micelles are formed with same radius and length of about 50 nm. The value of radius of gyration of polymer segment in the shell region of the micelle has been found to be 1.2 nm. The fraction of the rodlike micelles (ϕ_r) increases with increase in temperature. The values of ϕ_r at 30, 35 and 36 °C have been found to be 17, 23 and 26%, respectively.

References

1. I.W. Hamely, Block Copolymers in Solution: John Wiley & Sons (2005).
2. M. Duval et al., *Langmuir* 21 (2005) 4904.
3. V.K. Aswal et al., *Chem. Phys. Lett.* 425 (2006) 118.
4. J.S. Pedersen, *J. Appl. Cryst.* 33 (2000) 637.

About the Authors

Mr. Manoj Kumar Sharma joined FCD after graduating from 46th Batch of Training School in the year 2003. His area of interest is Electro-chemical techniques in Nanosciences, for development of sensors for quantitative and qualitative applications. He learnt about various electrochemical techniques with instruments like Controlled potential coulometry of U and Pu. Currently he is conducting Literature surveys on Conducting Polymers, Nanoparticles and Nanocomposites.

Dr V.K. Aswal joined SSPD after graduating from 36th Batch of Training School in the year 1993. His area of interest is Small-Angle Neutron Scattering and Soft Condensed Matter and Self-Association in Soft Condensed Matter (Micelles, Block Copolymers, Lipids), Magnetic Fluids and Protein Solutions. He is currently working with Structure and interaction in protein solutions as studied by SANS, unusual clouding in charged micelles, self-association of block copolymers.

Dr P. A. Hassan joined NM&SCD after graduating from 36th Batch of Training School in the year 1993. His area of interest is Soft Condensed Matter- Colloids, Surfactants, Micelles, Block copolymers, Light Scattering, Neutron Scattering, Rheology, Structure and dynamics of organized assemblies of surfactants, polymers etc. Nanomaterials synthesis in surfactant assemblies, Rheology control of surfactant fluids, particle diffusion in polymer-like micelles. He is currently working with tuning the structure of micelles using organic additives, nanoparticle synthesis in micelles and Microrheology of polymer-like micelles using light scattering.

BIOEVALUATION STUDIES OF ^{125}I-BAKUCHIOL IN TUMOR BEARING ANIMALS

Usha Pandey, Ketaki Bapat, Grace Samuel and Meera Venkatesh
Radiopharmaceuticals Division
Bhabha Atomic Research Centre

and

H.D. Sarma
Radiation Biology & Health Sciences Division
Bhabha Atomic Research Centre

This paper received the third Best Poster Presentation award at the International Conference on Application of Radiotracers in Chemical, Environmental and Biological Sciences (ARCEBS-06), held at Kolkata, during January 23-27, 2006

Introduction

Bakuchiol, a meroterpene phenol (Fig.1) is abundant in seeds and leaves of the plant *Psoralea corylifolia*[1]. Bakuchiol is widely used in Indian as well as Chinese medicine to treat a variety of diseases and it possesses anti-tumor, anti-bacterial, cytotoxic and anti-helmenthic properties[2]. The cytotoxicity of bakuchiol is mainly due to its DNA polymerase1 inhibiting activity[3]. ^{125}I, an auger electron emitter, is an effective radiotherapeutic agent when targeted close to DNA. We envisaged that the incorporation of ^{125}I in bakuchiol might augment its cytotoxic activity and had reported the radiolabeling of bakuchiol with ^{125}I and its *in vitro* evaluation in lymphosarcoma and lymphoma[4]. The current paper describes the *in vitro* and *in vivo* evaluation of ^{125}I-bakuchiol in fibrosarcoma cells.

Experimental

Cytotoxicity of bakuchiol was tested, in cell lines of human origin, approved by the National Cancer Institute, USA using MTT assay at the Advanced Centre for Training, Research and Education in Cancer (ACTREC), Kharghar, Navi Mumbai. Bakuchiol was radioiodinated using ^{125}I and using chloramine T, the pure ^{125}I-Bakuchiol was extracted into benzene. Final constitution was done in 0.1 M phosphate buffer (pH 7.5). ^{125}I-Bakuchiol was characterized by paper electrophoresis and HPLC. *In vitro* uptake in fibrosarcoma was studied, by incubating $\sim 10^6$ cells with different concentrations of ^{125}I-Bakuchiol for 30 min at 37°C. At the end of incubation, the cells were washed twice with cold phosphate buffer, centrifuged and radioactivity associated with the pellet was measured. Biodistribution of ^{125}I-Bakuchiol was carried out in Swiss mice, bearing fibrosarcoma of murine origin. Animals were injected i.v. with ^{125}I-Bakuchiol and sacrificed at 3h and 24 h post injection. The % radioactivity in different organs as well as in tumor was determined.

Results

Cytotoxicity testing of bakuchiol showed, that it was highly effective against leukemia cell line (K562) at

80 μM/mL which showed ~60 % growth inhibition. Other cell lines such as MCF7 (breast), SiHa (cervix) and A-2780 (ovary) also showed ~30-35 % growth inhibition at the same concentrations of bakuchiol. Radioiodination of bakuchiol could be feasible due to the presence of phenolic hydroxy group as shown in Fig. 1. ^{125}I-Bakuchiol could be prepared in ~ 80% yield and with ~95% radiochemical purity and had a retention time of 19.2 min on HPLC, while free ^{125}I- had a retention time of 2.2 min. Table 1 shows the results of the *in vitro* cell uptake studies in fibrosarcoma cells. Significant *in vitro* uptake of ^{125}I-Bakuchiol was observed, in all the concentrations studied in the range of 1.25 μM to 25 μM. Maximum uptake of (30±1.4%) was observed, at 6.25 μM of ^{125}I-bakuchiol. Results of the biodistribution studies in Swiss mice bearing fibrosarcoma are shown in Table 2. At 3 h p.i., ^{125}I-bakuchiol showed a tumor uptake of ~0.95 % ID/g, which reduced to ~0.2% ID/g at 24 h p.i. Major radioactivity was localized in liver and intestine at 3 h p.i. while >90 % of the radioactivity was excreted via the hepatobiliary pathway at 24 h p.i. Though the tumor uptake was less at 24 h p.i., the tumor to blood and tumor to muscle ratios increased appreciably resulting in radiation dose only to tumor.

Conclusion

^{125}I-Bakuchiol could be prepared in good radiochemical purity (>95 %) and showed significant uptake in fibrosarcoma *in vivo* and *in vitro*. As the cell uptake is

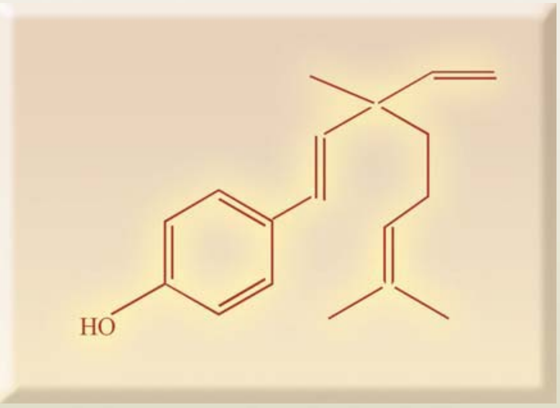

Fig.1: Structure of Bakuchiol

Table 1: Uptake of ^{125}I-bakuchiol in fibrosarcoma cells

Conc. of ^{125}I-bakuchol (μM/mL)	1.25	2.5	6.25	12.5	25
% Cell uptake*	26±0.8	28±4.9	30±1.4	20.2±0.1	20±0.1
% Blank*	0.9±0.1	0.7±0.4	1.4±0.1	1.1±0.3	0.9±0.02

*****(*Mean±SD, n=3*)

Table 2 : Biodistribution of ^{125}I-Bakuchiol in mice bearing Fibrosarcoma

Tissue /Organ	%ID/g (3h)	%ID/g (24h)
Blood	0.7±0.4	0.06±0.02
Liver	15.8±3.95	0.01±0.01
Int+GB	17.2±0.1	2.9±1.2
Kidney	0.82±0.2	0.15±0.02
Stomach	3.8±0.5	0.6±0.08
Heart	0.4±0.1	0.0
Lungs	0.5±0.15	0.06±0.04
Femurs	0.35±0.2	0.0
Muscles	0.18±0.08	0.0
Spleen	0.03±0.01	0.17±0.04
Tumor	**0.95±0.35**	**0.2±0.05**
Excreta	34.5±3.5	90.6±5.6

not receptor-mediated, ^{125}I-bakuchiol has the potential to be tested with various tumor cell lines of human origin.

Acknowledgements

We gratefully acknowledge the help of Dr G.J. Chintalwar, Bio-Organic Division (retd.) and Dr S. Chattopadhyay, Head, Bio-Organic Division for providing us the inactive bakuchiol.

References

1. P.G. Latha, D.A. Evans, K. R. Panikkar, K. K. Jayawardhanan, *Fitoterpia,* **71** (2000) 223.
2. P.G. Latha, K.R. Panikkar, J. *Ethnopharmacology,* **68** (1999) 295.
3. N.J. Sun, S.H. Woo, J.M. Cassady, R.M. Snapka, *J. Nat. Prod.* **61** (1998) 362.
4. K. Bapat, G.J. Chintalwar, U. Pandey, V.S. Thakur, H.D. Sarma, S. Chattopadhyay, M.R.A. Pillai, M. Venkatesh. *Appl. Radiat. Isot.* **62** (2005) 389.

About the Authors

Dr (Mrs.) Usha Pandey is a gold medallist in M.Sc. (Chem) from the University of Madras. She joined the Radiopharmaceuticals Division, BARC in 1997 after graduating from the 40th batch of BARC training school (Chemistry discipline). Since then she has been actively involved in the research and developmental work on therapeutic radiopharmaceuticals. She obtained her Ph.D. from the University of Mumbai in 2007. She has to her credit about 40 papers in various national and international journals.

Dr (Mrs.) Ketaki Bapat joined the Radiopharmaceuticals Division, BARC in 1985. She obtained her Ph.D. in Biology from Mumbai University in 1997. She has expertise in antisera generation (polyclonal and monoclonal) for various antigens. She is well versed in different *in vitro* and *in vivo* techniques for assessment of radiopharmaceuticals. She has served as IAEA expert to Srilanka. She has about 25 publications in national and international journals.

Dr (Mrs.) Grace Samuel obtained M.Sc. and Ph.D. in Chemistry from Mumbai University. She joined the Radiopharmaceuticals Division in 1976 and is currently Head, Radiopharmaceuticals Evaluation Section of Radiopharmaceuticals Division. She is actively involved in the radiolabeling and bioevaluation of various molecules with diagnostic and therapeutic radioisotopes for use as radiopharmaceuticals. She has been instrumental in the development of radioimmunoassay procedures for several hormones and drugs. She has served as an IAEA expert in the field of radioimmunoassay. She has published more than 100 papers in several national and international journals.

Dr Haladhar D. Sarma is Head of Laboratory Animal Facility and Radioisotope Laboratory in Radiation Biology and Health Sciences Division. He obtained M.V.Sc. with distinction from Assam Agricultural University, Guwahati in 1989. His Major research interest concerns radiation carcinogenesis and application of nuclear technology in human and animal health. Prior to joining BARC in 1994, Dr. Sarma was Assistant Professor in the faculty of Veterinary Sciences, Assam Agricultural University. He has published more than 50 publications in various national and international journals.

Dr (Mrs.) Meera Venkatesh joined the Training School of Bhabha Atomic Research Centre in the year 1976 after completing Bachelors Degree in Chemistry from Bombay University. She joined the Radiopharmaceuticals Division in 1977 and has been engaged in the research and development of Radiopharmaceuticals and radiometric assays since then. Dr. Meera obtained her doctorate degree from the Mumbai University in 1986 for her work in the field of Radioimmunoassays. She did her post-doctoral fellowship at the University of Missouri, USA during 1992-94 in the field of therapeutic radio-pharmaceuticals and later in 1999 served as a visiting professor at the same university. Currently, Dr. Meera is heading the Radiopharmaceuticals Division, BARC and concurrently serves in the capacity of General Manager of Quality Control at the Board of Radiation and Isotope Technology. She has published over 150 papers in the international journals, international and national symposia/ conferences and has authored a few invited articles. She has served as an expert in the field of Radiopharmaceuticals and Radiometric assays for the IAEA.

बीएआरसी न्यूज़लैटर
BARC NEWSLETTER

MINIATURE SPECIMEN TECHNIQUE AS AN NDT TOOL FOR ESTIMATION OF SERVICE LIFE OF OPERATING PRESSURE EQUIPMENT

Kundan Kumar, K. Madhusoodanan and B.B. Rupani
Reactor Engineering Division,
Bhabha Atomic Research Centre

This paper was selected as the Best Poster Paper at the International Conference & Exhibition on Pressure Vessel and Piping-"OPE-2006-CHENNAI" held during February 7-9, 2006

Abstract

Measurement of mechanical properties of the material of an equipment is required, to estimate its safe operating life. The Bhabha Atomic Research Centre has developed 'Boat Sampling Technique' to obtain a boat-shaped sample from the surface of the equipment without affecting its integrity. The samples removed can be used for preparation of miniature specimens for various types of tests like tensile, bend, fatigue, impact etc. Surface sampling technique, using specimens derived from boat sample can be considered as non-destructive, as the removal of sample does not affect the integrity of the equipment. It may serve as a useful tool for assessing the component integrity, for instance the weldment, HAZ and high stressed regions, which requires adequate strength, toughness and ductility properties. This paper highlights development of Boat Sampling Technique, layout of miniature test specimens in boat sample, testing procedures and co-relationship with conventional tests. It also highlights the methodology to obtain samples from Core Shroud of Boiling Water Reactors under irradiation environment.

Introduction

The material of an operating pressure equipment, viz. pressure vessel, piping etc. undergoes various degradation mechanisms, depending on its environment and service conditions. There have been continuous efforts, to miniaturize test specimens for various reasons like scope for deriving more number of specimens from the sample removed, reduction in size of test equipment, reduction in radiation exposure, saving in waste handling requirements etc.

Development of miniature specimen testing technique involves two aspects : namely, development of methods for preparation of miniature specimens and development of techniques to extract useful mechanical properties from such specimens.

The Bhabha Atomic Research Centre (BARC) has developed an *in-situ* sampling technique, which can be used to scoop material from operating components [1]. Miniature specimens can be prepared from the scooped sample and the same can be tested for determining the mechanical properties of the operating component. The scooping method is known as Boat Sampling Technique (BST) because the scooped sample has the shape of a boat. This paper highlights development of BST, layout of miniature test specimens in boat sample, preparation of test specimens, miniature specimen testing procedures and co-relationship with conventional procedures.

Miniature Specimen Technology

Materials are subjected to various types of tests like tensile, impact and fatigue-fracture characterization. Sub-sized conventional tests, which are essentially a scaled down version of conventional testing, utilize specimens of similar geometry loaded in a similar manner, to produce results equivalent to that obtained from larger specimens. Miniature specimen tests are employed for determination of residual service life of the operating component, by extrapolating the results of evaluation of small specimen. For this purpose, a compact and non-invasive material sampling technique can be adopted for obtaining a small sample of appropriate size from the operating plant, without affecting its integrity. The following major steps are involved in miniature specimen technology:

- Retrieval of representative metallic sample by BST
- Preparation of representative test specimen from the boat sample
- Modelling of test process and procedure for correlation to conventional tests.

Retrieval Of Metallic Sample

BST is used, to remove boat-shaped sample from the area of concern of the equipment. Using this technique, sample is obtained without plastic deformation or thermal degradation of the parent material.

BST mainly consists of a Sampling Module and a handling manipulator. The Sampling Module, shown in Fig. 1, consists of a cutter, a feeding device, a driving system and a device for controlling thickness of sample. The height of the cutter, above the surface being sampled, can be adjusted using a thickness controlling device, to vary sample thickness up to a maximum of 3 mm.

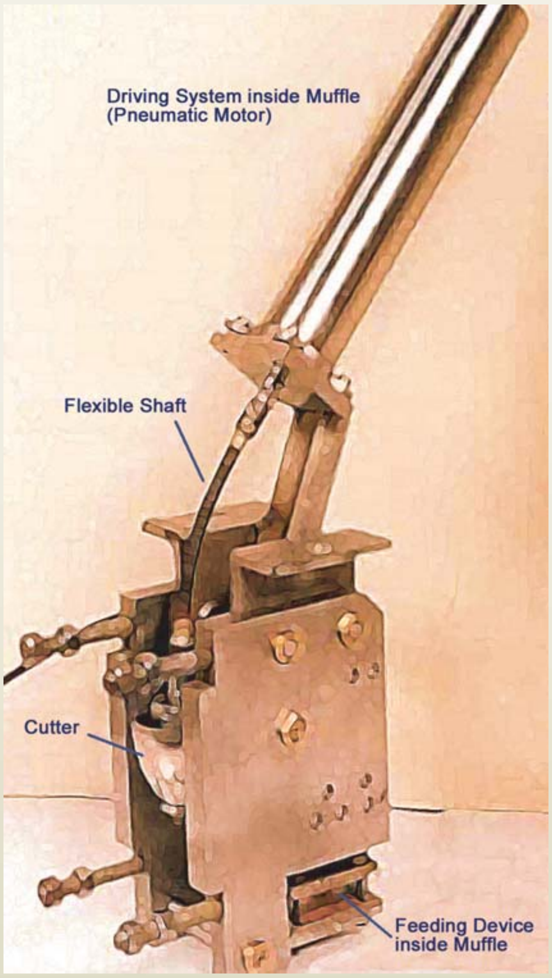

Fig. 1 : Sampling module

Sampling process

The sampling process, shown in Fig. 2, involves spinning the cutter about its axis of symmetry, while moving it slowly in a perpendicular direction into the parent material with the help of a feeding mechanism. During this operation, the cutter grinds out material from the parent material and the cutter shell follows the path cleared by its leading edge, through the material. In this process, kerf of approximately 1 to 1.2 mm width is produced. However, the actual kerf width may increase due to asymmetry in the operating conditions.

The rate at which the cutter can be fed into the material being cut, is greatly affected by the thickness of sample being cut. Typically, samples from soft material can be obtained in five minutes, whereas, in the case of hard material, the time required is about three hours.

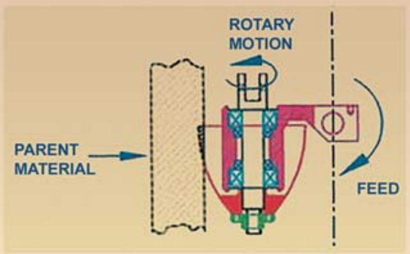

Fig. 2 : Sampling process

Contour of sample

The samples obtained by BST have the shape of a boat in side view and are of elliptical shape in front view. Boat shape has been selected for ease of sample retrieval and to preserve the integrity of the equipment being examined. The geometry of the sample is shown in Fig. 3 and its typical dimensions for 3 mm thick samples are given in Table 1. Due to the sampling operation, the scooped region generated in the base material, is equivalent to the sample thickness plus the kerf.

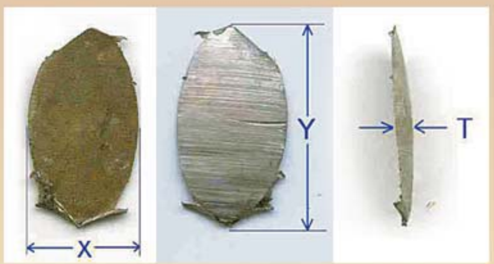

Fig. 3 : Geometry of boat sample

Table 1
Dimensions of sample(in mm)
(Refer Fig. 3)

Thickness (T)	Width (X)	Height (Y)
2.9	25	40.3

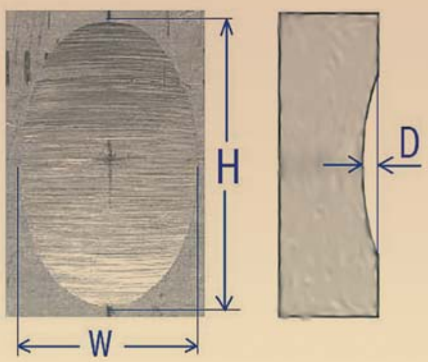

Fig. 4 : Geometry of scooped region

Table 2
Dimensions of scooped region (in mm)
(Refer Fig. 4)

Width (W)	Height (H)	Depth (D)
30.5	49.1	4.1

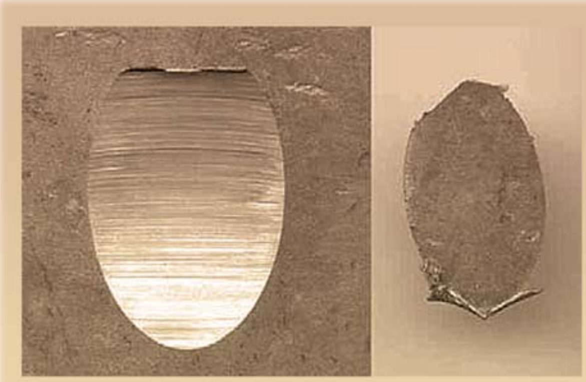

Fig. 5 : Sample from SS plate

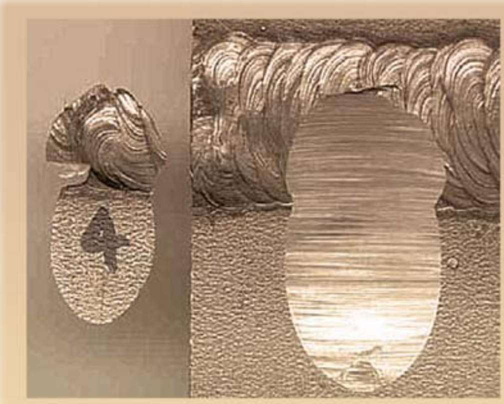

Fig. 6 : Sample from HAZ of welded SS plate

The contour of scooped region of the parent material is shown in Fig. 4 and corresponding dimensions are given in Table 2. Fig. 5 shows some samples obtained from a welded stainless steel plate during mock-up trials and the corresponding scooped region is shown in Fig. 6.

Preparation Of Miniature Test Specimen From Boat Sample

Material characterization of operating equipment can be done, by removing boat sample from the area of concern and preparing miniature test specimen using it. The schematic layout of miniature test specimens that can be obtained from a boat sample is shown in Fig. 7. The layout is based on the consideration of cutting allowances and cutting sequence, which are to be followed for preparing a proper test specimen. Fig.8 shows geometrical configurations of these miniature test specimens. Figs. 9 to 11 show photographs of some of the miniature test specimens of SS 304 material, prepared from boat sample.

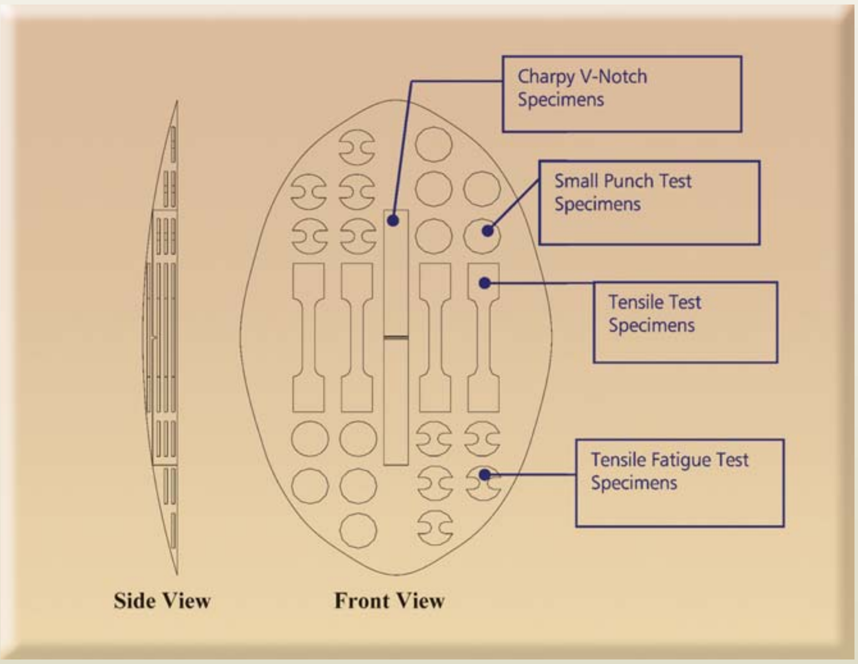

Fig. 7 : Layout of the various types of miniature specimens in a boat sample

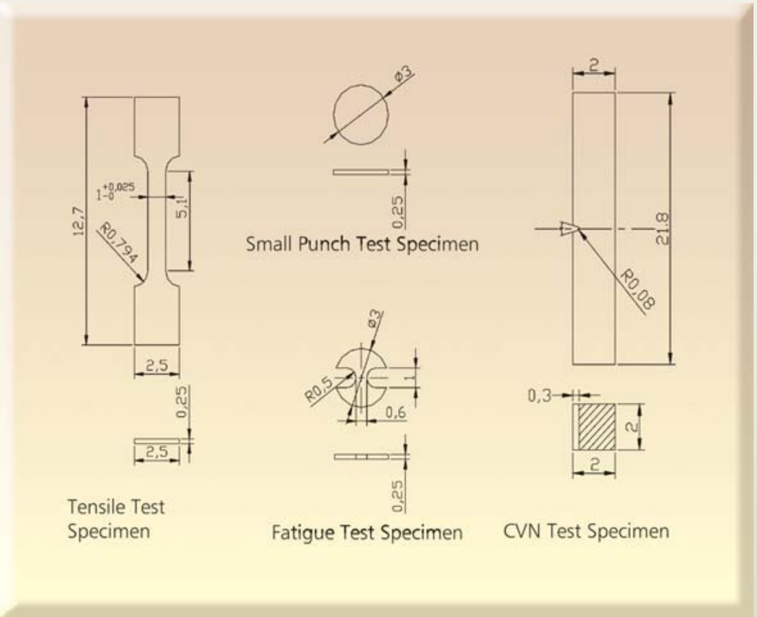

Fig. 8 : Miniature specimens for various tests

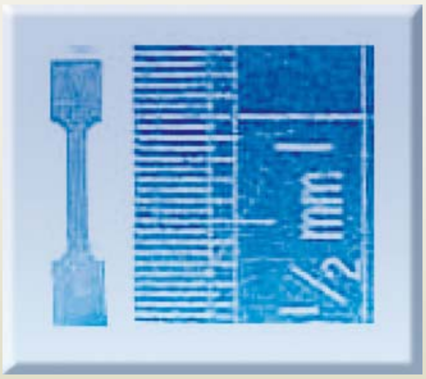

Fig. 9 : Tensile specimen

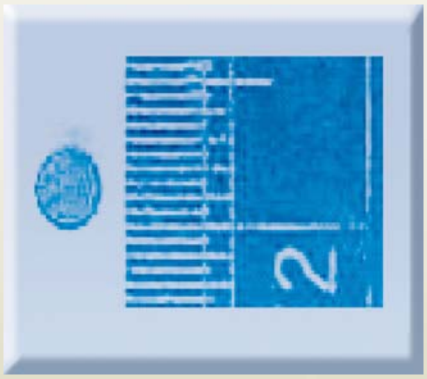

Fig. 10 : Small punch test specimen (3 mm diameter)

Fig. 11 : Tensile fatigue test specimen (3 mm diameter)

Modelling Of Test Process And Procedure For Correlation To Conventional Tests

Tensile test

Geometry and surface condition of the sample are very important in tensile testing. In order to reduce the scatter in measurements, dimensional control is very important and the specimen has to be polished well before testing. Parameters like ratio between thickness and grain size, ratio between width and thickness, ratio between length and width are very important, for which the following three guidelines are to be followed:

$$\text{Gauge length} \geq 5.65\sqrt{\text{Area of gauge section}} \qquad \text{(i)}$$

$$\text{Thickness} \geq 10 \times \text{Grain size} \qquad \text{(ii)}$$

$$\text{Width} \leq 8 \times \text{Thickness} \qquad \text{(iii)}$$

In miniature specimen testing, since it is not possible to monitor the extension of the gauge portion alone, movement of crosshead is used to monitor elongation. Keeping the stiffness of machine very high as compared to the specimen, reduces the error. Free cross head speed is of the order of 10^{-3}/s, giving a strain rate of the order of 10^{-4}/s, which is comparable with that used for estimation of yield stress in conventional testing.

Fracture toughness test

Small punch test can be used to estimate mechanical properties like yield stress, tensile strength, uniform elongation, fracture toughness and the Ductile Brittle Transition Temperature (DBTT) of the material. Load is applied on the specimen mounted in a die, using a hardened steel ball or a punch with a hemispherical tip. Load and corresponding deflection are recorded during the test, as shown in Fig. 12. A number of methodologies have been developed, to estimate the values of mechanical properties using the load-deflection data. One of the methodologies that can be employed for reactor vessels is given below [2].

$$\text{Yield stress, } \sigma_y = \beta \frac{P_y}{h^2} \qquad (1)$$

Where, 'P_y' is the load corresponding to intersection of elastic portion (elastic bending stage) and the uniform elongation portion (plastic bending stage) of load vs deflection curve, 'β' is a material constant and 'h' is the specimen thickness.

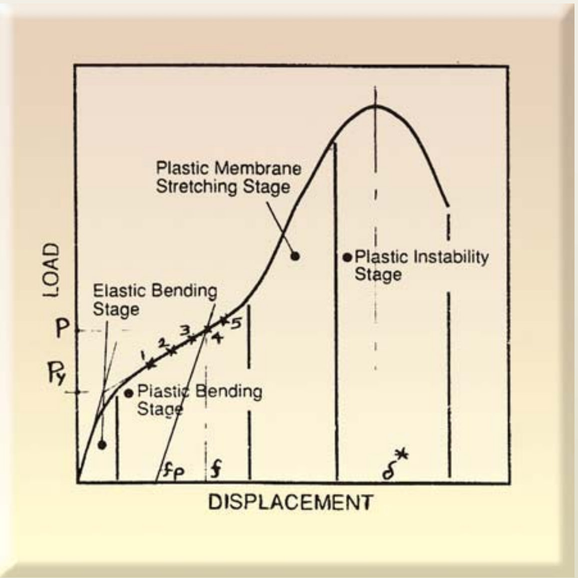

Fig. 12 : Deformation mode during small punch test

Five points from the uniform elongation portion are selected and corresponding to each point, values of equivalent plastic modulus, 'E_p' and true stress σ are calculated using equations (2) and (3).

$$E_p = \frac{3r^2(1-\nu)(3+\nu)P}{4\pi h^3 f} \qquad (2)$$

Where, 'P' is the load, 'r' is specimen radius, 'f' is total displacement and 'n' is the Poisson's ratio of the material.

$$\sigma = \beta \frac{P/h^2}{\left(1+\frac{f_p^{\,2}}{5h^2}\right)} \qquad (3)$$

Where, 'f_p' is the plastic part of displacement, corresponding to load P.

Based on the flow curve equation from initial yield to the end of region of uniform elongation given by,

$$\sigma = K\epsilon^n \qquad (4)$$

E_p can be written as,

$$\ln E_p = \frac{1}{n}\ln K + \left(1-\frac{1}{n}\right)\ln\sigma \qquad (5)$$

Where, 'K' is strength coefficient and 'n' is strain hardening exponent.

Corresponding to the five points on the region of uniform elongation, the values of σ and E_p are calculated. Then using equation (5), values of K and n are estimated by linear regression. The ultimate tensile strength is given by equation (6) and uniform elongation is given by equation (7).

$$\sigma_{UTS} = (n/e)^n K \qquad (6)$$

Uniform elongation, $\delta_u = e^n - 1$ (7)

Area under the load-deflection curve up to a point corresponding to the sudden drop in load is estimated and is designated as SP-energy. It is calculated at different temperatures and SP-DBTT is defined as the temperature corresponding to the average of upper and lower shelf energy values.

Parameters like presence of a notch, strain rate, punch tip shape and grain size can affect small punch test results. As the grain size increases, scatter in result will also increase. Since the effective strain rate in small punch test (10^{-3} to 10^{-4}/s) is much lower than in a Charpy (CVN) test (10^{6} to 10^{7}/s), estimated DBTT is also low and both are related as per equation (8).

$$\text{SP-DBTT} = \alpha \times \text{CVN-DBTT} \quad (8)$$

Where, a is a constant, normally in the range 0.35 to 0.45.

Since small punch tests produce a biaxial stress state that is favourable for brittle cracking, elastic plastic fracture toughness J_{IC} can be estimated using the test [3]. It is based on a linear relationship between J_{IC} and the equivalent fracture strain $\in_{qf.}$ Equivalent fracture strain is calculated using the relationship (9).

$$\in_{qf} = a(^{*}/h)^{b} \quad (9)$$

Where, 'd*' is the deflection corresponding to sharp drop in load, and 'a', 'b' are material constants.

Ductile fracture toughness, J_{IC} can be estimated using the relation (10) [4]

$$J_{IC} = c\in_{qf}\text{-}d \quad (10)$$

Where, 'c' and 'd' are material constants.

Impact test

Chapy impact test is done, to estimate the DBTT of the material. As the specimen size is reduced, the estimated value of DBTT is also reduced from that for full size specimen. The relationships (11) and (12) are used in the test to estimate DBTT [5].

$$\text{DBTT}_{\text{full size}} = \text{DBTT}_{\text{subsize}} + C \quad (11)$$

Where C is a material constant

$$\Delta\text{DBTT}_{\text{full size}} = \Delta\text{DBTT}_{\text{subsize}} \quad (12)$$

Hence, in order to estimate the absolute value of DBTT, it is necessary to establish the value of the constant C by testing full sized and sub sized specimens of the same material.

Fatigue test

The advantage of using an axial type specimen for evaluating the fatigue properties is that unlike a bend type specimen, the fatigue characteristics of the material are not affected by the size of the specimen. A dog-bone type specimen, which gives a stress concentration gradient of 1.21, is used to avoid the effect of any stress gradient and for ease of manufacture. It is necessary to polish the specimen well before testing. Design of the gripping system is very critical in this test. A servo-hydraulic testing machine is used to do the fatigue test at a typical stress ratio of 0.1 and frequency of 25 Hz under load control using a sinusoidal form wave [6].

Stress amplitude = Stress concentration factor x Load amplitude/Specimen cross section

Stress amplitude is plotted with the corresponding number of cycles to failure and is used as the fatigue design curve for the material.

Implications Involved In Miniature Specimen Technology

Boat sampling technique has many positive features as explained earlier. It is particularly suitable for evaluating mechanical properties near weld joint. It has some limitations, which are however minor in nature and can be overcome by suitable modeling.

Surface sampling technique

The sampling technique involved, is a type of surface sampling, assumed to represent the full thickness of the component. Guidelines are required, to select the most appropriate location to sample and the most reliable sampling techniques. The choice of location essentially requires the same decision that must be made, for estimation of residual service life:

- Sample material in the location that most effectively represents the most relevant to the assessment being carried out, or

- Sample material in the less damaged area in order to get a true representation of the component material's original strength.

The most effective sampling techniques will be more a matter of practical experience. "Less invasive" sampling generally requires particular techniques and often implies dedicated instrumentation, that needs to be applied to the component, to be sampled. Therefore, limitations like access for sampling devices need to be considered. For particularly inaccessible locations, these considerations need to be extended to cover the capture and removal of the detached sample, the extraction of the sampler and in the worst cases, recovery of the situation if sampling fails.

Simulation of conventional testing

Comparisons are to be carried out with surveillance specimen or fresh materials of similar grades. The actual material might have undergone some degradation mechanisms, which may affect the modeling.

Specimen size effects

In some cases small-scale or miniature testing may be the representative of the component being investigated, particularly where the component operates in thin sections. Where small-scale testing is attempting to simulate thicker section behaviour, however, specimen size must be considered in the light of structurally significant microstructural dimensions.

A further size effect, which is particularly important for small-scale conventional testing and to some extent for small punch, is the accuracy with which specimen alignment can be achieved. Misalignment giving rise to additional bending or torsion loads on specimens will be likely to increase experimental scatter.

Reproducibility of results

Because of the various factors already discussed, it is likely that small-scale testing will exhibit more scatter than conventional tests. Typical variation in nominally identical tests needs to be investigated.

Conclusion

Surface sampling can be considered as non-destructive technique, which is very useful for determination of residual service life of operating equipment. In the absence of any standards for miniature testing, different versions of test techniques and different geometries of specimen are adopted and test results are compared with conventional testing technique for qualification. A proper modeling is required, to derive equivalence for the loads applied in the various test geometries and interchangeability of results obtained, by different variants of the same technique or different techniques. In addition to this, load equivalence may vary from one class of material to another, so that, significant experience and background information is needed for interpretation of test result.

In the first phase, empirical relationships would be developed utilizing test results. In the second phase, optimization of test procedure and size relationship would be established, to reduce variation in test results, so that, it can be treated as standard for taking safety related decisions.

Acknowledgements

The authors are grateful to Mr. R.K. Sinha, Director, Reactor Design and Development Group, BARC and Mr. Dilip Saha, Head, Reactor Engineering Division, BARC for their support and guidance. We are also grateful to Mr. S.P. Prabhakar and Mr. R.K. Modi, Head, Special System Design Section, Division of Remote Handling and Robotics, BARC for development of handling manipulator for sampling TAPS core shroud. We are also grateful to Mr. E. Ramadasan, Head, IMCS, Post-Irradiation Examination Division, BARC for development of testing techniques for irradiated materials.

References

1. Kundan Kumar, T.V. Shyam, J.N. Kayal. B.S.V.G. Sharma and B.B. Rupani, 'Development of Boat Sampling Technique', BARC Report No. BARC/2002/I/013.
2. Yuanchao Xu, Guangshen Ning et. al., 'Application of miniature specimen technique to material irradiation tests and surveillance for reactor components', *International Journal of Pressure Vessels and Piping,* 77(2000) 715-721.
3. Suzuki, M., Eto, M., et. al., 'Small specimen test technique for the evaluation of toughness degradation', *Journal of Nuclear Materials,* V-191-194(1992) 1023-1027.
4. Kumar A.S., Louden B.S., et al 'Recent Improvements in size effects correlations for DBTT and upper shelf energy of ferrite steels', ASTM STP 1024, 1993, pp. 47-61.
5. Mao X., 'Small punch test to predict ductile fracture toughness J_{IC} and brittle fracture toughness K_{IC}', *Scripta Metallurgica,* V 25(1991), pp. 2481-2485.
6. Nunomura, S., Noguchi, S., et al, 'Two micro fatigue test methods for irradiated materials', Small Specimen Test Techniques applied to Nuclear Reactor Vessel Thermal Annealing and Plant Life Extension" ASTP STP 1204, 1993, pp. 275-288.

About the Authors

After graduating from the 37th Batch of Orientation Course of BARC Training School, **Mr. Kundan Kumar,** B.Sc.(Mechanical Engineering) from B.I.T. Sindri, joined RED in 1994. He has developed Integrated garter spring repositioning system and Sliver sample scraping tools for pressure tubes of Indian PHWRs. He has also developed boat sampling technique for pressure vessel components like core shroud of Tarapur Atomic Power Station. Presently he is working on development of futuristic inspection tools for coolant channels, viz. Hydrogen Equivalent Assessment Tool (HEAT), Replica Tool, Multi-head Scraping Tool etc. He is also associated with development of Tool Delivery System, which is a tool handling and manoeuvring system for inspection tools for coolant channels of Indian PHWRs.

After graduating from the 30th Batch of Orientation Course of BARC Training School, **Mr. K Madhusoodanan,** M.Tech. in Design Engineering, joined RED in 1987. He has developed analytical codes for assessment of fitness for service of pressure tubes of Indian PHWRs. Presently he is working on development of annulus leak monitoring system for AHWR and innovative tools and technology for in-situ measurement of mechanical properties and hydrogen content of pressure tubes.

After graduating from the 17th batch of BARC Training School, **Mr. B.B. Rupani,** M.E. in Machine Design, joined Dhruva project in 1974 and after successful completion of Dhruva project, he was transferred to Reactor Engineering Division (RED) in 1985. Presently he is heading Reactor Coolant Channel Section of RED. He has developed various innovative inspection and rehabilitation tools and techniques for life management of coolant channels of Indian Pressurized Heavy Water Reactors (PHWRs). Presently he is responsible for development of coolant channels of Advanced Heavy Water Reactor (AHWR) and development of technologies required for Zr-2.5%Nb pressure tubes of Indian PHWRs. He is a recipient of VASVIK award in "Mechanical & Structural Sciences & Technology-2000".

IDENTIFICATION OF A MULTIPROTEIN DNA METABOLIC COMPLEX FROM A RADIORESISTANT BACTERIUM *DEINOCOCCUS RADIODURANS*

Swathi Kota and Hari S. Misra
Molecular Biology Division
Bhabha Atomic Research Centre

This paper was awarded the Best Poster Prize at the International Symposium on Frontiers in Genetics and Biotechnology-Retrospect and Prospect held at Osmania University, Hyderabad during January 8-10, 2006

Abstract

Deinococcus radiodurans R1 (DEIRA) a member of Deinococcae family can survive ~12 kGy dose of γ radiation which can generate about 200 double strands and 3000 single strand breaks per genome. An efficient DNA strand break repair, contributes maximum to the radioresistance of Deinococcus radiodurans. Distinction in DNA strand break repair from others seems to lie in the mechanism of action of DNA metabolic proteins, in DNA catabolic and anabolic processes, involved in DNA strand break repair. Here, we report the identification of a multiprotein complex comprised of 15 proteins, from Deinococcus radiodurans. The complex showed DNA ends processing and end joining activities. Biochemical and immunological characterization showed the presence of several DNA repair proteins including PprA, DNA polymerase and DNA ligase. Complex lacked RecA but has three uncharacterized phosphoproteins. The results suggest the presence of various DNA metabolic proteins required for DNA repair functions, in the form of an active multiprotein complex and the regulation of DNA degradation function by high energy phosphate.

Introduction

Deinococcus radiodurans R1 can withstand the lethal and mutagenic effects of DNA damaging agents, including ionizing radiation, far-UV and desiccation (1, 2). Although the biochemical and physiological basis of Deinococci's extreme radiotolerance has not been adequately explained, it is clear that irradiated cells are not passively protected from damaging effects of the incident radiation instead; they suffer massive DNA damage following irradiation (3).The comparison of its genome sequences with *E. coli,* a radiosensitive bacterium and transcriptome analysis of cells recovering from ionizing radiation stress have indicated that, the functional modulation of proteins involved in DNA recombination / repair would be more important than mere presence, in regulating the extraordinary stress tolerance of this bacterium (4,5). To understand how these proteins functions *in-vivo,* the possible existence of different repair proteins in a multiprotein complex form and the functionality of these proteins in a functional module, were studied.

From the cell free extract of *Deinococcus radiodurans* R1, the multiprotein complexes were isolated on molecular sieve column chromatography and characterized on the basis of DNA metabolic activities. A fraction consisting of nearly 15 different size proteins, showed some interesting DNA metabolic activities such as metal independent topoisomerase, an uncharacterised ATP sensitive ends processing nuclease, DNA polymerase and ATP stimulated DNA ligase activities. The multiptotein complex nature of this particular fraction was ascertained, using chemical cross-linking, gradient centrifugation and repeated filtration through gel filtration columns. Immunoblotting experiments showed the presence of PprA (suspected homologue of Ku proteins), single stranded DNA binding protein, protein kinase activity and absence of RecA. Existence of several DNA metabolic proteins together in multiprotein complex would make them to work with greater efficiency and would further explain the mechanism of efficient DSB repair in this super bug.

Methodology

Molecular sieve column chromatography of Sepahcryl S-300 (Pharmacia, Sweden) was performed, to isolate the multiprotein complexes from the total cell free extract of the *Deinococcus radiodurans*. Protein contents of the different fractions were measured at 280nm. Peak fractions obtained were initially screened for the presence of DNA metabolic activity, by incubating with the supercoiled plasmid DNA.

The peak fraction showing the DNA nicking activity was further concentrated, using the Centricon Y10 spin columns and locked the stability of different proteins in multicomplex form using approaches like (i) sucrose density centrifugation (ii) gluteraldehyde cross linking and (iii) repeat gel filteration on the second Sephacryl S-300 column was examined.

Biochemical characterization of the multiprotein complex for different DNA metabolic activities like topoisomerase, differential end processing activity, DNA ligase, etc. was done as per standard protocols (6, 7, 8). Western blotting of the multiprotein complex was done, using the antibodies against SSB, PprA, RecA proteins and phosphoser/thr epitopes using standard protocols.

Results and Discussion

Fractionation of the total cellular protein of Deinococcus radiodurans

Total cellular proteins of the *Deinococcus* were extracted from the stationary phase cells and fractionated through the Sephacryl S 300 Molecular sieve column chromotography. All the fractions obtained were measured for their protein content at 280nm. Six different peak fractions were obtained based on their protein content. These peak fractions when analyzed on the SDS-PAGE, showed different patterns of proteins profile (Fig. 1A), indicating the distinct fractionation of all the proteins based on their molecular size. Activity screening of peak fractions showed the presence of metal-independent DNA relaxation of supercoiled plasmid DNA by peak II fraction (Fig. 1B). In the presence of Mg^{2+}, these fractions showed either reckless DNA degradation irrespective of DNA topology or no activity on DNA substrate (data not shown). This indicated that peak II fraction (hereafter referred to as Peak-II) contains topoisomerase (s) type proteins which have shown the important enzymes in DNA repair function, along with other proteins.

Proteins of peak II fraction exit in a multiprotein complex form

The coexistence of all the proteins, in the peak II fraction was ascertained, by glutaraldehyde crosslinking (Fig. 2A),

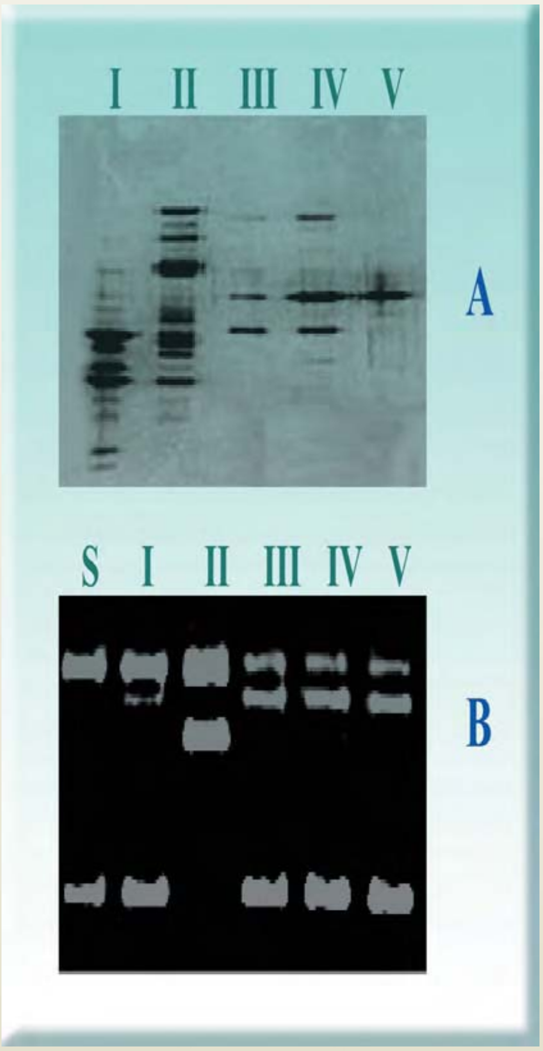

Fig. 1 : Size fractionation and metal independent DNA metabolic activity assay of soluble proteins isolated from stationary phase cells of Deinococcus radiodurans R1. (A) SDS-PAGE analysis of peak fractions (I-V) of Sephacryl S-300 column chromatography. (B) Covalently closed circular plasmid DNA was incubated with different peak fraction in absence of divalent metal ions and product were analyzed on 1% agarose gel

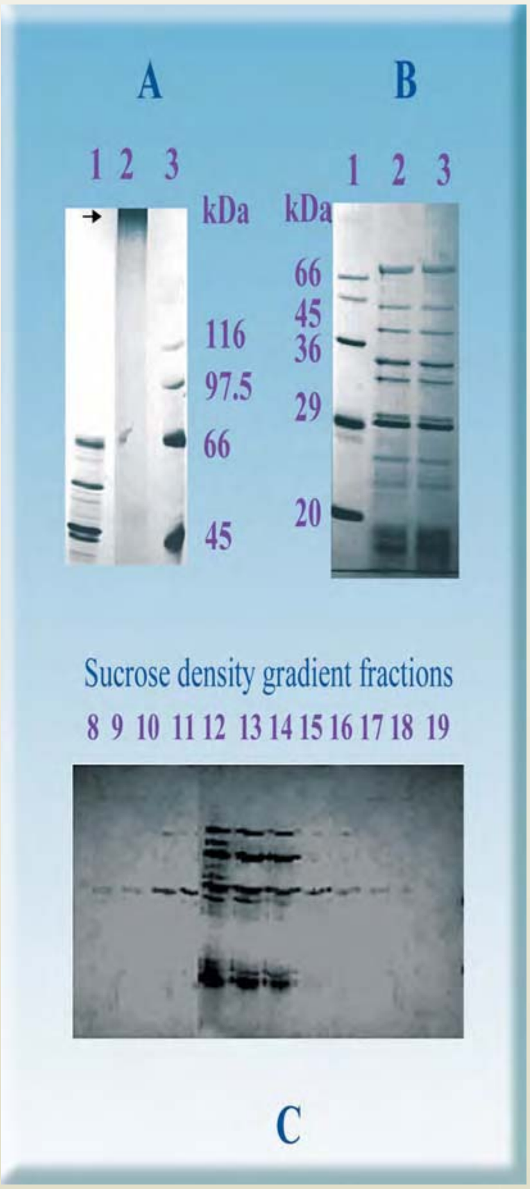

Fig. 2 :Peak II proteins characterization for their presence of these proteins in complex form. Peak II proteins were treated with glutaraldehyde (A), refiltered through second Sepahcryl S-300 (B) and sucrose density gradient centrifugation (C) and analyzed on SDS-PAGE

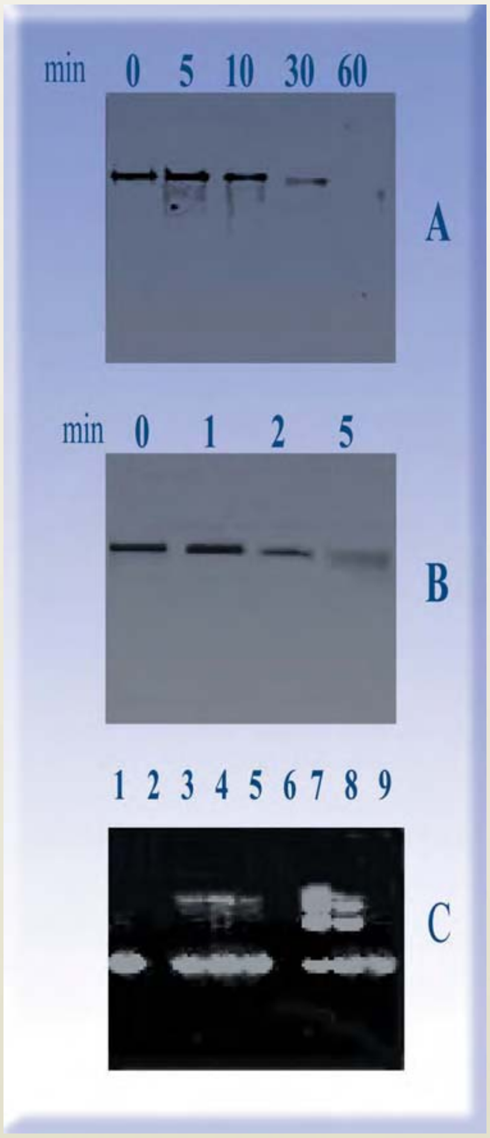

Fig. 3 : DNA metabolic activity characterization of multiprotein complex. Peak II proteins were checked for DNA end processing activity on DNA substrate labelled at 3′ end (A) and 5′ end (B) and incubated for different time interval (min) before products were analyzed on agarose gel and detected. Sticky end DNA substrate was incubated with peak II proteins and product were analyzed on agarose gel showing increase in size of the product due to ends joining (C).

repeat gel filtration (Fig. 2B) and sucrose density gradient centrifugation (Fig. 2C). Glutaraldehyde cross-linked complex showed that the majority of the proteins migrated as a single high molecular mass on 6% SDS-PAGE, when compared to uncross-linked peak-II and molecular size markers. This suggested the presence of nearly all the proteins of peak II fraction in a complex form. Similar conclusions were drawn from the data obtained from sucrose density gradient sedimentation and by repeat-filtration experiments. Existence of multiprotein complexes performing various functions has been reported across the organisms. Spliceosome (9), the cyclosome (10), the proteasome (11), the nuclear pore complexes (12), synaptosomes (13), from eukaryotes replisome (14) and membrane biogenesis complex (15, 16) from *E. coli* to name a few. Functionally these assemblies represent more than the sum of their interacting partners to the new functions.

Protein complex exhibits DNA end processing and ligase activities

In the presence of divalent metal ions, the complex showed nuclease activity. This activity was qualitatively higher with Mn^{2+} than equimolar concentration of Mg^{2+} ion (data not shown). Further nuclease activity was distinguished for its exo- and / or endo- nature on linear DNA substrate labelled on both 3′ (Fig. 3A) and 5′ (Fig. 3B) ends, separately. Results indicated that protein complex removes 5′ radiolabel much faster than label at 3′ end of double stranded DNA (Fig 3B), suggesting that complex has 5′→3′ end processing activity which is an important function in recombination repair of DNA double strand breaks. The importance of 3′→5′ recombinogenic ends in DSB repair and radiation tolerance phenotype of *Deinococcus* has been demonstrated (17). Multiprotein complex showed DNA end joining activity in presence of Mg2+ and exogenously added ATP (Fig. 3C). This suggested the association of DNA end processing and ends joining activity in multiprotein complex.

Multiprotein complex contains known DNA repair proteins

In addition to various DNA metabolic activities integral to DNA strand break repair, the complex also showed the presence of SSB, PprA and phosphoproteins while showing lack of RecA. Among the proteins present in complex, SSB is known as a DNA recombination repair protein (18) while PprA, a unique protein in *Deinococcus* that plays an important role in DNA damage repair function (19).

Thus this study suggested that *Deinococcus radiodurans*, a well known extraordinary radiation resistant organism, outperforms other organisms in DNA strand break repair, possibly by allowing the strong interaction of several DNA repair proteins together in a functional module.

Acknowledgement

Authors are thankful to Dr S. K. Apte, Molecular Biology Division, Bhabha Atomic Research Centre, Mumbai, for his constructive criticism and suggestions in data interpretation.

References

1. Smith, M.D., Masters, C.I., Moseley, B.E.B. (1992) Molecular biology and biotechnology of extremophiles, Chapman & Hall, New York, pp258-280.
2. Minton, K.W. (1994) *Mol. Microbiol*. **13**, 9-15.
3. Daly, M.J., Ouyang, L., Fuchs, P. and Minton KW. (1994) *J. Bacteriol*. **176**, 3508–3517.
4. Blattner, F. R., Plunkett, G., Bloch, C.A., Perna, N.T., Burland, V., Riley, M., Collado-Vides, J., Glasner, J. D., Rode, C.K., Mayhew, G.F. et al (1997) *Science* **277**, 1453-1462.
5. Tanaka, M., Earl, A.M., Howell, H.A. Park, M-J., Eisen, J.A., Peterson, S. N. and Battista, J. R. (2005) *Genetics* **168**, 21-33.
6. Krogh, B.O. and Shuman, S. (2002) *Proc. Natl. Acad. Sci*. (USA) **99**, 1853-1858.
7. Sambrook, J. and Russell, D. W. Molecular Cloning: A Laboratory Manual, third ed., Cold Spring Harbor Laboratory Press, 2002, Cold Spring Harbor, N.Y.
8. Gutman, P.D., Fuchs, P., Ouyang, L. and Minton K.W. (1993) *J Bacteriol* **175**, 3581–3590.
9. Nubauer, G King, A., Rappsilber, J., Calvio, C., Watson, M., Ajuh, P., Sleeman, J., Lamond, A. and Mann, M. (1998) *Nature Genet*. **20**, 46-50.
10. Zachariae, W., Shin, T.H., Galova, M., Obermaier, B. and Nasmyth, K. (1996) *Science* **274**,1201-1204.
11. Verma, R., Chen, S., Feldman, R., Schieltz, D., Yates, J. Dohmen, J. and Deshaies, R. J. (2000) *Mol. Biol. Cell* **11**, 3425-3439.
12. Rout, M.P., Aitchison, J.D., Suprapto, A., Hjertaas, K., Zhao, Y. and Chait, B. T. (2000) *J. Cell Biol*. **148**, 635-651.
13. Varga-Weisz, P.D., Wilm, M., Bonte, E., Dumas, K., Mann, M. and Becker, P. B. (1997) *Nature* **388**,598-602.
14. Johnson, A and O'Donnell, M. (2005) *Annu. Rev. Biochem.* **74**, 283-315.
15. Wu, T., Malinverni, J., Ruiz, N., Kim, S., Silhavy, T.J. and Kahne, D. (2005) *Cell* **121**, 235–245.
16. Ruiz, N., Falcone, B., Kahne, D. and Silhavy, T. J. (2005) *Cell* **121**, 307–317.
17. Misra H.S., Khairnar N.P., Kota S., Srivastava S., Joshi V.P., and Apte S.K. (2006) *Mol Microbiol* **59**, 1308-1316.
18. Witte, G., Urbanke, C. and Curth, U. (2005) *Nucleic Acids Res.* **33**, 1662–1670.
19. Narumi, I., Satoh, K., Cui, S., Funayama, T., Kitayama, S. and Watanabe, H. (2004) *Mol Microbiol* **54**, 278-285.

About the Authors

Ms Swathi Kota, M.Sc. Biochemistry from IARI, New Delhi, joined Molecular Biology Division, BARC after graduating from 46th batch of Biology-Radiobiology BARC Training School batch in 2002. Since then she has been actively involved in understanding the molecular mechanism underlying the extreme radioresistance of *Deinococcus radiodurans*. She has been a recipient of Homi Bhabha Meritorious Award for OCES-46th batch (Bioscience Group).

Dr Hari S Misra joined Bhabha Atomic Research Centre in 1990. Since then he has been working on molecular genetics of bacterial response to abiotic stress and the development of insect resistant transgenic plants. Dr Misra's group is currently working on the elucidation of molecular mechanisms underlying the radiation response to biological system by employing the advanced molecular biology tools. His group reports for the first time, the involvement of a signal transduction component in DNA strand break repair in bacteria. Dr. Misra is the recipient of INS Medal 2004 and is an elected Fellow of the Maharashtra Academy of Sciences, 2003.

SHIELDING ANALYSIS OF AHWR TOP END SHIELD AND DECK PLATE

P. Suryanarayana, C. Chandra, M.V. Gathibandhe, A.K. Kamath and R.A. Agrawal
Reactor Projects Division
Bhabha Atomic Research Centre

This paper won the best paper award in Oral Presentation at the 16th National Symposium on Radiation Physics (NSRP-16) held during January 16-18, 2006 at Chennai

Abstract

Shielding analysis of Advanced Heavy Water Reactor (AHWR) Top End Shield was carried out, using Radiation Transport theory code DOT-III. Geometry and material variation due to presence of lattice tubes makes the shielding analysis of end shield quite complex. Material composition within the lattice tube and outside are quite different neutronically. Hydrogen content within the lattice tube is very small due to boiling water coolant. The use of simpler 1-D Removal-diffusion theory code is inappropriate in such cases. Presence of streaming paths between lattice tube and end fitting and f20mm central hole in coolant channel increases complexity further. Lattice locations existing in end shield have been modeled in the form of annular rings by conserving material. The model used in the analysis has been validated against MCNP and measurements carried out at KAIGA generating station. Flux and dose variations have been plotted to observe the attenuation in different materials of shield.

Introduction

AHWR is developed with the specific aim of utilization of Thorium for power generation. This is a vertical pressure tube type reactor, cooled by boiling light water under natural circulation, with heavy water moderator. The reactor design incorporates advanced technologies, together with several proven positive features of Indian Pressurised Heavy water Reactors. These features include pressure tube type design, low-pressure moderator, on power refuelling, diverse fast-acting shutdown systems and availability of a large low temperature heat sink around the reactor core.

Detailed shielding analysis of top end shield and deck plate was carried out, using two-dimensional transport theory code DOT-III and Monte Carlo code, MCNP. Dose rates on top of deck plate due to N-16 activity in the tail pipes, radiation streaming through annular gap with step between end fitting and lattice tube and through ϕ20mm central hole for ECCS were also estimated.

General Shielding Arrangement

The Advanced Heavy Water Reactor building, is a cylindrical reinforced concrete structure, roofed by a hemispherical pre-stressed concrete dome. The double containment structure besides containing and controlling release of effluents, also provides necessary radiation shielding to the surroundings, from the radiation sources present in the reactor building, during normal operation and accident conditions.

The Calandria vault provides enclosure and shielding for the reactor vessel. The vault is filled with light water to provide neutrons. Top of the Calandria is shielded with top end shield and deck plate and bottom of the Calandria has bottom end shield. All the equipment and pipelines containing the primary coolant and moderator, are located in shielded rooms. The details of shielding provided around Calandria are shown in the following figure.

Top End Shield

The top end shield is designed to limit the dose rate, in tail pipe vault after reactor shut down and also above the deck plate, during reactor operation. The end shield also provides integral support to Calandria vessel along with its internals and supports and locates assemblies like coolant channels, in-core neutron detectors, ion chambers etc.

It is a cylindrical compsite box closed by two tube sheets to form single compartment for containing mixture of water and steel balls (57:43 volume ratio) for shielding against neutrons and gammas. The box is pierced by 500 lattice tubes arranged on 245 mm square pitch.

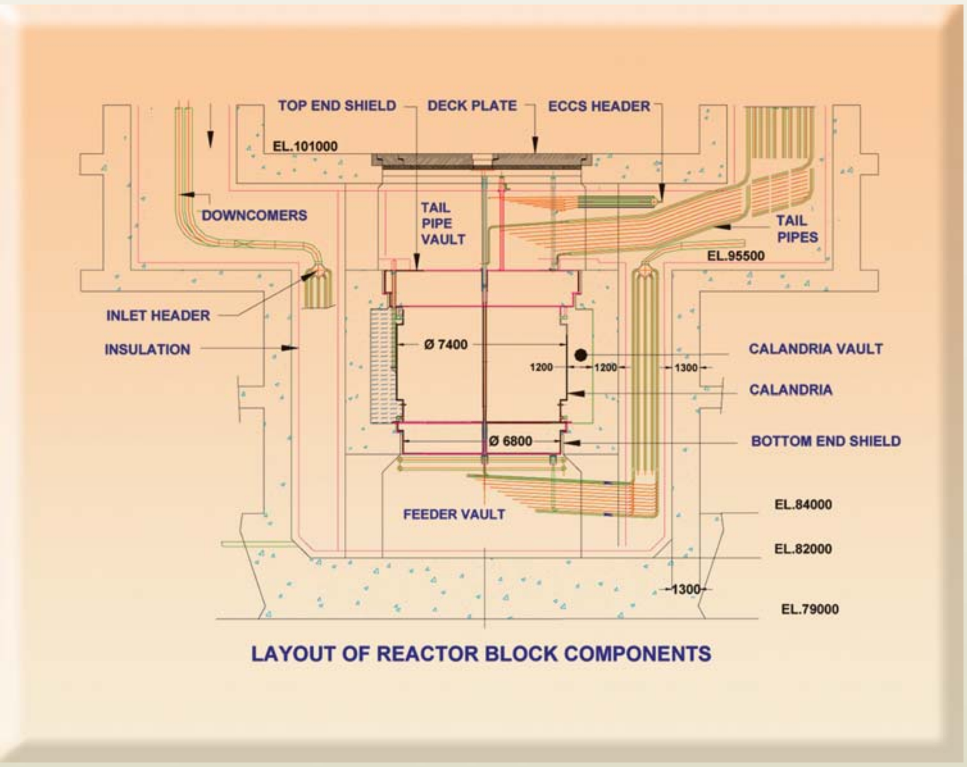

Layout of reactor block components

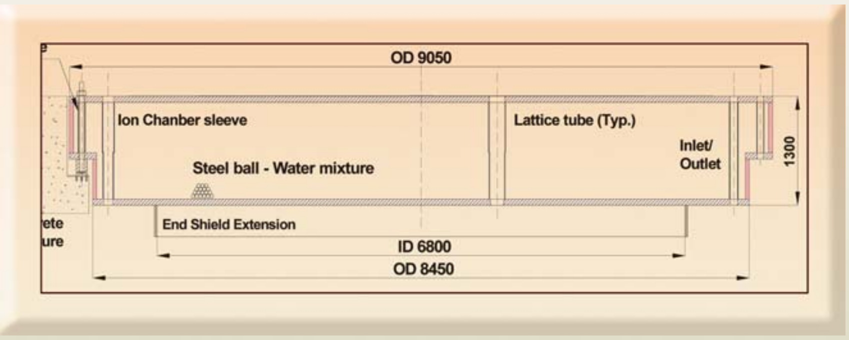

Top End Shield

Air gap with a step between lattice tube and end fitting is provided, to reduce heat transfer from MHT. Shield plug with helical flutes and central hole is located inside the end fitting in end shield region.

Deck Plate

The deck plate is designed to provide shielding to main operating floor area of reactor hall, seal V1 and V2 areas and to provide a working platform for fuelling operations and handling of other assemblies. It consists of three components namely : fixed deck plate, outer deck plate and inner deck plate. The outer deck plate is supported and rotated through anti-friction roller bearings. The outer deck plate provides support for an eccentrically located inner deck plate. The inner deck plate has an eccentrically located stepped hole to provide access to the fuelling machine for coupling to channel. The hole is normally closed by a shielding plug, which will be removed at the time of refuelling and can be aligned to any channel of the core by an appropriate combination of rotation of inner and outer deck plates. At the bottom of the deck plate, compressed borated wood encased in steel is provided, as neutron shield material.

Design Dose Rates

On top of deck plate (during reactor operation) : 0.6 mR/hr.

The dose rate in tail pipe vault (after 24 hours of reactor shutdown) : 20 mR/hr.

Method Of Analysis

Analysis has been carried out by 2-dimensional transport theory code DOT-III. Actual 3D geometry of shielding above core has been modeled in 2-D as shown in figure below. Relative area occupied by different materials and material compositions are the same. This model has been validated with 3-D Monte Carlo code MCNP.

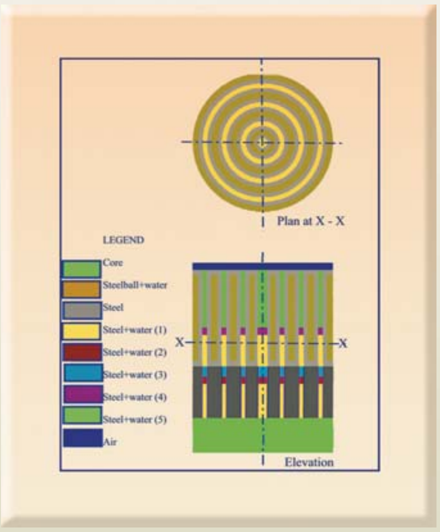

Actual 3-D geometry of shielding above the core using MCNP

Gamma dose rates due to N-16 activity, in tail pipes and due to fission product activity in fuel assembly on top of deck plate, have been calculated, using point kernel buildup factor technique. Dose rates due to radiation streaming are estimated using the incident flux predicted by code DOT-III and empirical formula as given in [1].

Computer code DOT-III

DOT-III solves the Boltzman transport equation in 2-D geometry, using the method of discrete ordinates. Balance equations are solved, for the density of particles moving along discrete directions, in each cell of two-dimensional spatial mesh. Anisotropic scattering is treated using Legendre expansion of arbitrary order. Neutron only, photon only or neutron-photon coupled problems, for both homogeneous and external source problems can be solved using this code. In the present analysis, anisotropic scattering is treated by Legendre expansion of order P3. Forward biased quadrature set with 210 angles is used to represent the discrete directions. Point convergence in all regions with step model to avoid negative flux is used. Calculations are carried out in fixed source mode with 40 group coupled CASK library.

Validation of model used by DOT-III

Actual 3-D shield geometry above the core has been modeled in 2-D as shown in the figure below. Verification of the model adopted is done, by comparing the results of DOT-III with MCNP, for a smaller size of source and shield.

Analysis has been carried out for core and end shield region of AHWR. Model size used in the analysis is 70 cm (radius)x 130 cm (height). Core size for both the

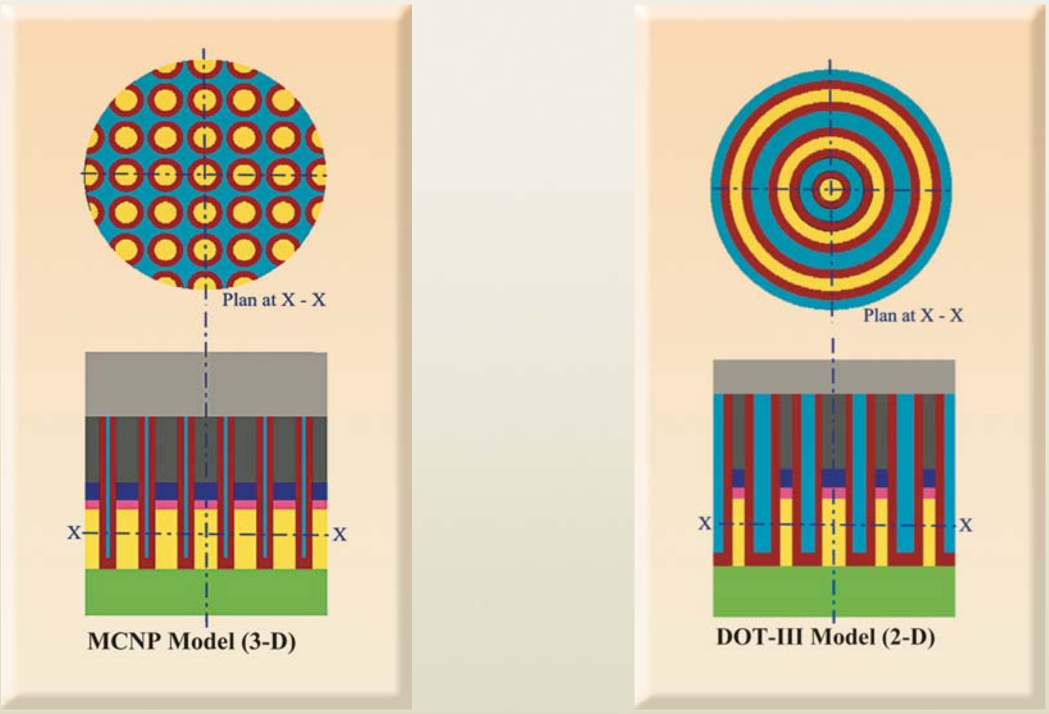

Actual 3-D shield geometry above the core : a comparison of MCNP and DOT-III codes is 70 cm (radius) x30 cm (height). Material composition and the relative area occupied are same in both the codes. 22 group neutron fluxes, obtained from DOT-III are further merged in 3 groups, for comparison. Results are compared after 100 cm thickness of shield. R=0 corresponds to center of model.

Flux on the top of End Shield Surface

From the table it can be seen, that the results for neutron flux and gamma dose rates compare well. 2-D Model used by DOT-III to represent 3-D geometry, gives slightly conservative results. Difference of this order can arise due to different cross-section libraries used.

Results for neutron flux

LOCATION	R=0 to 6.95 cm		R=6.95 to 11.1 cm		Opposite SB+Water	
	DOT	MCNP	DOT	MCNP	DOT	MCNP
Fast neutron flux	0.877	0.602	0.633	0.383	0.420	0.262
Thermal neutron flux	0.468	0.346	0.205	0.294	2.07	3.94

MCNP vs measured values in KGS-2

Validation was carried out by modelling 220MWe PHWR lattice tube geometry in MCNP and compared with measured values in KAIGA Generating Station-2 operating at 200 MWe. Measurements were made at 1.3 m from FSTS at C-10 location.

Neutron Flux	Calculated value n/sq. cm-s	Measured Value n/sq. cm-s
Fast	1.5E6	6.0E5
Thermal	3.1E4	2.0E4

Results and Discussions

Following set of calculations has been carried out

i Estimation of neutron and gamma flux and dose rates due to core in tail pipe vault area.

ii. Neutron and gamma dose rates due to radiation streaming through gaps in end shield in tail pipe vault area and above deck plate.

To limit the dose rate due to activation of materials to less than 5 mR/hr, it is desirable to reduce the neutron flux in tail pipe vault area to less than 2.0 X10^{6} n/s-sq.cm.

Following can be concluded from the above.

i. Intermediate Neutron flux is predominant in tail pipe vault due to deficiency of hydrogen atoms within the coolant channel.

ii. Fast flux, thermal neutron flux and gamma dose rates are quite less in tail pipe vault.

iii. By comparing graphs 1 & 2, it can be seen that high neutron flux in tail pipe vault is due to presence of lattice tubes and material within the lattice tubes. Steel ball + water portion of end shield is quite strong from shielding point of view.

iv. Large reduction in intermediate neutron flux in Jabroc due to high H_2 content in material.

Neutron dose rates and gamma dose rates due to core on top of deck plate are much less than the permissible values in the range of 0.03 mR/hr. Intermediate neutrons determine the dose rate.

Main coolant activity important from shielding point of view is N-16. Dose due to N-16 activity above deck plate is 0.2 mR/hr.

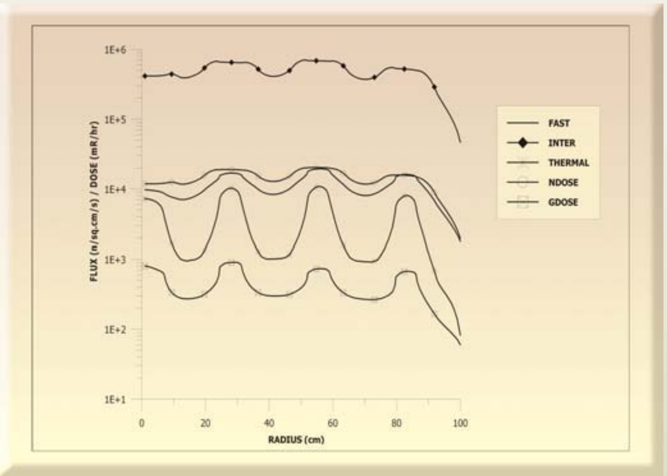

Graph 1: Variation of dose rates on the top of end shield

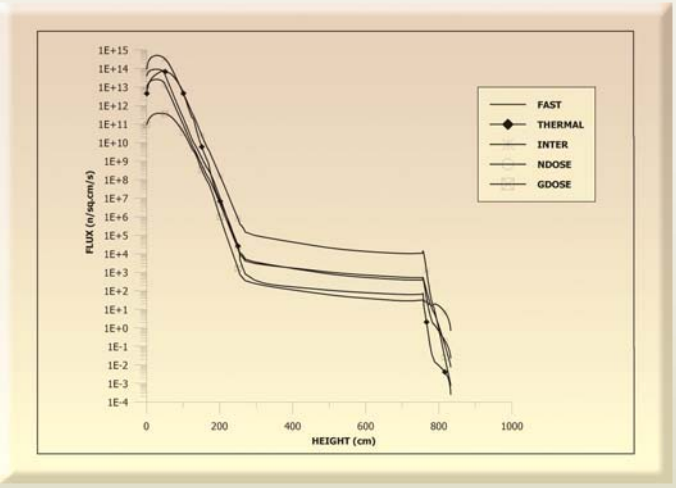

Graph 2 : Variation of neutron flux and dose rates along the core centerline

Annular gap of 3mm between lattice tube and end fitting and 20 mm central hole in the coolant channelgive rise to high radiation field in tail pipe vault area and above deck plate. Dose rate due to ϕ20 mm central hole in fuel assembly is 0.12 mR/hr and the dose rates due to 3mm annular gap with step between end fitting and lattice tube is 0.15 mR/hr.

Conclusions

Based on the analysis carried out the following conclusions are made.

i. End shield thickness of 130 cm having single compartment of steel ball +water is required. Any reduction from this, increases the neutron flux higher than permissible.

ii. Jabroc thickness in deck plate should be 28 cm due to large epithermal neutron flux in tail pipe vault emanating from neutronically weaker material within end fitting and streaming.

References

1. Reactor shielding design manual by Theodore Rockwell
2. Engineering Compendium on Radiation Shielding, Vol. 1
3. Engineering Compendium on Radiation Shielding, Vol. 3
4. Principles of Radiation Shielding by Arthur B Chilton, J. K Shultis & Richard E Faw
5. Reactor Physics Constants – Report no. ANL-5800 (Argonne National Laboratory).

About the Authors

Mr. P. Suryanarayana joined the Reactor Design & Development Group in 1996 from the 39th batch of BARC training school. He obtained M.Tech., degree from Regional Engineering College, Warangal. His fields of interest are shielding and process systems design.

Mr. Arvind K. Kamath obtained M.Sc. in Physics (Electronics) from Ruia College, University of Bombay. He joined the Reactor Projects Division, BARC in 1986. He is actively involved in Shielding Design and Analysis of reactors like LWR, PHWR and AHWR.

Miss C. Chandra has done her M.Sc. in Physics with specialization in Solid State Physics from Benaras Hindu University, Varanasi in the year 2002. She belongs to the 46th batch of training school. She joined the Reactor Projects Division, BARC in 2003. She has actively participated in various kinds of Shielding Design and Analysis of reactors like LWR and AHWR.

Mr. R. A. Agrawal is Head, Shielding Section of the Reactor Projects Division. He obtained his B.E. (Mechanical) degree from Jabalpur University in 1972. He joined BARC in 1973 after completing one-year orientation course from 16th batch of training school. He is involved in design and analysis of reactor shielding (LWR, PHWR, AHWR) and other shielding systems.

Mr. M. V. Gathibandhe joined the Reactor Projects Division in 1994 after completing one-year orientation course from 37th batch of BARC training school. He obtained his M.Sc. degree in Physics from Nagpur University in 1993. He is involved in design and analysis of reactor shielding.

A COMPARATIVE STUDY OF 20 MOLE % Gd_2O_3 DOPED CeO_2 PREPARED BY DIFFERENT SYNTHETIC ROUTES

R.V. Wandekar, B.N. Wani and S.R. Bharadwaj
Chemistry Division
Bhabha Atomic Research Centre

This paper was selected for the 2nd Best Oral Presentation Award
at the 15th National Symposium on Thermal Analysis
held in February 2006 at Jaipur

Abstract

In recent years, a growing interest in properties of nanostructured ion conductors, has been observed. Solid electrolytes for Solid Oxide Fuel cell (SOFC) should be highly dense material due to gas-tight requirement. It is noted that the sintering and densification behavior of ceria-based electrolytes rely on synthetic route and temperature of calcinations. Hence, gadolinium doped ceria samples were prepared, by the cation complexation technique which is a variant of sol-gel technique, using citric acid as complexing agent and also by ceramic route. X-ray diffraction (XRD) and simultaneous TG/DTA technique were used, to characterize the samples. The purpose of this work was to prepare the powders with 10-20 nm of crystallite size at a relatively low temperature. A comparative study of their particle size, densification, thermal expansion and ionic conductivity was carried out.

Introduction

High oxide-ion conducting solid electrolytes, based on zirconia, have been extensively investigated at higher temperatures (~1000°C). In case of SOFC operating at intermediate temperature (800°C), ceria based electrolyte materials are more suitable. Out of various dopants in ceria, samarium and gadolinium showed maximum ionic conductivity at ~800°C. Samarium and gadolinium doped (20 mol %) cerium oxide is a solid solution, formed by replacing Ce^{4+} sites of the CeO_2 lattice by Sm^{3+} or Gd^{3+} cation. These materials have been recognized as leading electrolyte materials [1-3] for application in solid oxide fuel cell. Traditional ceramic method for fabricating dense electrolytes, involves extensive heating of oxide mixture at higher temperature, to yield a single phase solid solution. The materials derived by wet chemical methods show better reactivity than those obtained by solid state reaction, but these materials also require typical densification temperature of ~1300°C to reach maximum theoretical density. Nanocrystalline powders, that can be fully densified at a lower temperature (~1000°C), can be obtained via sol gel route. A sol-gel technique has been considered as an alternative method, for the preparation of homogeneous material with the molecular level mixing than those prepared by ceramic route. In this communication, we report a simple citrate gel procedure to prepare nano-sized ceria-based electrolyte material at low temperature. The citrate gel procedure offers a number of advantages like low cost, is relatively simple, generates less carbon residue and is quite effective in producing highly sinterable ceramic powders [4].

Experimental

Gadolinium doped ceria of composition $Ce_{0.8}Gd_{0.2}\ O_{2-d}$ (GDC) was synthesized, by sol gel and ceramic route. In sol gel route, cerium nitrate and gadolinium nitrate was mixed in the required stoichiometric ratio. Citric acid was added to this mixture so as to maintain the total metal to citric acid molar ratio of 1:2 and final mixture was dissolved in a minimum amount of water. On heating this solution mixture at 150°C a gel was formed after evaporation of water. Subsequently the gel was dried at same temperature and the gases were released to form a fine yellow color precursor, which is a citric acid complex of rare earth metal. The gel initially started to swell and a foamy precursor is formed. This foam contains very light and homogeneous flacks of very small particle size. Precursor was found to be hygroscopic in nature. For comparison these materials were also prepared by standard ceramic route using CeO_2 and Gd_2O_3 as reactants and calcined at 900°C.

Powder XRD patterns of all the samples were recorded (Phillips X-ray Diffractometer, PW 1710, Ni filter and Cu Ka radiation and 2q range 10-70°). The crystallite size of the calcined powder was estimated using Scherrer equation. Their linear thermal expansion behavior was studied using dilatometer. AC impedance of pellets sintered at 1400°C were measured from 300 to 450°C in air using SI 1260 Impedance Analyzer (Solartron, UK) between 10 MHz to 1 Hz. Platinum paste (MaTeck GmbH, Germany) was applied on the pellets as electrodes.

Results and Discussion

TG/DTA curve of the precursor metal complex is shown in Fig. 1. TG curve shows two overlapping steps of weight loss: first step starts at 50°C and completes at 200°C and the loss in second step continues up to 720°C. The 2.03 % weight loss in first step is probably due to dehydration. During second step ~ 1.45 % continuous weight loss is seen which can be due to decomposition of precursor metal complex. The DTA curve exhibits an endothermic peak around 100°C and a large exothermic peak at ~ 320°C which extends up to 400°C. Endothermic peak can be assigned for dehydration of adsorbed water from the precursor. Exothermic peak can be ascribed to the burning of organic material in the

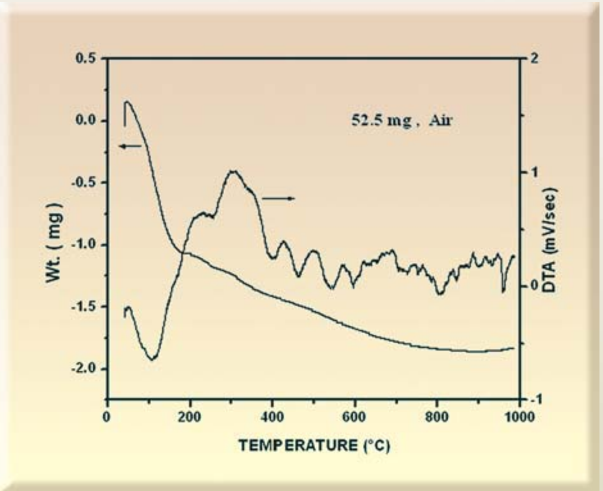

Fig. 1: TG/DTA scans of precursor

sample and to the gradual crystallizing process of GDC.

In order to compare it with TG/DTA data, the X-ray diffraction patterns of GDC, heated at different temperatures during sol gel synthesis as well as by ceramic route, were examined (Fig. 2). XRD data shows no peaks due to impurity at 600°C and the observed pattern corresponds to CeO_2. The peaks are relatively broader for the sol gel synthesized samples, indicating that the powder is composed of smaller crystallites. The broadening of the peaks gradually decreases with increasing temperature of pyrolysis.

The average crystallite size of GDC powder, calculated by the Scherrer equation using d_{220} is given in Table 1. It clearly indicates that sol gel synthesized samples have smaller crystallite size as compared to solid state route sample.

The densities and the thermal expansion coefficients of the samples sintered at 1400°C are also given in Table 1. It can be seen that the density sol gel prepared sample is marginally higher as compared to that from the solid state preparation. The thermal expansion coefficients are, however, comparable for the two samples (Fig. 3).

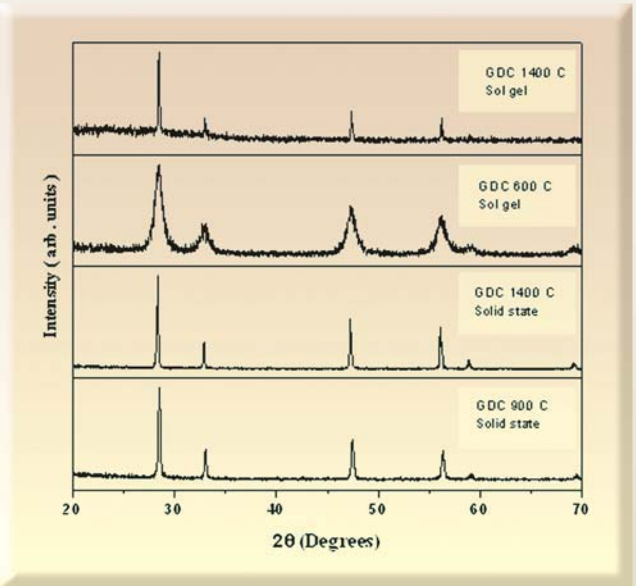

Fig. 2: XRD patterns of GDC prepared by different routes and calcined at different temperatures

Table 1 : Physical properties of GDC prepared by two different routes

Temperature(°C)	Particle size(in nm)		Density		α X 10^6 C^{-1}	
	SS	SG	SS	SG	SS	SG
900/600	54	12	--	--	--	--
1400	85	77	5.39	5.79	11.53	11.33

SS = solid state SG = Sol gel route

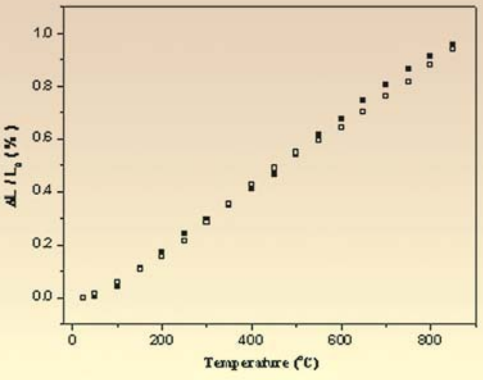

Fig. 3: Dilatometry curve of GDC prepared by sol gel ( ) and solid state (•)

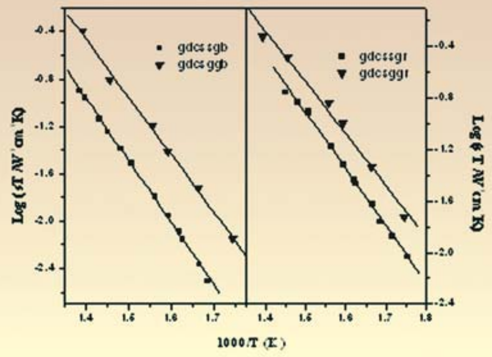

Fig. 4. Plot of log (σT) vs 1/T for grain (gr) and grain boundary (gb) of GDC prepared by sol gel (sg) and solid state (ss).

Impedance spectra of GDC prepared by sol gel as well as solid state route were recorded at different temperatures in the frequency range of 10 MHz to 1 Hz. The electrical conductivity of GDC for grain and grain boundary was obtained from impedance spectra and the activation energy was calculated from the linear Arrhenius plot of log (σ T) vs 1/T (Fig. 4).

The conductivities of sol gel synthesized samples are higher as compared to solid state synthesized samples and the activation energies E_a, derived from the log (σ T) vs 1/T plots are lower for sol-gel synthesized samples (Table 2).

Conclusion

Nanosized powders of gadolinium doped ceria were prepared, by heating the metal complex precursor using citric acid as complexing agent. Because of the smaller particle size ~12- 30 nm, the densification increases and the activation energy for conduction reduces.

Table 2: Energy of activation of GDC obtained from impedance studies prepared by two different routes

Synthesis route	Energy of activation (eV)		Temperature Range (K)	Conductivity at 640 K (Ω^{-1} cm^{-1})	
	Grain	Grain boundary		Grain	Grain Boundary
Solid state	0.873	1.034	573 - 723	9.375E-05	2.262E-05
Sol-gel	0.791	0.958		2.263E-04	9.813E-05

References

1. M.Mogensen in Catalysis by Ceria and Related Materials A.Trovarelli (Ed.) Imperial College Press (2002) p 453.
2. C.Peng, Y.Wang, K. Jiang, B.Q.Bin, H.W.Liang, J. Feng and J. Meng, *J Alloys Compd.,* 349 (2003) 273.
3. Ji-Guang Li, T. Ikegami, Y. Wang and T. Mori, *J. Am. Ceram. Soc.,* 86 (2003) 915.
4. R.A. Rocha and E.N.S. Muccillo, *Mat. Res. Bull* 38 (2003) 197.

About the Author

Ms. Rohini V. Wandekar, is pursuing her Ph.D in Chemistry at Bhabha Atomic Research Centre (BARC) Mumbai. She obtained her M.Sc. degree in Chemistry from University of Mumbai in 2003. Her research work involves the development of various cell components in Solid Oxide Fuel Cell at intermediate temperature (IT-SOFC) and study of thermodynamic properties of these materials

Dr (Ms) Bina N. Wani, Ph.D (Mumbai University) joined Chemistry Division of BARC in 1979. She has about 28 years of experience in utilization of various thermo-analytical techniques related to solid –state chemistry, studies on oxyfluoro compound including superconducting materials and catalysts based on mixed oxides. She has 49 publications in various reputed international journals to her credit. She worked as Visiting Scientist at Ames Laboratory, Iowa, USA in 1995. Her current interest lies in the development of a) various cell components in Solid Oxide Fuel Cell at intermediate temperature (IT-SOFC) and b) mixed oxide based catalyst for pollution control.

Dr (Ms) Shyamla Bharadwaj, M.Sc. and Ph.D. from Mumbai University joined BARC in 1977 through 20th Batch Training School. She has been working in the area of high temperature thermodynamics of nuclear as well as other refractory materials for the past 30 years. During the year 2000-01, she worked as Guest Scientist at Juelich Research Centre, Juelich, Germany. Presently, she is heading the Fuel Cell Materials and Catalysis Section of Chemistry Division, BARC. She is a Ph.D guide of Mumbai University and professor of Homi Bhabha National Institute, Mumbai. She has been honoured with the NETSH-ITAS Award 2006, for her contribution in the field of thermodynamics and thermal analysis.

SELECTIVE PRECONCENTRATION OF MOLECULAR IODINE BY COMPLEXATION WITH POLY (VINYLPYRROLIDONE) IN MEMBRANE AND ITS DETERMINATION BY NAA

A.K. Pandey, R. Acharya, A.G.C. Nair and A.V.R Reddy
Radiochemistry Division
Bhabha Atomic Research Centre,

and

Preeti Bhagat and N.S. Rajurkar
Department of Chemistry, University of Pune, Pune

This paper received one of the Best Papers Presentation award at the DAE-BRNS Symposium on "Emerging Trends in Separation Science and Technology (SESTEC 2006) held during September 29-October 1, 2006 at BARC, Mumbai

Molecular iodine (I_2) is an important bactericide and is added to drinking water as a disinfectant. It is one of the fission products in nuclear reactors and poses a problem in reactor water. It is also an important reactant or a product in many chemical reactions. Hence, its determination is of significance. I_2 forms complexes with several reagents, which can be used for its determination. A method is proposed which is based on the formation of poly(vinylpyrrolidone)-I_2 (PVP-I_2) complex in Polymer Inclusion Membrane (PIM) from aqueous solutions. This complex is yellow in colour and shows an absorbance maximum at 361 nm [1,2]. It is a promising bactericide with attractive merits [3]. The PVP-I_2 interaction has been employed in the determination of biocidal iodine in water samples stored in space shuttles by colorimetric solid phase extraction [4]. PVP-I_2 has also been used in the rapid and specific determination of I_2 and I^- by combined solid phase extraction and diffuse reflectance spectroscopy [5]. PVP-I_2 complex formation has also been investigated by Raman spectroscopy [3]. This complex has also been grafted on polypropylene films which have been efficiently used as bactericides [1]. In the present work, a PIM with immobilized PVP has been prepared for the determination of molecular I_2. Spectrophotometry has been used for the identification of PVP-I_2 complex in PIM from aqueous solution and Instrumental Neutron Activation Analysis (INAA) has been used, for the quantification of I_2.

Appropriate amounts of cellulose tri-acetate (CTA) polymer and PVP were dissolved in chloroform. The plasticizer, di-octyl phthalate (DOP) was dissolved separately in chloroform. The solutions of CTA, PVP and DOP were mixed and ultrasonicated for 2 min to form the casting solution for preparing the PIM and the details of the membrane preparation are given elsewhere [6]. A stock solution of iodine (100 mg/mL) was prepared, by dissolving accurate amount of crystalline iodine in 1 mL methanol and further diluting with distilled water (up to 100 mL). In order to study the uptake of I_2, the PIM samples (1 ´3 cm^2) were equilibrated for 1hr with solutions containing varying amounts of I_2. The volume of the equilibrating solution was kept same in all the cases. The spectra of the solutions before equilibration were recorded using a spectrophotometer. After equilibration, the membrane samples were taken out of the equilibrating solution and were washed with distilled water. The spectra of these PIM samples were recorded. INAA using reactor neutrons was used, for the determination of I_2 due to its high

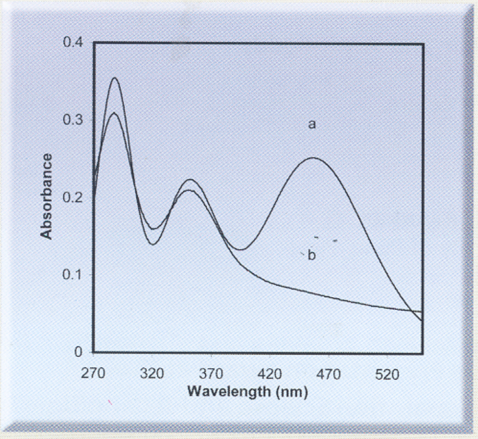

Fig. 1 : Spectrum of I_2 in solution before and after equilibration with PVP-PIM
a) Spectrum of I_2 in solution before equilibration;
b) Spectrum of I_2 in solution after equilibration with PVP-PIM

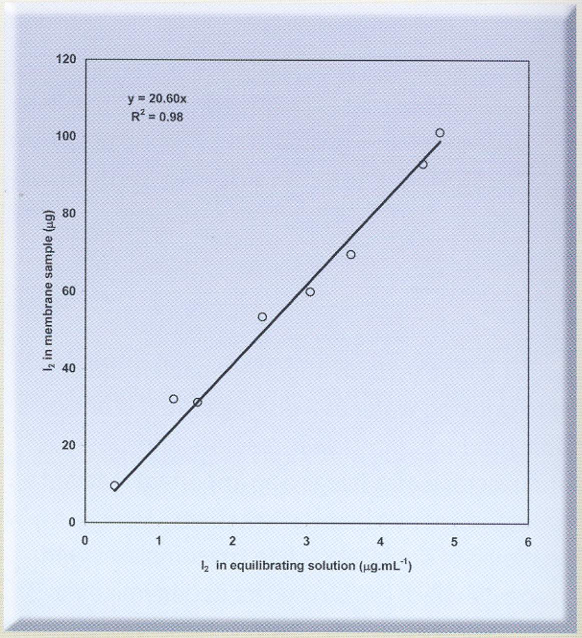

Fig. 3 : Amount of I_2 in PIM after NAA as a function of amount of I_2 in solution

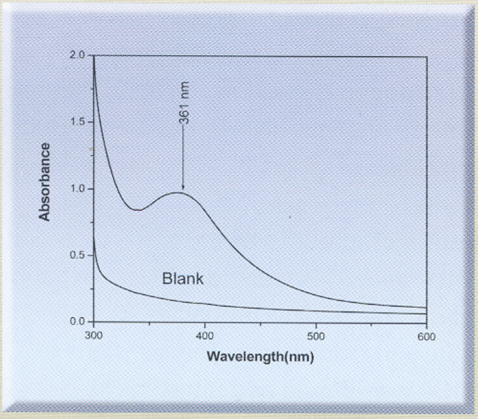

Fig. 2: Spectrum of Blank membrane and PVP-I_2 in the membrane

sensitivity. I_2 loaded membranes were neutron irradiated along with elemental standard. Neutron irradiation was carried out in Apsara reactor, BARC. The neutron flux at this position is ~ 5×10^{11} cm^{-2}. s^{-1}. The radioactivity of ^{128}I ($t_{1/2}$ = 25 min; E_γ = 443 keV) produced in the membrane samples was assayed by γ-ray spectrometry using a 40% relative efficiency HPGe detector.

In the absorption spectrum of iodine solution, three distinct peaks at 290, 355 and 460 nm were obtained. The peak at 460 nm is the characteristic peak of I_2 and the other two peaks (290 nm and 355 nm) belong to I_3^- [5]. After the equilibration with PVP-PIM the peak due to I_2 at 460 nm disappeared whereas the other two peaks were retained in the spectrum (Fig. 1). PVP has an absorption maximum at 341 nm and PVP-I_2 has an absorption maximum at 361 nm (Fig. 2). A calibration plot was obtained by plotting the amount of I_2 in equilibrating solution with that in the PIM obtained after NAA determination (Fig. 3). The percentage extraction obtained was 84% after the membrane samples were equilibrated with solutions containing 10 to 120 mg of I_2. The 84 % extraction efficiency of PIM towards I_2 can be attributed to the fact that some I_2 in the equilibrating solution was present as I_3^- which may not be sorbed in the membrane. This method can be used for selective preconcentration of I_2 and its determination in real samples like water and food stuffs.

Acknowledgement

One of the authors (Preeti Bhagat, JRF) gratefully acknowledges BRNS, DAE for financial assistance under the BARC-Pune University MoU. Authors thank Dr V.K.Manchanda, Head, Radiochemistry Division for his keen interest in this work.

References

1. C.M. Xing, J. P. Deng, *J .Poly. Sci.,* 97 (2005) 2026
2. N.A. Mazumdar, Varadrajan, J *Macro.Mol. Sci.Pure. Appl. Chem.,*33 (1996) 353
3. D. L.A. de Faria, H.A.C. Gil, A.A.A de Queiroz, *J. Mol.Struc.,*479 (1999) 93.
4. D.B.Gazda, R. J. Lipert, J. S. Fritz, M. Porter, *Anal.Chim.Acta.,*510 (2004) 241.
5. P. Arena, M. D. Porter, J.S. Fritz, *Anal. Chem.,* 74 (2002) 185.
6. P.R Bhagat, A.K. Pandey, R. Acharya, A.G.C. Nair, N.S. Rajurkar, A.V.R.Reddy, *Talanta,* 71 (2007) 1226.

About the Authors

Dr A.K. Pandey joined the Radiochemistry Division, BARC in 1983 after completing his M.Sc. in Inorganic Chemistry from Bundelkhand University. His research interests include synthesis and characterization of polymer membranes for separation and preconcentration processes and membrane-based optical sensors. He has to his credit 36 publications in peer- reviewed international journals.

Dr R. Acharya obtained M.Sc. from Utkal University and joined the 37th batch of BARC training school in Chemistry Discipline. He joined the Radiochemistry Division in 1994 and since then he is engaged in R&D work on conventional and k_0 based Neutron Activation Analysis (NAA), Prompt Gamma-ray NAA (PGNAA) and trace element speciation. He has more than 100 publications (journals and symposia) to his credit.

Dr A.G.C. Nair joined the Radiochemistry Division of BARC in 1969. His fields of interest include development of radiochemical separation procedures of fission products and trace element analysis by Neutron Activation Analysis (NAA) and Prompt Gamma ray NAA (PGNAA). He has about 130 publications (journals and symposia) to his credit.

Dr A.V.R. Reddy after undergoing one year orientation course in chemistry during 1976-77 joined the Nuclear Chemistry Section, Radiochemistry Division in 1977. Since then he has been working in the Nuclear Chemistry section and at present he is the Head of Nuclear Chemistry Section. His areas of research are nuclear fission, nuclear reactions, neutron activation analysis, radiochemical separations, heavy element chemistry and non destructive assay methods. He has about 250 publications in journals and symposia and has authored 3 books and edited 5 compilations.

Ms. Preeti Bhagat obtained her M.Sc. in Analytical Chemistry from University of Pune in 2002. She joined as a JRF under the Pune University-BARC MoU in Nov .2004. Since then she has been working for her PhD on "Estimation of iodine and iodine species in food and food products using neutron activation analysis methods" in the collaborative project between Radiochemistry Division and Department of Chemistry, University of Pune.

Dr (Mrs.) N.S. Rajurkar is Professor of Physical Chemistry at the University of Pune. Her main research field is Nuclear and Radiochemistry. She has guided 21 research students for Ph.D. and M.Phil. degrees and has more than 125 research publications. She has written a book "Nuclear Chemistry through Problems" and has contributed to the UGC sponsored "Countrywide Classroom Programme on Radioactivity". She is a member of many scientific associations.

STUDIES ON ELECTRICAL PROPERTIES OF $Cr_{2-x}Ti_xO_{3+\delta}$ BY IMPEDANCE SPECTROSCOPY

Rajesh V. Pai and S. K. Mukerjee
Fuel Chemistry Division
Bhabha Atomic Research Centre

V. Venugopal
RC & I Group
Bhabha Atomic Research Centre

and

R. Mishra and D. Das
Chemistry Division
Bhabha Atomic Research Centre

This paper won the third prize for Oral Presentation at Thermans 2006, held in Jaipur, during February 6-8, 2006

Abstract

The compounds with compositions $Cr_{2-x}Ti_xO_{3+\delta}$ (where x = 0, 0.1, 0.2 and 0.3) were prepared by gel-entrapment method and characterized by XRD and thermal techniques. The electrical properties, such a, dielectric constant and ionic conductivity of these compounds were studied in the frequency range 10 MHz to 1 Hz, in the temperature interval 400 to 800 K, using impedance spectroscopy. The study showed that the dielectric constant of the sample increases up to 10 mole% of TiO_2 doping and decreases on further increase in dopant concentration. In the dielectric constant versus temperature plot a phase transition is noted in the temperature range 650-700 K in all the samples. From Arrhenius plot, the activation energy for different compositions was derived, below and above the transition temperature. The results of the electrical measurement are explained on the basis of defect formation and ordering.

Introduction

In recent years, there has been increased demand to develop newer sensor materials for applications in electronic and other industries. Ternary transition metal oxides have been investigated extensively for this purpose for reactive gases, since they exhibit both high selectivity and sensitivity for several gases [1]. One of the ways to increase the selectivity of these sensors, towards a desired gas, is by doping a suitable ion in the host matrix. At elevated temperatures, it is seen that the resistivity of doped oxides changes even for trace levels of reactant gases. Therefore, the studies pertaining to the electrical properties of the semi-conducting oxide sensor materials are important to explain their sensing behavior. Mosely and Williams [2] used chromium titanium oxide of composition $Cr_{1.8}Ti_{0.2}O_{3+\delta}$ for monitoring ammonia in percentage level in air, at 773 K. Jayaraman et al [3] have studied the sensor properties of TiO_2-doped Cr_2O_3 ($Cr_{2-x}Ti_xO_{3+\delta}$). In this paper, we describe the synthesis of $Cr_{2-x}Ti_xO_{3+\delta}$ by a novel solution-based preparation method, their characterization and the electrical conductivity and dielectric properties of the compounds at different temperatures.

Experimental

The compounds, $Cr_{2-x}Ti_xO_{3+\delta}$ were prepared by gel-entrapment method [4]. For the preparation of the compounds, the metal nitrate solutions of appropriate concentrations were mixed together and gradually gelled at room temperature by slow addition of 3 molar hexamine solution with continuous stirring. The gel obtained in the process was then dried in an oven at 150°C and heated to 200°C to obtain the precursor material. The precursors were further heat-treated, at 750°C in air for 4 h, to get phase-pure compounds. The compounds were characterized by TG-DTA (Setaram, Model 92-16.18) and DSC (Setaram, Model 131) techniques. The samples were pelletized into 10 mm diameter disks of thickness 1.5 mm at a pressure of 250 MPa and sintered in air at 1000°C for 12 h. The pellets were then polished and coated with thin layer of silver on flat ends to have better contact with the electrode for electrical property measurement.

The electrical properties of the samples were measured using a Solartron AC Frequency Analyzer (Model 1260) in the frequency range 10 MHz to 1 Hz. The impedance spectra were recorded in the temperature interval of 400 to 800 K with the step of 25 K for all the samples. The temperature was controlled by a microprocessor and measured by a K-type thermocouple placed very close to the sample. At each temperature, the samples were equilibrated for 20 min. before recording the spectra.

Results

The room temperature XRD analysis of the samples indicates, that the materials are single phase with hexagonal lattice structure. The cell parameters of the compounds obtained from least square fitting of the XRD data were found to be in good agreement with the reported values. The DSC studies of these samples showed a diffused phase transition in the temperature range 650-700 K. However, the high-temperature XRD data for the sample did not show any crystallographic modification of the samples above the transition temperature. The observed phase transition in the DSC studies could, therefore be attributed to the electronic transition in the compounds.

The dielectric constants of the compounds, determined from the capacitance values obtained from the Nquist's plot, indicate that, there is a sharp increase in the values of dielectric constants around 650-700 K for all the samples. Fig. 1 gives the variation of dielectric constant of $Cr_{1.7}Ti_{0.3}O_{3+\delta}$ as a function of temperature for different

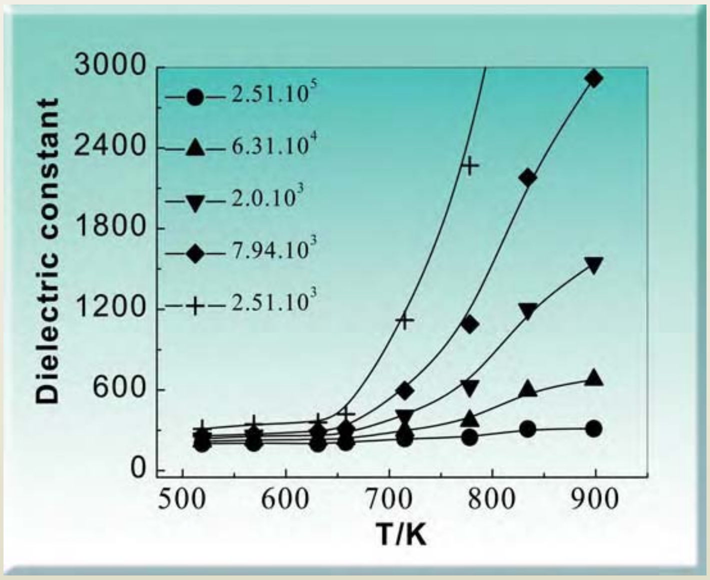

Fig.1: Variation of dielectric constant of $Cr_{1.7}Ti_{0.3}O_{3+\delta}$ as a function of temperature for different frequencies

Table 1: Variation of dielectric constants with temperatures for $Cr_{2-x}Ti_xO_{3+\delta}$ (x = 0.1, 0.2 and 0.3) calculated at (nmax)

Sample	Dielectric Constants								
	575 K	600 K	625 K	650 K	675 K	700 K	725 K	750 K	800 K
$Cr_{1.9}Ti_{0.1}O_{3+\delta}$	338	326	292	255	217	242	248	253	266
$Cr_{1.8}Ti_{0.2}O_{3+\delta}$	632	599	342	277	270	265	257	252	248
$Cr_{1.7}Ti_{0.3}O_{3+\delta}$	263	254	237	228	214	217	221	224	236

frequencies. From Fig. 1 it can be noted that there is a sharp increase in the values of dielectric constant in the temperature range 650 to 750 K for all frequencies. The corresponding plots for the other compositions are similar to Fig. 1. Table 1 gives the variation of dielectric constant of all the samples with temperature calculated from the maxima (nmax) of the Nquist's plot.

Fig. 2 gives the representative Nquist's plot for the composition $Cr_{1.9}Ti_{0.3}O_{3+\delta}$ at 660 K. From the real part of this plot, the resistance of sample was determined as a function of temperature. Using the measured cell constants, the conductivity (s) of the samples was calculated for all compositions, as a function of temperature. From the plot of ln (σT) vs 1/T, the activation energies for the movement of charge carriers were calculated. The extrapolation of linear least-square fitting of the experimental data at temperatures above and below the diffused transition gave the intersection point, which was attributed to the average transition temperature for the particular composition. Table 2 gives the transition temperature and the activation energies of the compositions. Fig. 3 gives the Arrhenius plot ln (σT) vs 1/T for all compositions.

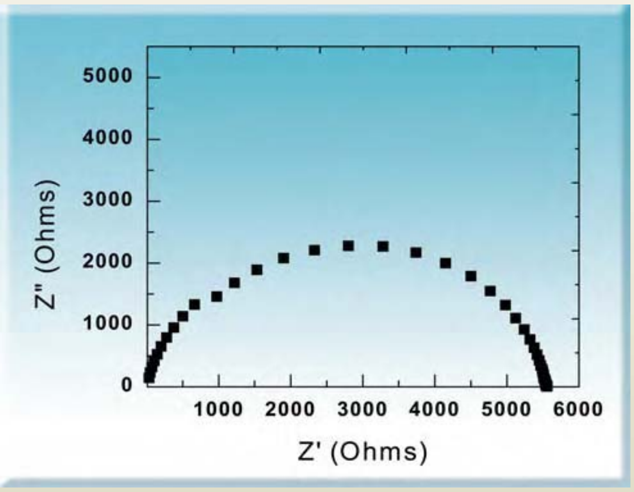

Fig. 2 : Nquist's plot for the composition $Cr_{1.9}Ti_{0.3}O_{3+\delta}$ at 660 K

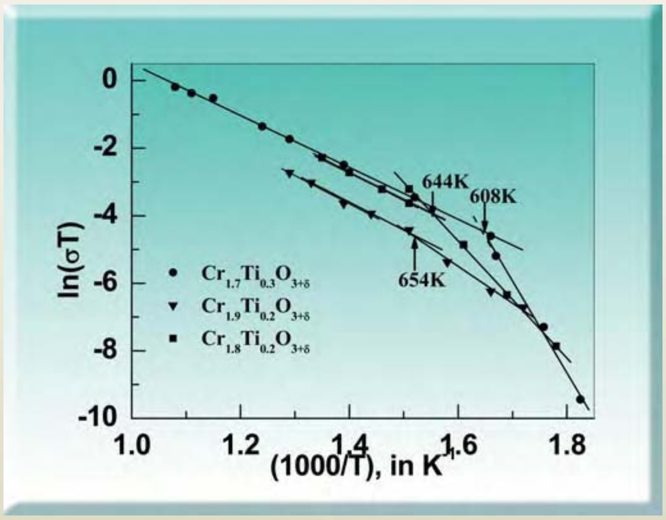

Fig. 3 : Arrhenius plot ln (σT) vs 1/T for all compositions

Table 2: Transition temperatures and activation energy of $Cr_{2-x}Ti_xO_{3+\delta}$ (x = 0.1, 0.2 and 0.3) from impedance study

Sample	Transition temperature (K)	Activation energy (Ea) (eV)	
		Before transition	After transition
$Cr_{1.9}Ti_{0.1}O_{3+\delta}$	644	1.49	0.72
$Cr_{1.8}Ti_{0.2}O_{3+\delta}$	654	0.941	0.72
$Cr_{1.7}Ti_{0.3}O_{3+\delta}$	608	2.34	0.662
Cr_2O_3	No transition	0.72	

Discussion

The decrease in dielectric constant of the samples, with increase in frequency at a constant temperature (Fig. 1), is indicative of decrease in the values of capacitance of the material with frequency. From the values of dielectric constant of the samples shown in Table 1, it is found that for compositions $Cr_{1.9}Ti_{0.1}O_{3+\delta}$ and $Cr_{1.7}Ti_{0.3}O_{3+\delta}$ the dielectric constant initially decreases with temperature below the "phase transitions" and increases after the transition. The decrease in the dielectric constant below the phase transition is generally attributed to the increase in lattice vibration with temperature. The sharp increase in the dielectric constant after 650 K is explained on the basis of electronic transition in the system, which has also been observed by DSC measurements. It can also be seen from Table 1, that the dielectric constant of the $Cr_{1.8}Ti_{0.2}O_{3+\delta}$ sample has higher values compared to $Cr_{1.7}Ti_{0.3}O_{3+\delta}$ and $Cr_{1.9}Ti_{0.1}O_{3+\delta}$. The higher dielectric value for the $Cr_{1.8}Ti_{0.2}O_{3+\delta}$ composition, may be due to the increase in the concentration of cationic vacancies. The observed decrease of dielectric constant on further doping of TiO_2, can be attributed to ordering of the cationic defect.

It is to be noted that the derived activation barrier of 0.72 eV in pure chromia, is comparable to those observed in the doped samples at higher temperatures, following the electronic transition. If one attributes the observed barriers to the band gaps of valence and conduction electrons, the similarity in the activation energies, is indicative of the doped chromia attaining electronic transport similar to pure chromia. The transition in the temperature range 650-700 K obtained from extrapolation of ln (σT) vs 1/T curve is attributed to the electronic transition from the valence band to the conduction band of the system. In contrast to the electronic transport at high temperatures, the transport below the transition is mainly governed by the cationic movements. From the analysis of powder XRD data it is clear, that TiO_2 forms a homogeneous solid solution with Cr_2O_3 up to 15 mole % TiO_2 and creates the cationic vacancies in the lattice.

Conclusion

$Cr_{2-x}Ti_xO_{3+\delta}$ (x = 0.1, 0.2 and 0.3) was prepared by a novel solution-based technique. The dielectric constant and the conductivity of the samples were measured. From the results of dielectric constant and conductivity measurements of the TiO_2 doped chromia samples ($Cr_{2-x}Ti_xO_{3+\delta}$ (x = 0.1, 0.2 and 0.3), a diffused transition leading to increased electronic conductivity in the samples is indicated. The activation energies for electronic transport above the transition temperature have been determined.

References

1. D. E. Williams, *Anal. Proc.*, 28 (1991) 366
2. P.T. Moseley, D.E. Williams, *Sensors and Actuators,* B 21 (1990) 113-115.
3. V. Jayaraman, K.I. Gnanasekar, E. Prabhu, T. Gnanasekaran, G. Periaswami, *Sensors and Actuators,* B 55 (1999) 175.
4. R.V. Kamat, K.T. Pillai, V.N.Vaidya and D.D. Sood, *Materials Chemistry and Physics,* 46 (1996) 67.

About the Authors

Mr. Rajesh V. Pai joined Fuel Chemistry Division, BARC after graduating from the 40th batch of Training School in the year 1997 after completing his M.Sc. (Applied Chemistry) from Cochin University of Science & Technology. He is mainly associated with the development of sol-gel process thoria, urania and plutonia-based ceramics. In this, he has developed process sheets for the fabrication of ThO_2, $(Th,U)O_2$, UO_2, $(U,Pu)O_2$ dense pellets based on internal gelation process. His research interest includes development of sensor materials, high technology materials and nanoceramics.

Dr S.K. Mukerjee joined Department of Atomic Energy after completing his M.Sc. (Chemistry) from Nagpur University. Currently he is Head, Process Chemistry Section, Fuel Chemistry Division, BARC. He has been mainly associated with the development of ceramic materials for application of nuclear technology. He has extensively studied sol-gel processing of nuclear materials for advanced fuel fabrication. He has obtained doctorate from Mumbai University in the year 1993.

Dr V. Venugopal is the Director, Radiochemistry & Isotope Group, BARC. He is a specialist in the field of high temperature thermodynamics and chemical quality control of Pu based fuels. He has worked at Nuclear Research Centre, Julich on the development of nickel-based binary super alloys required for Rocket Jet Nozzle and turbine blades and also on the development of high intensity metal halide vapour lamps at high temperature. He has been honoured with NETZSCH-ITAS and ISCAS for his outstanding contributions in the field of thermal science and solid state chemistry respectively. He is the regional editor for the *Journal of Thermal Analysis and Calorimetry.*

Dr R. Mishra, Ph.D (Mumbai University) is working in Chemistry Division, BARC. He specialized in high temperature chemistry and chemical thermodynamics. He derived thermodynamic data on several nuclear materials and intermetallic compounds, phase diagram studies of binary and ternary oxide systems. He was been awarded the TA instrument –ITS Young Scientist Award-2004 and Alexander von Humboldt Fellowship for post-doctoral studies in the University of Munich, Germany.

Dr D. Das, M.Sc. in Chemistry (University of Calcutta), joined BARC through Training School in 1974. He is currently the Head, Chemistry Division. His contributions include thermodynamic characterization of compounds, alloys and intermetallics, the physico chemical compatibility studies of corrosive liquids and vapours in high temperature contaminants, the development of techniques of pyrometric calibrations up to 3000 K, the development of high power electron beam source for large scale evaporation of metals etc.

DISTRIBUTION OF TECHNETIUM IN PUREX PROCESS STREAMS

C.S. Dileep, Poonam Jagasia, P.S. Dhami, P.V.Achuthan, A.D. Moorthy,
U. Jambunathan, S.K. Munshi and P.K.Dey
Fuel Reprocessing Division
Bhabha Atomic Research Centre

and

B.S. Tomar
Radiochemistry Division
Bhabha Atomic Research Centre

This paper was given the Best Paper Award at the DAE-BRNS Symposium on "Emerging Trends in Separation Science and Technology (SESTEC-2006) held at BARC, Mumbai, during September 29-October 1, 2006

Technetium-99 is one of the long-lived fission products ($T_{1/2}$ = 2.11 x 10^5 y) having high fission yield (6.13%) and therefore is an important radionuclide from the point of view of long term nuclear waste management. Technetium exists as TcO_4^- under oxidizing conditions and gets reduced to TcO_2 under reducing conditions. Tc is therefore found in almost all the steps of reprocessing streams. A part of TcO_4^- is extracted together with uranium, during the PUREX process as per the following reaction [1, 2]:

$$UO_2(NO_3)_2(TBP)_2 + TcO_4^- \ \hat{U} \leftrightarrow UO_2(NO_3)(TcO_4)(TBP)_2 + NO_3^- \qquad (1)$$

Extraction depends upon the concentration of nitrate. Likewise during partitioning, TcO_4^- may be reduced to TcO_2 and may go with Pu^{3+}.

Measurement of ^{99}Tc in various streams of the process is a difficult task as it is a pure beta emitter. With this in view, a γ-emitting relatively long-lived radioisotope of technetium (^{95}Tc) has been used in the present work, as a tracer for technetium and its distribution in various streams of the PUREX process, has been studied.

^{95}Tc ($T_{1/2}$ = 60d) is a gamma emitting radioisotope of technetium. It was produced by ^{96}Mo (p, 2n) reaction using 24 MeV proton beam from pelletron accelerator at TIFR, Mumbai and radiochemically separated from irradiated MoO_3 target by solvent extraction, using methyl ethyl ketone from alkaline medium.

In batch extraction studies, known volume (generally 2 mL) of an aqueous phase spiked with trace quantity of ^{95}Tc was contacted with desired volume of pre-equilibrated 30%TBP in n-dodecane, for 15 minutes, which was enough to attain equilibrium. The phases were separated and assayed for Tc activity. Extraction of Tc was done under varied experimental conditions such as increasing concentration of nitric acid in the feed, increasing concentration of uranium in 2-3M HNO_3 etc. To follow the path of Tc, experiment was carried out under conditions similar to those used in PUREX process. Phase ratio of 3:1 was maintained during extraction, 5:1 during scrubbing and ~8:1 in the partitioning step where uranous solution [U^{4+} ~40 g/L at an acidity of ~0.6M HNO_3 containing 0.2M N_2H_4 as stabilizer] was used as partitioning agent for Pu. Behaviour of Tc was also studied in an experiment where the composite loaded organic phase was given scrub with varying concentrations i.e. 2.5, 5.0 and 10.0M of HNO_3 as Tc is known to interfere in the partitioning step. Advanced PUREX flow sheets recommend a high acid scrub to eliminate Tc from the loaded organic phase. In the present study, emphasis was given on the effectiveness of scrubbing out of Tc from the loaded organic by concentrated nitric acid. Some reprocessing plants follow an ion-exchange purification step for tail end purification of Pu. Therefore sorption behaviour of Tc was also studied on an anion exchanger, at varying concentrations of nitric acid.

Table 1: Distribution of Tc at varying concentrations of HNO_3 using PUREX solvent

$[HNO_3]$ (M)	D_{Tc}
2.5	0.280
5.0	<0.01
10.0	<0.01

The analysis of ^{95}Tc was done by γ-spectrometry (γ-energy = 204 keV), using HPGe detector coupled to a 4K multi-channel analyzer.

Table 1 shows the distribution ratio of ^{95}Tc at three acidities. It can be seen, that in the absence of metal ions, the distribution ratio is higher at lower acidities and the extraction is practically negligible (D_{Tc} <0.01) above 5M HNO_3. Table 2 shows the effect of uranium concentration at 2.5M HNO_3. The distribution ratio increases with increase in the concentration of uranium and reaches a maximum at about 200 g/L.

Table 2 : Distribution of Tc at varying concentration of Uranium using PUREX solvent from 2.5M HNO_3

[U] (g/L)	D_{Tc}
0	0.280
19.0	0.283
95.0	0.412
190.0	0.504
350.0	0.469

The high active extraction cycle of PUREX process, normally employs a 3:1 organic to aqueous phase ratio, to limit the uranium loading for avoiding Pu reflux and loss to the raffinate. A simulated PUREX feed solution with ~350 g/L uranium at 2.5M HNO_3 containing ^{95}Tc was prepared and contacted with pre-equilibrated 30% TBP in n-dodecane at a 3:1 organic to aqueous phase ratio. The raffinate was successively contacted twice with TBP and the organic phases were collected together. The composite organic phase was scrubbed with different concentrations of nitric acid at a 5:1 organic to aqueous phase ratio. In order to study the effect of partitioning on the distribution of Tc, the loaded organic phase containing ^{95}Tc tracer was contacted with an aqueous solution, containing 40 g/L U^{4+} with 0.2M hydrazine in 0.6M HNO_3, at an organic to aqueous phase ratio of

Table 3 : Distribution of Tc in PUREX Streams

Nos. of Batch Contacts	Percentage of activity				
	Extraction (O/A=3)	Scrubbing (O/A=5)			Partitioning (O/A=8)
		2.5M	5.0M	10M	
1	66.63	8.0	28.63	27.52	71.00
2	18.88	-	16.81	15.04	20.00
3	13.25	-	8.67	10.09	-

8:1. The results of the experiments are given in Table 3. Quantitative extraction of Tc was obtained, in the extraction cycle of PUREX process, where more than three stages are always provided. Scrubbing of loaded organic phase with 2.5M HNO_3 was found to remove lesser amounts of Tc from the loaded organic phase as compared to 5M HNO_3. Changing the scrub to 10M HNO_3 did not improve the Tc removal. When the loaded organic phase containing Tc was contacted with the partitioning agent, almost all the Tc followed the aqueous stream along the plutonium product as TcO_2. Similar results were obtained when a simulated feed containing U, Pu and ^{95}Tc was used in the experiments.

The behaviour of Tc in the partitioning cycle is complex and some of its reactions are known to be as follows [3].

When an aqueous solution of U^{4+} is used in partitioning, TcO_4^- is reduced to TcO_2.

$$2\ TcO_4^- + 3U^{4+} + 2H_2O \longrightarrow 2\ TcO_2 + 3UO_2^{2+} + 4H^+ \quad \text{(rapid)} \qquad (2)$$

$$TcO_2 + NO_3^- \longrightarrow TcO_4^- + NO \quad \text{(rapid)} \qquad (3)$$

Hence TcO_4^- serves as a catalyst for oxidation of U^{4+} with nitric acid.

Relative distribution ratios of Pu and Tc using anion exchange resin TcO_4^- ions have also been proved to catalyze the decomposition of hydrazine used for stabilization of Pu^{3+} and U^{4+}. Technetium is successively reduced to its pentavalent and tetravalent states which are re-oxidized with nitric acid to TcO_4^-.

$$3\ N_2H_5^+ + 4\ TcO_4^- + H^+ \longrightarrow 4\ TcO_2 + 3\ N_2 + 8\ H_2O \qquad (4)$$

$$TcO_2 + NO_3^- \longrightarrow TcO_4^- + NO \qquad (5)$$

In this process, the TcO_4^- concentration remains constant while hydrazine is completely consumed. These complicated reaction cycles necessitate the addition of U^{4+} very much in excess of the stoichiometry. The kinetics of the re-oxidation of Tc will be the path deciding factor. A large excess of U^{4+} seems to keep Tc in the Pu stream as seen in the present study.

Tail-end purification of Pu in some of the PUREX plants is carried out by anion exchanger in 7.2 M HNO_3. The feed conditioning step in this case is likely to keep all the Tc in the TcO_4^- state. Hence its path in the ion exchange cycle needs investigation. The distribution ratio of Tc was found to decrease with increase in acidity. The relative distribution ratio of Pu and Tc are plotted as a function of nitric acid concentration in Fig. 1. Most of the Tc will be eliminated in the loading effluent. Hence Pu decontamination factor will not be affected by the presence of Tc in the Pu streams.

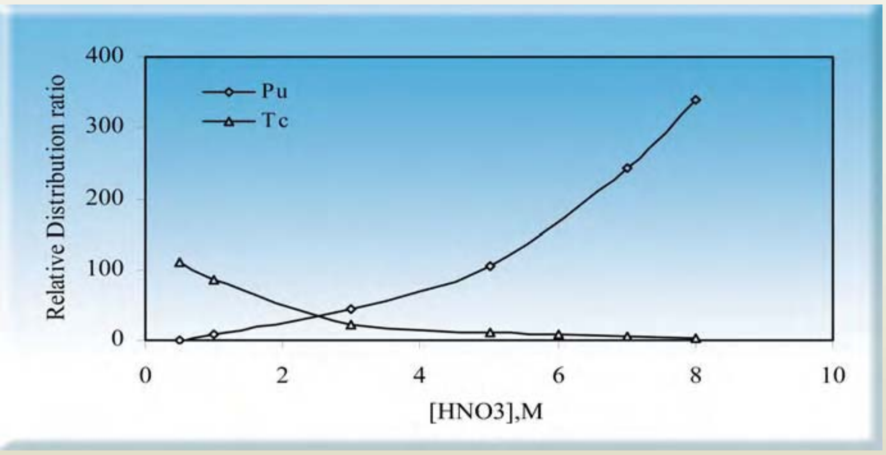

Fig. 1: Relative distribution ratios of Pu and Tc using anion exchange resin

References

1. W.W. Schulz; L. Burger; J.D Navratil and K.P Bender (Eds.), Applications of Tributyl phosphate in nuclear fuel processing, Science and Technology of Tributyl Phosphate, Vol. III, CRC Press Inc, Boca Raton, Florida USA (1990).
2. K.H. Lieser., *Radiochem. Acta.* 63, 5(1993).
3. N. N. Popova, I. G. Tananaev, S. I. Rovnyi and B. F. Myasoedov, Technetium behaviour during reprocessing of spent nuclear fuel and in environmental objects. Russian, *Chemical Reviews.* 72 (2) 101-121 (2003).

About the Authors

Mr. C.S. Dileep joined BARC in 1997 after completing B.Sc. in Chemistry from the University of Calicut in the year 1993. His areas of interest include process control analysis relevant to PUREX and THOREX processes. He is also involved in studies on the analytical estimation of ^{90}Sr, ^{99}Tc in various PUREX streams. He has eight publications to his credit in national symposia and international journals.

Ms Poonam Jagasia joined BARC in 1997 after completing B.Sc. in Chemistry from the University of Mumbai in 1993. Her areas of interest are process control analysis and analytical development studies of relevance to fuel reprocessing. She is involved in the characterization of HLLW, for various metallic constituents using ICP-AES. She has eight publications to her credit in national symposia and international journals.

Dr P.S. Dhami joined BARC in 1982 after completing B.Sc. from Kumaon University, Nainital in 1981. He obtained his M.Sc. degree in Chemistry in 1988 and Ph.D. in Chemistry from the University of Mumbai in 1990. His areas of interest are process and analytical development studies of relevance to fuel reprocessing, Development of radiochemical separation processes based on solvent extraction, ion exchange and extraction chromatography. He has more than 90 publications to his credit in various international journals and symposia.

Dr P.V. Achuthan joined BARC in 1978. He obtained Ph.D. in Chemistry from the University of Mumbai in the year 1990. His area of interest is reprocessing chemistry relevant to PUREX and THOREX processes. He is involved in separations based on solvent extraction, ion-exchange and extraction chromatographic technique. He has more than 90 publications to his credit in various international journals and symposia.

Mr. A.Dakshinamoorthy joined BARC in 1969. He is a specialist in the field of thermal ionization mass spectrometry and was a member of the Nuclear Material Management team during the IAEA safeguarded fuel reprocessing campaigns at PREFRE, Tarapur. His other areas of interest are actinide chemistry, fuel reprocessing process and analytical chemistry, solvent extraction, ion-exchange and extraction chromatography. His current activities include studies on the separation of useful fission products such as Pd, ^{90}Sr etc from PUREX high level waste. He has more than 95 publications in his credit in various international journals and symposia. Presently he is Supdt. PC&R Laboratory, Plutonium Plant, Trombay.

Dr U. Jambunathan joined BARC in 1969. He participated in the production of plutonium for PNE in 1974. Over the years he has developed expertise in reprocessing chemistry. He has developed techniques for the recovery of americium from different streams of plutonium reconversion operations. He has more than 100 publications in national and international journals/symposia.

Mr. S.K. Munshi, B.E. (Chemical Engineering), joined BARC in 1971 after graduation from Kashmir University. His field of expertise is reprocessing of spent fuel of research reactors and Power reactors (PHWR). He is also involved in the safety assessment of fuel cycle facilities and Heavy Water Plants. He has more than 50 papers to his credit in various international journals and symposia. Currently he is Chief Superintendent Reprocessing Facilities, Trombay

Mr. P.K. Dey is a graduate in chemical Engineering from Jadavpur University, Kolkata. He joined BARC in the year 1971 and is associated with the activities of spent fuel reprocessing of the Department. He has vast experience in construction, commissioning and operation of reprocessing plants. He has carried out extensive R&D studies to improve the reprocessing technology for better recovery and minimization of radioactive waste generation. He has more than 120 papers to his credit in various international journals and symposia. Presently he is Head of Fuel Reprocessing Division of BARC and is responsible for the operation of all the reprocessing plants in the country.

Dr B.S.Tomar joined the 25th Batch of the BARC Training School in 1981 and is the recipient of Homi Bhabha Prize and subsequently joined Radio-chemistry Division in 1982. He obtained his Ph.D. degree in Chemistry from the University of Mumbai in 1990. His research interests include nuclear chemistry and actinide speciation. He has initiated studies on speciation of actinides in aquatic environment, particularly with regard to the role of colloids and humic substances in radionuclide migration. He has more than 50 publications in international journals.

THIRD PHASE FORMATION IN THE EXTRACTION OF U (VI), Th (IV) AND Pu (IV) BY N, N-DIALKYL ALIPHATIC AMIDES

R.K. Jha, K.K.Gupta, P.G. Kulkarni, P.B. Gurba, P. Janardan, R.D. Changarani and P.K.Dey
PREFRE Plant, Nuclear Recycle Group
Bhabha Atomic Research Centre, Tarapur

and

P.N. Pathak and V.K.Manchanda
Radiochemistry Division
Bhabha Atomic Research Centre

This paper was awarded the Best Award in the poster category at the DAE-BRNS Symposium on "Emerging Trends in Separation Science and Technology (SESTEC-2006) held at BARC, Mumbai, during September 29-October 1, 2006

In recent years, dialkyl aliphatic amides are being explored as potential alternate extractants to tri-n-butyl phosphate (TBP), for the reprocessing of uranium, plutonium and thorium-based fuels. This is due to the fact, that these ligands possess certain distinct advantages like poor extraction of fission products, benign nature of their degradation products, complete incinerability of the spent solvent and easy synthesis. In this regard, several dialkyl aliphatic amides have been synthesized and investigated in our laboratory, under the conditions prevailing in the PUREX process [1,2]. Among the amides studied, N, N- dihexyl derivatives of n-hexanamide (DHHA), n-octanamide (DHOA) and n-decanamide (DHDA) are identified as suitable candidates for actinide extraction [1,2].

Third phase formation in nuclear solvent extraction system is observed at high metal and / or mineral acid loading of the organic phase. Under certain conditions, the organic phase splits into two layers, the light layer containing most of the diluent, little extractant and metal; and a heavy or third phase containing high concentration of extractant, metal and little diluent. The phenomenon of third phase formation is mainly caused by the limited solubility of the metal-ligand complex in the non-polar organic phase [3].

During the reprocessing of spent nuclear fuel by solvent extraction, the occurrence of third phase in the extraction system is undesirable and hence should be avoided. Apart from posing operational problems and limiting the throughput of the plant, the third phase formation during the extraction of fissile elements like plutonium, constitutes criticality hazard. This is particularly relevant to fast reactor fuel reprocessing, where the plutonium concentration is fairly high. Third phase formation in the TBP extraction of Th (IV), U (IV) and Pu (IV) is well known [4]. In our earlier publication, we reported the third phase formation in the extraction of uranyl nitrate by DHHA and DHOA [5]. The present work reports the Limiting Organic Concentrations (LOC), above which third phase formation occurs during extraction of Pu (IV) with 1.1M DHOA in n-dodecane; U (VI) with1.1M DHDA in n-dodecane; and Th (IV) with 1.1M DHOA and 1.1M DHDA in n-dodecane(n-DD) and normal paraffin hydrocarbon (NPH) as a function of nitric acid concentration at 25° C. In the case of Th (IV), LOCs were also measured with 1.1M TBP in n-DD/NPH for comparison.

The LOC determination was carried out as follows : A stock solution of 100 mg/ml of Pu (IV) was prepared in 2M HNO_3 by purifying Pu (IV) nitrate solution by anion exchange separation method. Stock solutions of U (VI) & Th (IV) of 300-350 g/l were prepared by dissolving nuclear grade U_3O_8 and Th $(NO_3)_4$ in 0.5 M nitric acid. Suitable aliquots of the stock solution were evaporated and dissolved in the desired concentration of nitric acid. In the case of plutonium, the oxidation state was adjusted to Pu (IV) by passing N_2O_4 gas through the solution at room temperature and was confirmed analytically by TTA extraction method.

Equal volumes (2ml) of the aqueous phase containing Pu (IV) (100- 300 mg/ml)/ U(VI) (300-350 mg/ml)/ Th(IV) (300-350 mg/ml) at the desired concentration of nitric acid (1-7 M) and pre-equilibrated organic phase (1.1 M DHOA/DHDA/ TBP in n-DD/NPH) were equilibrated by magnetic stirring for 30 minutes in thermostated water bath adjusted to 25°C. The third phase so formed in the system was redissolved by diluting the aqueous phase with nitric acid solution of the required concentration. After equilibration, the two phases were allowed to settle for one hour. The organic phase was assayed for metal concentration to compute the LOC. Plutonium assay was carried out by ICP-AES employing 300.057 nm emission line. Prior to estimation, Pu from the organic phase was quantitatively stripped in to the aqueous phase (0.5 M HNO_3), using 0.5 M solution of tertiary butyl hydroquinone in 1.1 M TBP/NPH as an organic soluble reductant. Uranium was determined by redox titrimetry (Davis & Gray method). Thorium estimation was carried out by complexometric titration at pH 1-2 with 0.01 M EDTA using Xylenol Orange as indicator. Nitric acid concentration of the aqueous phase at equilibrium was determined by potentiometry, using standard NaOH solution after complexing metal ions with saturated solution of potassium oxalate. The LOC data obtained for Pu (IV) & U (VI) are given in Table 1 and that for Th (IV) in Table 2.

Table 1 : LOC of Pu (IV) and U (VI) as a function of nitric acid concentration at 25°C

Pu(IV) Extractant:1.1 M DHOA in n-DD		U(VI) Extractant:1.1 M DHDA in n-DD	
$[HNO_3]$,M (Aq.phase)	LOC, g/l	$[HNO_3]$,M (Aq.phase)	LOC, g/l
1.07	29.49@	0.51	25.41@
1.79	36.60	1.19	28.38@
3.27	49.30	2.33	30.35@
3.96	39.83	2.91	31.65@
4.91	34.63	3.64	31.95@
6.08	27.15	4.80	55.45@
6.93	13.15	5.58	68.54
----	----	7.23	64.08
----	----	7.90	39.09

@ Third phase in the form of crud

Table 2 : LOC of Th (IV) as a function of nitric acid concentration at 25^{0}C (LOC values are in g/l)

$[HNO_3]$, M	LOC,Th(IV)					
	1.1 M DHOA in		1.1 M DHDA in		1.1 M TBP in	
	n-DD	NPH	n-DD	NPH	n-DD	NPH
1	39.55	38.56	64.96	59.35	45.15	44.25
2	37.35	36.48	62.17	58.46	42.22	41.32
3	35.72	34.58	57.54	56.60	38.97	37.95
4	32.48	31.72	49.65	48.36	36.67	35.82
5	29.93	28.32	43.61	42.15	33.40	32.72
6	24.94	23.95	38.86	36.25	25.06	24.34
7	14.15	13.25	19.92	18.21	15.16	12.99

The LOC value of Pu (IV) in DHOA-n-DD system, increases from 29.49 g/l (at 1 M HNO_3) to 49.30 g/l (at 3.3 M HNO_3); thereafter it decreases gradually to 13.15 g/l at 7M HNO_3. This variation in the trend can be due to the change in the proportions of the extractable species like $Pu(NO_3)_4.2DHOA$, $HNO_3.DHOA$ and $[Pu(NO_3)_6]^{2-}[HDHOA]^+_2$ with varying aqueous phase nitric acid concentration [2,5]. At lower nitric acid concentrations (0.5-1 M), the third phase appeared in the form of crud, that can be attributed to the extensive aggregation of the extractable species in the organic phase [6]. The LOC data in U (VI)-DHDA-n-DD system indicates no definite trend from 0.5 to 5 M HNO_3 (25.41 – 55.4 g/l). Third phase appeared in the form of crud which redissolved on diluting the aqueous phase with the respective concentration of nitric acid. However, at higher nitric acid concentration (from 5.5 to 8 M), the crud formation was not observed and the LOC values decreased from 68.5 g/l (at 5.6 M HNO_3) to 39.1 g/l at 8 M HNO_3.

The data from Table 2 indicates that the LOC of Th(IV) with DHOA are lower than that of TBP & DHDA at all the nitric acid concentrations studied(1- 7 M) and for DHDA-n-DD/ NPH is the highest. In all the cases, LOC decreases with increasing nitric acid concentration. This may be due to increasing polarity of the organic phase due to increased extraction of nitric acid resulting in decreased solubility of Th solvated species. The LOC varies from 39.55 g/l to 14.15 g/l for DHOA-n-DD system,38.56 g/l to 13.25 g/l for DHOA-NPH system,64.96 g/l to 19.92 g/l for DHDA-n-DD system,59.35 g/l to 18.21 g/l for DHDA-NPH system, 45.15 g/l to 15.16 g/l for TBP-n-DD system and 44.25 g/l to 12.99 g/l for TBP-NPH system from 1 to 7 M HNO_3. It is significant to note that the LOC values for all the extractants are marginally higher in n-dodecane as compared to NPH, unlike the Pu(IV) and U(VI) , which exhibit higher solubility in relatively polar diluents like NPH[5].

The study is part of the extensive work taken up in our laboratory for evaluating the usefulness of the commonly used amides in various spent fuel reprocessing schemes.

References

1. P.B. Ruikar, PhD Thesis, Bhabha Atomic Research Centre, Bombay University (1992).
2. K.K.Gupta, PhD Thesis, Bhabha Atomic Research Centre, Mumbai University (1997).
3. Y.Marcus, A.S. Kertes, Ion Exchange & solvent extraction of Metal complexes; Wiley Interscience: New York, p.715 (1969).
4. P.R.Vasudeva Rao, Z.Kolarik, *Solvent Extr. Ion Exch.*, 14,955 (1996).
5. K.K.Gupta, V.K. Manchanda, S.Sriram, G.Thomas, P.G.Kulkarni and R.K.Singh, *Solvent Extr. Ion Exch.*, 18, 1,421 (2000).
R.Chiariza, M.P.jensen, M.Borkowski, J.R.Ferraro, P.Thiyagarajan and K.C.Littrel, *Solvent Extr. Ion Exch.*, 21, 1, 1-27, (2003).

About the Authors

Mr. P.K. Jha joined Plutonium Plant Trombay in 2000 after completing his B.Sc. in Chemistry (Hons.) from L.N.Mithila University, Darbhanga. He is currently working as a Chemist in PREFRE, Tarapur. He has registered for M.Sc. from the University of Mumbai. His topic for research is "Evaluation of N, N-dialkyl amide as thorium-based fuel".

Dr K.K.Gupta (B.Sc. Chemistry (Hons.), University of Delhi, Ph.D., University of Mumbai, 1998) joined PREFRE Plant BARC, Tarapur in 1977 and is currently working in Spectroscopy Laboratory of the Plant. His main area of research is development of alternate extractants to TBP in PUREX process and Spectrochemical Analytical methods for the assay of actinides in the various streams of the PUREX process.

Mr P.G.Kulkarni (Chemistry graduate, Karnataka University, Dharwar 1971), joined Fuel Reprocessing Division, BARC in 1972. He is currently working in Quality Control analysis group of Laboratory Section, PREFRE, Tarapur. His area of interest is characterization of nuclear materials with respect to trace elemental impurities employing ICP-AES. He is also working on the development of analytical technique using ICP-AES for process control in re-processing plants and investigations on the dialkyl amides as alternate extractants in PUREX process.

Mr. P. Janardan (B.Tech., Chemical Engineering from Osmania University Hyderabad, 1st Class with distinction) Joined PREFRE plant in 1975. He was associated with the commissioning trials of PREFRE Plant and carried out required modifications based on the commissioning trials experience. Presently he is holding the post of Plant Superintendent of PREFRE plant and is fully responsible for the operation of the Plant. He was also involved in the Spent Fuel Storage Facility Tarapur for commissioning trials and later took charge of the SFSF. He also attended the international training course on Implementation of State System of Accounting for the Control of Nuclear Material at Moscow during Oct. 2004. He has also attended the Technical meeting of IAEA to review and develop a safety guide on classification of radioactive wastes at Vienna during Nov.2006.

Mr R.D.Changrani graduated in Chemical Engineering in 1974 from M.S. University Baroda, joined BARC, Tarapur in 1975 from 18th batch of BARC Training School. He was associated with commissioning of PREFRE plant and completed several campaigns of reprocessing of PHWR fuel from different reactors. He was elevated to the post of Chief Superintendent of NRG facilities since 2003 and is responsible for the continuous operation of the reprocessing and waste management plants. He has been involved in commissioning of AVS, resin fixation facility and Spent Fuel Storage Facility. He has participated in many International Conferences. He was an active member of a committee formed by Crisis Management Group, DAE to provide guidelines for the transport of spent fuel by road.

Mr P.K. Dey is a graduate in chemical Engineering from Jadavpur University, Kolkata. He joined BARC in the year 1971 and is associated with the activities of spent fuel reprocessing of the Department. He has vast experience in construction, commissioning and operation of reprocessing plants. He has carried out extensive R&D studies to improve the reprocessing technology for better recovery and minimization of radioactive waste generation. He has more than 120 papers to his credit in various international journals and symposia. Presently he is Head of Fuel Reprocessing Division of BARC and is responsible for the operation of all the reprocessing plants in the country.

Dr P.N. Pathak joined Radiochemistry Division in 1995 after completing the 38th batch of Chemistry training course. He has contributed towards the basic studies dealing with reprocessing of thorium-based fuels using branched dialkyl amides and the use of macrocyclic ligands for 90Sr / 90Y separation. He has worked as a post-doctoral research fellow in Prof. G.R. Choppin's laboratory at the Florida State University, Tallahassee, Florida, USA. He has studied the interaction of actinides, fission products and structural elements with different forms of silica. He is the recipient of Tarun Dutta Memorial Award instituted by Indian Association of Nuclear Chemists and Allied Scientists (IANCAS). He has 53 publications in international journals and 90 conference / symposium papers.

Dr V.K. Manchanda joined the Radiochemistry Division, B.A.R.C. in 1969 after graduating from Delhi University and from B.A.R.C. Training School . He was awarded Ph.D. by Bombay University in 1975 and carried out Post-Doctoral work at UTEP, Texas, U.S.A. as a Fulbright Scholar (1985-87). His research interests include; thermodynamics and kinetics of complexes of macrocyclic ligands with lanthanides and actinides, design and synthesis of novel extractants of actinides relevant in the back end of the fuel cycle, chemical quality control of Pu-based fuels and speciation of actinides in aquatic environment. He is a Ph.D. guide for Chemistry at the University of Mumbai and HBNI. He has about 150 publications in international journals and about 400 conference / symposium papers. He is currently on the Advisory Board of an internationally reputed journal *"Radiochimica Acta"* and is a member of Board of Studies in Chemical Sciences of HBNI (Deemed University). He is the President of IANCAS and is founder President of Indian Association of Separation Scientists and Technologists (INASAT). He currently heads the Radiochemistry Division of BARC.

BEAM DYNAMICS FOR THE 1 GeV PROTON LINAC FOR ADS

Rajni Pande, Shweta Roy, T. Basak, S.V.L.S. Rao and P. Singh
Nuclear Physics Division
Bhabha Atomic Research Centre

The paper was awarded the Oral Presentation prize during
DAE-BRNS Indian Particle Accelerator Conference (InPAC-2006)
held at BARC, Mumbai, during November 1-4, 2006

High-power proton linacs have various applications such as Accelerator Driven Systems (ADS) for transmutation or energy production, neutron spallation source for condensed matter studies, neutrino factories and muon colliders, production of rare isotope beams for nuclear physics studies, etc. These linear accelerators are required to deliver proton beams of up to several MW to several tens of MW power and operate with CW or pulsed high intensity beams. In particular, Accelerator Driven Systems (ADS) [1] have evoked considerable interest in the nuclear community the world over because of their capability to incinerate the MAs (minor actinides) and LLFPs (Long-lived Fission Products) radiotoxic waste and utilization of Thorium as an alternative nuclear fuel. Since India has vast resources of Thorium, ADS is particularly important as one of the potential routes for accelerated thorium utilization [2]. An ADS consists of a sub-critical reactor coupled to a high power proton accelerator through spallation target as shown in Fig. 1. The linac for an Accelerator Driven System is required to deliver a 1 GeV proton beam at

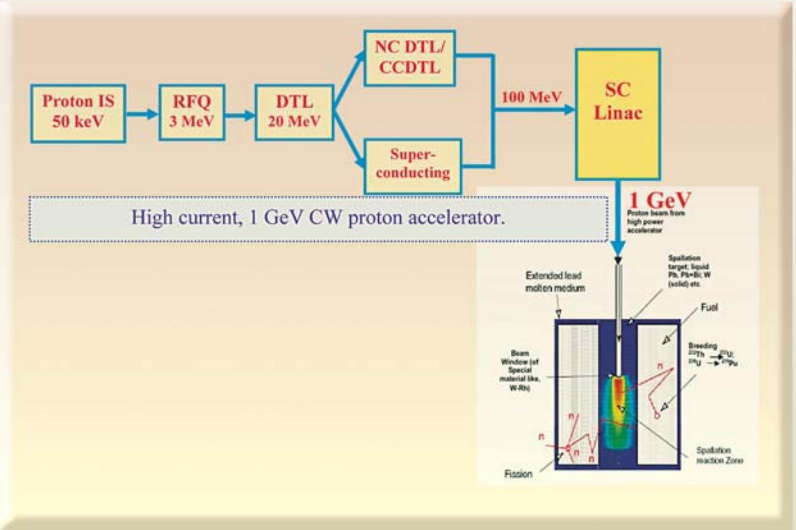

Fig.1: Schematic of Accelerator Driven System

tens of milliamperes of current. The main design criterion for such a linac, is low beam loss in the accelerator to allow hands-on-maintenance of the entire linac. With this criteria, the beam dynamics simulations for a 1 GeV, 30 mA proton linac have been done, the details of which are presented in this paper. The linac consists of an ECR ion source, a normal-conducting Radio-Frequency Quadrupole (RFQ), Drift Tube Linac (DTL) and Coupled Cavity Drift Tube Linac (CCDTL) structures that accelerate the beam to about 100 MeV followed by Superconducting (SC) elliptical cavities, which accelerate the beam from 100 MeV to 1 GeV [3].

Introduction

The 1 GeV linac consists of a 3 MeV RFQ, DTL upto 50 MeV, CCDTL upto 100 MeV and 5 cell superconducting elliptical cavities to accelerate the beam to 1 GeV. While the RFQ and DTL operate at 352.21 MHz, the operating frequency of CCDTL and SC linac is 704.42 MHz. The layout of the proposed 1 GeV accelerator is shown in Fig. 2. The transverse and longitudinal phase advances per unit length, are maintained constant at all transitions between the structures, to provide a current independent match into the next structure [4]. For this, the quadrupole gradients and accelerating electric fields are varied between the structures. The various accelerating structures are described below.

It is planned that the development of the 1 GeV accelerator for ADS will be pursued in three phases, namely, 20 MeV, 100 MeV and 1 GeV [2]. The most challenging part of this CW proton accelerator is development of the low-energy injector, typically up to 20 MeV, because the space charge effects are maximal here. Therefore, BARC has initiated a programme for the development of a Low Energy (20 MeV) High Intensity Proton Accelerator (LEHIPA) as front-end injector [5] of the 1 GeV accelerator for the ADS programme. The major components of LEHIPA are a 50 keV ECR ion source [6], a 3 MeV Radio-Frequency Quadrupole (RFQ) and a 20 MeV Drift Tube Linac (DTL). Extensive studies related to LEHIPA have been done to design the RFQ [5,7], DTL [5,8] and low energy and medium energy transport lines LEBT [9, 10] and MEBT [11] respectively.

RFQ

The RFQ operating at 352.21 MHz accelerates the 30 mA proton beam from 50 keV to 3 MeV. The RFQ has been designed with a varying vane voltage keeping the peak electric field less than 1.8 times the Kilpatrick limit.

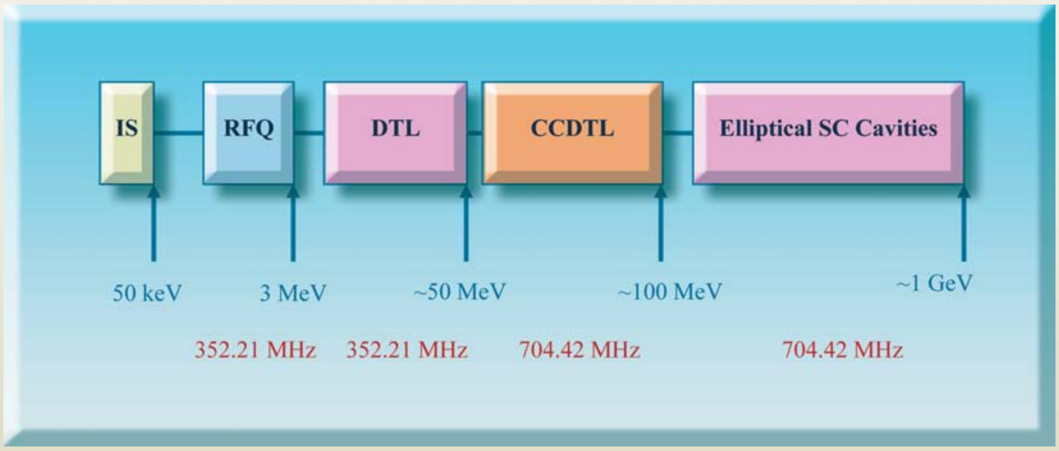

Fig. 2 : Layout of the 1 GeV linac

The parameters of the RFQ are shown in Table 1. The total length of the RFQ is 3.45 m and the total rf power requirement is 500 kW.

DTL

The beam from the RFQ is accelerated to 50 MeV using a 352.21 MHz DTL. This 3 MeV beam is matched into the DTL using a matching line (MEBT), which consists of 4 quadrupoles for transverse matching and 2 rf gaps for longitudinal matching. The DTL cavity has been designed using SUPERFISH [12]. The parameters of the DTL cavity are listed in Table 2. The face angle in the drift tubes is kept 0° from 3 MeV to 20 MeV where the drift tube lengths are small and increased to 10°(#) beyond 20 MeV where the drift tubes become long enough to accommodate the quadrupoles. This increases the effective shunt impedance at 20 MeV as can be seen in Fig. 3. Fig. 4 shows the electric fields in the half cells of the DTL cavity at 3 MeV, 20 MeV and 50 MeV respectively.

Table 1: Parameters of the RFQ

Parameters	Value
Frequency	352.21 MHz
Input energy	50 keV
Output energy	3 MeV
Input current	30 mA
Transverse emittance	0.02/0.0217 π cm-mrad
Synchronous phase	-30^0
Vane voltage	82-111.58 kV
Peak surface field	32.8 MV/m
Avg. aperture R0	3.63-4.53 mm
Length	3.45 m
Total RF power	500 kW
Transmission	97 %
Focusing parameter	4.07 – 4.8
Max. modulation	1.95

Table 2 : Cavity parameters of the DTL

Parameter	3-50 MeV
Frequency (MHz)	352.21
Tank Diameter (cm)	52
Drift Tube Diameter (cm)	12
Bore Radius (cm)	1.0
Face Angle (degrees)	0/10(#)
Corner Radius (cm)	1.5
Inner Nose Radius (cm)	0.5
Outer Nose Radius (cm)	0.5

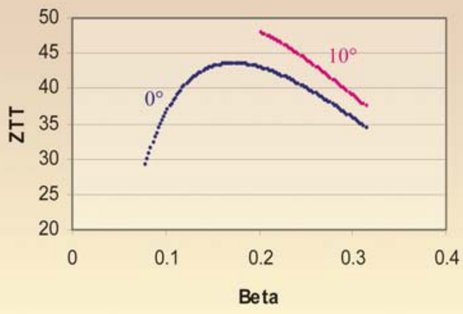

Fig.3 : Effect of increasing face angle in DTL on effective shunt impedance

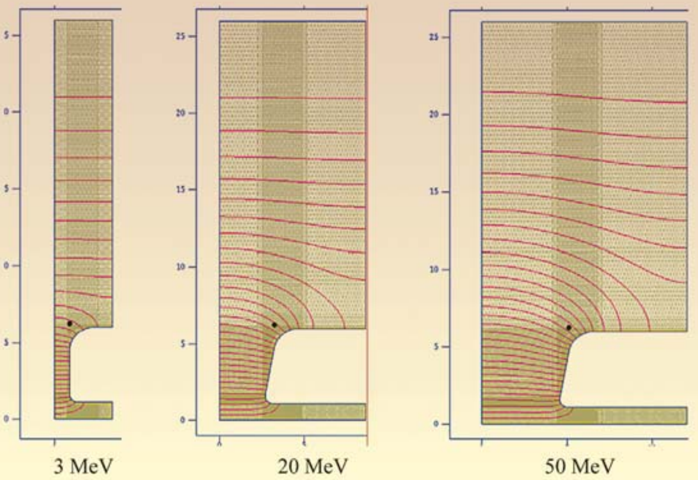

Fig. 4 : Half cell in DTL cavity at 3 MeV, 20 MeV and 50 MeV

A FODO lattice is used in the DTL for transverse focusing. For this lattice, the quadrupole gradient required to match the transverse phase advance between RFQ and DTL for current independent matching comes out to be 100 T/m. This can be achieved by permanent magnet quadrupoles placed inside the drift tubes. The focusing lattice period is 2βλ throughout the DTL. The total length of the DTL is 28 m and the RF power required is 4 MW. The DTL will be built in 5 tanks. The axial electric field is kept constant at 2.58 MV/m in all the tanks. The main parameters of the DTL are shown in Table 3.

Table 3 : Parameters of each DTL tank

DTL Tank No.		1	2	3	4	5
Input Energy (MeV)		3.0	11.48	20.11	30.58	40.52
Output Energy (MeV)		11.48	20.11	30.58	40.52	50.10
No. of Cells		51	33	31	26	23
Synch. Phase (deg)		-30	-30	-30	-30	-30
Accelerating field gradient (MV/m)		2.58	2.58	2.58	2.58	2.58
Total Power (kW)		732.2	708.9	838.7	818.3	804.0
Tank Length (m)		5.07	5.04	5.98	5.91	5.86
Norm. rms trans. Emitt. (π cm-mrad)	In x	0.0233	0.0233	0.0231	0.0230	0.0230
	In y	0.0222	0.0225	0.0228	0.0230	0.0230
Long. Emitt. (deg-MeV)		0.1167	0.1190	0.1206	0.1189	0.1261

The 3D design of the DTL tanks to include post couplers, tuners and vacuum ports is also being done. Figs. 5 and 6 show post couplers and tuner modelled in CST Microwave Studio respectively, in a single DTL tank.

Fig. 5: Model of post couplers in DTL

Fig. 6 : Model of tuner in DTL

CCDTL

The 50 MeV beam from the DTL is then accelerated to 98.6 MeV using 2 gap CCDTL cavities at 704.42 MHz as shown in Fig. 7. Each cavity contains a single drift tube inside mounted by stems and electromagnetic quadrupoles are mounted between two CCDTL cavities for transverse focusing. The CCDTL cavity is designed in SUPERFISH and the cavity parameters are shown in Table 4. The transverse focusing lattice is FODO and the focusing period is 5bl at this frequency. The beam from the DTL is transversely matched into the CCDTL by using the first four quadrupoles in the CCDTL. The accelerating gradient is kept constant at 1.6 MV/m in the CCDTL. Its total length is 75 m and the RF power requirement is 5 MW. The beam dynamics parameters of the CCDTL are shown in Table 5.

The 3D design of the DTL tanks to include post couplers, tuners and vacuum ports is also being done. Figs. 5 and 6 show post couplers and tuner modelled in CST Microwave Studio respectively, in a single DTL tank.

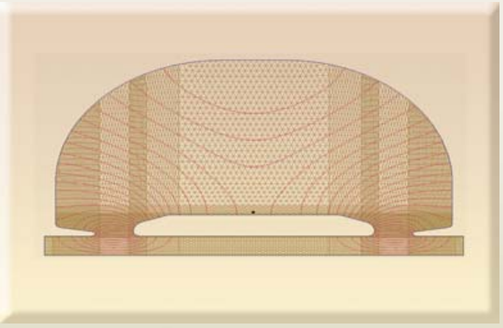

Fig.7: Two cell CCDTL cavity designed in SUPERFISH

Table 4 : Cavity parameters of CCDTL.

Parameter	Value
Frequency (MHz)	704.42
Diameter (cm)	24
No. of gaps	2
Drift tube diameter (cm)	5
Bore radius (cm)	1.2
Equator flat (cm)	3
Cone angle (Deg)	10
Drift tube face angle (deg)	70
Inner corner radius (cm)	0.25
Outer nose radius (cm)	0.05
Inner nose radius (cm)	0.2
Drift tube corner radius (cm)	0.5
Drift tube outer nose radius (cm)	0.6
Drift tube inner nose radius (cm)	0.3

Table 5 : Beam Dynamics parameters of CCDTL

Parameter		Value
Energy range (MeV)		50-98.6
Current (mA)		29.3
Focusing lattice		FODO
Lattice period		5βλ
Quadrupole gradient (T/m)		58.2-19.6
Eff. length of quad. (cm)		8.0
No. of quadrupoles		182
Synchronous phase (deg)		-30
Avg. acc. gradient (MV/m)		1.60
Aperture radius (cm)		1.2
Total length (m)		75
Norm. rms trans. Emitt. (π cm-mrad)	x	0.0230- 0.0236
	y	0.0230- 0.0237
Long. Emitt. (deg-MeV)		0.126-0.327

Superconducting linac

Superconducting elliptical cavities at 704.42 MHz are used, to accelerate the beam from 100 MeV to 1 GeV. The cavities are designed to perform over the given velocity range and are identified by a design velocity called the geometric velocity, $\beta_{G.}$ The design approach takes advantage of the large velocity acceptance of the superconducting cavities. For a cavity with N identical cells, the transit time factor T can be expressed as a product of two separate factors $T=T_G T_S$ [13]. In order to choose the number of cells per cavity, a compromise must be made between many competing effects. SUPERFISH is used to compute the gap factor T_G and the synchronism factor T_S is computed analytically for varying no. of cells/cavity. The results are plotted in the Fig. 8. As can be seen from the figure, a small number of cells/cavity provides a large velocity acceptance. On the other hand, using a larger number of cells/cavity has the advantage of reducing the overall number of system components, system size and system complexity. As a compromise between the two, in our design, we have chosen 5 cells/cavity.

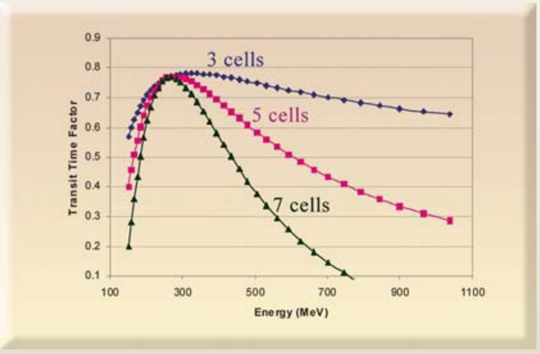

Fig. 8: Variation of velocity acceptance of the cavity with no. of cells per cavity

In order to efficiently design a linac it is necessary to divide it in sections, each using a different cavity geometry in a given energy range. To begin with, the b_G values for the cavities, the number of constant b_G sections and the beam velocity limits for each section have to be determined. Based on velocity acceptance, the entire energy range from 100 MeV to 1 GeV is divided into 3 sections of constant beta cavities as shown in Fig. 9. The cavity parameters of the 3 sections are shown in Table 6. The parameters of the elliptical cavity are shown in Fig. 10(a) and the 5 cell elliptical cavity for $\beta_G = 0.47$ is shown in Fig. 10(b).

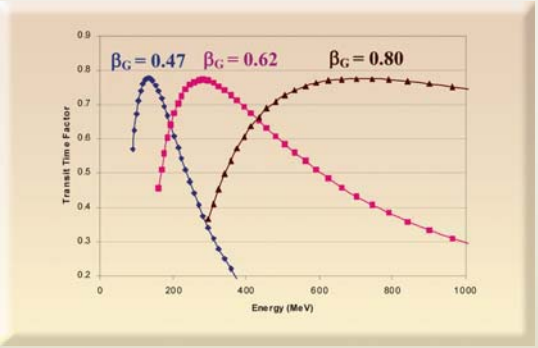

Fig. 9: Transit time factor curves for the 3 constant beta cavities

Table 6. Cavity parameters of the SC cavities

Parameters	$\beta_G = 0.47$	$\beta_G = 0.62$	$\beta_G = 0.8$
No. of cells	5	5	5
Diameter (cm)	36.27	35.83	37.34
Dome B (cm)	2	3	5.5
Dome A/B	1.5	1.5	1
Wall Angle (degrees)	5	5	7
Iris a/b	1.2	1	0.5
Bore Radius (cm)	4	4	4

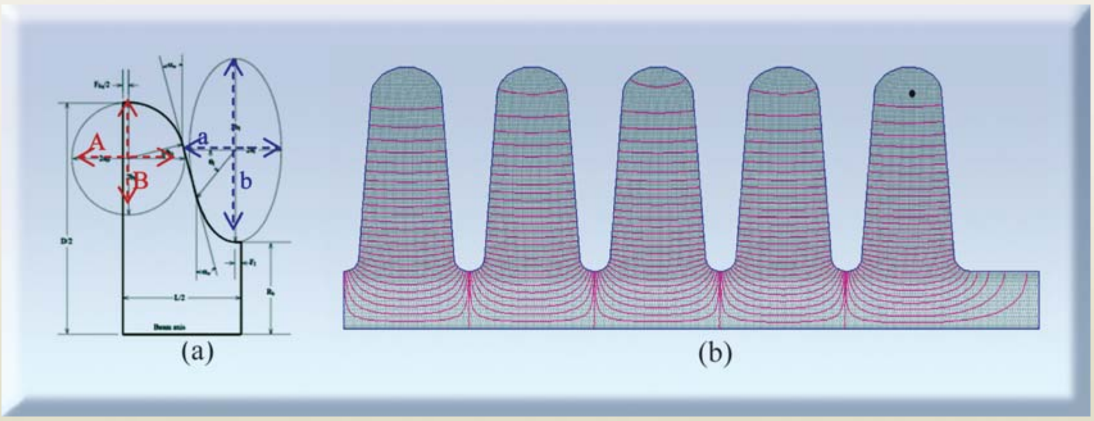

Fig.10: (a) Parameters of the elliptical cavity (b) Five cell elliptical cavity for $\beta_G = 0.47$

The transverse focusing is achieved, by using room temperature electromagnetic quadrupole doublets in between the cryomodules containing the superconducting cavities. The focussing doublets are placed after every 2 cavities in the first section, which will have 35 cryostats, after every 3 cavities in the second section having 40 cryostats and after every 4 cavities in the third section having 51 cryostats. To obtain a current independent match between the normal conducting linac and superconducting linac, which has a weaker focusing, the quadrupole gradients in the CCDTL are gradually reduced with energy. Transverse matching is done using the last 2 quadrupoles in the CCDTL and the first 2 qaudrupoles in the superconducting linac. Transverse matching between two superconducting sections was done, by making small adjustments to the quadrupole gradients at the transition between the sections.

Table 7 : Parameters of the superconducting linac

Parameter		β_G=0.47	β_G=0.62	β_G=0.80
Energy range (MeV)		98.6-198.3	198.3-498.3	498.3-1008.3
Frequency (MHz)		704.42	704.42	704.42
Current (mA)		29.3	29.3	29.3
Trans. focusing lattice		Doublet	Doublet	Doublet
Lattice period (cm)		300.1	608.0	810.7
Quad. gradient (T/m)		5.8-5.37	4.5	4.4
Eff. length of quad. (cm)		35	40	45
Synchronous phase		-30	-23.44	-23.44
Cavities/cryomodule		2	3	4
No. of cryomodules		35	40	51
Aperture radius (cm)		4.0	4.0	4.0
Total length (m)		105.04	243.2	413.46
Norm. rms trans. Emitt. (π cm-mrad)	x	0.0236-0.0253	0.0253-0.0285	0.0285-0.0299
	y	0.0237-0.0251	0.0251-0.0276	0.0276-0.0271
Long. Emittance (deg-MeV)		0.3270-0.4440	0.4440-0.4820	0.4820-0.4990

Longitudinal matching was achieved, by adjusting the synchronous phase ϕ_s in the superconducting cavities to maintain constant longitudinal phase advance per unit length on both sections and maintaining a constant energy gain in each cavity. This was done by keeping ($\Delta W \tan\phi_s/L$) constant on both sides of the transition, where ΔW is the energy gain per cryomodule and L is the length of the focusing period. The parameters of the SC linac are shown in Table 7.

The computer code PARMILA [14] was used to do the end-to-end beam dynamics simulations from 3 MeV to 1 GeV. Fig. 11 shows the beam at the end of the DTL, CCDTL and the SC linac and the x, y and phase profiles of the beam from the DTL through the superconducting linac for a beam current of 29.3 mA. The maximum beam radius never exceeds 1.1 cm in the linac as can be seen from Fig. 12. The aperture is 10-12 times the rms beam size in the normal conducting linac and is more than 16 times the rms beam size in the superconducting linac, where the risk due to activation is more. The beam transmission is 100% from 3 MeV to 1 GeV. The variation of transverse emittance through the linac is shown in Fig. 13.

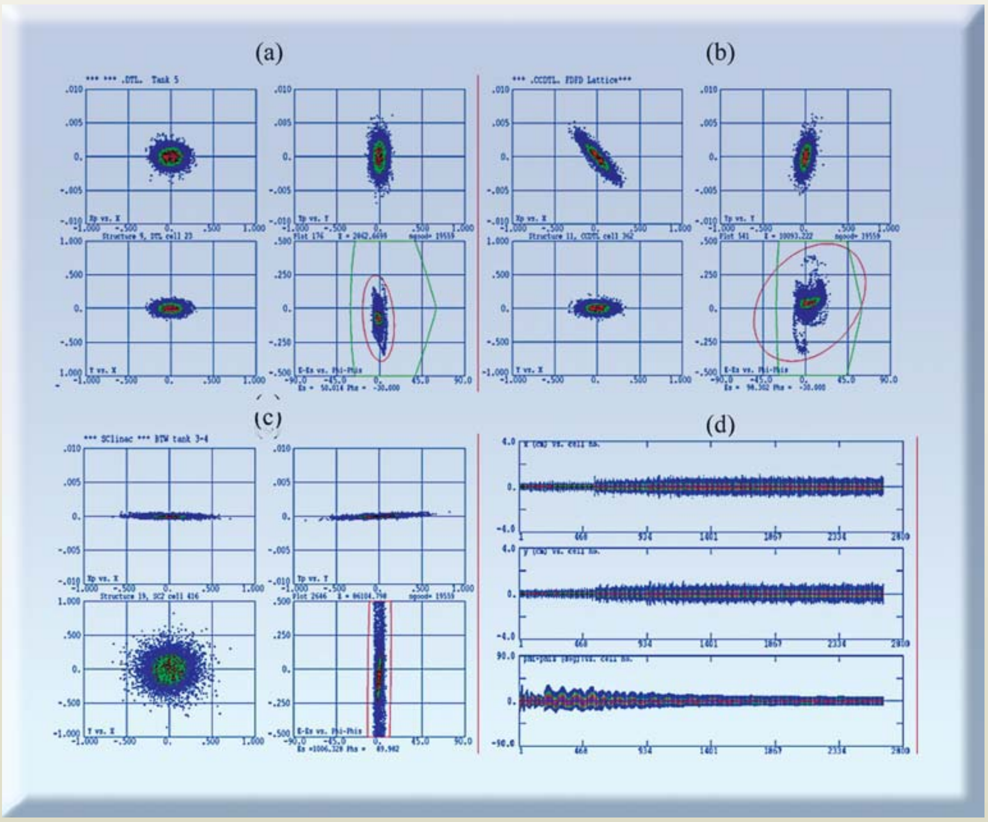

Fig. 11: Beam at the end of (a) DTL (b) CCDTL (c) SC Linac and (d) Beam profile through the entire linac

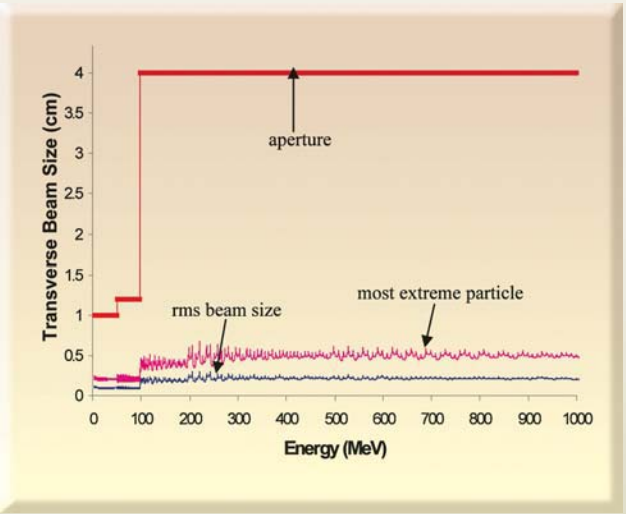

Fig. 12 : Variation of beam size and aperture with beam energy

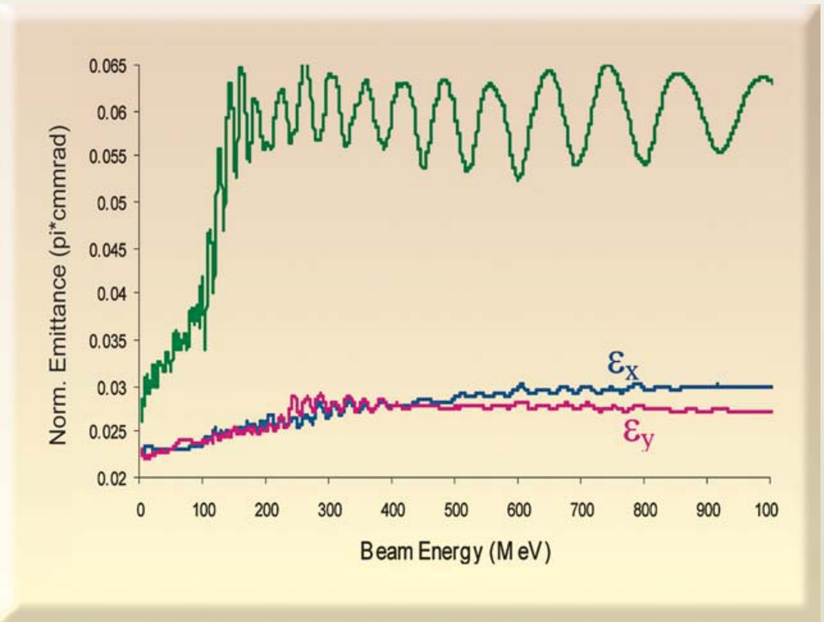

Fig. 13: Variation of transverse (ε_x, ε_y) and longitudinal (ε_z) emittances with beam energy

Present status and future studies

The design of the 20 MeV, 30 mA proton accelerator (LEHIPA), being built in connection with our ADS programme, is complete. The fabrication and procurement of various subsystems are in progress. The Low Energy Beam Transport line (LEBT) uses two solenoids for focusing the diverging beam from the ion source. The beam dynamics of LEBT was studied using 'TRACE 2D" code and its layout is shown in Fig. 14. Fabrication of the LEBT solenoids is in progress at RRCAT, Indore.

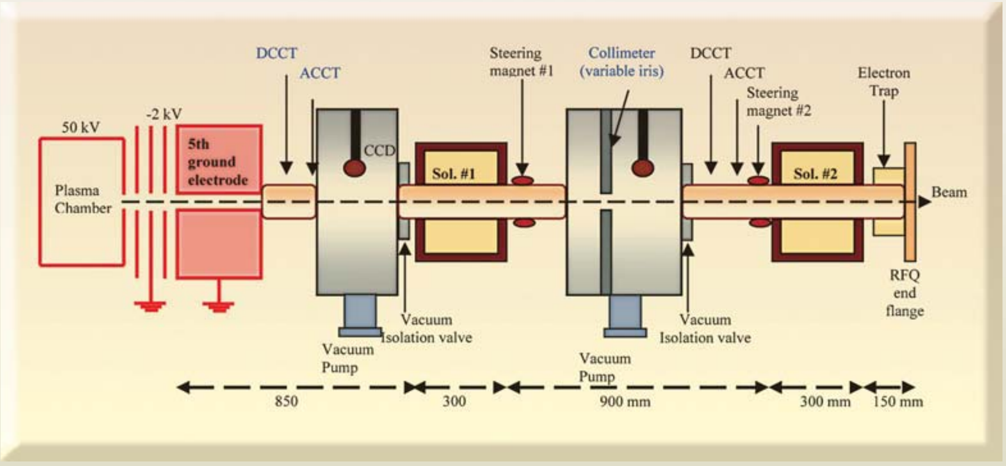

Fig. 14 : Layout of the Low Energy Beam Transport (LEBT) system

The CAD model of the 3 MeV RFQ for LEHIPA is shown in Fig. 15. This 3.45 m long RFQ will be made in 4 sections, resonantly coupled using coupling cells [15]. The fabrication of the RFQ is in progress at M/s KELTEC, Thiruvananthapuram.

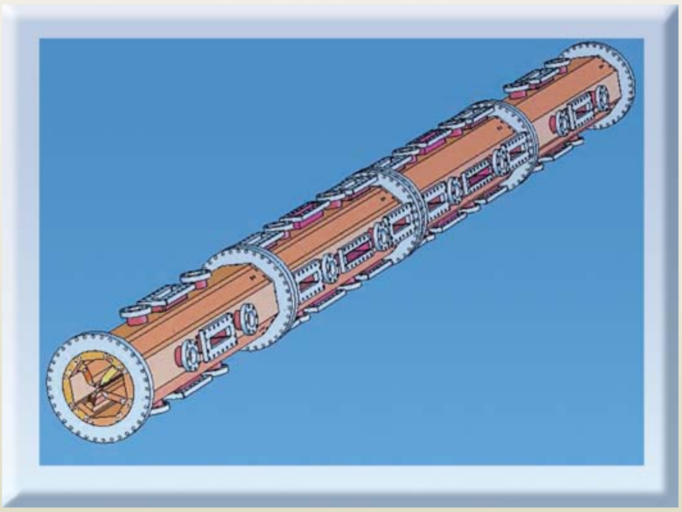

Fig.15: CAD model of the 3 MeV RFQ for LEHIPA

The current design of the 1 GeV linac has been done using modest gradients of about 5 MV/m in the superconducting cavities. Because of the high beam current, the major design issue is not attainment of high cavity gradients, but high power rf coupler capability [16]. In view of advancement in SC technology and higher gradients achievable that have been demonstrated at various labs around the world, it is planned to design the linac with higher accelerating gradients and also considering other structures like the spoke cavities. It is also planned to incorporate equipartioning in the design in future, to avoid beam halo formation in the linac.

Acknowledgement

We thank Dr V.C. Sahni, Dr S. Kailas and Dr R.K. Choudhury for their keen interest in this work.

References

1. F. Carminati, R. Klapisch, J.P. Revol, J.A. Rubio and C. Rubbia CERN/AT/93-47 (ET); C. Rubbia et al; CERN/AT/95-44 (ET); CERN/LHC/96-01 (EET); CERN/AT/95-53 (ET); CERN/LHC/97-01 (EET).
2. S.S. Kapoor, "Roadmap for development of Accelerator Driven Sub-Critical Reactor Systems", BARC/2001/R/004.
3. P. Singh et. al. "Accelerator Development in India for ADS Programme", *Pramana -Journal of Physics,* Vol 68, No.2, February 2007, pp. 331-342.
4. R.S. Mills, K.R. Crandall and J.A. Farrell, "Designing Self-Matching Linacs", Proc. 1984 Linac Conf.
5. T. Basak, B. Biswas, S. Kailas, S. Krishnagopal, Arvind Kumar, Rajni Pande, P.K. Nema, S.V.L.S. Rao, Shweta Roy, V.C. Sahni and P. Singh, "Physics Design of a Low Energy High Intensity Proton Accelerator", BARC/2004/I/007.
6. P. Roychowdhury, P. Jain, V. Yadav, K.P. Dixit and R.C. Sethi, "Design and development of a high current Microwave ion source", Proc. InPAC-2003, Feb. 3-6, 2003, CAT, Indore, p 179.
7. S.V.L.S. Rao, Rajni Pande, Shweta Roy, T. Basak, P. Singh, S. Krishnagopal, P. K. Nema, S. Kailas and V.C. Sahni, "Physics Design of the 3 MeV RFQ", InPAC-2005, VECC, March 1-5, 2005, page 60.
8. T. Basak, Rajni Pande, Shweta Roy, S.V.L.S. Rao and P. Singh, "Comparison of FD and FFDD lattices for DTL", InPAC-2005,VECC, March 1-5, 2005, page 174.
9. Rajni Pande, S.V.L.S. Rao, T. Basak, P. Singh, P.K. Nema, S. Kailas, V.C. Sahni, A. Kumar, B. Biswas

and S. Krishnagopal, "Effect of Space Charge Compensation on LEBT Design", Proc. DAE Symp. Nucl. Phys.(India), 46B, 466 (2003).

10. S.C.L. Srivastava, S.V.L.S. Rao and P. Singh, "Development of 2D PIC code to simulate high current, low energy beam in a beam transport system", *Pramana.-J. Phys.* (In press).
11. S.V.L.S. Rao, R. Pande, T. Basak, P. Singh, P.K. Nema, S. Kailas, A. Kumar, B. Biswas and S. Krishnagopal, "Simulation studies of MEBT for 10 MeV high-current proton linac", Proc. Ind. Part. Acc. Conf.(InPAC2003), Feb. 3-6, 2003, CAT Indore, p 84
12. J.H.Billen & L.M.Young, *POISSON SUPERFISH*, LA-UR-96-1834. L.A.N.L.
13. R.W. Garnett and T.P. Wangler, "A Design Approach for Superconducting High-Current Ion Linacs", Proc. 18th International Linac Conference, Geneva (Switzerland), August 26-30, 1996, Page 707.
14. J.H.Billen, *PARMILA* Code, LA-UR-98-4478, Revised July 26, 2005.
15. Rajni Pande, Shweta Roy, S.V.L.S. Rao, T. Basak, P. Singh, P.K. Nema, S. Kailas and V.C. Sahni, "3-D design of the RFQ cavity", DAE-BRNS Nucl. Phys. Symp., 47B(2004) 474.
16. G.P. Lawrence, XIX Int.Linear Accelerator Conf. Chicago, Ill. (August, 1998).

About the Authors

Ms. Rajni Pande is from the second batch of RRCAT Training School and is working in Nuclear Physics Division since 2002. She did her M.Sc. in Physics from Lucknow University. Ms. Rajni Pande is involved in Physics Studies of the 20 MeV High Intensity Proton Accelerator being developed for ADS Programme.

Ms. Shweta Roy is working in Nuclear Physics Division, BARC since 2003. She is from the 46th batch of BARC Training School. She did her Masters in Physics from IIT, Delhi. Ms. Shweta Roy is involved in Physics Studies of the 20 MeV High Intensity Proton Accelerator being developed for ADS Programme.

Ms. T. Basak was working in Nuclear Physics Division, BARC as a Ph.D. student since 2002. She did her Masters in Physics from University of Mumbai. Ms. Basak is involved in Physics Studies of the 20 MeV High Intensity Proton Accelerator being developed for ADS Programme.

Mr. S.V.L.S. Rao did his Masters in Physics from University of Hyderabad in 2000 and joined Nuclear Physics Division in 2001 after one year of Orientation programme at BARC. Mr Rao is presently involved in development of High Current Accelerator for ADS.

Dr Pitamber Singh, a graduate of the 19th batch of BARC Training School, joined Nuclear Physics Division, BARC in 1976. He received his Ph.D. degree in Physics from Mumbai University in 1983. In addition to designing and building the first 2 MV Tandem Accelerator, he has made an outstanding contribution in setting up the 6 MV Foded Tandem Ion Accelerator (FOTIA) facility at BARC. He was conferred DAE's Technical Excellence Award for the year 2000 for his contributions towards indigenous development of accelerator technology in the country. He is a life member of "The National Academy of Sciences, India". Dr. Singh is working on the development of High Intensity Proton Accelerators for the ADS programme of DAE. Presently, he is Head, FOTIA Section of the Nuclear Physics Division, BARC.

DEVELOPING SOMATIC EMBRYOGENIC CULTURE SYSTEM AND PLANT REGENERATION IN BANANA

Meenakshi Sidha, P. Suprasanna , V. A. Bapat, U.G. Kulkarni and **B.N. Shinde**
Nuclear Agriculture & Biotechnology Division
Bhabha Atomic Research Centre

This paper was awarded the Consolation Prize at the National Symposium on Plant Biotechnology held at Dehra Dun, during October 12-14, 2006

Abstract

Bananas and plantains are one of the major fruit crops and a staple food in the developing world. Most of the edible bananas are triploid, highly sterile and hence integration of in vitro techniques banana improvement becomes crucial. In this milieu, technique of somatic embryogenesis in combination with genetic manipulation, has become pertinent. In the present study, results are presented on developing embryogenic culture systems in banana. Immature Male Flowers (IMFs) of different banana cultivars (Ardhapuri, Basrai, Grande Naine, Lalkela, Mutheli and Shrimanti) were tested for callus induction on medium containing 2,4-D, IAA and NAA. In terms of callus induction from IMFs of AAA genomic group, Lalkela showed highest response (77.7%) followed by medium response in Shrimanti (52.2%), Basrai (51%), Grande Naine (42.5%), Ardhapuri (42%) and Mutheli (40%). Compared to this group, Safed Velchi (BB) was found to be highly responsive to IMF culture (70%) similar to Lalkela. Embryogenic response was higher in Lalkela (83.3%), Grande Naine (62%) Ardhapuri (50%), Basrai and Mutheli (45%) and Shrimanti (40%) while Safed Velchi showed less response (20%). Experiments with different auxins (2,4-D & its analogs, Dicamba, Picloram and PAA) showed varied response among the cultivars tested. This is a first step in optimizing in vitro culture conditions for somatic embryogenesis in diverse Indian banana cultivars belonging to different genomic groups.

Bananas and plantains are one of the world's important food commodity and rank fourth in terms of gross value, exceeded only by rice, wheat and milk/milk products. These are important staple food crops in the humid and sub-humid tropical regions of the world. Banana provides nourishment and a well-balanced diet to millions of people around the globe and contributes to livelihood through crop production, processing and marketing (Sundararaju, 1999). India is the largest producer of banana with an annual production of 11.7 million tonnes on 404,000 ha, contributing to 27% of the world production and about 37% of the total fruit crop production in the country (FAOStat, 2006). India has a rich genetic diversity of banana with more than 90 distinct clones. Depending on the contribution of *Musa acuminata* and *Musa balbisiana*, the cultivars have been classified into genomic groups (AAA, AAB, ABB, BB, AB, BBB, AAAA, ABBB).

Banana is grown under diverse conditions and production systems and hence selection of varieties is based on needs and situations. Around 20 cultivars viz. Dwarf Cavendish, Robusta, Monthan, Poovan, Nendran, Red banana, Safed Velchi, Basrai, Ardhapuri, Rasthali, Karpurvalli, Karthali and Grande Naine etc. are commercially cultivated.

Banana cultivation and production are threatened by many pests and diseases (weevil borers, nematodes, sigatoka complex, fusarium wilt, moko disease and viruses) resulting in the application of high doses of pesticides with serious consequences for the environment. Because of its high sterility (i.e., seedlessness) and polyploidy of the edible varieties (Stover and Simmonds, 1987), classical breeding is difficult (Ganry, 1990) and have resulted in increasing efforts to genetically improve the crop. In this regard, plant tissue culture and molecular genetic techniques have shown great potential to overcome some of the factors limiting traditional approaches to banana and plantain improvement. Such procedures largely depend on successful regeneration of plants from cultured banana cells. Therefore the integration of biotechnology into banana and plantain breeding programmes require access to reliable cell culture protocols.

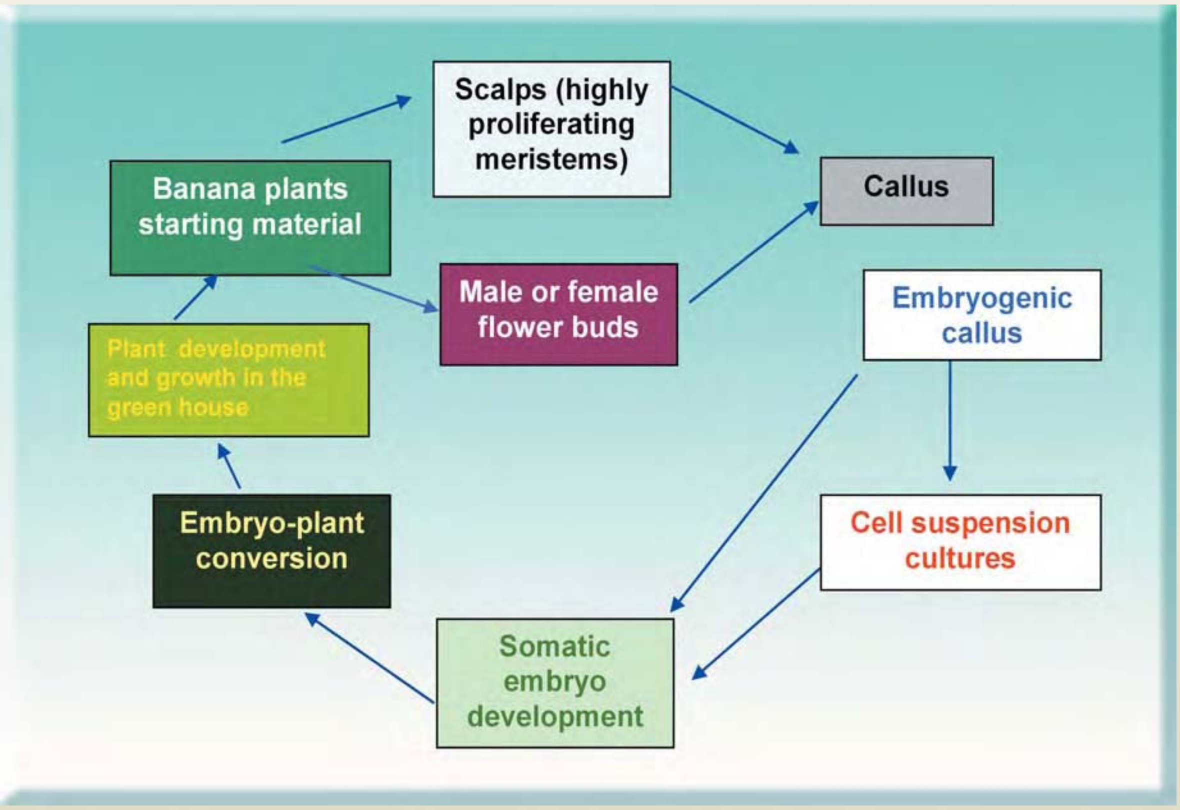

Fig. 1 : Potential pathways for somatic embryogenesis and plant regeneration in banana

Somatic embryogenesis is one of the important prerequisites for genetic engineering, however, this has been successful with limited numbers of banana cultivars such as Bluggoe (ABB) (Novak et al, 1989; Dheda et al, 1991; Panis et al, 1993); Grand naine (AAA) (Novak et al, 1989; Escalant et al, 1994; Cote et al, 1996; Becker et al, 2000); Rasthali (AAB) (Escalant et al, 1994; Ganapathi et al, 2001) and Mas (AA) (Jalil et al, 2003). The banana explants that have been used in somatic embryogenesis studies have been proliferating meristems (Cronauer-Mitra and Krikorian, 1983); zygotic embryos (Cronauer-Mitra and Krikorian, 1988; Escalant and Teisson, 1989; Marroqin et al, 1993); rhizome leaf sheaths (Novak et al, 1989); immature male flowers (Escalant, 1994; Cote et al, 1996; Grapin et al, 1996) and female flowers (Grapin et al, 2000). Among the explants that have been used, immature male flowers and scalps are the most responsive starting material, for initiating regenerable, embryogenic cell suspension cultures (Fig. 1). Considering the need to optimize culture protocols for diverse Indian banana cultivars, there have been efforts to establish regenerable cultures (Ganapathi et al, 2002, Suprasanna et al, 2002, Kulkarni et al, 2006). Herein, we present our results on the induction of somatic embryogenesis and plant regeneration in different commercial cultivars of banana: AAA genotype (Lalkela, Grand naine, Ardhapuri, Shrimanti, Basrai, Mutheli) and BB genotype (Safed Velchi).

Materials and method

Inflorescence male flowers of banana cultivars (Grand naine, Ardhapuri, Basrai, Shrimanti, Mutheli, Lalkela and Safed Velchi; obtained from Banana Research Station, Jalgaon, Maharashtra) were used as explant material. The male bud was shortened to 6-8cm in length by removing the enveloping bracts and these explants were sterilized in 70% ethanol for about 5 minutes and rinsed three to five times with sterile water. The male buds were further reduced to 1.5 cm in length for culture and immature male flower clusters from position 0-15 were removed and cultured on Murashige and Skoog medium (MS) supplemented with 18.10μM 2,4-dichlorophenoxy acetic acid (2,4-D), 5.71μM indole 3-acetic acid (IAA) and 4.09 μM d-Biotin, 3% sucrose and 0.2% gelrite for callus induction and for proliferation of callus d-Biotin, 2.4-D, malt extract and glutamine were used. For somatic embryo induction the medium the embryogenic callus was grown on Schenk and Haberlandent (SH) and MS (vitamin) supplemented with glutamine (100mg), malt extract (100mg) and picloram (1mg) and for development of somatic embryos, 0.22μM-benzyl amino purine (BA) and 1.14μM IAA, 3% sucrose, glutamine and malt extract were used.

Callus was also cultured on the different analogs of 2,4-D, (2,4-Dichlorophenoxyacetic acid) 2,4,5-P (2,4-5 -trichloropropionic acid), 2,4,5T (2,4,5-trichloro-phenoxyacetic acid), CPA (p-chlorophenoxyacetic acid), Dicamba (3, 6-Dichloro-o-anisic acid), PAA (phenylacetic acid) and Picloram (4-amino-3, 5, 6-trichloropicolinic acid). The pH of the medium was adjusted to 5.7 prior to autoclaving. All culture media were autoclaved at 121^0C for 20 min. Cultural conditions for initiation of embryos, maintenance of suspension culture and development of embryos were maintained at 28^0C under a 16h-photoperiod with light intensity of $31.4\mu mol^{-2}S^{-1}$. Cell suspensions were initiated from embryogenic callus and maintained at weekly intervals at 70 rpm continuously on a shaker under above cultural conditions. For conversion of somatic embryos into plantlets, ½ strength MS basal medium with 0.5% ME + 0.1% AC and 0.2% gelrite was used and after plantlets emerged, these were separated and transplanted into paper cups and then into pots in the green house for further growth.

Results and discussion

Developing embryogenic culture systems with reliable regeneration efficiency from important varieties of banana is a prerequisite for realizing the potential of cellular and molecular tools of crop improvement (Smith et al 2005). Towards this goal, studies were made to develop protocols for somatic embryogenesis

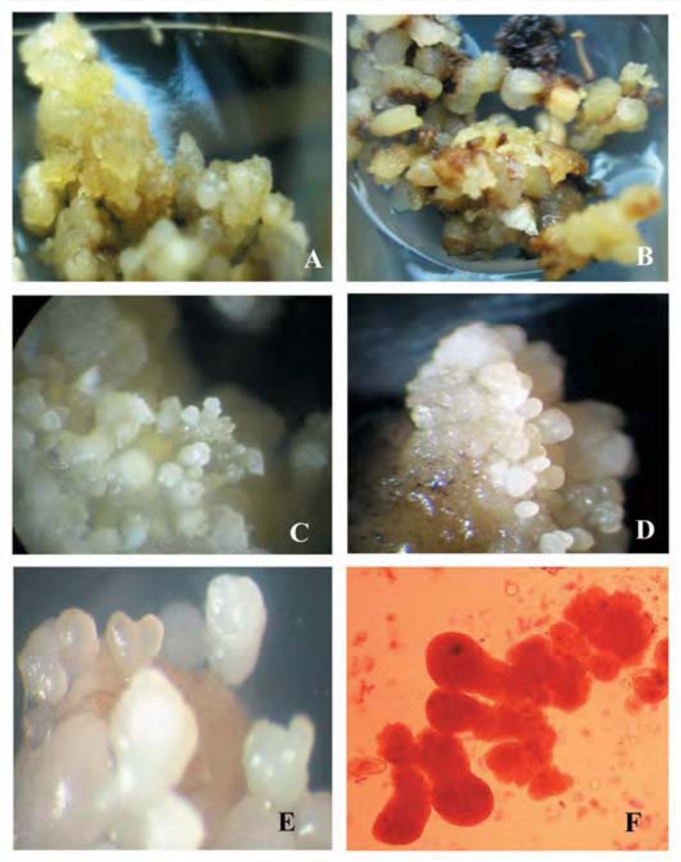

Fig. 2 : Stages from callus induction to embryo development in different cultivars of banana

A) Nodular to creamish white callus, B) Initiation of yellow nodular callus, C) Embryo initiation, D) Clump of embryos, E) Different stages of somatic embryo, F) Microscopic observation of somatic embryo development in cell suspension cultures.

and plant regeneration from different banana cultivars. Young flowers responded after 2 to 3 months of culture by forming a small yellow callus, and during the following 3 to 5 months, a white and translucent callus formed on the yellow callus and development of somatic embryos appeared on its surface. Fig 2. (A-F) shows different developmental stages from the callus induction to embryo development in different cultivars. In terms of callus induction from IMFs, Lal-kela showed highest response (77.7%) among AAA genomic group followed by Shrimanti and Basrai (52.2 and 51%), Grand Naine, Ardhapuri and Mutheli (42.5, 42 and 40%). Compared to this, Safed velchi (AB) was found to be highly responsive (70%) to IMF culture. The original explants became brown at the base within a week of culture and began to swell and the size also increased after 2-3 weeks. In terms of embryogenic callus induction, it was highest in Lal-kela 83.3% than other cultivars which were in the range (50-40%) and in Safed velchi it was the lowest (20%). Upon transfer to suspension medium, friable embryogenic callus released embryogenic cells with dense cytoplasm. Suspension cultures obtained consisted of heterogeneous cells: the embryogenic cells were smaller, more spherical in shape and had dense yellow cytoplasm with very few small vacuoles; the non-embryogenic nature was distinct with large vacuolated cells with meager cytoplasm and irregularly shaped cells.

In general, the cultivars exhibited differential response in terms of the time taken for callus proliferation, embryo development and embryo conversion to plants. Cultivars like Grand naine, Lal-kela, Basrai completed all these stages till regeneration while in case of Ardhapuri, Shreemanti, Mutheli the embryo to plant conversion was slow. Compared to these cultivars of AAA genotype, in case of Safed Velchi (AB), callus initiation was found to be good, however, the nodular callus developed only into mucilaginous type and further development into other stages of friable or loose callus was not observed.

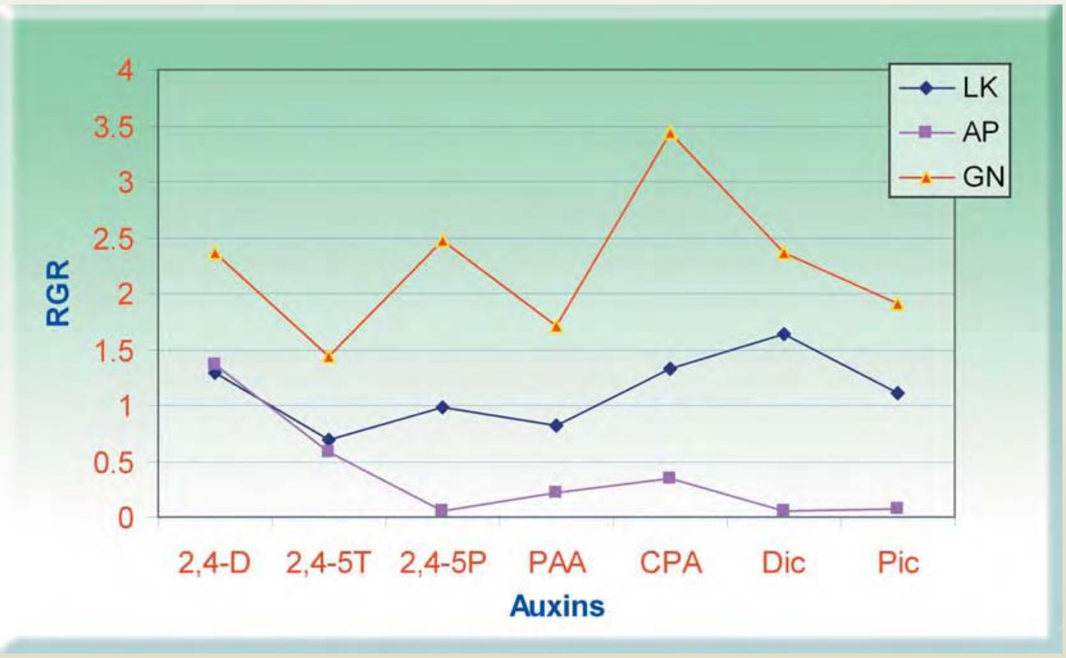

Fig. 3 : Effect of auxins on proliferation of embryogenic callus in banana cvs. Ardhapuri, Lalkela, Grand Naine

This is suggestive of the fact, that the cultivars of the same genotype onto the same medium do not behave similarly. For this differential behavior, the different analogs of 2,4-D, picloram, dicamba and PAA were used, to see the proliferation (Fig. 4) and embryo initiation. Of all the auxins tested, 2,4,5-P and 2,4,5 T showed good response towards the initiation of embryos while Dicamba and Picloram showed highest rate of proliferation. Safed velchi did not show any response with any of the auxins, which could be attributed to the genotypic variation. Among the rest of the cultivars (AAA), Ardhapuri displayed superiority of 2,4-D. Hormones are the most likely candidates in the regulation of morphogenetic and developmental cues. Auxins and cytokinins are the principal growth regulators in plants in the regulation of cell division and differentiation (Feher et al 2003). In banana, for the initiation of callus, medium is supplemented with three auxins IAA, NAA, 2,4-D and different auxins for the proliferation while a cytokinin with auxin (IAA+BA) is necessary for embryo development (Navarro et al 1997; Ganapathi et al 1999).

The features of somatic embryos (translucent and whitish) obtained in this study, were similar to those obtained by (Cote et al 1996, Escalant et al 1994). In general, higher numbers of somatic embryos per flower cluster were obtained in LK (4-10) as compared to other cultivars (4-6).

The embryos passed through different developmental stages and finally green plumules emerged from these embryos. Somatic embryos developed into the plantlets (Fig. 4 :A-C) (highest in LK 70% followed by Grand Naine) on ½ strength MS basal medium with 0.5%ME+0.1% AC and 0.2% gelrite and the time span for the development of shoot and root was within 6 to 8 weeks. Once the plantlets developed, these were separated and transplanted into paper cups (Fig. 4D).

Among the different explants tested for somatic embryogenesis, immature male inflorescences have mostly been used, to initiate embryogenic cultures of several banana and plantain cultivars (Escalant et

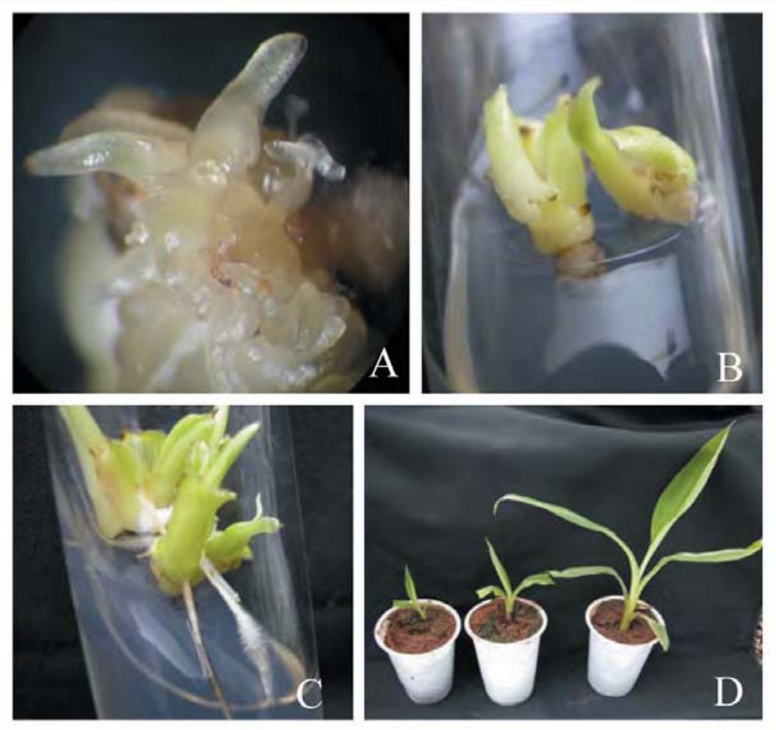

Fig. 4. : Different stages in plant regeneration through Somatic embryogenesis in banana cv. Lal kela
A. Somatic embryo, B & C. Embryo to plant conversion,
D. Hardening of regenerated plants in the green house

al. 1994; Côte et al. 1996; Navarro et al 1997; Becker et al. 2000, Kulkarni et al 2006). Genetic manipulation using Embryogenic Cell Suspensions (ECS) has become a tangible and useful approach for an integrated genetic improvement via different biotechnological approaches. Protocols have been developed for the induction of somatic embryogenesis using immature male flowers as well as proliferating *in vitro* cultures (Dheda et al 1991, Ganapathi et al 1999, Suprasanna et al. 2001, Kulkarni et al 2006). Immature male inflorescences have also been used to initiate cultures with the objective of developing a protocol for primary and secondary somatic embryogenesis (Khalil et al 2002). In our study, we have also observed secondary embryos on pre-existing somatic embryos (Fig. 2:E). Secondary embryos typically appeared directly from primary somatic embryos and were in clusters at the globular stage. Secondary embryogenesis is a process of induction of new somatic embryos from existing embryos and since new embryos are continually formed from existing embryos, this method has the potential to produce many plants over a long period of time. The use of secondary embryogenesis could also offer an efficient solution, to the problems limiting plant regeneration in some banana cultivars.

Somatic embryogenesis is an established method for raising regenerable suspension cultures in case of banana. Although several commercial and elite clones have been induced into embryogenesis, a large number of banana genotypes still need to be explored for embryogenic potential for use in propagation and genetic improvement. Developing protocols for *in vitro* plant regeneration from diverse banana genotypes, as attempted in this study, will usher efforts in conservation, propagation and for genetic manipulation for improving desirable traits.

Acknowledgements

The senior author would like to thank Dr C. D. Badgujar, Banana Research Station, Jalgaon and R.M. Kulkarni, Fruit Research Station, Aurangabad for providing plant material.

References

1. Becker, D.K., Dugdale, B., Smith, M.K., Harding, R.M and Dale, J.L. (2000). Genetic transformation of Cavendish banana (Musa spp. AAA group) cv. Grand Nain via micro-projectile bombardment. *Plant Cell Rep.* 19:229-234.
2. Cote, F.X., Domergne, R., Monmarson, S., Schwendiman, J., Teisson, C and Escalant, J.V. (1996). Embryogenic cell suspensions from male flower of Musa AAA cv. *Grand Nain. Physiol. Plant,* 97: 285-290.
3. Cronauer-Mitra, S.S and Krikorian, A.P (1983). Somatic embryos from cultured tissue of triploid plantains (Musa ABB). *Plant Cell Rep.* 2: 289-291.
4. Cronauer-Mitra, S.S, and Krikorian, A.P (1988). Plant regeneration via somatic embryogenesis in the seeded diploid Musa onnata Roxb. *Plant Cell Rep.* 7: 23-25.
5. Dhed'a, D., Dumortier, F., Panis B., Vuylsteke, D., De Langhe, E. (1991). Plant regeneration in cell suspension cultures of the cooking banana cv."Bluggoe" (Musa spp. ABB group). *Fruits* 46:125-135.
6. Escalant, J.V and Teisson, C. (1989). Somatic embryogenesis and plants from immature zygotic embryos of the species Musa acuminata and Musa balbisiana. *Plant Cell Rep.* 7: 665-668.
7. Escalant, J.V., Teisson, C and Cote, F.X. (1994). Amplified somatic embryogenesis from male flowers of triploid banana and plantain cultivar (Musa spp). *In Vitro Cell. Dev.Biol*.30 p: 181-186.
8. FAO. 2006. FAOSTAT Agriculture Data. www.fao.org
9. Feher, A., Pasternak, T.P., Dudits, D. (2003). Transition of somatic cell to an embryogenic state. *Plant Cell Tissue and Organ Cult.* 74: 201-228.
10. Ganapathi TR, Suprasanna P, Bapat VA. (2002) Biotechnological approaches for banana propagation and improvement. In: Proc. National Seminar on Biotechnology - challenges and prospects. St. Aloysius College, Mangalore. 125-149.
11. Ganapathi, T.R., Higgs, N.S., Balint-Kurti, J., Arntzen, C.J., May, G.D and Van- Eck, J.M. (2001). Agrobacterium mediated transformation of embryogenic cell suspensions of the banana cultivar Rasthali (AAB). *Plant Cell Rep.* 20: 157-162.
12. Ganapathi, T.R., Suprasanna, P., Bapat, V.A, Kulkarni, V.M, Rao, P.S. (1999). Somatic embryogenesis and plant regeneration from male flower buds in banana. *Curr Sci* 79:1229-1231.
13. Ganry, J. (1990). Les recherches sur les bananiers et plantains à 1'Institut de Recherches sur les Fruits et Agrumes.Situation actuelle et environnement international. Fruits numéro special: 7-22.
14. Grapin, A., Ortiz, J.L., Lescot, T., Ferriere, N., Cote, F.X. (2000). Recovery and regeneration of embryogenic cultures from female flower of False Horn Plantain (Musa AAB). *Plant Cell Tissue and Organ Cult.* 61: 237-244.
15. Grapin, A., Schwendiman, J., Teisson, C. (1996). Somatic embryogenesis in plantain bananas. In vitro cellular developmental biology-*Plant.* 32: 66-71.
16. Jalil, M., Khalid, N., Othman, R.Y. (2003). Plant regeneration from embryogenic suspension cultures of Musa acuminata cv. Mas (AA). *Plant Cell Tissue and Organ Cult.* 75: 209-214.
17. Khalil, S.M., Cheah, K.T., Perez, E.A., Gaskill, D.A., Hu, J.S. (2002). Regeneration of banana (*Musa* spp. AAB cv. 'Dwarf Brazilian') via secondary somatic embryogenesis. *Plant Cell Reports.* vol. 20, (12), 1128-1134.
18. Kulkarni, V.M., Suprasanna, P., Bapat, V.A.(2006) Plant regeneration through multiple shoot formation and somatic embryogenesis in a commercially important and endangered Indian banana cv. Rajeli. *Curr. Sci.,* 90(6): 842-846.
19. Marroquin, C.G., Paduscheck, C., Escalant, J.V., Teisson, C. (1993). Somatic embryogenesis and plant regeneration through cell suspension in Musa acuminata. In Vitro *Cell.Dev.Biol.* 29: 43-46.
20. Navarro, C., Escobedo, R.M, Mayo, A. (1997). In vitro plant regeneration from embryogenic cultures of a diploid and a triploid, Cavendish banana. *Plant Cell Tissue and Organ Cult.* 51: 17-25.

21. Novak, F.J., Afza, R., Van Duren, M., Parea-Dallos, M., Conger, B.V and Xialang, T. (1989). Somatic embryogenesis and plant regeneration in suspension cultures of dessert (AA and AAA) and cooking (AAB) bananas (Musa spp). *Bio/Technology,* 7:154-159.
22. Panis, B., Wauwe, A.V and Swennen, R. (1993). Plant regeneration through direct somatic embryogenesis from protoplast of banana (Musa spp). *Plant cell Rep.* 12: 403-407.
23. Smith, M.K., Hamill, S.D., Becker, D.K., Dale, J.L. 2005. *Musa* spp. Banana and Plantain. In: Litz, R.E. (ed.), Biotechnology of Fruit and Nut crops. CABI Publ., Cambridge, USA. Pp 366-391.
24. Stover, R.H and Simmonds, N.W. (1987). Bananas. Longman Scientific and Technical London.
25. Sundararaju, P., Status paper on banana in India. In Bananas and Food Security (eds Picq, C., Fouré, E. and Frison, E. A.), International Symposium, Douala (CMR), 10–14 November 1998, INIBAP, Montpellier, France, 1999, pp. 209–225.
26. Suprasanna P, Panis B, Sági L, Swennen R (2002) Establishment of embryogenic cell suspension cultures from Indian banana cultivars. 3rd and Final Research Coordination Meeting of the FAO/IAEA on Cellular biology of banana. KUL, Leuven, Belgium. Pp.

About the Authors

Miss Meenakshi Sidha is a research fellow doing her Ph.D in Pomology from Marathwada Agriculture University (MAU), Parbhani. This is a collaborative research programme on bannana between MAU and BARC. She obtained her M.Sc degree in Horticulture with specialization in Pomology from MAU, Parbhani. She was a University topper and second in state (among all the four agriculture universities in the state) during her graduation and University topper during post graduation. Her main area of research is in the field of plant biotechnology.

Dr Penna Suprasanna joined BARC in 1991 after obtaining his Ph.D. degree in Genetics from Osmania University, Hyderabad. He is working in the Plant Cell Culture Technology Section of NA&BTD and is engaged in plant biotechnological research on rice, banana and sugarcane. His contributions have been in the areas of cell and tissue culture, somatic embryogenesis, *in vitro* selection and transgenics. Dr. Suprasanna has to his credit, more than 100 research publications in journals and books published by national and international publishers. His interests are in using plant cell cultures for cellular and molecular genetic manipulation.

Dr Vishwas A. Bapat is working in the area of plant tissue culture for the last 31 years. Currently he is heading the Plant Cell Culture Technology Section. The main thrust area of his work is on Micropropagation and Genetic Transformation of Plants. He has extensively contributed in the areas of clonal propagation, cell and protoplast culture, synthetic seeds, disease resistance and molecular farming. He has several publications in national and international journals to his credit. He is a Fellow of the National Academy of Sciences, India and the Maharashtra Academy of Sciences.

Dr Umakant G. Kulkarni did his Ph. D in Genetics & Plant Breeding from University of Agricultural Sciences, Dharwad. He is responsible for the release of groundnut cultivars LGN-1 & LGN-2. He has served as the Head of Agricultural Botany and Biotechnology Department at Marathwada Agricultural University, Parbhani and Officer In-Charge, Tissue Culture Project. Presently he is the Associate Dean and Principal, College of Agriculture, Osmanabad, MAU, Parbhani.

Dr B.N. Shinde did his Ph.D in Horticulture from Marathwada Agricultural University (MAU), Parbhani. Presently he is working as a Senior Research Officer in Pomology in Horticulture Research Scheme at MAU: Parbhani Dr. Shinde has 40 research papers, 35 articles in Marathi and two books to his credit.

बीएआरसी न्यूज़लैटर
BARC NEWSLETTER

PREPARATION AND CHARACTERIZATION OF $BaO-ZnO-SiO_2$ GLASS-CERAMICS FOR POSSIBLE USE IN SOFC

M. Goswami, A. Sarkar and G.P. Kothiyal
Technical Physics and Prototype Engineering Division
Bhabha Atomic Research Centre

The paper was given the Best Poster Presentation award at the National Symposium on Science & Technology of Glass and Glass-Ceramics (NSGC-06) held during September 15-16, 2006 at BARC, Mumbai

Abstract

Development of suitable sealant materials is one of the major requirements for implementation of planar solid oxide fuel cells. Among several approaches, rigid glass or glass-ceramic seals have been found to be useful. Glasses having composition $51.0BaO-9.0ZnO-(40-y)SiO_2-yNd_2O_3$ (y = 1, 2 wt. %) were prepared by melt-quench technique and converted to glass-ceramics by controlled crystallization. Thermal Expansion Coefficient (TEC) and electrical insulating properties for glass with y = 1 wt. % were found closer to the required values for a suitable sealant. However, flow properties are to be modified in view of making a seal, which is a major task.

Introduction

One of the major challenges for implementation of planar Solid Oxide Fuel Cells (SOFCs), is the development of suitable sealant materials, to separate the air and fuel. Several approaches have been used to achieve the necessary adherence, mechanical integrity and stability, including both rigid seals (no applied load during operation) and compressive seals (load applied to seal during operation) [1, 2]. The most common approach is to use rigid glass [3] or glass–ceramic seals [4, 5], the properties of which can be tailored specifically, for use in SOFCs, through variation of the glass composition [6, 7]. The key requirements for sealing materials include thermo-mechanical and chemical stability along with Thermal Expansion Coefficients (TECs) similar to those of other cell components, $(9 – 13) \times 10^{-6} /^0C$ [1, 5, 7]. The seal should also behave as an electrical insulator, with total conductivity (σ′) lower than 10^{-4} S/cm, in order to avoid parasitic currents decreasing the system efficiency. Here, we report the preparation of BaO-ZnO-SiO_2 based glass and glass-ceramics samples and some initial studies on their thermo-mechanical and electrical properties, with a view to develop materials for high temperature sealants. The most important point is that, all these properties should hold good at high operating temperature (800 – 900 °C). This is possibly the first attempt on the national scene, to initiate glass-ceramic sealant work for SOFC.

Experimental

The glass samples having composition $51.0BaO\text{-}9.0ZnO\text{-}(40\text{-}y)SiO_2\text{-}yNd_2O_3$ with y = 1,2 wt % were prepared by melt-quench technique. Analytical grade compounds of ZnO, $BaCO_3$, SiO_2 and Nd_2O_3 were used as starting materials, for the preparation of base glass. Starting charge for making glass was prepared, by double calcination. Calcination was carried out at maximum 950°C for 24 h after thorough mixing and grinding. The melting of doubled calcined material was carried out in a covered Pt-10% Rh crucible at a temperature of 1550°C for 1 to 2 h duration for proper mixing and then poured in to a pre-heated graphite mould. The annealing was carried out at 725°C for 4 h in inert atmosphere and then cooled down to room temperature at a rate of 20°C/h.

To convert these glass samples into glass-ceramics, crystallization temperature was measured using a TG-DTA system (Model: DTA-92-15, M/s. SETARAM, France). Measurements were done in the temperature range of 30–1000 °C employing a heating rate of 10 °C/min. Based on the results of DTA, conversion of glass into glass–ceramics was carried out, at 1050 °C in a programmable resistance furnace, using a controlled heating schedule. Initially for nucleation, the temperature of the sample was kept at around 750°C for 2 h and raised to 1050 °C to facilitate the crystallization.

Both the glass and glass-ceramics samples were characterized for their density, thermal expansion coefficient and microhardness measurements. Density (ρ) was measured at room temperature by Archimedes principle using water as an immersion liquid with an accuracy of ± 0.03 g/cm^3. Thermal expansion coefficients, glass-transition temperature (T_g) and glass softening temperature (T_{ds}) were measured using a Dilatometer (Model: TMA - 92, M/s. SETARAM, France) in the temperature range of 30-800°C, using a silica probe. The samples about 3 mm thick, with both ends flat, were kept in quartz sample holder with a constant load of 5gm for all measurements. Before starting the experiment, the chamber was evacuated up to 10^{-2} mbar pressure and then the chamber was flushed with high purity Argon gas. All the measurements were carried out in flowing Argon atmosphere with a constant flow rate of 40-50 l/h. The temperature was raised up to maximum 1000°C at a rate of 10 °C/min. Thermal expansion coefficient being reported, is the average in the temperature range of 30-500 °C.

Micro hardness measurements were carried out, under a constant load of 100g for 5 s duration using Vicker's microhardness tester (Model: VMHT-30M). Before measurements, the samples were polished with 0.3mm alumina powder to get good reflective surface. From the measurements of the diagonals of Vickers impressions on the sample surface, microhardness was found out by using standard formula. An average of at least 10 indentations was taken as the value of microhardness.

Identification of various crystalline phases in glass–ceramics samples was carried out, using powder X-ray diffractometer (Philips, model PW 1710) with CuKα as X-ray radiation source. The crystalline phases were identified by matching the peak positions of the intense peaks with PCPDF standard cards.

The electrical measurements were carried out, in the frequency range of 10Hz to 10MHz and over the temperature range of 323- 673K using an impedance analyzer (Alpha-A high performance frequency analyzer, M/s. Novocontrol technologies, Germany). Electrical connections were provided on both sides of the glass sample using conducting gold coating.

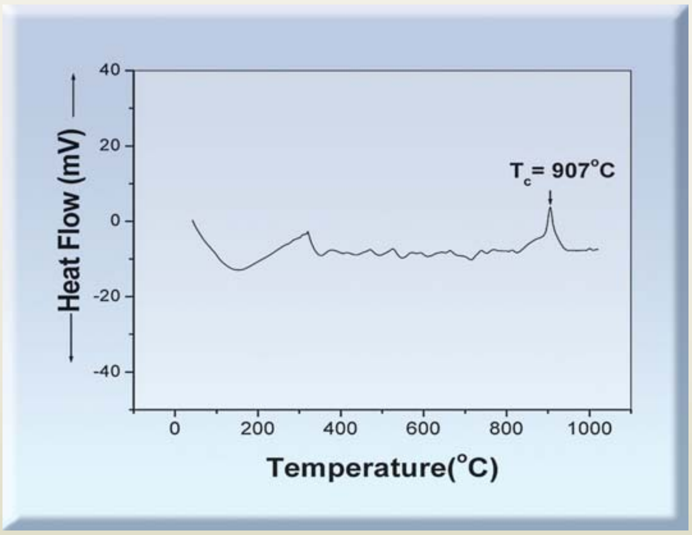

Fig. 1: DTA Plot for 51.0BaO-9.0ZnO-39.0SiO_2-1.0Nd_2O_3 glass

Results and discussion

Clear bubble-free transparent glasses were prepared for all compositions. For glass having composition 51.0BaO-9.0ZnO-39.0SiO_2-1.0Nd_2O_3, DTA plot is shown in Fig. 1. It is found that crystallization temperature is 907 ^{0}C for this glass. Nominal composition, density, T_g, T_{ds}, TEC and MH of glasses and glass-ceramics are given in Table1. The density values for the glass and glass ceramics samples are found to be 3.91 and 3.86 gm/cc, respectively for 51.0BaO-9.0ZnO-39.0SiO_2-1.0Nd_2O_3 (y = 1 wt %) composition. Thermal expansion increases from 10.39 to 15.06 x 10^{-6}/ ^{0}C, after conversion of base glass to glass-ceramics. The glass transition and dilatometric oftening temperature obtained from the dilatometer measurements are 693 ^{0}C and 720 ^{0}C, respectively. For the glass-ceramics, softening point was not observed up to 1000 ^{0}C. The microhardness was found to increase from 4.25 to 4.70 GPa after conversion into glass-ceramics.

Table 1: Nominal composition, density, T_g, T_{ds}, TEC and MH of glasses and glass-ceramics

	y	T_g ^{0}C	T_{ds} ^{0}C	α (TEC) (30-500)^{0}C	MH GPa	Density gm/cc
BZS-1 Glass	1	693	720	103.6 x 10^{-7}	4.25	3.91
BZS-1 Glass-Ceramic	1	---	---	150.1 x 10^{-7}	4.70	3.86
BZS-2 Glass	2	--	729	107.8 x 10^{-7}	3.23	3.84
BZS-2 Glass-Ceramic	2	---	--	150 x 10^{-7}	4.53	4.03

XRD plot for the glass-ceramic having composition $51.0BaO-9.0ZnO-39.0SiO_2-1.0Nd_2O_3$ is shown in Fig. 2. It is found that major crystalline phase is Barium orthosilicate ($BaSi_2O_5$). Thermal expansion of this phase is 140 x 10^{-7}/ ^{0}C, therefore, this phase is responsible for observed high thermal expansion coefficient.

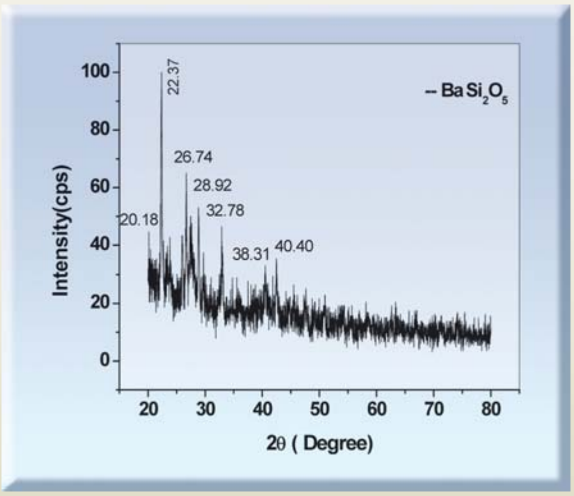

Fig. 2 : XRD pattern for $51.0BaO-9.0ZnO-39.0SiO_2-1.0Nd_2O_3$ glass-ceramic

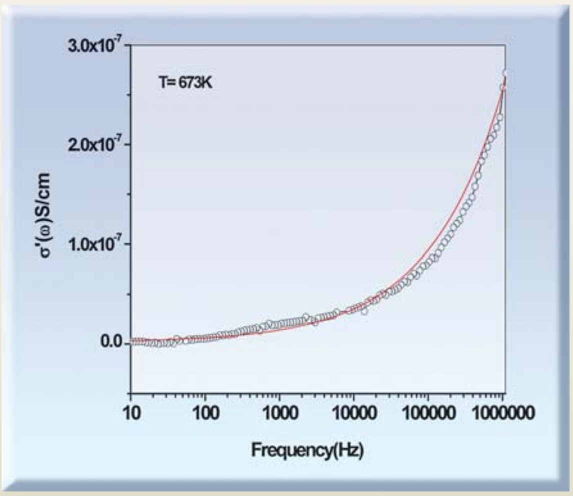

Fig. 3 : Variation of σ'(w) with frequency for BZS glass sample at 673K.

The dc conductivity (σ_{dc}) was extracted from Jonscher Universal Power (JUP) law fit as shown in Fig. 3. The σ_{dc} was found to increase from 2.6E-10 to 2.9E-9 S/cm with increase in temperature upto 673K. The higher resistivity value even at higher temperature, with the thermal expansion value 10.39 x10^{-6}/ ^{0}C (30-500 ^{0}C) for the glass sample, is an advantage in using this material as a possible sealant in SOFC.

Conclusion

Glass and glass-ceramic having composition $51.0BaO-9.0ZnO-39.0SiO_2-1.0Nd_2O_3$ were prepared which showed good insulating properties even at high temperature (673K). Thermal expansion coefficient was found to be matching with the other components of the SOFC cell. These glass ceramics also show high glass transition and softening temperature as required for SOFC sealants. However, the glass did not show good flow properties so further work is needed to improve the flow properties by changing the composition of glass and processing.

Along with this, studies will also be carried out to check the suitability of sealant material with interconnect, electrode and electrolyte materials, chemical and thermal stability at high operating temperature and harsh fuel cell environment.

Acknowledgement

The authors wish to thank Dr J V Yakhmi for support and encouragement. They would also like to thank Ms. Babita Tiwari for doing TMA analysis of glass and glass-ceramic, Dr Sundaraman for XRD and Dr R Mishra for DTA measurements.

References

1. J. W. Fergus, J. Power Sources. 147 (2005) 46.
2. Shiru Le, K Sun, N Zhang, M An, D Zhou, J Zhang, D Li, J. *Power Sources.* 161 (2006) 901.
3. Sung-Bum Sohn, Se-Young Choi, Gyeung-Ho Kim, Hue-Sup Song, Goo-Dae Kim, J. *Non-Cryst. Solids.* 297 (2002) 103.
4. C. Lara, M.J. Pascual, A. Duran, J. *Non-Cryst. Solids.* 348 (2004) 149.
5. K L Ley, M Krumpelt, R Kumar, J H Meiser, I Bloom, *J. Mater. Res.* 11(6) (1996) 1489.
6. R. Barfod, S. Koch, Y.-L. Liu, P.H. Larsen, P.V. Hendriksen, *Proc. Electrochem. Soc.* 2003–07 (SOFC VIII) (2003) 1158.
7. C. Lara, M.J. Pascual, A. Duran, *Bol. Soc. Esp. Ceram. Vidr.* 42(2) (2003) 133.

About the Authors

Dr Madhumita Goswami joined Technical Physics & Prototype Engineering Division in 1997 through BARC Training School (40th Batch of Chemistry Discipline). She has obtained her Ph.D. degree in Chemistry from Mumbai University in 2006. The topic of research was Physico-chemical characteristics and structural aspects of oxide glass-ceramics. She has done her Postdoctoral work at the University of Science and Technology of Lille, France, on P_2O_5 based high temperature sealants for SOFC. Her field of interest is glass and glass-ceramics for various applications.

Mr. A. Sarkar has obtained diploma in Mechanical Engineering from West Bengal Board of Technical Education and joined Technical Physics & Prototype Engineering Division / BARC in 1999. He later completed his B. E. (Mechanical) from Mumbai University in 2006. During this period he has been working on the machinable glass-ceramics (MAS) and high temperature sealing materials.

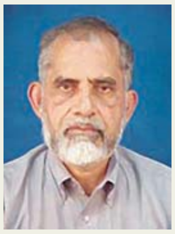

Dr G. P. Kothiyal joined Bhabha Atomic Research Centre in 1970 as a Scientific Officer after completion of Post Graduate Training in Physics from 13th batch of BARC Training School. Currently serving as Head, Glass and Ceramics Technology Section of TPPED, BARC, he is spearheading the programme on special glasses and glass-ceramics and produced them with designed/tailored properties for applications in high voltage and Ultra High Vacuum (UHV) related devices/systems. Such materials/devices have also been delivered for use in nuclear, laser, defence and space applications as level sensors, multi-pin feedthroughs, spacers/isolators, sealant/electronic microcircuit packing, etc. He is a PhD guide in Physics at University of Mumbai and Homi Bhabha National Institute (HBNI) Mumbai. He is a referee for various journals like Pramana, J Non Crystalline Solids, J. Material Science, Materials Science and Engineering, Materials Science Forum, Bulletin of Materials Science, J Thermal Analysis and Calorimetry, etc. He has published more than 180 papers in International/National journals/proceedings and delivered a number of invited talks/lectures. He is a recipient of Materials Research Society of India (MRSI) Medal (Lecture award) for the year 2003.

PREPARATION AND CHARACTERIZATION OF PHOSPHATE GLASSES CONTAINING TITANIUM

Babita Tiwari, Anupam Dixit and G. P. Kothiyal
Technical Physics and Prototype Engineering Division,
Bhabha Atomic Research Centre

and

M. Pandey and S. K. Deb
High Pressure Physics Division,
Bhabha Atomic Research Centre

The paper was awarded the Best Poster Presentation award at the National Symposium on Science & Technology of Glass and Glass-Ceramics (NSGC-06) held during September 15-16, 2006 at BARC, Mumbai

Abstract

Clear bubble-free phosphate glasses, having composition $40Na_2O$-$10Al_2O_3$-$xTiO_2$-$(50-x)P_2O_5$, (x = 0-20 mol %), were prepared by conventional melt quench method. Density, molar volume, glass transition temperature (Tg), MicroHardness (MH), and Thermal Expansion Coefficient (TEC) were measured as a function of TiO_2 content. Structural investigation was done using Raman and FTIR spectroscopy. Substitution of TiO_2 for P_2O_5 up to 10 mol %, in the ternary $40Na_2O$-$10Al_2O_3$-$50P_2O_5$ glass increases the density, Tg and MH. Above the 10 mol % TiO_2 content, all these properties show a reverse trend. Spectroscopic investigations reveal the depolymerization of the phosphate glass network by systematic conversion of Q^2 structural units into Q^1 and finally into Q^0 structural units. Even though Q^2 to Q^1 conversion is taking place due to breaking of P-O-P linkages, formation of P-O-Ti and P-O-Al linkages provide cross linking between short P-structural units, which make the glass network more rigid. Above 10 mol % TiO_2 content, network is highly depolymerized due to the formation of Q^0 structural units, resulting in poor cross-linking, making the glass network less rigid.

Introduction

Phosphate glasses are finding ever-increasing applications in many emerging technologies e.g. vitrification of radioactive waste [1], photonics [2], fast ion conductors [3], glass-to-metal seals [4] and biomedical engineering etc. [5]. These glasses possess a series of interesting properties such as low glass transition temperature (T_g), lower melting temperature (compared to silicate glass), high thermal expansion coefficient and biocompatibility [6]. In recent years, there has been lot of research on improving the physical properties and the chemical durability of alkali phosphate glasses by adding different metal oxides of high valence cations like Al^{3+}, Ti^{4+}, Bi^{3+}, etc., because of the formation of relatively stable M^{3+}-O-P bond [7]. These ions modify thermo-mechanical, physical and structural properties, basically due to change in glass structural network, through formation of cross-linked bonds.

Sodium aluminophosphate (NAP) glasses have been the subject of various investigations [8,9], and it has been found that addition of Al_2O_3 up to 10 mol % to sodium phosphate glasses, convert P-O-Na and some P-O-P linkages to P-O-Al linkages. This results in improved thermal and chemical durability with modification of thermophysical properties like TEC, Tg etc. Similarly, TiO_2 incorporation in the glass not only improves the chemical durability of the phosphate glasses but also increases the nonlinear refractive index (n_2 values) of the glass, thereby making them promising candidates for nonlinear optical applications [10, 11]. Structural studies of TiO_2 containing phosphate glasses, based on a variety of spectroscopic techniques like MAS-NMR [12], EXAFS, XANES [13], Raman [11] and FTIR [14] established that, TiO_2 modifies the P-O-P linkages and exists as both TiO_6 and TiO_5 distorted polyhedra. Optical absorption and electron spin resonance studies on some of the TiO_2 containing phosphate glasses also revealed that, paramagnetic Ti^{3+} ions may also exist in the glass with distorted octahedron environments [15]. The relative concentration of both 'P' and 'Ti' structural units present in the glass is a strong function of the composition of different constituents forming the glass. Hence, understanding the details of the different structural units present in the glass, is necessary to explain the variation in the thermophysical properties of these glasses, as a function of composition. Keeping this in mind, we have prepared a number of sodium aluminophasphate glasses, containing different amounts of TiO_2 and investigated their structural aspects using Raman and FTIR spectroscopy. Thermophysical properties like density, molar volume, thermal expansion coefficient, glass transition temperature, microhardness were also determined and their variation as a function of composition has been correlated with different structural units present in the glass. Such studies are essential for selecting a suitable titanium phosphate glass composition for different applications. To the best of the authors' knowledge no such studies have been reported for this type of glasses.

Experimental

Transparent bubble-free phosphate glasses having composition $40Na_2O$-$10Al_2O_3$-$xTiO_2$-$(50-x)P_2O_5$, where x = 0-20 mol % were prepared by conventional melt quench method. Analytical grade $NaNO_3$, Al_2O_3, TiO_2 and $NH_4H_2PO_4$, were used as starting materials in such proportions that the O/P ratio changed from 3.2 to 4.33. The initial charge (≈ 90 g) was thoroughly mixed and ground for 20-30 min in a mortar pestle and then calcined in an alumina crucible for 15-20 h by heating in a predetermined manner considering the decomposition temperatures of individual compounds. This charge was reground and recalcined in the same manner. The calcined charge was then melted in a platinum-rhodium crucible using lowering and raising hearth furnace (Model OKAY 70R 10, M/s Bysakh and Co., Kolkata) and held at temperatures ranging from 1250-1350 °C, depending on the composition, for 1 h for thorough mixing in air ambient. When the melt was thoroughly homogenized and attained the desirable viscosity, it was poured into pre-heated graphite moulds. The glass was then annealed at appropriate temperature (in the range 400 - 460 °C) for 4 h and cooled to room temperature at the rate of 20°C/ h and stored in a desiccator prior to evaluation.

Amorphous nature of prepared glasses was confirmed by powder X-ray diffraction. Density (r) was measured at room temperature by Archimedes principle using toluene as an immersion liquid with an accuracy of ± 0.03 g/cm^3. Thermal expansion coefficient, glass-transition temperature and glass softening temperature were measured on a dilatometer (Model 92-12 TMA, M/s. SETARAM, France) using a silica probe. The samples about 3 mm thick with both ends flat were kept in quartz sample holder with a constant load of 5gm for all measurements. Before starting the experiment the chamber was evacuated up to 10^{-2} mbar pressure and then the chamber was flushed with high purity Argon gas. All the measurements were carried out in flowing Argon atmosphere with a constant flow rate of 40-50 l/h. The temperature was raised up to maximum 550^{0}C at a rate of 10 ^{0}C/min. Thermal expansion coefficient being reported is the average in the temperature range of 30-300^{0}C. Micro-hardness of glass samples was measured by Vickers indentation technique using micro hardness tester (Leica model VMHT30M). Before measuring, the samples were polished with 0.3mm alumina powder to get good reflective surface. Indentation was obtained by applying a 50g load for 5 seconds. From the measurements of the diagonals of Vickers impressions on the sample surface, microhardness was found out by using the standard formula. An average of at least 10 indentations was taken as the value of microhardness.

Raman spectra were recorded using CCD based spectrometer (1.5 cm^{-1} resolution) in the frequency range 200-2000 cm^{-1}. All measurements were done on solid polished glass disk, using 532 nm excitation line from SHG of Nd -YAG laser. Infrared spectra of all glasses at room temperature were recorded over the frequency range 400 - 4000 cm^{-1} using Bomem MB102 FTIR spectrometer with 4 cm^{-1} resolution. For recording FTIR spectra, samples were prepared in pellet form, by mixing the glass powder (3 wt %) in KBr.

Result and discussion

Bubble-free, clear and transparent glasses were obtained for the compositional series of $40Na_2O$-$10Al_2O_3$-$xTiO_2$-(50-x) P_2O_5, with x = 0-20 mol% TiO_2. Fig. 1 shows the variation of density and molar volume with respect to composition. The density of these glasses first increases and then decreases with the content of TiO_2 while corresponding molar volume first decreases and then increases. The density of these glasses should decrease due to replacement of high molecular weight P_2O_5 by low molecular weight TiO_2. But it is found that the density of these glasses increases with addition of TiO_2 and correspondingly molar volume decreases, indicating that the titanium polyhedra form some new interconnections within the structural network and thus stabilize the glass structure.

Fig.2 shows the dependence of TEC, Tg and microhardness with TiO_2 concentration in the glass. With the addition of TiO_2, glasses showed increase in T and microhardness, whereas decrease in the TEC up to 10 mole %, reflects the stronger bonding in the glass network, up to this composition.

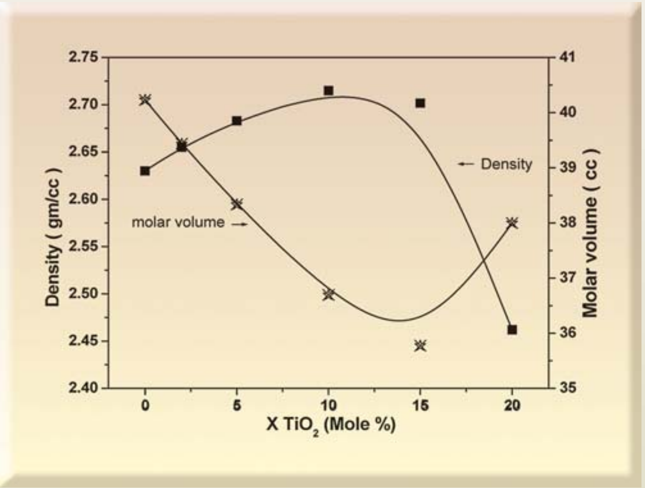

Fig.1: Variation of density and molar volume of $40Na_2O$-$10Al_2O_3$-$xTiO_2$-(50-x)P_2O_5 glasses

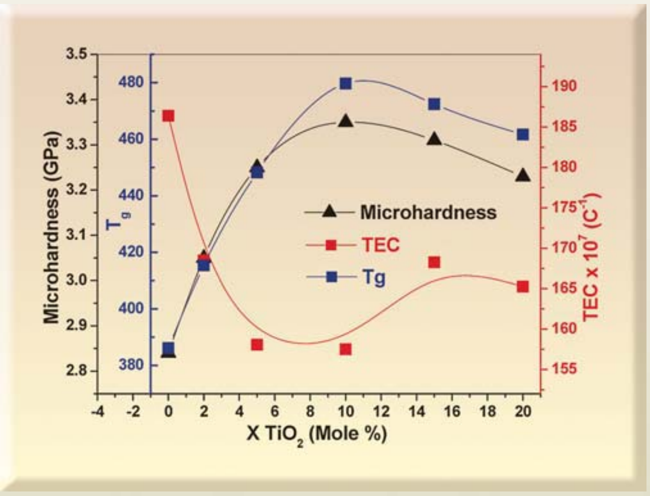

Fig. 2: Variation of microhardness, TEC and glass transition temperature with composition of $40Na_2O$-$10Al_2O_3$-TiO_2- (50-x) P_2O_5 glasses

Further addition of TiO_2 (x >10 mol %) in the glass, results in a reverse trend in these values, this indicates the weakening of glass network. Thus all these changes in the properties with varying concentrations of TiO_2 indicate, that TiO_2 stabilizes the glass network up to 10 mol % and beyond that makes some what less rigid. The changes in the type and number of the phosphate structural units are strongly reflected in Raman spectra, especially in their high frequency region. Fig. 3 shows the Raman spectra of $40Na_2O$-$10Al_2O_3$-$xTiO_2$-(50-x) P_2O_5, ($0 \leq x \leq 20$ mol %) glasses in the frequency region between 200 and 1400 cm^{-1}. Observed Raman spectra of TiO_2 free (x = 0) glass matches well with the available literature [10, 16]. The most intense band around 1170 cm^{-1} and the less intense band around 1280 cm^{-1} in this spectrum, has been attributed to the symmetric and asymmetric stretching vibrations of PO_2 groups (Q^2 structural units) respectively. Another band at 700 cm^{-1} is assigned to the symmetric stretching of P-O-P linkages in Q^2 and Q^1 structural unit. With the addition of TiO_2 in the glass, intensity of the bands around 1280, 1170 and 700 cm^{-1} decreased and new bands around 1210, 1090, 900, 750, 625 cm^{-1} evolved. Among these new bands, bands around 1210 and 1090 cm^{-1} are assigned to asymmetric and symmetric stretching vibrations of PO_3 groups (Q^1 structural units) respectively. As the TiO_2 content in the glass increases up to 10 mol %, position of these bands shifts slightly towards lower wave number. The bands at 900 and 750 cm^{-1} are attributed to asymmetric and symmetric stretching vibrations of P-O-P linkages respectively in Q^1 structural unit. Appearance of band around 750 cm^{-1} reflects the presence of pyrophosphate (Q^1) structural units and increase in the intensity of this band at the expense of band at 700 cm^{-1}, with increase in TiO_2 content reflects the conversion of Q^2 structural units in to Q^1 structural units. Increase in the

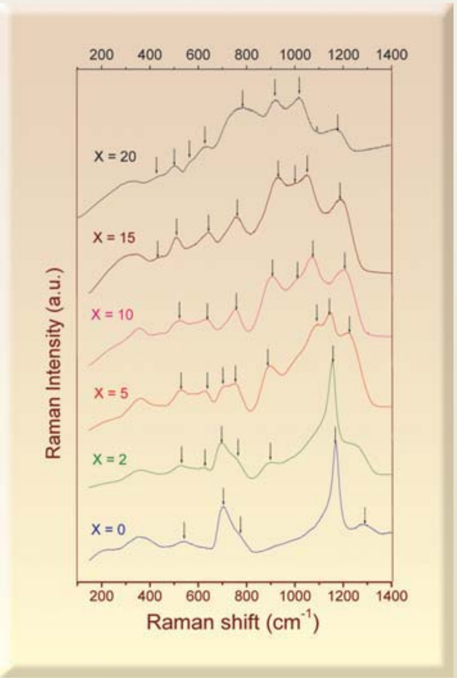

Fig. 3 : Raman spectra of $40Na_2O$-$10Al_2O_3$-$xTiO_2$-(50-x) P_2O_5 glasses

intensity of the band at 900 cm^{-1} and a shift of position slightly towards higher wave number with increasing TiO$_2$ content, reflects the depolymerization of longer chains in to shorter chains and Q^1 structural units. Glass sample with 10 mol % TiO$_2$ content shows only one band around 750 cm^{-1} and no band at 1170 cm^{-1} (of PO$_2$ groups), which confirms the presence of only Q^1 structural units (pyrophosphate).

The coordination of Ti^{4+} ions by oxygen atoms is also reflected in Raman spectra. Based on the previous Raman studies on TiO$_2$ containing glasses [10, 11], band around 625 cm^{-1} has been attributed to the vibration of octahedral titanate units TiO$_6$, because its relative intensity increases with increasing TiO$_2$. Raman spectra of glass samples having 15 and 20 mol % TiO$_2$ show a new band at 930 cm^{-1}, which can be due to much shorter Ti-O bond than for octrahedral titanium and attributed to the titanyl bonds (Ti=O or –Ti-O-Ti-) associated with a 5 coordinated Ti [11]. Raman spectrum of glass containing 20 mol % TiO$_2$, shows a different pattern from the remaining glasses. For this glass band, around 1010 cm^{-1} is attributed to stretching vibrations of orthophosphate (Q^{0}structural units).

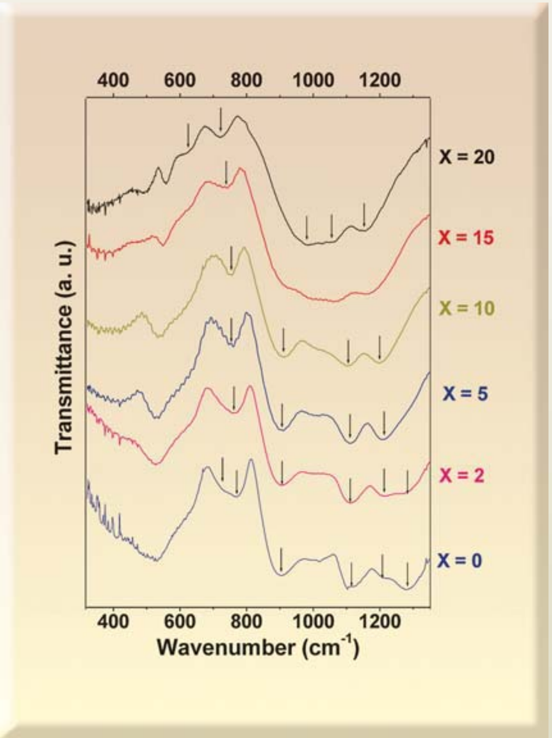

Fig. 4 : Infrared spectra of 40Na$_2$O-10Al$_2$O$_3$-xTiO$_2$-(50-x) P$_2$O$_5$ glasses

Fig. 4 shows the FTIR spectra of glass series as a function of TiO$_2$ concentration. For the glass sample without TiO$_2$ (x = 0 mole %), five absorption bands approximately at 1280, 1210, 1120, 900, 750 cm^{-1} can be clearly seen. Based on the previous infrared studies on sodium aluminophosphate glasses [14], the band at 1280 cm^{-1} has been attributed to the asymmetric stretching vibration of PO$_2$ groups (characteristic of Q^2 structural units). The absorptions bands around 1210 and 1120 cm^{-1} are assigned to asymmetric and symmetric stretching of PO$_3$ groups (characteristic of Q^1 structural units) respectively. The band at 900 cm^{-1} is assigned to asymmetric stretching of P-O-P bridges. This absorption band indicates that the phosphate network is built from short chains and pyrophosphate groups (P$_2$O$_7^{-4}$) because it is intermediate between the value observed in NaPO$_3$ chains (865 cm^{-1}) and in sodium pyrophosphate (920 cm^{-1}) or sodium aluminium pyrophosphate (940 cm^{-1}). The bands at 700 and 750 cm^{-1} are due to the symmetric stretching of P-O-P bridges. The band at 525 cm^{-1} is due to bending vibrations of P-O bonds. With increase in titanium content in the glass up to 10 mol %, patterns of FTIR spectra remain the same except the bands around 1210 and 1280 cm^{-1}. The intensity of 1280 band keeps on diminishing and it finally disappears at x = 10 mol %, while band around 1210 cm^{-1} becomes pronounced. It indicates that as TiO$_2$ concentration (O/P ratio) increases, phosphate network depolymerizes and Q^2 structural units are replaced by Q^1 structural units. Moreover, the frequency of the P-O-P asymmetric vibration shifts towards higher wave number, which is characteristic of the transition from longer chains to pyrophosphate groups. Above 10 mol % TiO_2 incorporation, the IR patterns for glasses containing 15 and 20 mol % TiO_2 change significantly and show the disappearance of band at 900 cm^{-1} (n_{as} P-O-P) and development of bands around approximate 1000, 1070 and 1170 cm^{-1} characteristics of the isolated 'P' tetrahedra $(PO_4)^3$ (Q^0 structural units) connected to different cations. These changes suggest that a highly depolymerized phosphate network is taking place with isolated orthophosphate (Q^0 structural units).

Conclusions

Clear, transparent and bubble-free NATP glasses were prepared for all compositions. Structural investigation by Raman and FTIR spectroscopy revealed that substitution of P_2O_5 with TiO_2 up to 10 mol % depolymerize the phosphate glass network by systematic conversion of Q^2 structural units in to Q^1 structural units. Even though Q^2 to Q^1 conversion is taking place due to breaking of P-O-P linkages the formation of P-O-Ti and P-O-Al linkages provide cross linking between shorten 'P' structural units which makes the glass network more rigid. Therefore the net effect is an increase in Tg, density and MH and a decrease in molar volume and TEC, up to 10 mol % TiO_2. For further addition of TiO_2 above 10 mol %, Q^1 structural units gets converted in to Q^0 structural units and glass network becomes highly depolymerized, therefore cross linking is not sufficient to give strength to glass network. This results in decrease in density, Tg and MH and an increase in molar volume and TEC for the glasses containing more than 10 mol % TiO_2.

Acknowledgement

The authors wish to thank Dr J V Yakhmi for support and encouragement and Dr V Sudarsan for help in FTIR measurements.

References

1. P. Bergo, S. T. Reis, W. M. Pontuschka, J. M. Prison, C. C. Motta, *J. Non-Cryst. Solids,* 336 (2004) 159.
2. F. F. Sene, J. R. Martinelli, L Gomes, *J. Non-Cryst. Solids.* 348 (2004) 63.
3. Sundeep Kumar, Philippe Vinatier, Alain Levasseur, K. J. Rao, *J. Solid State chem.,* 177 (2004) 1723.
4. J. Y. Wei, Y. Hu and L. G. Hwa, *J. Non-Cryst. Solids.,* 288 (2001) 140.
5. A. G. Dias, J. M. S. Skakle, I. R. Gibson, M.A. Lopes, J. D. Santos, *J. Non-Cryst. Solids.,* 351 (2005) 810.
6. R. K Brow, *J. Non-Cryst. Solids.,* 263 & 264 (2000) 1.
7. T. Minami and J. D. Mackenzie, *J. Am. Ceram. Soc.,* 60 (1977) 232.
8. R. K. Brow, *J. Am. Ceram. Soc.*, 76 (4) (1993) 913.
9. R. K. Brow,R. J. Kirkpatrick, G. L. Turner, *J. Am. Ceram. Soc.,* 76 (4) (1993) 919.
10. R. K. Brow, D. R. Tallant, W. L. Warren, A. McIntyre, D. E. Day, *Phys. Chem. Glasses.,* 38 (6) (1997) 300.
11. S Krimi,.A El Jazouli,L Rabardel, M. Couzi, I Mansouri, G Le Flem, *J. Solid State Chem.,* 102 (1993) 400.
12. L Montagne, G Palavit, A. Shaim, M Et-tabirou,P Hartmann, C Jager, *J. Non-Cryst. Solids.,* 293-295 (2001) 719.
13. E Fargin, C Duchesne, R Olazcuaga, G Le Flem, C Cartier, L Canioni et al, *J. Non-Cryst. Solids.,* 168 (1994) 132.
14. A. Shaim, M Et-tabirou, *Mat. Chem. Phys.,* 80 (2003) 63.
15. S. Kaoua, S Krimi,.A El Jazouli, E. K Hlil, D. De Waal, *J. Alloys Compd.,* (2006) in press.
16. JIN yifen, J Dehua, C Xiangsheng, B Behya and H Xihuai, *J. Non-Cryst. Solids.,* 80 (1986) 147.

About the Authors

Ms. Babita Tiwari obtained her Master's Degree in Physics from Rajasthan University, Jaipur. She graduated from BARC training school in 2000 (43rd OCES Batch, Physics discipline, and joined Technical Physics & Prototype Engineering Division, BARC. Since then she is doing research and development work on single crystal growth and characterization. Currently she is working on phosphate based glass and glass-ceramics and high temperature sealing materials for SOFC.

Mr. Anupam Dixit graduated in science from Rajasthan University. He joined Technical Physics & Prototype Engineering Division in 2005. He is involved in the preparation of different glasses and glass-ceramics.

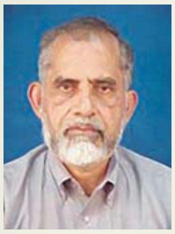

Dr G. P. Kothiyal joined Bhabha Atomic Research Centre in 1970 as a Scientific Officer after completion of Post Graduate Training in Physics from 13th batch of BARC Training School. Currently serving as Head, Glass and Ceramics Technology Section of TPPED, BARC, he is spearheading the programme on special glasses and glass-ceramics and produced them with designed/tailored properties for applications in high voltage and Ultra High Vacuum (UHV) related devices/systems. Such materials/devices have also been delivered for use in nuclear, laser, defence and space applications as level sensors, multi-pin feedthroughs, spacers/isolators, sealant/electronic microcircuit packing, etc. He is a PhD guide for Physics at the University of Mumbai and at the Homi Bhabha National Institute (HBNI) Mumbai. He is a referee for various journals like Pramana, J Non Crystalline Solids, J. Material Science, Materials Science and Engineering, Materials Science Forum, Bulletin of Materials Science, J Thermal Analysis and Calorimetry, etc. He has published more than 180 papers in National/ International journals / proceedings and delivered a number of invited talks / lectures. He is a recipient of Materials Research Society of India (MRSI) Medal Lecture award for the year 2003.

Dr Mukesh Pandey obtained his M.Sc. degree in Physics from Indian Institute of Technology, Delhi. He joined BARC through 37th batch (1993) of training school. He obtained PhD (Physics) from University of Mumbai in 2003 in diamond and diamond-like carbon films prepared using chemical vapour deposition methods. His current research interests include studies of phosphate glasses, spintronic materials and Si-Ge strained layers.

Dr Sudip Kumar Deb joined BARC through the 20th batch of Training School in Physics discipline. His primary research interest is Raman spectroscopy from condensed matter, in particular its application in investigation of structural phase transition in solids. He has worked as Post Doctoral fellow in Hawaii Institute of Geophysics, University of Hawaii and Center for Solid State Science, Arizona State University. His current field of interest includes Synchrotron Radiation utilization for investigation of material properties and he has worked in several synchrotron source centres in the world. Currently he heads the High Pressure Raman Scattering Section in the High Pressure Physics Division.

बीएआरसी न्यूज़लैटर
BARC NEWSLETTER

CONVENTIONAL RADIOGRAPHY : A FEW CHALLENGING APPLICATIONS

S.P. Srivastava, T.G. Unni, S.P. Pandarkar,
K. Mahajan, R.L. Suthar
Centre for Design and Manufacture
Bhabha Atomic Research Centre

This paper was adjudged as the Best Poster Paper at the National Seminar on Non-Destructive Testing held at Hyderabad, during December 7-9, 2006

Abstract

Conventional radiography, which uses X-ray machine and radioactive isotopes such as Iridium-192 and Cobalt 60 for generating penetrating radiation, is used for recording the internal defects of an object on a radiographic film. Advance radiography methods such as Micro Focal Radiography, Digital Radiography, and Real Time Radiography have been developed to offer an edge over conventional radiography for better definition and detectability of small defects, quick result and image processing. However, with all its limitations, conventional radiography can give results beyond expectation, provided the technique selected is proper and adequate. At the Centre for Design and Manufacture (CDM) capability of conventional radiography was explored for the examination of Boron Carbide Pellets and Friction Stir Welded Aluminium plates, having challenging requirements.

Boron Carbide (B_4C) is an extremely hard ceramic material used in tank armor, bulletproof vests and numerous industrial applications. Control rods of nuclear reactors contain pellets of Boron Carbide, which act as neutron absorber. Pellets of Boron Carbide are manufactured by sintering process in which objects of different shapes are formed by heating metal powder at temperature below its melting point. Pores and microscopic imperfections in ceramic give rise to cracks, which can lead to potentially dangerous equipment failure. Radiography technique was developed to detect cracks, micro pores and local density variation in pellets of various sizes, as an effective quality control tool.

Friction Stir Welding (FSW) is a solid state welding process, in which metals are joined together without fusion or filler metal. The welds are created by the combined action of frictional heating and mechanical deformation due to rotating tool. This process is primarily used on Aluminium and most often on large pieces which cannot be easily heat-treated post weld, to recover tempering characteristics. To establish the FSW process for welding of 5mm thick aluminium plates, number of trials using different parameters were carried out at CDM. In one of the welded pieces, it was a tricky task to detect lack of penetration under the Titanium foil, which was sandwiched between two Aluminium plates butting each other.

This paper presents a brief description of these two applications, radiographic technique developed for their examination and analysis of the results.

Introduction

Centre for Design and Manufacture (CDM) at Bhabha Atomic Research Centre is involved in the development of engineering products required for nuclear applications and various R & D activities. Jobs are designed and manufactured as per quality control requirements of the referencing codes, applicable for nuclear components. During manufacturing, components are subjected to various interstage nondestructive tests, such as Radiography Test (RT), Ultrasonic Test (UT), Liquid Penetrant Test (PT), Magnetic Particle Test (MT), Helium Leak Test (HLT), etc. to achieve the required quality, stipulated for the final product. Jobs are innovative in nature, therefore for each job, new NDT technique has to be developed depending upon the material, design, shape, manufacturing process and expected defects. Radiography testing of Boron Carbide pellets and Friction Stir Welded Alminium plates, using conventional X-ray machine, proved to be a very powerful quality tool as it revealed discontinuities even at micro level. This paper presents the detail of radiography testing of these two components developed at CDM.

Boron Carbide Pellets

Boron Carbide (B_4C), a black crystalline compound of Boron and Carbon is a ceramic material and is used in cutting tools, abrasive, bulletproof vests, nuclear power plants and in composite structural materials as a reinforcing filament. It is an extremely hard material and with a hardness of 9.3 on Mohs scale it is the fifth hardest material known. Its ability to absorb neutrons, without forming long-lived radionuclides, makes the material attractive as an absorbent for neutron radiation, arising in nuclear power plants. Nuclear application of B_4C also includes shielding. It is used in the form of pellets in control rods and shut down rods for controlling the power of nuclear reactor.

Ceramic-based materials are manufactured by sintering process in which objects of different shapes are formed, by heating the metal powder at a temperature below its melting point. When the powder is compacted into desired shape and heated i.e. sintered for up to three hours, the particles of powder join together to form a single solid object. Ceramic materials are usually ionic or covalently bonded materials and can be crystalline or amorphous. A material held together by either type of bond will tend to fracture before any plastic deformation takes place and this is responsible for the low toughness of such materials. Additionally, because these materials tend to be porous, the pores and other microscopic imperfections act as stress concentrators, decreasing the toughness further and reducing the tensile strength. These combine to give catastrophic failures as opposed to the normally much gentle failure modes of metals.

Radiography Testing Procedure

Boron carbide pellets of various diameters and lengths are being manufactured by sintering process at the Bhabha Atomic Research Centre for nuclear applications. It was necessary to develop a reliable NDT method to check and control the quality of pellets. Normally ultrasonic and radiography are common methods for detailed examination of ceramic components. Because of small size of pellet and in-homogeneity of the material, low inspection rate and restriction for using couplant, ultrasonic testing was not found suitable and therefore radiography was used as an NDT tool to check the internal details of B_4C pellets. Number of trials were performed, to establish the technique and radiographic parameters for a good quality radiograph. For complete coverage and detection of defects having different orientation, it was decided to radiograph each pellet in two mutually perpendicular directions : axial and radial. Because of cylindrical shape, proper masking was required to avoid undercut. Choice of masking material and its thickness depends upon few factors – a) Masking materials must be able to stop undercut and b) it should not produce very low density image surrounding the image of the pellet to restrict glare on the eyes while viewing the film on the illuminator. Steel and Aluminium plates of 2 mm thickness, having circular holes of diameter equal to that of pellet were used for masking the pellets in axial direction. As far as radiography in radial direction was concerned, it was observed that, pellets kept close to each other offered better solution for preventing under cut and scatter than using any external masking material. To assess the quality of radiograph it was necessary to use Image Quality Indicator (IQI). Since IQI for B_4C is not available it was manufactured out of the same pellets as given in Fig. 1. Slots having depth equal to 1% or 2% of the thickness penetrated by X-ray were machined on curved as well as flat surface. While taking radiograph IQI were placed at extreme edges to occupy most unfavourable conditions. Radiographic parameters were optimized in such a way that radiographs were able to record the image of 2% slot of IQI (Fig. 2), however, even 1% slot was visible on the radiograph.

After receiving the sintered pellets, first of all visual inspection is carried out to segregate the damaged and broken pellets. Acceptable pellets are ground to achieve the required dimensions and after grinding, pellets are subjected to radiographic examination.

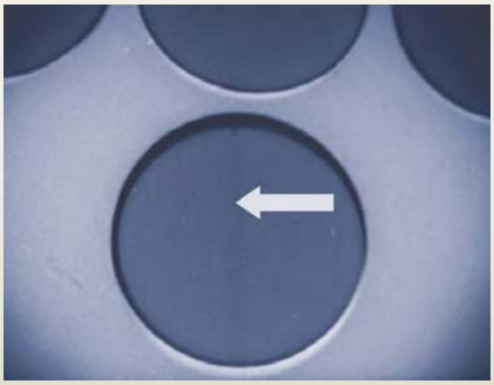

Fig. 2 : IQI (2% slot) image in axial direction

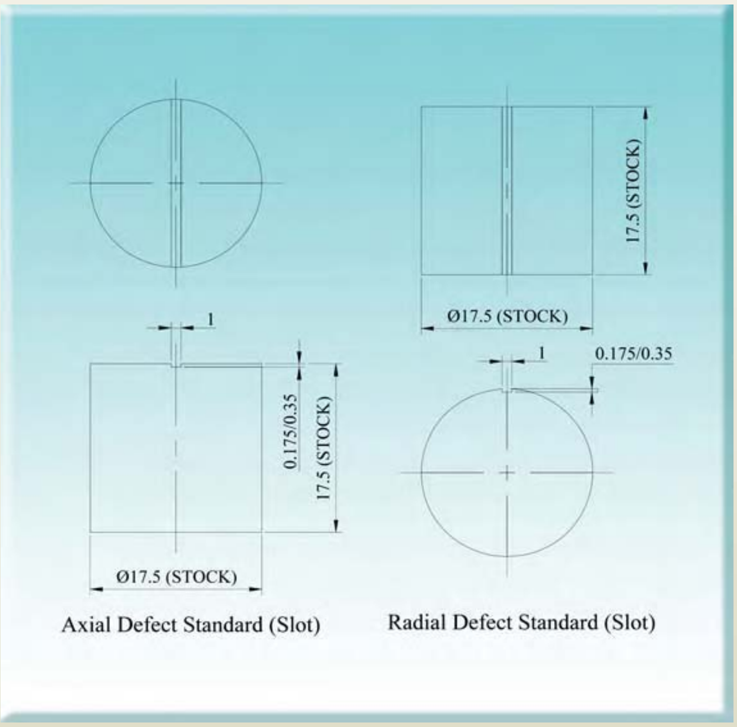

Fig.1 : Slot type IQI (Axial and Radial) for pellets

Result and Analysis

Radiograph of pellet in axial direction with Steel sheet masking was found to be better than with Aluminium sheet because back ground density was less than that of pellet image in case of steel masking. In axial direction, slight undercut between the pellets was observed, however it did not pose any problem during interpretation. Radiograph was able to detect porosity, crack, inclusion, in-homogeneity, density variation etc. (Figs. 3 & 4).

Even improper compactness was revealed in the radiograph and the feedback was utilized to improve the manufacturing process for the next lot of pellets.

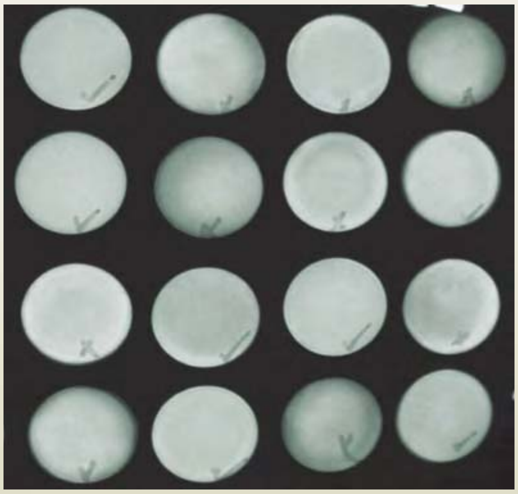

Fig. 3 : Inadequate sintering and compactness in few pellets

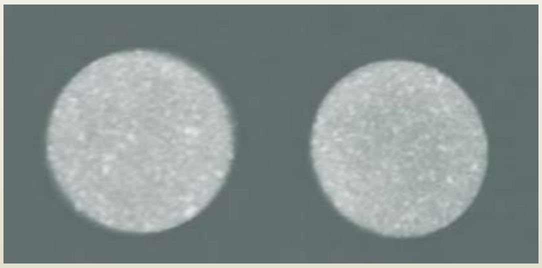

Fig. 4 : Inclusions and different phases seen in the pellets

Since no radiography standard is available for the acceptance and rejection of pellet, acceptance criteria were established by us based on our past experiences. Any type of crack, porosity and inclusion were cause for rejection. As far as local density variation within the pellet was concerned, reference radiographs were prepared. Initially, based on the radiographic image, few pellets having no defect and less density variation were selected for finding out their mass density. Since higher the mass density, better the compactness and lesser the porosity/void, pellets having higher mass density were considered as standard pellets. Radiographic image of these standard pellets were used for comparison in case of local density variation. Till now more than 500 pellets have been radiographed and the feedback has helped in improving the quality of pellets, which in turn has reduced the rejection.

Friction Stir Welding (FSW)

Friction Stir Welding is a type of friction welding which has been used by the automotive industry for manufacturing different parts used in vehicles.

Friction welding is carried out by moving one component relative to the other (linear or rotational motion) along a common interface, while applying a compressive force across the joint. The frictional heat generated at the interface, softens both the components and when they attain plastic state the interface material is extruded out of the edges leaving clean soft material of each component along the original interface. The relative motion is then stopped, and a higher final compressive force is applied before the joint is allowed to cool. The key to friction welding is that no molten material is generated, the weld being formed in the solid state [1].

Friction Stir Welding also produces a plasticized region of material, but in a different manner. In FSW, a cylindrical shouldered tool, with a profiled threaded/ unthreaded probe (nib or pin) is rotated at a constant speed and fed at a constant traverse rate into the joint line between two pieces of sheet or plate material, which are butted together (Fig. 5). The parts are clamped rigidly onto a backing bar in a manner that prevents the abutting joint faces being forced apart. The length of the nib should be slightly less than the weld depth required and the tool shoulder should be in intimate contact with the work surface.

The heat is generated primarily by friction between a rotating-translating tool, the shoulder of which rubs against the work piece. There is volumetric contribution to the heat generation from the adiabatic heating (due to deformation and relative motion around the pin), due to which the stirred material softens without reaching the melting point temperature. The tool traverses along the weld line containing the plasticized tubular shaft of metal. The leading face of the pin forces plasticized material to the back of the pin whilst applying a substantial forging force to consolidate the weld metal joint. The welding of the material is facilitated, by severe plastic deformation in the solid state, involving dynamic re-crystallization of the base material.

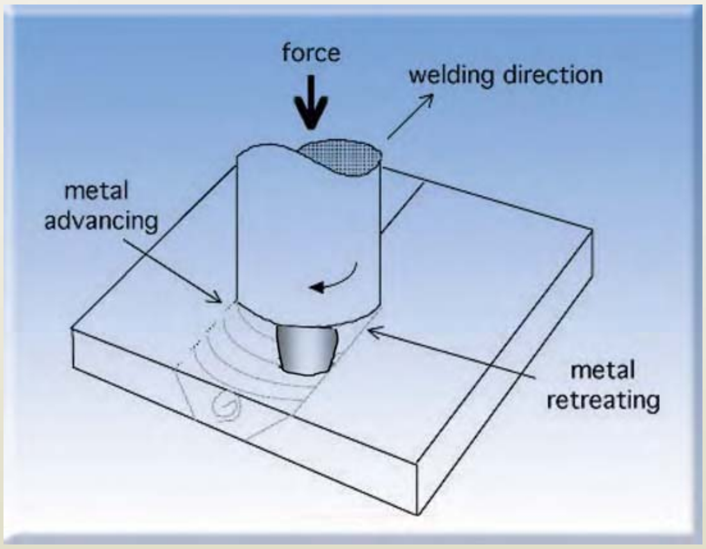

Fig. 5 : Principle of Friction Stir Welding

Application

It is already used in routine as well as critical applications, for joining of structural components made of Aluminium and its alloys, where the original metal characteristics must remain unchanged as far as possible. The process is most suitable for components which are flat and long (plates and sheets) and most often on large pieces which cannot be easily heat-treated post weld, to recover temper characteristics [2]. However, the process can be adapted for large pipes, hollow sections and positional welding. Ability to join dissimilar material makes it popular for the fabrication of components made of two different materials, each one suitable for different duty cycles in service. In the automotive sector the drive to build more fuel-efficient vehicles has led to the increased use of Aluminium in an effort to save weight. Friction stir welding is being used increasingly to replace fusion welding techniques where Aluminium alloys are involved mainly in aerospace, ship building, railway industries, automotive sector, space shuttle, launch vehicles etc.

Advantages

Since it is a solid state welding process, any problem associated with cooling from the liquid phase is immediately avoided. FSW can offer low distortion and lower shrinkage. Problems like porosity, solute redistribution, solidification and liquification cracking are not an issue during FSW. It is suitable for joining dissimilar materials. The process is environmentally friendly, because no fumes or spatters are generated and there is no arc glare. Generally, good weld appearance and minimal thickness deposit under/over the joint minimizes the need for expensive machining after welding.

Defect Associated with FSW

FSW is associated with a number of unique defects. Insufficient weld temperatures due to low rotational speeds or high transverse speeds may result in long, tunnel defects running along the weld, which may be surface or subsurface. If the pin is not long enough or the tool rises out of the plate then the interface at the bottom of the weld may not be disrupted and forged by the tool, resulting in a lack of penetration defect. The light contact between the materials has given rise to the name 'kissing bond'. This defect is particularly worrying since it is very difficult to detect using non-destructive methods such as radiography or ultrasonic testing. Steel can be friction stir welded but the essential problem is that tool materials wear rapidly and the wear debris from the tool can frequently be found inside the weld.

Process Development

Process of Friction Stir Welding of Aluminium plate is being jointly developed by the Materials Science Division (MSD) and the Centre for Design and Manufacture (CDM) of Bhabha Atomic Research Centre (BARC), Mumbai. Trial weld of 5 mm thick Aluminium 6061 plates (Fig. 6) have been carried out using tools of various geometry and various welding parameters such as tool rotation, (rpm-revolution per minute), transverse speeds (mm per minute) and tool tilt (degree). Following qualifying tests have been incorporated in the process to find the soundness of the weld:

a) Tensile test to check the mechanical properties of the joint.

b) Liquid penetrant test (PT) and Radiography test (RT) to detect surface and subsurface defects respectively.

c) Micro-structural characterization to identify the nature of microstructure in the nugget zone, heat affected zone, thermo-mechanically affected zone and the base metal.

NDT of Friction Stir Welding

To study the nature of defects, each welded piece was subjected to Liquid Penetrant Test (PT) and Radiography Test (RT). PT was carried out on face as well as on root side of the weld using solvent removable visible dye penetrant method. Mostly indications on root side corresponding to lack of penetration were observed in PT (Fig. 7). After PT, joint was radiographed using parameters given in Table 1. Result of RT was in agreement with that of PT. Other than Lack Of Penetration (LOP) no other defect such as porosity, lack of fusion, crack etc. was observed in the radiograph. Weld was considered to be of good quality except for LOP, which could be eliminated simply by increasing the length of the nib and controlling its relative position during welding. Further, radiograph was free from mottling effect, which is very common in fusion welding of Aluminium plates.

Fig. 6 : Friction Stir Welded Plate

Fig. 7 : LOP revealed by PT

In one of the experiments 0.2mm thick Titanium foil was inserted between the interface of the butting plates, to study the behavior of material transport in the stir nugget region, where material is heavily deformed giving rise to appearance of several concentric rings commonly known as 'onion-ring' structure. During PT of root side

Table 1: Exposure Detail

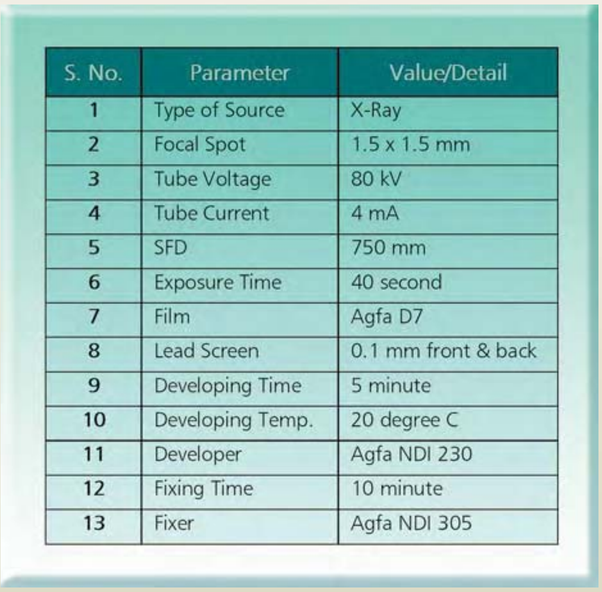

S. No.	Parameter	Value/Detail
1	Type of Source	X-Ray
2	Focal Spot	1.5 x 1.5 mm
3	Tube Voltage	80 kV
4	Tube Current	4 mA
5	SFD	750 mm
6	Exposure Time	40 second
7	Film	Agfa D7
8	Lead Screen	0.1 mm front & back
9	Developing Time	5 minute
10	Developing Temp.	20 degree C
11	Developer	Agfa NDI 230
12	Fixing Time	10 minute
13	Fixer	Agfa NDI 305

of the sample weld, lack of penetration was observed, throughout the weld and it was expected that RT would also reveal the same. However, to our surprise, radiograph did not show any lack of penetration. A continuous thick white line was seen throughout the length of the joint at the weld center. Matter was further investigated and effort was made to detect the LOP by RT in the welded plate having Titanium foil. Since the density of Titanium (4.5 g/cm^3) is higher than that of Aluminium (2.9 g/cm^3), image of the Titanium foil appears white in comparison to the parent metal, which is Aluminium. LOP being just below the Titanium foil could not be revealed as kilo voltage (80 kV) used was appropriate for Al and not for Ti. Since the low kV X-ray was not able to penetrate the Ti foil the detail of LOP under it was not seen on the radiograph. Considering the high sensitivity requirement to detect the fine image of LOP a new radiograph was prepared with following modifications: (a) Kilo voltage was increased from 80 to 110, suitable for Ti and (b) Fast and low contrast film (Agfa D7) was replaced by slow and high contrast (Agfa D4) film. Result was encouraging, since LOP was revealed as an intermittent dark line at the center of white image of Ti foil on a radiograph prepared using these new parameters. Distribution of Titanium, near the interface, indicates the transportation of the material under the influence of force applied by the rotating tool (Fig. 8).

Results and Analysis

Most common defect for friction stir welding is lack of penetration, which is more likely to exist at the start of the weld where nib plunges or at the end of the weld where tool is withdrawn due to inadequate frictional force. For this reason, additional material is removed from both the ends. However, if the nib is shorter than the required length, LOP may occur throughout the weld, which is difficult to detect by low sensitivity RT, if interface contains foil of some high-density materials such as Titanium or Copper. Therefore, for such joints in addition to RT, PT must be carried out from the root side which will ensure the detection of LOP. High sensitivity radiography developed by the authors, is able to detect complete internal details of the weld including LOP, material transportation and effect of inadequate force applied by the tool. Fig. 9 is a radiograph showing LOP and circular pressure mark at the start of the weld. The pressure mark in Fig. 9 indicates the change of microstructure of the material, under the shoulder of the tool at the beginning of the welding process, where as Fig. 10 indicates severe deformation of the material without reaching the plastic state.

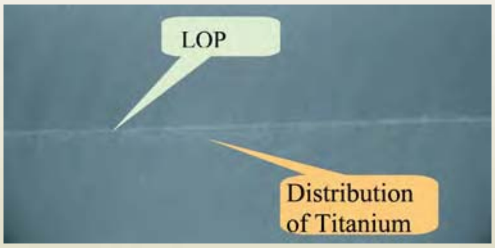

Fig. 8 : Radiograph of FSW Aluminium plates with Titanium foil at the interface

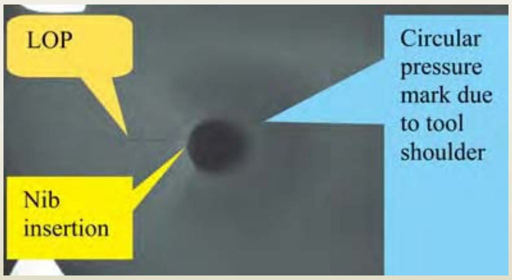

Fig. 9 : Defects at the start of FSW

Fig. 10 : Severely deformed material

Conclusion

An attempt has been made, to establish RT as a quality control tool, for the development work of Boron Carbide pellets and Friction Stir Welding at BARC. Radiographs prepared, using conventional X-ray machine are capable of revealing density distribution, inclusions, porosities, improper compactness and cracks in case of Boron Carbide Pellets and LOP, material deformation and material transport in case of Fiction Stir Welding. Feedback of NDT methods has been utilized, for improving the manufacturing process to get superior quality products with less chances of rejection.

References

1. Richard Johnson and Stephan Kallee, "Friction Stir Welding", *Materials World,* Vol. 7, no. 12, pp 751-53, December 1999.
2. Thomas W M, Nicholas E D, Needham J C, Murch M G, Temple-Smith P, Dawes C J, "Friction Stir Butt Welding", GB Patent No. 9125978.8, International Patent No. PCT/GB92/02203, (1991).

External Links

Friction Stir Welding- Wikipedia, the free encyclopedia (www/Friction stir welding/wikipedia.html).

Friction Stir Welding a process invented at TWI, Cambridge (www.msm.ac.uk/phase-transe/2003/FSW/aaa.html).

About the Authors

Mr. S.P. Srivastava obtained his degree in B.Sc. Engineering (Mechanical) from B.I.T., Mesra, Ranchi in 1984. After completing one year course of BARC Training School (29th Batch) he joined Non-destructive Unit of CDM in 1986. In the capacity of Engineer-In-Charge of Material Testing Laboratory, he is responsible for Non-Destructive Testing, Mechanical Testing, Quality Control Activities and Organization of Training and Certification Programme at CDM. He has developed various NDT techniques and systems for the examination of critical components required for nuclear power plants and research equipment. He has obtained certifications in Ultrasonic Testing Level 3, Radiography Testing Level 3, Leak Testing Level 2 and Eddy Current Testing Level 2.

Mr. T.G. Unni is Engineer-In-Charge, of Non-Destructive Testing Unit of CDM. He is involved in testing of various equipment and accessories manufactured at CDM for nuclear power plants & research activities. He has specialized in the field of Radiography Testing, Ultrasonic Testing, Liquid Penetrant Testing, Hydrostatic Pressure Testing and Magnetic Particle Testing. He has passed Ultrasonic Testing Level 3, Magnetic Particle Testing Level 3, Radiography Testing Level 2 and Eddy Current Testing Level 2 Certification Examinations.

Mr. S. P. Pandarkar joined CDM, BARC in 1978. Since then he is involved in Non-Destructive Testing of nuclear components manufactured at CDM. He is also responsible for third party QS activities for jobs manufactured by private companies. His field of specialization is Radiography Testing, Liquid Penetrant Testing, Helium Leak Testing and Mechanical Testing. He has passed Radiography Testing Level 2 and Ultrasonic Testing Level 1 Certification Examinations.

Mr. K. Mahajan, after obtaining his B.E. (Production Engineering) degree from Punjab Engineering College, Chandigarh in 1973, joined CDM (Centre for Design & Manufacture), (then CWS), BARC in the year 1974. Subsequently, he did his Postgraduate Degree [M.Tech. (Production Engineering)] from the Indian Institute of Technology, New Delhi in 1984. He has been associated with manufacture of Fuelling Machine Head assemblies, Special purpose machines, Precision instruments for various Nuclear Power Stations & Research Reactors for the last 33 years. Guide Tube Cutting Machine was successfully used to cut the bend tube into two parts and brought out of the FBTR and the new guide tube installed in the reactor. In order to study/determine earth's magnetic characteristics accurately, 1 Axis and 2 axis Barker Coil Systems were manufactured in CDM under his supervision and installed at the Indian Institute of Geomagnetism, Alibagh. He was also involved in refurbishing the old imported electrical & pneumatic control systems of Food Package Irradiator (FTD) using indigenous components and the system was upgraded incorporating additional safety features. At present, Mr Mahajan is functioning as Head, Human Resource Development & Industrial Engineering (HRD&IES), Maintenance and Quality Management Sections (QMS) in CDM.

Mr. R. L. Suthar, after obtaining his B.E. (Mechanical Engineering) degree from the University of Jodhpur, joined CDM (then CWS) in the year 1971. He has been associated with design and development of Special Purpose Machines and Precision Instruments & Equipment for Nuclear Power & Research Reactors for the last 32 years. Boring & Grooving Machines developed by him under MAPS Rehabilitation Project have been successfully used under his supervision. Power generation of these reactors then could be raised from 75% FP (Full Power) to 100% FP. Mr Suthar is now heading the Centre for Design and Manufacture and is involved in development of SPMs, Precision Instruments for INDUS-I & II Beam Lines at RRCAT, Indore, and other users of BARC; manufacture of equipment for AHWR Critical Facility, Sub-Critical Facility for RPDD and RED and 5 Axis Mechanism for Sub-reflector of 32 Meter DSN Antenna for ISRO under MoU with ECIL, etc.

ANALYSIS OF QTLS FOR EARLINESS COMPONENTS IN BREAD WHEAT (*TRITICUM AESTIVUM L.*)

E. Nalini and N. Jawali
Molecular Biology Division
Bhabha Atomic Research Centre

and

S.G. Bhagwat
Nuclear Agriculture and Biotechnology Division
Bhabha Atomic Research Centre

This paper was awarded the Best Poster Presentation award at the BARC Golden Jubilee and DAE-BRNS Life Science Symposium 2006 (LSS-2006) on "Trends in Research and Technologies in Agriculture and Food Sciences" held at BARC, Mumbai, during December 18-20, 2006

Abstract

Earliness, is an important trait in plant breeding. Its constituent traits flowering time and days to heading are largely controlled by vernalization genes (Vrn), photoperiod response genes (Ppd) and developmental rate genes ('earliness per se', Eps). Mapping of major genes controlling these quantitative traits, Flowering Time (FT) and days To Heading (DTH) was carried out in an intervarietal wheat cross. We constructed a genetic linkage map based on an F_2 population (150), derived from a cross between two Indian bread wheat (Triticum aestivum L.) varieties, Sonalika and Kalyansona. The map consisted of 236 markers and spanned a distance of 3639 cM. Field data for FT and DTH were collected on the F_2 population in Trombay environment. Totally six QTLs for flowering time and 21 for days to heading were identified with LOD threshold of >2.0 and the phenotypic variation ranging from 10.8 % to 67.8 %. At five of the QTLs for flowering time, the marker closest was also found to be closest to the QTLs for days to heading. Five markers that showed association with the traits were identified by t-test. STMS marker Xgwm325-6D showed association with both the traits. These five markers could be useful in Marker Assisted Selection (MAS) for these traits in wheat breeding.

Introduction

Many of the economically important traits in crop plants are quantitative in nature and are controlled by many genes or gene complexes, that are described as Quantitative Trait Loci (QTL). Mapping of the QTL has been greatly facilitated due to the availability of molecular markers and the development of improved and powerful statistical methods. The development of genetic maps is a prerequisite for mapping the loci that control these traits by QTL analysis and to identify the loci (QTLs) that could be useful in plant breeding via marker-assisted selection.

The first intervarietal map of bread wheat, based on RFLP markers, was published in 1997[1]. An updated version of this Chinese Spring - Courtot intervarietal genetic map was published in 2003[2]. More recently three intervarietal maps based on Australian bread wheat varieties[3] and other intervarietal maps have been reported[4-7]. Flowering time (FT) in wheat is a complex trait, controlled by three groups of major genes viz. photoperiod response genes (*Ppd*), vernalization response genes (*Vrn*) and developmental rate genes ('earliness per se', *Eps*). Days to Heading (DTH) is a trait correlated with FT and is also controlled by the vernalization and photoperiod genes.

Several QTLs have been reported for FT and DTH, which are listed in Table 1. Here, we report the identification of QTLs for FT and DTH, using a genetic linkage map, constructed using a cross between two Indian bread wheat (*Triticum aestivum* L.) varieties, Sonalika and Kalyansona.

Materials and Method

Plant Materials: The mapping population consisting of 150 F_2 plants was from a cross between Sonalika and Kalyansona (bread wheat: *Triticum aestivum L.*). The plants were grown in fields of BARC at Trombay, Mumbai, India. The data on DTH (ear emergence) and FT on these field grown plants was recorded at the appropriate growth time.

Chemicals: The chemicals for isolation of DNA and Agarose were from Sigma-Aldrich USA. PCR reagents were from Bangalore Genei Pvt. Ltd. Primers were from Genetix Ltd. The Hoechst dye was procured from Amersham Pharmacia biotech.

Method

DNA Isolation and Quantification: DNA was isolated from leaves following a method developed in our

Table 1 : List of QTLs detected in the present study and reported in literature for the two quantitative traits.

Name of trait	QTLs detected in the present study*	QTLs reported in literature	References
Flowering time (FT)	3A1, 5A1, 5B, 6B, 6D, 7B, Linkg11	3A	Shah et al. 1999
		5BL	Sarma et al, 2000
		2DS, 2BS, 5DS, 3AL	Borner et al, 2002
		5A (Vrn-A1)	Galiba et al. 1995
		5BL (Vrn-B1), 7BL (Vrn-B4)	Law et al, 1976
		5D	Snape et al, 2001
Days To Heading (DTH)	2A, 2B1, 2B2, 3A1, 3D2, 5A2, 5A3, 5A4, 5B, 6A, 6B, 6D, 7A, 7B, Linkg8, Linkg11, Linkg12	7DS (Vrn-B4)	Law 1966; Law and Wolfe 1966; McIntosh et al, 1998
		5A, 5D	Law et al, 1976
		2DS, 5DL, 7DS	Borner et al, 2002
		1DL, 2DS, 4AL	Kulwal et al, 2003
		2B, 2D, 5A, 7D (Ppd), 2B, 5A, 5B, 5D, 6D (Vrn)	Hanocq et al, 2004
		5A	Liu et al, 2005
		3BL2, 5B, 6B	Marza et al, 2006
		2DS, 3DS	Narasimhamoorthy et al, 2006

* = *The chromosomes in bold are the new QTLs detected in the present study*

laboratory[21]. DNA was quantitated by measuring fluorescence emission using Hoechst dye on a fluorimeter DyNA Quant 200.

PCR amplification: This was carried out in an Eppendorf Mastercycler-Gradient cycler. AP-PCR, RAPD, ISSR, STMS, AFLP, gene specific PCR markers viz. ITS, puroindoline gene and *Rht* genes, seed proteins and morphological markers were used for genotyping the mapping population.

Data analysis: The polymorphic bands were scored as presence (1) and absence (0) of band among the F_2 population. The segregation of individual markers was analyzed by chi-square test at 1% and 5% level of significance for a goodness-of-fit to a 3:1 ratio.

Linkage map: The linkage analysis was performed using Mapmaker ver 3.0b.[22]

QTL map: The genetic map thus constructed was used to derive QTL map by Composite Interval Mapping (CIM) and Multitrait Composite Interval Mapping (MCIM) for quantitative traits using QTL Cartographer ver. 2.5[23].

T-test: Marker association with the trait of the markers closest to the QTL identified by CIM was analyzed by t-test. Software such as Origin ver. 6.1 (Originlab corporation, USA) was used for performing t-test.

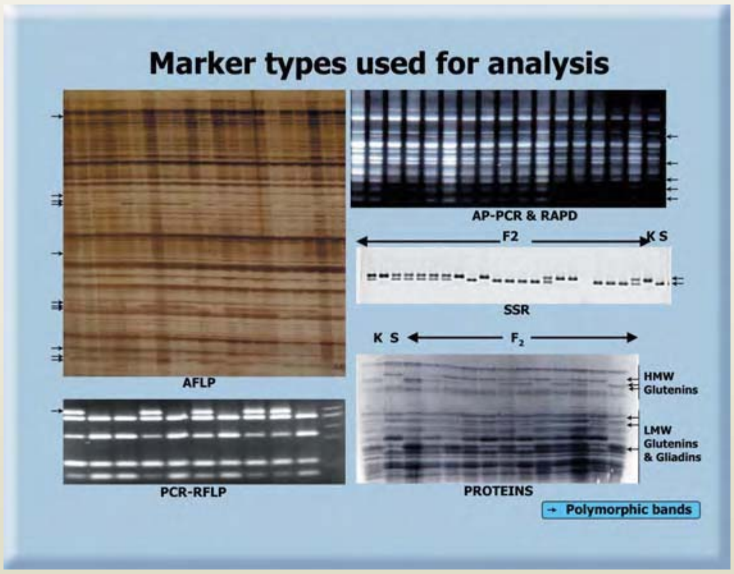

Fig. 1 : Different types of PCR-based marker techniques used for genotyping the mapping population

Results and Discussion

Construction of linkage map

Segregation of 280 markers (11 AP-PCR, 26 RAPD, 8 ISSR, 14 STMS, 210 AFLP, 5 proteins, 2 morphological and 4 gene specific markers (Fig.1) among the mapping population was used, to construct a genetic linkage map hereafter referred to as "SK map". Of the 280 markers, 236 mapped into 37 linkage groups and 44 markers remained unlinked. The map spanned 3639 cM with 1211.2 cM for A genome, 1669.2 cM for B genome, 192.4 cM for D genome and 566.2 cM for unassigned groups. Twenty-four linkage groups were assigned to 17 chromosomes using anchor markers such as STMS, physically mapped AFLP markers using nullitetrasomic lines and some gene specific loci such as *Rht* etc. No linkage group was assigned to the chromosomes 1D, 2D, 4D and 7D. The number of markers mapped was highest in B genome (97) followed by A genome (72) and D genome (17). The average distance between two markers was 15.4 cM.

Construction of QTL map

The genetic linkage map obtained above was utilized to construct QTL map for the two quantitative traits. Composite Interval Mapping is an extension of Simple Interval Mapping; it considers both the markers flanking the QTL and background markers, which may or may not be linked to the QTL. CIM is said to give more power and precision in the detection of QTLs than SIM. One of the most important advantages of CIM is that the markers can be used as boundary conditions to narrow down the most likely QTL position. The resolution of QTL locations can be greatly increased.

A total of eight QTLs were identified for FT of which one each was located on chromosomes 3A, 5A, 5B, 6B, 6D, 7B and two on the unassigned linkage group 11. The phenotypic variation in these QTLs ranged from 13.3 % to 42.0 % and the LOD ranged between 2.0 and 3.2. A total of 21 QTLs for DTH were identified that were located on chromosomes 2A, 2B, 3A, 3D, 5A, 5B, 6A, 6B, 6D, 7A, 7B and on unassigned linkage groups 8, 11 and 12. The QTLs for DTH were with LOD values ranging between from 2.1 and 6.8 and the phenotypic variation ranging between 10.8% and 67.8 % (Table 2).

Table 2 : Composite interval map for the quantitative traits DTH and FT

Sr. No.	Trait and linkage group	LOD score	QTL position and interval (cM)^a	Closest marker (Distance of marker from peak in cM)^b	QTL effect (R^2 %)
Flowering Time (FT)					
1.	3A1	3.2	144.1 (20)	E1_M3I (20)	26.7
2.	5A1	2.5	22.3 (10)	CT2D (10)	14.7
3.	5B	2.0	187.0 (34)	E17_M7B (36)	42.0
4.	6B	2.1	0.0 (24)	SS13RA (0)	33.8
5.	6D	2.6	14.0 (22)	Xgwm3256D**(14)	13.3
6.	7B	2.6	20.4 (36)	E17_M7A (2)	19.2
7.	Linkg11	3.0	44.2 (22)	E2_M7E** (8)	20.2
8.	Linkg11	2.7	100.0 (19)	E6_M1A (7.4)	28.1
Days To Heading (DTH)					
1.	2A	5.7	17.8 (19)	E2_M7D (10)	59.5
2.	2B1	2.7	78.7 (14)	E7_M4H* (20)	52.8
3.	2B2	4.2	0.0 (16)	E18_M7A (0)	50.0
4.	3A1	3.6	86.4 (6)	E16_M8I (6)	51.5
5.	3A1	2.4	140.1 (28)	E1_M3I (16)	15.0
6.	3D2	2.5	46.3 (6)	E3_M5O (20)	40.0
7.	5A2	3.0	133.7 (31)	E17_M7F (8)	40.6
8.	5A2	6.7	14.0 (12)	E1_M7G (14)	60.3
9.	5A3	4.0	163.2 (16)	E17_M7N (16)	54.5
10.	5A4	2.9	83.1 (23)	E6_M4C (28)	41.5
11.	5B	5.8	185.0 (24)	E17_M7B (34)	59.3
12.	6A	3.6	40.0 (18)	Xgwm1696A (40)	61.9
13.	6B	6.8	14.0 (24)	SS13RA (14)	53.4
14.	6D	2.1	12.0 (22)	Xgwm3256D**(12)	10.8
15.	7A	2.1	51.0 (37)	E5_M5C (12)	48.7
16.	7B	2.5	32.4 (32)	E17_M7A* (14)	23.9
17.	Linkg8	3.5	28.1 (28)	E5_M5B (28)	52.4
18.	Linkg11	6.3	195.3 (10)	CT2B (20)	67.8
19.	Linkg11	3.3	91.6 (16)	E2_M7H (34)	34.7
20.	Linkg11	3.1	103.0 (17)	E6_M1J* (0)	33.9
21.	Linkg12	2.3	81.6 (46)	E19_M7A (8)	46.1

*,** *Means for marker allele classes, which differed significantly at* $P < 0.05$ *and 0.01 respectively*

[a] *Intervals in cM were obtained by marking positions ± 1 LOD from the peak*

[b] *Values in parentheses are the distances (cM) of the marker from the peak*

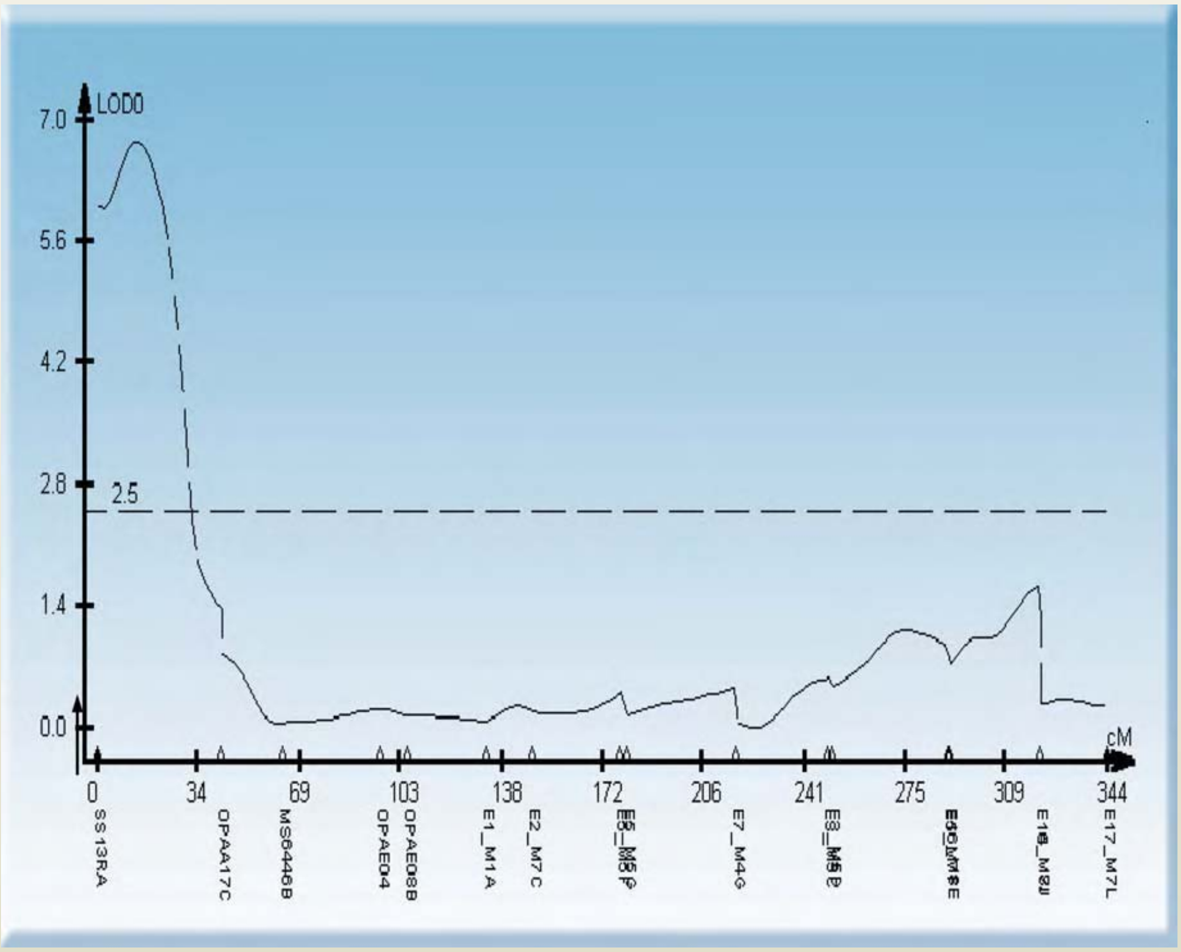

Fig. 2 : A representative QTL cartographer plot involving chromosome 6B obtained using Composite Interval Mapping (CIM) for the trait DTH. The LOD value is given on the Y-axis and the name of the markers and distance between them in cM on the X-axis. The arrow point at the QTL at the position 0.0 cM and the marker associated is SS13RA having a LOD score of 6.8.

As an example a representative QTL cartographer plot involving chromosome 6B obtained using Composite Interval Mapping (CIM) for the trait DTH is shown in Fig. 2. The markers closest to the QTLs for FT on chromosome 3A, 5B, 6B, 6D and 7B were also closest to the QTLs for DTH viz. 1) E1_M31 on chromosome 3A1, 2) E17_M7B on chromosome 5B, 3) E17_M7A on chromosome 7B, 4) SS13RA on chromosome 6B and 5) Xgwm325-6D on chromosome 6D.

Association of a marker with a QTL was analyzed by two-population t-test. The F_2 population was divided into two groups, based on the alleles of a marker closest to a QTL. The trait means of the two groups were subjected to t-test for significance. Significant differences between the means were obtained for five markers (Table 2). These five markers that are associated with the trait could be useful in Marker Assisted Selection (MAS) for these traits in wheat breeding.

References

1. Cadalen, T., Boeuf, C., Bernard, S. and Bernard, M. (1997). *Theor. Appl. Genet.* 94: 367-377.
2. Sourdille, P., Cadalen, T., Guyomarc'h, H., Snape, J.W., Perretant, M.R., Charmet, G., Boeuf, C., Bernard, S. and Bernard, M. (2003). *Theor. Appl. Genet.* 106: 530-538.
3. Chalmers, K.J., Campbell, A.W., Kretschmer, J., Karakousis, A., and Henschke, P.H. (2001). *Aust. J. Agric. Res.* 52: 1089-1119.
4. Paillard, S., Schnurbusch, T., Winzeler, M., Messmer, M., Sourdille, P., Abderhalden, O., Keller, B. and Schachermayr, G. (2003). *Theor. Appl. Genet.* 107: 1235-1242.
5. Liu, Z.H., Anderson, J.A., Hu, J., Friesen, T.L., Rasmussen, J.B. and Faris, J.D. (2005). *Theor. Appl. Genet.* 111: 782-794.
6. Quarrie, S.A., Steed, A., Calestani, C., Semikhodskii, A. and Lebreton, C (2005). *Theor. Appl. Genet.* 110: 865-880.
7. Suenaga, K., Khairallah, M., William, H.M. and Koisington, D.A. (2005). *Genome* 48: 65-75.
8. Shah, M.M., Gill, K.S., Baenziger, P.S., Yen, Y., Kaeppler, S.M. and Ariyarathne, H.M. (1999). *Crop Sci.* 39: 1728-1732.
9. Sarma, R.N., Fish, L., Gill, B.S. and Snape, J.W. (2000). *Genome* 43: 191-198.
10. Borner, A., Schumann, E., Furste, A., Coster, H., Leithold, B., Roder, M.S. and Weber, W.E. (2002). *Theor. Appl. Genet.* 105: 921-936.
11. Galiba, G., Quarrie, S.A., Sutka, J., Morgounov, A. and Snape, J.W. (1995). *Theor. Appl. Genet.* 90: 1174-1179.
12. Law, C.N., Worland, A.J. and Giorgi, B. (1976). *Heredity* 36: 49-58.
13. Snape, J.W., Sarma, R., Quarrie, S.A., Fish, L., Galiba, G. and Sutka, J. (2001). *Euphytica* 120: 309-315.
14. Law, C.N. (1966). *Genetics* 53: 487-493.
15. Law, C.N. and Wolfe, M.S. (1966). *Can. J. Genet. Cytol.* 8:462-470.
16. McIntosh, R.A., Hart, G.E., Devos, K.M., Gale, M.D. and Rogers, W.J. (1998). August. University Extension Press, University of Saskatchewan, Saskatoon, Sask. Pp. 77-83.
17. Kulwal, P.L., Roy, J.K., Balyan, H.S. and Gupta, P.K. (2003). *Plant science* 164:267-277.
18. Hanocq, E., Niarquin, M., Heumez, E., Rousset, M. and Gouis, J. Le. (2004). *Theor. Appl. Genet.* 110: 106-115.
19. Marza, F., Bai, G.H., Carver, B.F. and Zhou, W.C. (2006). *Theor. Appl. Genet.* 112: 688-698.
20. Narasimhamoorthy, B., Gill, B.S., Fritz, A.K., Nelson, J.C. and Brown-Guedira, G.L. (2006). *Theor. Appl. Genet.* 112: 787-796.
21. Nalini, E., Bhagwat, S.G. and Jawali, N. (2004) *BARC Newsletter, Founder's Day Special issue,* No. 249; 208-214.
22. Lander, E.S., Green, P. Abrahamson, J. Barlow, A.. Daley, M. Lincoln, S and Newburg, L. (1987) *Genomics* 1: 174–181.
23. Wang, S., Basten, C.J., Gaffney, P. and Zeng, Z.-B. (2005) QTL Cartographer, version 2.5, Department of statistics, North Carolina State University, Releigh, NC.
24. Roder, M.S., Korzun, V., Wandehake, K., Planschke, J., Tixier, M.H., Leroy, P. and Ganal, M.W. (1998b). *Genetics* 149: 2007-2023.

About the Authors

Ms. Nalini Eswaran, a DAE-Mumbai University collaborative fellow, is a first rank holder in M.Sc. degree in Life Sciences (Specialization in Biomacromolecules,) from Mumbai University in the year 2001. She was awarded the DAE-Mumbai University collaborative fellowship for doing Ph.D., in 2001. She is carrying out her research project entitled "Genetic Linkage Map of Bread Wheat With an Emphasis on Genes Controlling Plant Morphology" in the Molecular Biology Division under the guidance of Dr. Narendra Jawali. The paper titled "Analysis of QTLs for Earliness components in bread wheat (Triticum aestivum)" was awarded best poster presentation, at the BARC Golden Jubilee and DAE-BRNS Life Science Symposium 2006 (LSS-2006) on "Trends in Research and Technologies in Agriculture and Food Sciences" at BARC, Trombay, Mumbai 18-20 Dec 2006.

Dr S.G. Bhagwat did his M.Sc. in Botany from Poona University, Pune in the year 1975. He joined the 19th Batch of Training School in the Biology and Radiobiology discipline. He did his PhD. on "Grain protein variation in wheat". Currently, he is working in the Nuclear Agriculture and Biotechnology Division of the Bioscience group, BARC. His research interests are genetics and genetic improvement of wheat.

Dr Narendra Jawali obtained M.Sc., Degree in Biochemistry from Central College, Bangalore University Bangalore in 1975. He joined the 19th Batch of Training School in the Biology and Radiobiology discipline. He obtained his Ph.D. in 1988 from Mumbai University. He is working in the Molecular Biology Division of the Bioscience group, BARC. His research interests are plant and microbial molecular genetics.

GENETIC VARIATION AND RELATEDNESS IN *VIGNA UNGUICULATA* REVEALED BY MICROSATELLITES

V. Archana and N. Jawali
Molecular Biology Division,
Bhabha Atomic Research Centre

The paper was awarded a prize for the Best Poster Presentation at the BARC Golden Jubilee and DAE-BRNS Life Science Symposium 2006 (LSS-2006) held at BARC, Mumbai, during December 18-20, 2006

Abstract

Sequence- Tagged Microsatellite Site (STMS) markers were used to analyze genetic variation, among 21 geographically diverse accessions of V. unguiculata, belonging to Section Catiang. Of the total 22 cowpea STMS markers screened, 12 were found to be polymorphic with a minimum of two and a maximum of 11 alleles. Presence of null alleles was observed in six loci. A total of 88 alleles was obtained. Variability in the size and the number of alleles was obtained with an average of 7.3 alleles per locus. Genetic Distances were calculated using Unweighted Pair Group Method with Arithmetic averages (UPGMA) and a Principal Coordinate Analysis (PCO) of the data was carried out using the NTSYSpc (version 2.02i) software. Results revealed a large amount of intersubspecies variability within V. unguiculata species in Subgenus Vigna. The accessions clustered into six groups, which showed correlation to their geographical origin and clearly distinguished the wild genotypes from the cultivars. The results indicate interplay of geographic isolation (founder effect) and intra-species hybridization for the observed phenomenon. Microsatellite analysis also confirmed that, in the large cowpea genepool, the cultivated cowpeas (ssp. unguiculata var. unguiculata) form a genetically coherent group and are closely related to the annual cowpeas (ssp. unguiculata var. spontanea), which may include the most likely progenitor of cultivated cowpeas.

Introduction

Genus *Vigna* of family Leguminosae (subfamily Papilionoideae), was created by Savi in 1824 and now comprises of around 80 species originating from different regions of Africa, America and Asia. Genus *Vigna* is grouped into six subgenera viz., *Vigna, Ceratotropis, Plectrotropis, Sigmoidotropis, Lasiospron* and *Haydonia*. Subgenus *Macrorynchus* that was previously in genus *Vigna* has been transferred recently to genus *Wajira* (Thulin et al. 2004). Subgenera *Vigna* and *Ceratotropis* include several agriculturally important species viz., *V. unguiculata* (Cowpea), *V. subterranea* (Bambara groundnut), *V. radiata* (mungbean), *V. mungo* (blackgram), *V. aconitifolia* (mothbean), *V. umbellata* (ricebean) etc. Of these, subgenus *Vigna* includes two important culti-groups viz. *V. unguiculata (L.) Walp* and *V. subterranea (L.) Verdn*. The cultivated forms of *V. unguiculata* are further divided into five groups: *Unguiculata*, *Biflora, Sesquipedalis, Textilis* and *Melanophthalmus* (Pasquet, 1998).

V. unguiculata is globally and economically an important grain legume. It is also referred to as black-eyed peas, field peas, or *Chawli* (here in India). At least 12.5 million hectares of cowpea are cultivated with an annual production of over three million metric tons, worldwide. However, most of these farming systems make limited use of modern agricultural inputs, which compel breeding programs to screen wild and cultivated germplasm, for sources of disease and insect resistance and other desirable traits. Better knowledge of the genetic similarity of breeding materials could help to sustain long-term selection gain. The knowledge on the genetic diversity within and among subspecies, will help to provide an insight into subspecies divergence and to exploit genetic resources for breeding.

V. unguiculata L. Walp has 11 subspecies that includes ssp. *unguiculata* having both cultivated forms (var. *unguiculata*) and wild forms (var. *spontanea*); and 10 wild perennial subspecies (Pasquet, 1999). Diversity among *V. unguiculata* and its subspecies has been analyzed by morphological (Padulosi, 1993), biochemical - seed storage proteins (Fotso et al, 1994) and isozymes (Panella and Gepts, 1992; Vaillancourt et al, 1993 and Pasquet, 1999, 2000) and DNA markers like chloroplast DNA (Vaillancourt and Weeden, 1992), AFLP (Coulibaly et al, 2002), RAPD (Ba et al, 2004) etc.

Microsatellites or Simple Sequence Repeats (SSR) are DNA sequences with repeat lengths of a few base pairs. The repeat regions are generally composed of di-tri-tetra and sometimes greater perfectly repeated nucleotide sequence (Tautz and Renz, 1984). They are also referred to as Sequence Tagged Microsatellite Site (STMS) markers, their polymorphism is due to variations in the number of core repeat unit. Variation in the number of repeats at a loci, can be detected by PCR, using primers for the sequence flanking the SSR. As molecular markers, SSR combines many desirable marker properties including high levels of polymorphism and information content, unambiguous designation of alleles, even dispersal, selective neutrality, high reproducibility, codominance and rapid and simple genotyping assays. Microsatellites have become the molecular markers of choice for a wide range of applications such as genetic mapping and genome analysis (Chen et al, 1997; Li et al, 2000), genotype identification and variety protection (Senior et al. 1998), seed purity evaluation and germplasm conservation (Brown et al, 1996), diversity studies (Xiao, et al, 1996), paternity determination and pedigree analysis (Ayres et al, 1997; Bowers et al, 1999; van de Ven and McNicol, 1996), gene and quantitative trait locus analysis (Blair and McCouch, 1997; Koh et al, 1996) and marker-assisted breeding (Ayres et al, 1997; Weising et al, 1998). Our study demonstrates the, applicability of cowpea microsatellites for estimating genetic relatedness among diverse accessions of *V. unguiculata*.

The present study reveals the relatedness among wild and cultivated taxa of *V. unguiculata* originated from different eco-geographical locations. These studies lead to recognition of variations among genetically divergent groups of germplasm, which are fundamental in breeding programs and genetic engineering.

Materials and Method

Plant Material

Twenty-one accessions of *V. unguiculata* belonging to section *Catiang* were obtained from the National Botanic Garden, Belgium (Meise collection). All accessions used in this study have originated in different locations in African continent except one each from China and Yemen (Table 1).

Table 1 : List of *Vigna unguiculata* accessions used in this study

Sr. No	Subspecies/Var	Country of Origin
1	ssp. *unguiculata* cv-gr. *unguiculata*	Democratic Republic of Congo
2	ssp. *unguiculata* cv-gr. *sesquipedalis*	China
3	ssp. *unguiculata* var. *textilis*	Togo
4	ssp. *unguiculata* var. *spontanea*	Tanzania
5	ssp. *unguiculata* var. *spontanea*	Namibia
6	ssp. *unguiculata* var. *spontanea*	Kenya
7	ssp. *unguiculata* var. *spontanea*	Yemen
8	ssp. *unguiculata* var. *spontanea*	Malawi
9	ssp. *unguiculata* var. *spontanea*	Botswana
10	ssp. *unguiculata* var. *spontanea*	Niger
11	ssp. *unguiculata* var. *spontanea*	Democratic Republic of Congo
12	ssp. *unguiculata* var. *spontanea*	Zimbabwe
13	ssp. *tenius*	South Africa
14	ssp. *tenius*	Zambia
15	ssp. *tenius*	Mozambique
16	ssp. *alba*	Angola
17	ssp. *alba*	Congo
18	ssp. *baoulensis*	Ivory Coast
19	ssp. *stenophylla*	Botswana
20	ssp. *pubescens*	Tanzania
21	ssp. *pubescens*	Kenya

ssp: subspecies; var: variant

DNA Isolation and PCR amplification

Genomic DNA was isolated from young leaves (Nalini et al, 2004) and the quality and quantity of DNA was checked on a 1% agarose gel (Prasad et al, 1999). Twenty-two STMS developed by Li et al, (2001) were used here (Table 2).

Each 25µl reaction mixture contained 20mM Tris-HCl pH 8.8, 10mM KCl, 10 mM $(NH_4)_2SO_4$, 2 mM $MgSO_4$, 0.1 % Triton X-100, 0.2mM of each dNTP, 0.2µM of each oligonucleotide primer, 1.0 unit of Taq Polymerase Enzyme and 50-100 ng of genomic DNA. Amplification was performed using an Eppendorf Master Cycler gradient PCR with an initial denaturation at 94°C for 5 min followed by 45 cycles of: denaturation at 94°C for 1 min, annealing at 40-50°C for 1 min and elongation at 72°C for 1 min with a final elongation at 72°C for 10 mins. Amplified products were size-separated by gel electrophoresis on a 3% high-resolution agarose gel (Roche Diagnostics, Germany) in 1X TBE at a constant voltage of 80V and visualized by ultraviolet illumination of the ethidium bromide stained gel. However for the detection of alleles having length difference of 2bp and less, the products were analyzed on a 6% sequencing polyacrylamide gel, at a constant current of 80W for 3h followed by silver staining. Sizes of the PCR products were estimated by GeneTools software of the Gel-doc system by comparing with the DNA size standards. A 100 bp ladder (Bangalore Genei Pvt. Ltd, India), served as a standard molecular weight marker.

Table 2 : List of cowpea STMS used in this study

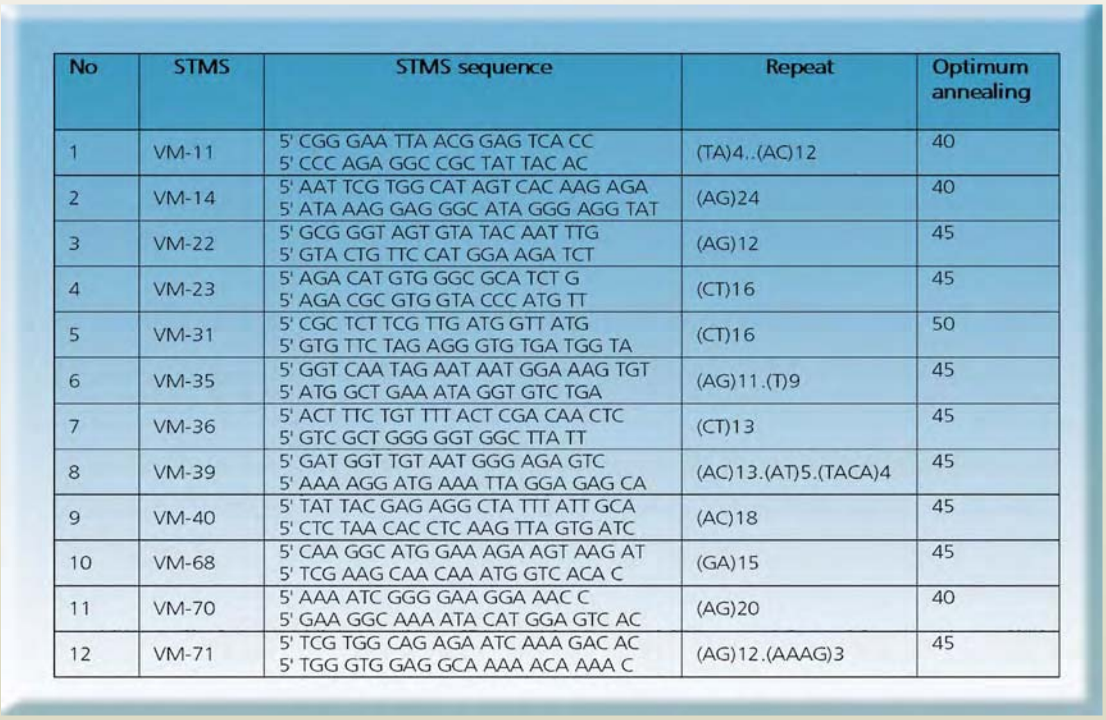

No	STMS	STMS sequence	Repeat	Optimum annealing
1	VM-11	5' CGG GAA TTA ACG GAG TCA CC 5' CCC AGA GGC CGC TAT TAC AC	(TA)4..(AC)12	40
2	VM-14	5' AAT TCG TGG CAT AGT CAC AAG AGA 5' ATA AAG GAG GGC ATA GGG AGG TAT	(AG)24	40
3	VM-22	5' GCG GGT AGT GTA TAC AAT TTG 5' GTA CTG TTC CAT GGA AGA TCT	(AG)12	45
4	VM-23	5' AGA CAT GTG GGC GCA TCT G 5' AGA CGC GTG GTA CCC ATG TT	(CT)16	45
5	VM-31	5' CGC TCT TCG TTG ATG GTT ATG 5' GTG TTC TAG AGG GTG TGA TGG TA	(CT)16	50
6	VM-35	5' GGT CAA TAG AAT AAT GGA AAG TGT 5' ATG GCT GAA ATA GGT GTC TGA	(AG)11.(T)9	45
7	VM-36	5' ACT TTC TGT TTT ACT CGA CAA CTC 5' GTC GCT GGG GGT GGC TTA TT	(CT)13	45
8	VM-39	5' GAT GGT TGT AAT GGG AGA GTC 5' AAA AGG ATG AAA TTA GGA GAG CA	(AC)13.(AT)5.(TACA)4	45
9	VM-40	5' TAT TAC GAG AGG CTA TTT ATT GCA 5' CTC TAA CAC CTC AAG TTA GTG ATC	(AC)18	45
10	VM-68	5' CAA GGC ATG GAA AGA AGT AAG AT 5' TCG AAG CAA CAA ATG GTC ACA C	(GA)15	45
11	VM-70	5' AAA ATC GGG GAA GGA AAC C 5' GAA GGC AAA ATA CAT GGA GTC AC	(AG)20	40
12	VM-71	5' TCG TGG CAG AGA ATC AAA GAC AC 5' TGG GTG GAG GCA AAA ACA AAA C	(AG)12.(AAAG)3	45

Data Analysis

Each band was treated as a separate locus and scored as present (1) or absent (0) in each accession. The Polymorphism Information Content (PIC) of each microsatellite was determined as described by Weir

(1996) using the following formula: PIC= $1-\Sigma(P_i)^2$; where P_i is the proportion of the population carrying the i^{th} allele.

Cluster Analysis

Genetic similarity by Jaccard's coefficient, Principal Coordinate Analysis (PCO) and cluster analysis using UPGMA method was performed with NTSYSpc software (version 2.02i).

Results and Discussion

Twenty-two STMS were analyzed of which 12 gave clean amplified products, which fell in the range of 100-300 bp (Fig. 1). The number of alleles detected at the 12 loci, ranged between two (VM-14) and 11 alleles (VM-39) with an average of 7.3 alleles per locus. Average PIC value was found to be 0.75 (0.3-0.9). Some microsatellite loci were observed more frequently in cultivated taxa than in wild taxa. Four microsatellite loci namely VM-70, VM-71, VM-31 and VM-11 were specifically present in cultivated tax and absent in all wild taxa included in this study. High average number of alleles amplified per locus along with high PIC value suggests that, these microsatellite loci in *V. unguiculata* are highly polymorphic.

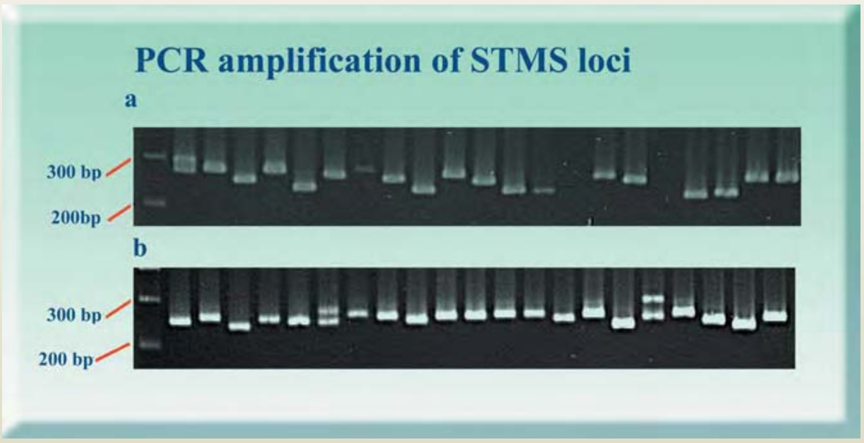

Fig. 1: Variation in STMS loci (a) VM-70 & (b) VM-68 among the 21 *V.unguiculata* accessions

To infer among different taxa of *V. unguiculata*, a UPGMA dendrogram was constructed using Jaccard's similarity matrix. Dendrogram comprised of six clusters (I-VI) and clearly differentiated the wild and cultivated taxa. Cluster I comprised of cultivated *V. unguiculata* where cv-gp. *unguiculata* is closely related to the cv-gp. *sesquipedalis* (d: 0.500) than the primitive cv-gp. textilis (d: 0.800). Cultivated *V. unguiculata* was less diverse as compared to the wild accessions. The wild taxa accessions belonging to ssp. *unguiculata,* ssp. *alba* and ssp. *tenuis* did not form sub-species specific cluster (Clusters II-VI). In fact, the diverse eco-geographic types of these sub-species, clustered with accessions of other sub-species, originating in similar eco-geographic locations. *V. unguiculata* var *spontanea* were dispersed among other wild taxa and formed the closest link to the cultivated types. Principal coordinate analysis was carried out using the NTSYSpc software (version 2.02i), which gave a picture similar to the cluster data (Data not shown). Our results indicate that wild cowpea is highly variable genetically across Africa.

The present study shows the utility of microsatellite markers in assessing genetic relationships among the wild and cultivated *V. unguiculata*. Information generated from such relationship studies, can have a long-term impact on plant breeding, particularly by use of inter-subspecies hybridization and bridging species in introgressing agriculturally important traits such as, resistance/ tolerance to biotic/ abiotic stresses.

Microsatellite markers have shown high levels of polymorphism in many important crops including rice (*Oryza sativa* L., Chen et al, 1997),

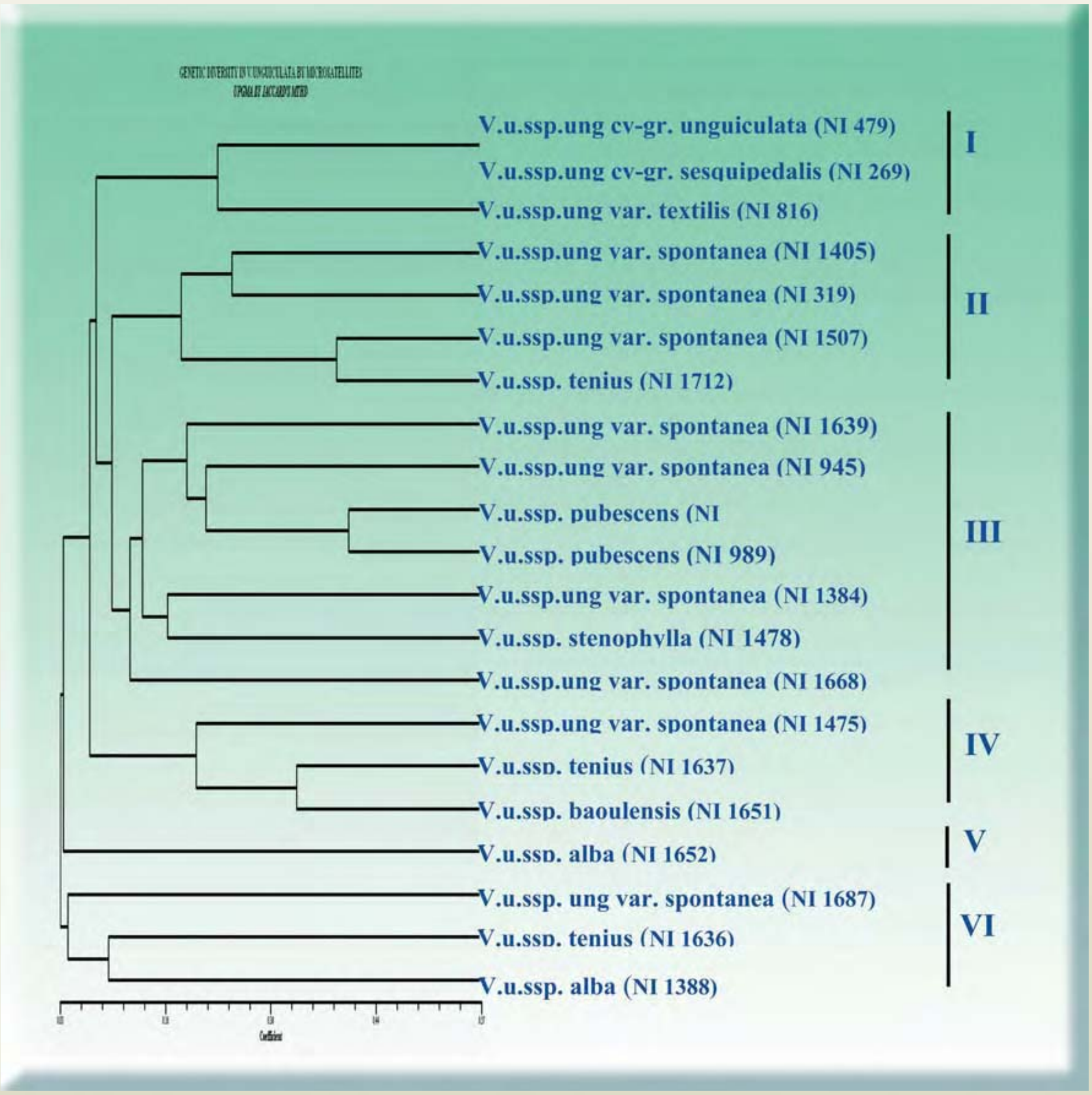

Fig. 2 : UPGMA cluster by Jaccard's method reveals the relationship among 21 accessions of *V. unguiculata*

wheat (*Triticum aestivum* L., Devos et al, 1995; Roder et al, 1995), barley (*Hordeum vulgare* L., Liu et al, 1996), oat (*Avena sativa* L., Li et al, 2000), maize (*Zea mays* L., Senior et al, 1998), sorghum [*Sorghum bicolour* (L.) Moench, Brown et al, 1996], soybean [*Glycine max* (L.) Merr., Akkaya et al, 1992], beans (*Phaseolus* and *Vigna*, Yu et al, 1999), Brassica species (Szewc-McFadden et al, 1996), alfalfa (*Medicago* spp., Diwan et al, 1997), sunflower (*Helianthus annuus* L., Brunel. 1994) and tomato (*Lycopersicon esculentum* Mill., Smulders et al, 1997). The present study showed that microsatellite markers were also highly polymorphic in cowpea.

We conclude that cultivated cowpeas form a genetically coherent group and were closely related to the wild cowpeas (var. *spontanea*), which may be the most likely progenitor of cultivated cowpea (var. *unguiculata*). This information would help us to gain an insight into subspecies divergence and to exploit genetic resources for hybridization breeding. The study also revealed that certain accessions belonging to *V. unguiculata* from different eco-geographic locations have evolved differentially due to geographical isolation (also referred as 'founder effect'). On the other hand, high similarity among certain accessions, belonging to different subspecies originating from same eco-geographic location, suggests the interplay of intra-species hybridization and subsequent homogenization among them.

Acknowledgement

Grateful thanks are due to Dr T. Vanderborght, National Botanic Garden of Belgium for the supply of seed samples. Thanks are also due to Dr Ajay Sainis for the help in data analysis and critically reviewing the manuscript.

References

1. Akkaya, M.S., Bhagwat, A. A. and Cregan, P.B. (1992). *Genetics* 132, 1131-1139.Ayres, N.M., McClung, A.M., Larkin, P.D., Bligh, H.F.J., Jones, C.A. and Park, W.D. (1997). *Theor. Appl. Genet*. 94, 773-781.
2. Ba, F.S., Pasquet, R.S., Gepts, P., 2004. *Genetic Resources and Crop Evolution*. 51-5, 539-550.
3. Blair, M. and McCouch, S.R. (1997). *Theor. Appl. Genet*. 95, 174-184.Bowers, J., Boursiquot, J., This, P., Chu, K., Johansson, H. and Meredith, C. (1999). *Science* 285, 1562-1565.
4. Brown, S.M., Hopkins, M.S., Mitchell, S.E., Senior, M.L., Wang, T.Y., Duncan, R.R., Gonzalez-Candelas, F. and Kresovich,S. (1996). *Theor. Appl. Genet*. 93,190-198.
5. Brunel, D. (1994). *Plant Mol. Biol*. 24: 397-400.
6. Chen,X., Temnykh, S.,Xu,Y., Cho, Y.G. and McCouch, S.R. (1997). *Theor. Appl. Genet*. 95,553-567.
7. Coulibaly, S., Pasquet, R.S., Papa, R., Gepts, P., 2002. *Theor. Appl. Genet*. 104, 358-366.
8. Devos, K.M., Bryan, G.J., Collins, A.J., Stephenson,P. and Gale, M.D.(1995). *Theor. Appl. Genet*. 90,247-252.
9. Diwan, N., Bhagwat, A.A., Bauchan, G.B. and Cregan, P.B. (1997). *Genome* 40, 887-895.
10. Fotso, M. Azanza, J.L., Pasquet, R. and Raymond, J (1994). *Plant. Syst. Evol.* 191, 39-56.
11. Jaccard, P. (1908). *Bull Soc Vaud Sci Nat* 44, 223-270.
12. Koh, H.J., Heu, M.H. and McCouch, S.R. (1996). *Theor. Appl. Genet*. 93, 257-261.
13. Li, C.D., Rossnagel, B.G. and Scoles, G.J. (2000). *Theor. Appl. Genet*. (in press).
14. Li, C-D., Fatokun, C.A., Ubi, B., Singh, B.B. and Scoles, G.J. (2001). *Crop Sci*. 41, 189-197.
15. Liu, Z.W., Biyashev, R.M. and Saghai Maroof, M.A. (1996).
16. Nalini, E., Bhagwat, S.G., Jawali, N., 2004. *BARC Newsletter, Founder's Day Special issue,* No. 249, 208-214.
17. Padulosi, S., 1993. Thèse, Université catholique. Louvain la Neuve, Belgium.
18. Panella, L. and Gepts, P (1992). *Genet. Res. Crop. Evol*. 39, 71-88.
19. Pasquet, R. S., 1998. *Agronomie* 18, 61-70.
20. Pasquet, R.S (1999) *Theor. Appl. Genet*. 98, 1104-1119.
21. Pasquet, R.S., Vanderborght, T., 2000. *Biochemical Systematics and Ecology*. 28, 29-43.
22. Prasad, S., Reddy, K.S., Jawali, N., 1999. *Asia Pacific Journal of Molecular Biology and Biotechnology*. 7, 73-177.
23. Roder, M.S., Plaschke, J., Konig, S.U., Borner, A., Sorrels, M.E., Tanksley, S.D. and Ganal, M.W. (1995). *Mol. Gen. Genet*. 246, 327-333.
24. Rohlf, F.J. (1998). NTSYS-PC Numerical Taxonomy and Multivariate Analysis System, version 2.02i, Exter Publications, Setauket, NY.
25. Senior, M.L. Murphy, J.P., Goodman, M.M. and Stuber, C.W. (1998). *Crop. Sci*. 38, 1088-1098.

26. Singh BB, Mohan Raj DR, Dashiell KE, Jackai Len (1997). *Advances in cowpea research*. IITA-JIRCAS, Ibadan, Nigeria.
27. Smulders, M.J.M., Bredemeijer, G., Rus- Kortekaas, W., Arens, P. and Vosman, B. (1997). *Theor. Appl. Genet*. 97, 264-272.
28. Szewc-McFadden, A.K., Kresovich, S., Bliek, S. M., Mitchell, S.E. and McFerson, J.R. (1996). *Theor. Appl. Genet*. 93, 534-538.
29. Tautz, D. and Renz, M. (1984). *Nucleic Acids Res*. 12, 4127-4138.
30. Thulin, M., Lavin, M., Pasquet, R., Delgado-Salinas, A., 2004. *Syst. Bot*. 29-4, 903-920.
31. Vaillancourt, R.E. and Weeden, N.F (1992). *Am. J. Bot*. 79, 1194-1199.
32. Vaillancourt, R.E., Weeden, N.F. and Barnard, J (1993). *Crop. Sci*. 33, 606-613.
33. Van de Ven, W.T.G. and McNicol, R.J. (1996). *Theor. Appl. Genet*. 93, 613-617.
34. Weising, K., Winter, P., Huttel, B. and Kahl, G. (1998). *J. Crop. Prod*. 1, 113-143.
35. Xiao, J., Li, J., Yuan, L., McCouch, S.R. and Tanksley, S.D. (1996). *Theor. Appl. Genet*. 92, 637-643.
36. Yu, K., Park, S.J. and Poysa, V. (1999). *Genome* 42, 27-34.

About the Authors

Ms. Archana Vijaykumar, JRF, DAE-Mumbai University collaborative fellowship, is a University rank holder in M.Sc. degree in Biochemistry from Mumbai University in the year 2005. She was awarded the DAE-Mumbai University collaborative fellowship for doing Ph.D. in 2006. She is carrying out her research project entitled "Molecular Phylogenetic analysis of species and subspecies belonging to Subgenus *Vigna*" in the Molecular Biology Division under the guidance of Dr Narendra Jawali.

Dr Narendra Jawali obtained M.Sc., Degree in Biochemistry from Central College, Bangalore University, Bangalore in 1975. He joined the 19th Batch of Training School in the Biology and Radiobiology discipline. He obtained his Ph.D. in 1988 from Mumbai University. He is working in the Molecular Biology Division of the Bioscience group, BARC. His research interests are plant and microbial molecular genetics.

बीएआरसी न्यूज़लैटर
BARC NEWSLETTER

THERMAL AND X-RAY CHARACTERIZATION OF $K_2U_4O_{13}$-$Rb_2U_4O_{13}$ SOLID SOLUTIONS

N.L. Misra, S. Dhara and K.D. Singh Mudher
Fuel Chemistry Division,
Bhabha Atomic Research Centre

This paper won the first prize for Poster Presentation at Thermans 2006, held at Jaipur during February 6-8, 2006

Abstract

The preparation, characterization and thermal behavior of $(K_{1-x}Rb_x)_2U_4O_{13}$ solid solutions have been studied in the range of $0<x<1$. The solid solutions were prepared by heating $K_2U_4O_{13}$ and $Rb_2U_4O_{13}$ in required stoichiometry at about 600-700 °C. The XRD patterns suggest formation of the solid solutions in full range of concentrations. The thermal patterns of the solid solutions in helium atmosphere indicates that these solid solutions are reduced to $K_2U_4O_{12}$ and $Rb_2U_4O_{12}$ on heating in inert atmosphere.

Introduction

Alkali metals are present in a nuclear reactor either as a fission product of nuclear fuel or coolant. Alkali metal uranates may be formed by fission product – fuel or fuel – coolant interactions either in operating or transient conditions. These uranates have less density as compared to nuclear fuel and these can cause swelling of the irradiated fuel and may result in rupture of the fuel cladding. Because of this reason the preparation, characterization and other properties of alkali metal uranates have been reported by different workers from time to time. Earlier, we had prepared mixed valent uranates $K_2U_4O_{12}$ and $Rb_2U_4O_{12}$, by heating the corresponding U(VI) uranates i.e. $K_2U_4O_{13}$ and $Rb_2U_4O_{13}$ in inert atmosphere [1]. Though $K_2U_4O_{13}$ and $Rb_2U_4O_{13}$ are isostructural [2-4] the corresponding mixed valent uaranates $K_2U_4O_{12}$ and $Rb_2U_4O_{12}$ are not isostructural [1]. In this paper, we have studied the formation of solid solutions of $K_2U_4O_{13}$ and $Rb_2U_4O_{13}$ and their reduction in inert atmosphere.

Experimental

K_2CO_3 and Rb_2CO_3 used for preparations were of AR grade. Due to hygroscopic nature of Rb_2CO_3, it was handled in a dry box. Stoichiometric quantities of Rb_2CO_3 or K_2CO_3 and UO_2, required for preparations of $Rb_2U_4O_{13}$ and $K_2U_4O_{13}$, were taken in pestle mortar and mixed well with little acetone, to form a paste. The resultant powder obtained by heating this paste under an IR lamp, was carefully transferred to alumina boats. These boats were heated in a furnace at 600 °C to prepare corresponding U(VI) uranates $Rb_2U_4O_{13}$ and $K_2U_4O_{13}$. The progress of the reaction was monitored by recording the XRD patterns of the products on a STOE X-ray diffractometer, using Cu K_a radiation (1.5405 Å).

Table 1: Cell parameters of $K_2U_4O_{13}$, $Rb_2U_4O_{13}$ and their solid solutions

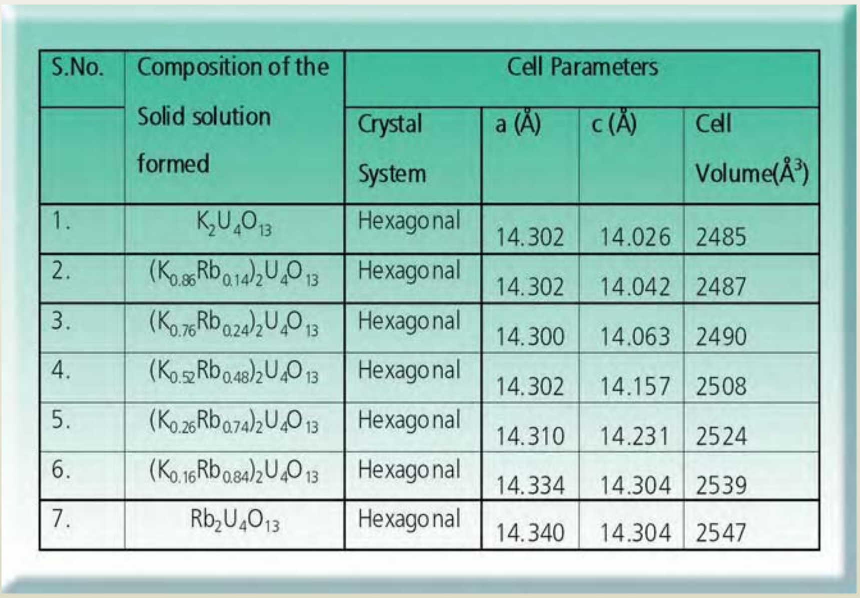

S.No.	Composition of the Solid solution formed	Cell Parameters			
		Crystal System	a (Å)	c (Å)	Cell Volume($Å^3$)
1.	$K_2U_4O_{13}$	Hexagonal	14.302	14.026	2485
2.	$(K_{0.86}Rb_{0.14})_2U_4O_{13}$	Hexagonal	14.302	14.042	2487
3.	$(K_{0.76}Rb_{0.24})_2U_4O_{13}$	Hexagonal	14.300	14.063	2490
4.	$(K_{0.52}Rb_{0.48})_2U_4O_{13}$	Hexagonal	14.302	14.157	2508
5.	$(K_{0.26}Rb_{0.74})_2U_4O_{13}$	Hexagonal	14.310	14.231	2524
6.	$(K_{0.16}Rb_{0.84})_2U_4O_{13}$	Hexagonal	14.334	14.304	2539
7.	$Rb_2U_4O_{13}$	Hexagonal	14.340	14.304	2547

$Rb_2U_4O_{13}$ and $K_2U_4O_{13}$ were mixed in different ratios and heated to at 700 °C for 48 hours to form the solid solutions of the corresponding compositions as shown in Table 1. The formation of the solid solutions was ascertained from their XRD patterns. These solid solutions were heated in a Metller-Toledo thermal analyzer in alumina cups up to 1000°C at a heating rate of 10°C/min. in flowing helium gas.

Results and Discussion

$K_2U_4O_{13}$ and $Rb_2U_4O_{13}$ are reported in literature [2-4]. These compounds are isostructural and have hexagonal lattice and are expected to form solid solutions. However, the corresponding lower valent uranates $K_2U_4O_{12}$ and $Rb_2U_4O_{12}$ [3] are not isostructural and the probability of formation of solid solutions of these uranates, is uncertain. The XRD patterns of the solid products formed by heating $K_2U_4O_{13}$ and $Rb_2U_4O_{13}$ in different ratios at 700°C could be indexed on the basis of cell parameters of $K_2U_4O_{13}$ and $Rb_2U_4O_{13}$. There is a systematic change in Bragg angles of different hkl planes of these solid solutions. A part of the X-ray diffraction pattern of these solid solutions is shown in Fig. 1. As the concentration of K^+ ions increases in the solid solution lattice, the cell parameter "a" decreases up to a certain stage, after which it shows no appreciable change. The cell parameters "c" and cell volume systematically decrease with increase of K^+ concentration in the solid solution lattice. A plot of cell volume with atomic ratio of K in Rb+K is shown in Fig. 2. This indicates that $(K_{1-x}Rb_x)_2U_4O_{13}$ solid solutions are formed in complete concentration range. The TGA and DTA plots of the compounds $K_2U_4O_{13}$ and $Rb_2U_4O_{13}$ in inert atmosphere show that they start losing oxygen molecule at about

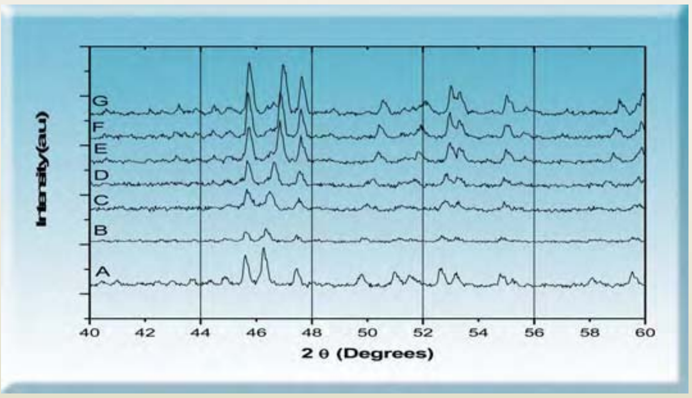

Fig.1: XRD Patterns of $(K_{1-x}Rb_x)_2U_4O_{13}$ solid solutions A: $Rb_2U_4O_{13}$, B: $(K_{0.16}Rb_{0.84})_2U_4O_{13}$, C: $(K_{0.26}Rb_{0.74})_2U_4O_{13}$, D: $(K_{0.52}Rb_{0.48})_2U_4O_{13}$, E: $(K_{0.76}Rb_{0.24})_2U_4O_{13}$, F: $(K_{0.86}Rb_{0.14})_2U_4O_{13}$ and G: $K_2U_4O_{13}$

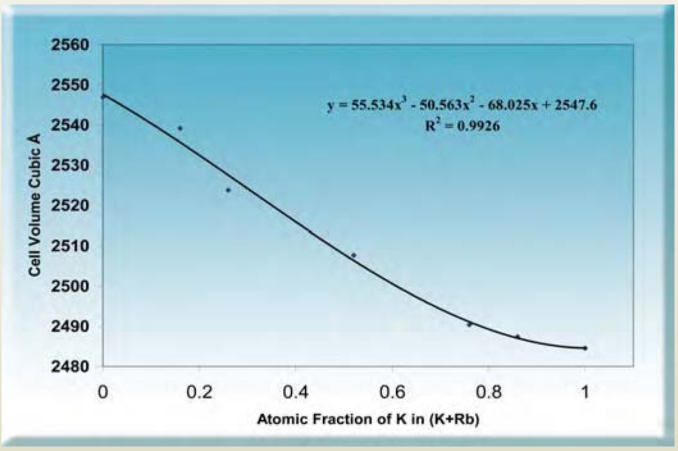

Fig. 2 : Variation of cell volume of $(K_{1-x}Rb_x)_2U_4O_{13}$ solid solutions with respect to atomic fraction of K in (K+Rb)

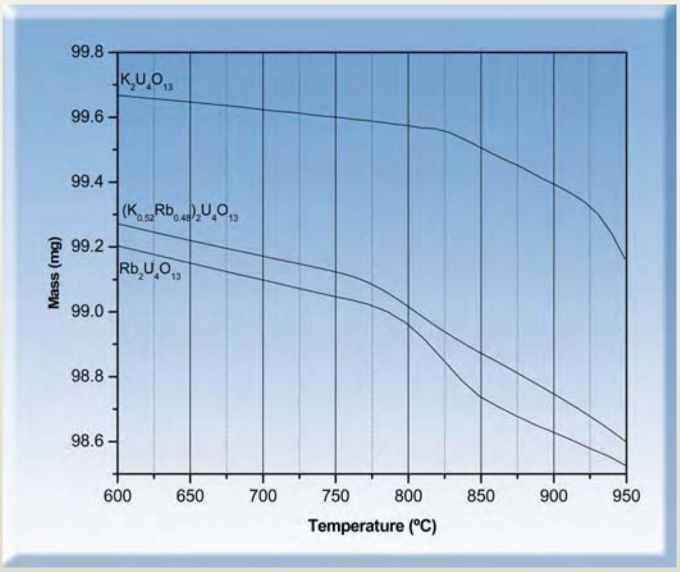

Fig. 3 : TGA plot of $K_2U_4O_{13}$, $Rb_2U_4O_{13}$ and $(K_{0.52}Rb_{0.48})_2U_4O_{13}$

825ºC and 780ºC respectively, to form either $K_2U_4O_{12}$ or $Rb_2U_4O_{12}$. However, the solid solutions of these compounds lose oxygen at comparatively lower temperature. The XRD pattern of the residue obtained after complete reduction of these solid solutions, indicate that, these are mixtures of $K_2U_4O_{12}$ and $Rb_2U_4O_{12}$. The lower temperature of reduction of solid solutions $(K_{1-x}Rb_x)_2U_4O_{13}$ as compared to $K_2U_4O_{13}$ and $Rb_2U_4O_{13}$, may be due to comparatively unstable lattice of $K_2Rb_2\text{-}xU_4O_{13}$. Also, as the $K_2U_4O_{12}$ and $Rb_2U_4O_{12}$ are not iso-structural, formation of any one of these, breaks the solid solution lattice and starts a mass loss. The TGA plots of a representative solid solution $(K_{0.52}Rb_{0.48})_2U_4O_{13}$ have been compared with that of $K_2U_4O_{12}$ or $Rb_2U_4O_{12}$ as seen in Fig. 3.

Conclusion

The $(K_{1-x}Rb_x)_2U_4O_{13}$ solid solutions are formed in complete range. The indexing of the XRD pattern of the solid solutions indicate that decrease in cell volume with increasing amount of K in the solid solution lattice. These solid solutions are reduced to lower valent uranates $K_2U_4O_{12}$ and $Rb_2U_4O_{12}$ at comparatively lower temperature to that of $K_2U_4O_{13}$ and $Rb_2U_4O_{13}$.

Acknowledgements

The authors are thankful to Dr V. Venugopal, Director, Radiochemistry and Isotope Group and Dr S.K. Aggarwal; Head fuel Chemistry Division for their constant encouragement during this work.

References

1. K.L.Chawla, N.L.Misra and N.C.Jayadevan *J.Nucl. Mater.* 154 (1988) 181.
2. A. Van Egmond, Thesis, University of Amsterdam, Amsterdam, (1976).
3. A. Van Egmond and E.H.P. Cordfunke, *J. Inorg and Nucl. Chem.* 38 (1976) 2245.
4. PC-PDF Card no. 37-638 and 29-1107.

About the Authors

Dr N.L. Misra joined the Fuel Chemistry Division in the year 1983 and has been working in the area of application of Total Reflection X-ray Fluorescence (TXRF) for trace element determination in different matrices and solid state chemistry of uranates, molybdates, their solid solutions and uranyl molybdates. During his stay at Paul Scherrer Institute, Switzerland from May 2000 to April 2001, as a Post Doc. Fellow, he studied the applicability of TXRF for trace element determination in Ice Core samples.

Dr K.D. Singh Mudher joined BARC in the year 1971 after completing his Ph.D. Degree from Indian Institute of Technology, Bombay. He has been working in the different areas of solid state chemistry of nuclear materials and has expertise in X-ray diffraction, X-ray spectrometry and thermal methods of characterization of solid materials.

Ms. Sangita Dhara joined the Fuel Chemistry Division, BARC in the year 2004 from the 47th bach of BARC training school and is currently working in the area of TXRF applications for trace element determination in different matrices and solid state chemistry of alkali metal uranates and their solid solutions.

बीएआरसी न्यूज़लैटर
BARC NEWSLETTER

DIFFERENTIAL UP-TAKE AND FLUORESCENCE OF CURCUMIN, A YELLOW PIGMENT FROM TURMERIC, IN NORMAL VS TUMOR CELLS

A. Kunwar, A. Barik, B. Mishra and K. I. Priyadarsini
Radiation & Photochemistry Division
Bhabha Atomic Research Centre

K. Rathinasamy
School of Biosciences and Bioengineering,
IIT-Bombay, Mumbai

and

R. Pandey
Radiation Biology & Health Sciences Division
Bhabha Atomic Research Centre

This paper received the Best Poster award at the NASI Platinum Jubilee Symposium on "Science and Technology in the Service of Society", held at IIT Mumbai, during October 6-8, 2006

Abstract

Using absorption and fluorescence spectroscopic methods, quantitative cellular uptake of curcumin, was calculated in two types of normal cells: spleen lymphocytes and NIH3T3 and two tumor cell lines: EL4 & MCF7. Both the uptake and fluorescence intensity of curcumin were significantly higher in tumor cells as compared to the normal cells. Using laser confocal microscopy, intracellular localization of curcumin was monitored and the results indicated that curcumin is located both in the cell membrane and in the nucleus.

Introduction

Curcumin is a polyphenolic yellow pigment isolated from the rhizomes of *Curcuma longa* (turmeric), a medicinal plant widely used in traditional Indian and Chinese medicine [1]. In spite of great advancement on the therapeutic research of curcumin, there are still very few studies reporting the methodologies to quantitatively estimate intracellular curcumin uptake and localization. In the present study, cellular uptake measurements of curcumin in four different cell types, two normal cells, *viz.*, mouse spleen lymphocytes, NIH3T3 (mouse fibroblast cells), and two tumor cell lines, *viz.*, EL4 (T cell lymphoma of murine origin) and MCF7 (breast cancer cells of human origin). Following absorption spectra of the cell lysate and the fluorescence spectra of cellular curcumin, quantitative uptake was calculated. Further, following curcumin fluorescence by confocal microscopy, its intracellular localization was monitored.

Materials and Method

Chemicals and equipment

Curcumin, 4 '6-diamidino-2-phenylindol (DAPI), cell culture medium (RPMI 1640 & DMEM) were procured from the local agents**.** Mouse spleen lymphocytes were freshly isolated as given in reference [2] and EL4, MCF7 and NIH3T3 cell lines were obtained from National Centre for Cell Science (NCCS), India. JASCO V-530 spectrophotometer and Hitachi F-4010 fluorimeter were used, to record absorption and fluorescence spectra respectively. Solutions were prepared in nanopure water from a Millipore Milli-Q system.

Cell culture and uptake studies

Spleen, NIH3T3 & EL4 cell lines were cultured in suspension with RPMI medium and MCF7 cell line in DMEM medium. The treatment of cells with curcumin and then quantitative estimation of cellular curcumin for uptake studies was done as described in earlier reference [2].

Confocal microscopy and image analysis

Slides for confocal microscopy were prepared by fixing curcumin-loaded cells and then sealed with cover slip using mounting medium. Fluorescence imaging of cells was performed with an Olympus Fluoview 500 confocal laser-scanning microscope (Olympus, Tokyo, Japan) equipped with a multi-Argon laser for excitation at 458, 488 and 515 nm [3]. The images were acquired either with 20X objective or a 60X water immersion objective using the fluoview software (Olympus, Tokyo, Japan). The curcumin emission was collected using the barrier filter BA505. Fluorescence images of DAPI stained cells were excited using Coherent Mira 900F Titanium: Sapphire infrared laser (Coherent Verdi-V5, Santa Clara, CA, USA) tuned to 720 nm and the fluorescence in the range 400-470 was collected. At least five monochrome images were accumulated from five different microscopic fields of the same slide. The desired region on each fluorescent cell was selected and the mean fluorescence intensity/area for the region was determined and the average values of 15 different regions are presented in Table 1. To quantify the co-localization of fluorescent probes (curcumin and DAPI), images acquired separately for each of the probe were merged using the software.

Results

Uptake measurements

Cellular uptake of curcumin by the three cell lines

Table 1: Cellular uptake, fluorescence spectral properties and intensity variations of curcumin in different cells

Cell lines	λ_{fl}, nm (λ_{ex}= 420 nm)	Cellular uptake (pmoles/ 10^6 cells)	Fl. Intensity/ pmole of curcumin uptake (λ_{ex} = 420 nm)	Confocal imaging data Fl. Intensity / area of cell (λ_{ex} = 458 nm)		
				Control	Treated	Difference
Spleen lymphocytes	504	23.2 ± 4.3	0.023	69 ± 12	125 ± 35	56 ± 35
EL4	500	34.5 ± 6.4	0.064	106 ± 8	212 ± 23	106 ± 23
NIH3T3	535	22.6 ± 3.5	0.007	220 ± 27	259 ± 60	39 ± 5
MCF7	520	44.2 ± 4.5	0.067	208 ± 66	382 ± 91	174 ± 91

(EL4, NIH3T3 and MCF7) and spleen lymphocytes was calculated at different curcumin treatment concentrations of 10 and 20 nmole/million/ml. After normalization to one nmoles/ ml/million cells of curcumin treatment, cellular uptake was found to vary in the range of 20-40 p moles/million cells for different cells and the actual values are listed in table 1. It can be seen that the tumor cells (EL4 and MCF7) showed higher uptake as compared to normal cells (NIH3T3 and lymphocytes).

Fluorescence spectroscopic studies of intracellular curcumin

Fig.1 gives the fluorescence spectra of curcumin-loaded cells after excitation at 420 nm, along with the normalised fluorescence spectra given as inset of Fig.1. The fluorescence spectrum of curcumin in lymphocytes and EL4 cells is sharp and the maximum is at 500 to 505 nm, while in MCF7 and NIH3T3 cells, the fluorescence spectrum is broad with maximum at 520 to 535 nm. The fluorescence intensity, when compared in these two sets of cells, showed significantly higher intensity in the two tumor cell lines. One of the reasons for such increase in fluorescence could be its increased uptake. To verify this, we calculated the fluorescence intensity to the same level of uptake and compared the fluorescence per unit uptake and the normalized results are listed in Table 1. It is clear that the fluorescence is at least 3-8 times more intense in the tumor cells than the normal cells. The shift in fluorescence spectra and intensity variations clearly indicate that curcumin experiences different hydrophobic environments inside these tumor cells and interacts with the cells differently.

Fluorescence microscopy studies

The above observed fluorescence changes, prompted us to understand its intracellular localization, by fluorescence imaging after exciting intracellular curcumin at 458 nm. Although, the absorption maximum of curcumin is at ~ 420 nm, at 458 nm, it has considerable absorption (45 to 70 % of the maximum absorption in different cells). Figs. 2A and 2B give the confocal micrographs of lymphocytes and EL4 respectively and Figs. 3A and 3B for NIH3T3 and MCF7 cell lines along with their corresponding phase contrast images and a few magnified images. From these images, the average fluorescence intensity per unit area was calculated and the results are listed in Table 1.

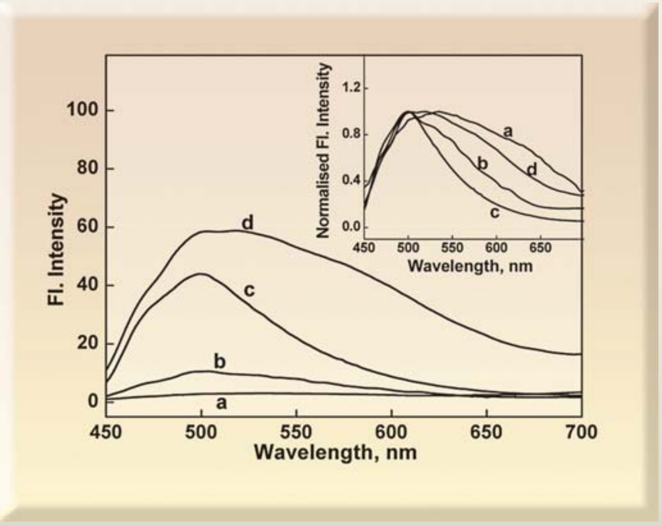

Fig. 1: Fluorescence spectra of curcumin in different cells: (a) NIH3T3, (b) spleen lymphocytes, (c) EL4 and (d) MCF7 after treating with aqueous-DMSO solution of curcumin at concentration of 20 nmoles/million cells/ml. The excitation wavelength was 420nm. Inset shows normalized fluorescence spectra to clearly indicate variation in I^{fl}_{max} for different cells

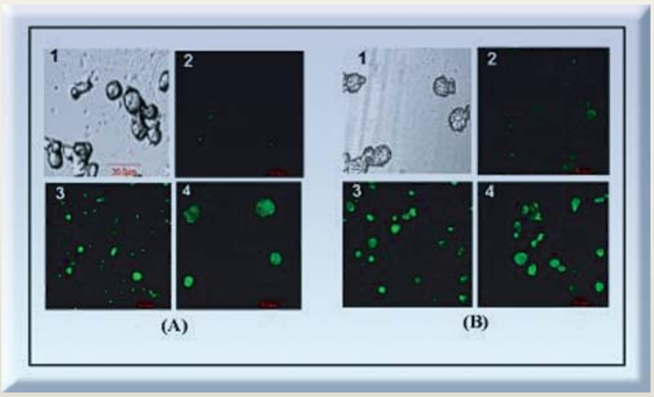

Fig. 2 : Confocal micrographs of cells after treating with curcumin at concentration of 10 nmoles/million cells/ml.
(A) Spleen lymphocytes (20X Objective); 1- Phase contrast image, 2-Cells without curcumin treatment,
3- Cells treated with curcumin (2X zoom), 4- Cells treated with curcumin (6X zoom). (B) EL4 cells; 1- Phase contrast image, 2-Cells without curcumin treatment, 3- Cells treated with curcumin (2X zoom), 4- Cells treated with curcumin (3X zoom)
Excitation wavelength 458 nm.

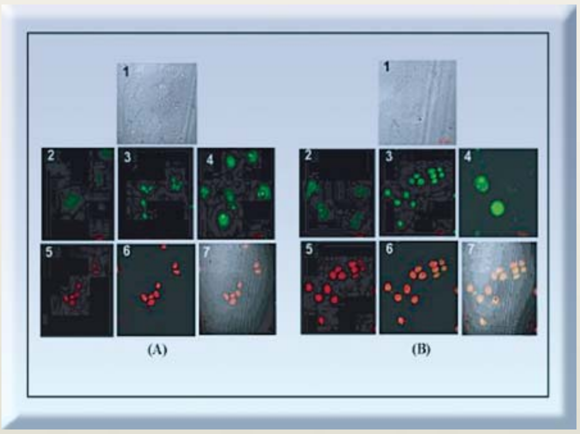

Fig. 3 : Confocal micrographs of cells after treating with curcumin at concentration of 10 nmoles/million cells/ml.
(A) NIH3T3 cells (60X objective); 1- Phase contrast image, 2-Cells without curcumin treatment, 3- cells treated with curcumin (1X zoom), 4- Cells treated with curcumin (2X zoom), 5 Cells stained with DAPI (1X zoom), 6 –Images 4 and 5 merged together (1X zoom), 7- Image 4 and 5 merged with image 1 (1X zoom). (B) MCF7 cells (60X objective); 1- Phase contrast image, 2-Cells without curcumin treatment, 3- Cells treated with curcumin (1X zoom), 4- Cells treated with curcumin (2X zoom), 5 Cells stained with DAPI (1X zoom), 6 –images 4 and 5 merged together (1X zoom), 7- image 4 and 5 merged with image 1 (1X zoom).
For Curcumin, λ_{ex}– 458 nm and DAPI, λ_{ex}–720 nm, two photon

The results supported our earlier observation that curcumin exhibits more fluorescence in both EL4 and MCF7 cells. Curcumin, being a lipophilic molecule is expected to be localized in the membrane. However, the images of EL4 and lymphocytes show fluorescence emission from the entire cells. Since in these cells, majority of the cell volume is occupied by the nucleus with very little cytoplasm, the emission could be from both the membrane and the nucleus.

In case of MCF7 and NIH3T3 cells, due to their distinct morphology, fluorescence images clearly indicate selective localization in the cell membrane and the nucleus. To further confirm its nuclear localization, these cells were stained with DAPI, a DNA selective fluorescent probe [4]. Fluorescence images of DAPI stained cells were excited using infrared laser tuned to 720 nm and the fluorescent emissions in the range 400-470 were collected. The cells were then subjected to dual staining for which cells treated with curcumin were thoroughly washed, stained with DAPI, and after fixation the images were recorded. The fluorescence from curcumin was pseudo-colored as green and that from DAPI as red

(Image 5, & 6 of Figs. 3A and 3B). The two images were superimposed as shown in image 7 of Figs. 3A and 3B respectively for NIH3T3 and MCF7 cells. The images clearly showed green and red areas overlapping, confirming the co-localization of curcumin and DAPI in the nucleus.

Discussion

In the recent past, there was extensive research on curcumin and several reports on antioxidant, anti-tumor and chemopreventive activity and preclinical studies, have appeared in literature. However, there are very few papers addressing its cellular uptake and localization. In this paper, applying absorption and unique fluorescence spectral properties of curcumin, we made an attempt to measure quantitative uptake and intracellular localisation of curcumin in four different cell types.

Our results clearly support the earlier reported observation, that tumor cells show preferential uptake of curcumin as compared to normal cells [2]. The fluorescence spectra of cellular curcumin show two interesting factors. The fluorescence intensity is always higher in tumor cells as compared to normal cells and the fluorescence maximum of curcumin in suspension cells is more blue shifted as compared to that in adherent cells. Several recent reports indicate that the fluorescence maximum and fluorescence quantum yield of curcumin are highly sensitive to the medium polarity and availability of the hydrophobic pockets [5,6]. Therefore, the present observations clearly indicate that curcumin interacts differently with different cells. Our preliminary fluorescence imaging studies are very encouraging and clearly show localization of curcumin inside the cells. In all the cells, curcumin fluorescence could be seen in the membrane but in MCF7 and NIH3T3 cells, due to their distinct morphology, localization inside the nucleus is also observed. This is a new and unexpected observation, which needs to be addressed in future.

In conclusion, our present study provides a method to estimate quantitative uptake of curcumin and the results provide confirmation, that tumor cells preferentially take up more curcumin. The fluorescence spectrum of curcumin in tumor cells is easy to detect and can be used as a marker to understand its interaction with different cellular proteins. The fluorescence imaging studies show localization in the cells and a surprising observation of its nuclear localization, this provides a chance to explore new avenues of research to understand its interactions with different nuclear factors and target proteins.

Acknowledgements

The authors are thankful to Dr T. Mukherjee, Dr K. B. Sainis and Dr S. K. Sarkar, of Bhabha Atomic Research Centre for the encouragement and support and Prof. Dulal Panda, IIT-Bombay, for helping in confocal imaging studies.

References

1. B. B. Aggarwal, C. Sundaram, N. Malani, H. Ichikawa, (B. B. Aggarwal, S.Young-Joon, S. Shishodia, Eds), Springer, NY USA, (2007) pp. 1-76.
2. A. Kunwar, A. Barik, R. Pandey, K. I. Priyadarsini, *Biochim. Biophys. Acta* 1760 (2006) 1513-1520.
3. Z. Földes-Papp, U. Demel, G. P. Tilz, Int. *Immunopharmacology* 3 (2003) 1715–1729.
4. T. Suzui, K. Fujikura, T. Higashiyama, K. Takata, J. *Histochem. Cytochem.* 45 (1997) 49-53.
5. A. Barik, K. I. Priyadarsini, H. Mohan, *Photochem. Photobiol.* 77 (2003) 597-603.
6. G. Began, E. Sudharshan, K. Udaya Sankar, A. G. Appu Rao, *J. Agric. Food Chem.* 47 (1999) 4992-4997.

About the Authors

Mr. A. Kunwar obtained M. Sc degree in Biotechnology from Centre For Plant Molecular Biology, Tamil Nadu Agricultural University in 2003. After graduating from BARC Training School in 2005 (48th Batch, Bioscience discipline),

Dr A. Barik obtained M. Sc degree in Chemistry from Burdwan University (West Bengal) in 1999. After graduating from BARC Training School in 2000 (43rd Batch, Chemistry discipline), he joined Radiation & Photochemistry Division, BARC. Since then he is actively involved in free radical chemistry and excited state properties of important biomolecules employing photochemical and radiation chemical techniques. He obtained Ph. D. degree in Chemistry from University of Mumbai in 2006.

Dr B. Mishra received her M.Sc. degree in Inorganic Chemistry from Institute of Science, Mumbai, in 2001. She was a DAE research fellow working in Radiation and Photochemistry Division, BARC. She has obtained her Ph.D. degree in chemistry from University of Mumbai in 2007. She has joined the same division as a K. S. Krishnan Research Associate. Presently she is working on free radical and biochemical studies of organoselenium compounds.

Mr. K. Rathinasamy has completed his Bachelor's degree in Pharmacy from the Dr. M. G. R. Medical University, Chennai. He has completed his M. Tech Biotechnology degree from Jadavpur University, Kolkata. Currently, doing Ph. D. under the guidance of Prof. Dulal Panda in the School of Biosciences and Bioengineering, IIT Bombay, Mumbai. His research interest is to understand the antiproliferative mechanism of the relatively non-toxic antifungal drugs griseofulvin and benomyl and their possible use in the treatment of cancer.

After graduating from the 41st batch of BARC training school, **Dr R. Pandey** has been working at Radiation Biology & Health Sciences Division. She has made significant contribution towards the understanding of effects of low dose radiation on the immune system and has recently been awarded Ph. D. in Applied Biology from University of Mumbai for her work on the immunosuppressive activity of a novel tri-pyrrole pigment. Presently she is working on immunomodulation by natural products.

Dr K. I. Priyadarsini joined Bhabha Atomic Research Centre in 1983. She is currently working on the elucidation of mechanisms of antioxidant action involving natural products and herbal extracts with potential application as radioprotectors, employing electron pulse radiolysis and *in vitro* biochemical studies. Dr Priyadarsini has co-authored more than 100 papers in peer reviewed international journals on radiation chemistry, photochemistry and radiation biology. She has been elected as the Fellow of the National Academy of Sciences, India and is a recipient of the Homi Bhabha Science & Technology Award.

बीएआरसी न्यूज़लैटर
BARC NEWSLETTER

β-CYCLODEXTRIN INCLUSION COMPLEX OF CURCUMIN

S. Swaroop
School of Chemical Sciences
Mahatma Gandhi University, Kottayam, Kerala

and

Beena Mishra and K. Indira Priyadarsini
Radiation & Photochemistry Division
Bhabha Atomic Research Centre

This paper was adjudged as one of the Best Posters at the "Trombay Symposium on Radiation & Photochemistry (TSRP-2006)" held at BARC, Mumbai, during January 5-9, 2006

Abstract

Formation of inclusion complex of curcumin with β-cyclodextrin (β-CD) has been characterized by absorption and fluorescence spectroscopy. From temperature-dependent fluorescence measurements, the thermodynamic parameters ΔH and ΔS, for the complexation were estimated. Kinetics of binding was studied by stopped flow technique, from which the binding constants for inclusion complex was estimated. Further, influence of such inclusion complex on change in superoxide radical scavenging property of curcumin was examined using xanthine/ xanthine oxidase assay.

Introduction

Curcumin is a lipid soluble polyphenolic antioxidant from *curcuma longa*, turmeric, with antioxidant, anti-inflammatory, anti-carcinogenic properties [1]. One of the disadvantages of curcumin, limiting its physiological activities, is its insoluble nature in aqueous solutions. It is possible to increase its water solubility by forming inclusion complexes with water-soluble hosts [2]. There are several studies on host-guest complex formation of curcumin [2]. Formation of such host-guest systems can be probed by following absorption and fluorescence changes in curcumin. The photophysical properties of curcumin vary significantly depending on the medium and therefore act as suitable tools for following the inclusion behavior to different systems [3]. Cyclodextrins are one of the most widely used synthetic model host cavities, which provide a conical cavity for the water insoluble guests to be encapsulated, thereby making them water soluble [4].

Here, we made an attempt to estimate the binding constant of 1:1 curcumin and β-cyclodextrin (β-CD) complex by following the absorption, fluorescence properties and also by stopped-flow studies. The superoxide radical scavenging ability of such a complex was compared with that of free curcumin.

Materials and Method

Curcumin, β-CD, xanthine, xanthine oxidase and cytochrome c, were of the highest purity available from the local market and used as received. Nano pure water from Millipore Q system & Spectrograde solvents from Spectrochem India were used for the preparation of solutions.

The absorption spectra were recorded on a JASCO V-530 spectrophotometer and emission spectra on Hitachi 4010 spectrofluorimeter. The stopped flow experiments were carried out using SX.18MV stopped flow reaction analyzer (from Applied Photo Physics Ltd. UK) with absorption detector.

Superoxide was generated by enzymatic methods employing xanthine and xanthine oxidase assay. For binding studies, the stock solution of curcumin in DMSO was diluted to 100 μM in 10 mM β-CD such that the solution contained less than 1% DMSO solvent. This solution was mixed with the above matrix to obtain solutions of curcumin with varying concentrations.

Results and Discussion

Absorption spectral studies

Curcumin in the absence of β-CD shows absorption maximum at 420 nm and β-CD does not absorb appreciably in the wavelength region. On addition of β-CD, the absorption maximum of curcumin showed red shift from 420 nm to 430 nm and the absorbance at 430 nm was nearly doubled on addition of 10mM β-CD. This spectral change is attributed to a complex formation between curcumin and β-CD, represented by equation (1):

$$\text{Curcumin} + n\beta - \text{CD} \leftrightarrows \text{Complex} \qquad (1)$$

The equilibrium constant for the above equilibrium is given by equation (2)

$$K = \frac{[Complex]}{[Curcumin][\beta\text{ - }CD]^n} \qquad (2)$$

Here n indicates number of β-CD molecules involved in complexation. For the above equilibrium, assuming 1:1 complex formation, binding constant was estimated by employing the double reciprocal plot known as Benesi-Hildebrand equation [3]. Thus linear fit of the double reciprocal plot of absorption changes (ΔA) at 430 nm as a function of β-CD concentration (90.5 to 10 mM) gave binding constant (K) to be $6.9 \pm 0.3 \times 10^2\ M^{-1}$.

Fluorescence spectral studies

The changes in fluorescence intensity and spectra of curcumin were also used, to evaluate the binding constant. For this study, curcumin was excited at 350 nm, the isosbestic point for the complex formation, in the absence and presence of different concentrations of β-CD (0-10 mM). At pH 7, curcumin has very weak and broad fluorescence maximum at 550 nm (Fig.1). The fluorescence intensity was found to increase with increasing concentration of β-CD. Also in presence of 10 mM β-CD the fluorescence maximum shifted from a broad featureless band to a well-defined blue shifted band λ_{max}^{em} at 520 nm. The blue shift (~30 nm) in the fluorescence spectrum confirms the binding of curcumin to the hydrophobic cavity of β-CD. Even at the limiting solubility of β-CD (10 mM), no saturating value for fluorescence was observed. The fluorescence changes are related to the association constant (K) for the 1: 1 complex as [5]

$$I_f = \frac{I_f^o + I_{complex}K[\beta - CD]_o}{1 + K[\beta - CD]_o} \qquad (3)$$

Were I_f^o and $I_{complex}$ are the respective fluorescence intensities at 520 nm in the absence and presence of different concentrations of β-CD. Inset of Fig. 1 shows the variation of fluorescence intensity of curcumin at 520 nm as a function of β-CD concentration (0 to 10 mM).

Fitting this data to equation (3) by using non-linear least square fitting gave binding constant (K) of $2.6 \pm 0.3 \times 10^2\ M^{-1}$.

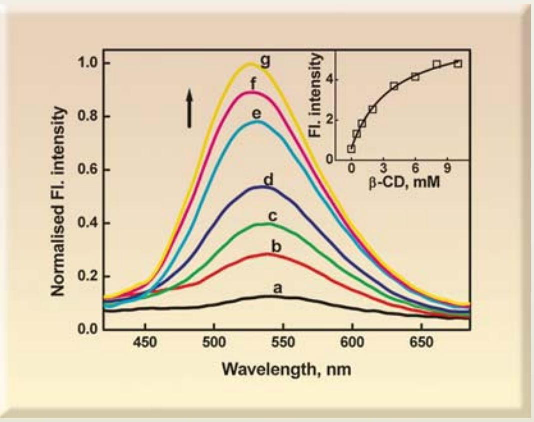

Fig. 1: Fluorescence spectra of curcumin (10 μM) in the absence (a) and in the presence of different concentrations of b-βD (b = 0.5 mM, c= 1 mM, d = 2 mM, e = 4 mM, f = 6 mM, g = 10 mM). Inset shows plot of fluorescence intensity as a function of β-CD concentration, which is non-linear fitting to equation (4)

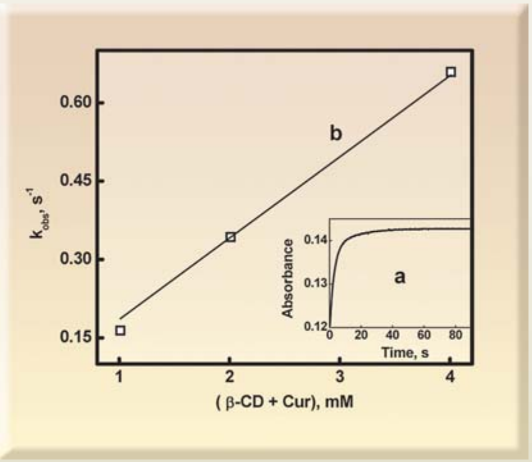

Fig. 2: (a) Absorbance-time profile obtained on mixing of 10 mM curcumin with 2 mM β-CD at 430 nm. (b) Variation in k_{obs} as a function of sum of equilibrium concentration of curcumin and β-CD, line shows fitting to equation (5).

Kinetics of binding of curcumin to β-cyclodextrin

The kinetics of binding of curcumin to β-CD was followed using stopped-flow spectrometer. For this study, aqueous solutions of 10 μM curcumin containing 1% methanol was mixed with different concentrations of β-CD (0.5 – 10 mM) in the stopped flow cell and the absorption changes at 430 nm were monitored as a function of time. The absorption-time profile obtained as shown in the inset (a) of Fig. 2 was fitted to an exponential function, to obtain the observed first order rate constant (k_{obs}).

For the formation of 1: 1 complex, k_{obs} is related to the equilibrium concentration of curcumin and β-CD according to equation (4) [3].

$$k_{obs} = k_f\left(\left[Cur\right]+\left[\beta - CD\right]\right)+k_b \qquad (4)$$

k_f and k_b are the forward and backward rate constants for the equilibrium in equation (1), where n =1. Fig. 2b, shows linear plots for the change in first order rate constant as a function of sum of the equilibrium concentrations of β-CD and curcumin. From the intercept and slope of the plot, the binding constant for 1:1 complex is found to be 5.2 ± 0.2 x 10^3 M^{-1}. This value is higher than that determined by absorption and fluorescence method. This higher value indicates that there are more than one kinetic steps involved in complex formation.

Effect of temperature on the binding of curcumin with β-CD

Thermodynamic parameters associated with binding of curcumin with β-CD for 1:1 stoichiometry have also been calculated by estimating the binding constant at different temperatures, measured at 293, 308 and 323 K. The binding constant at each temperature was determined by following the fluorescence changes in curcumin with β-CD concentration and fitting the data to equation (3).

The equilibrium constant was found to decrease with increasing temperature and according to equation (5), the plot of logarithm of binding constant as a function of inverse temperature gave a linear plot, whose intercept and slope corresponds to DS/R and –DH/R respectively [5]. From this enthalpy (DH) and entropy (DS) values were estimated to be –8.5 kJ/mol and –0.02 kJ/mol/K respectively.

$$\ln K = \left(\frac{-\Delta H}{RT}\right) + \frac{\Delta S}{R} \quad (5)$$

Thus under the present conditions, the DH values for the transfer of curcumin from water to β-CD is negative and ΔS is also negative but to a very small extent. The main driving force for complex formation could, therefore, be the release of enthalpy rich water from the cyclodextrin cavity. The water molecules located inside the cavity cannot satisfy their hydrogen-bonding potentials, therefore are of higher enthalpy. The energy of this system is lowered when suitable guest molecules, that are less polar than water, replace these enthalpy-rich water molecules.

Effect of complexation on superoxide scavenging ability of curcumin

After studying the photophysical properties and estimating the thermodynamic properties, we studied its free radical scavenging ability by following its reactions with enzymatically-produced superoxide radicals. Xanthine oxidase is an enzyme that converts xanthine to uric acid, during which superoxide radical is generated [6]. This is one of the important sources of superoxide ions in living systems. In presence of cytochrome c, superoxide radical reduces the Fe^{3+} in cyctocrome c to Fe^{2+} form, which absorbs at 550 nm and is a direct measure of superoxide radical formation in the system. When antioxidants capable of reacting with superoxide radical are added to the system, due to the competition for the reaction of superoxide radical, the yield of Fe^{2+} form and the absorbance at 550 nm decreases [6]. The percentage inhibition (%I) of superoxide radical inhibition can be calculated from the following equation (6)

$$\%I = \frac{(A_0 - A_S)x100}{A_0} \quad (6)$$

Here A_0 and A_s are the maximum absorbance values at 550 nm in the absence and in the presence of curcumin-β-CD complex. By plotting the %I as a function of the complex concentration, the IC_{50} value was estimated to be 59 μM. Under similar conditions, the absorbance changes were also monitored in the presence of uncomplexed curcumin, from which the IC_{50} value for curcumin was estimated to be 88 mM. This clearly shows that on complexation with β-CD, the superoxide radical scavenging ability of curcumin is increased.

Conclusions

Curcumin, a phenolic and lipid soluble antioxidant, has been examined for its complexing ability with β-CD. The binding constant of the complex was determined by following absorption, fluorescence spectral changes and stopped-flow studies. Stopped-flow kinetic studies which showed binding between curcumin and β-CD, have been estimated. From the temperature dependent studies, the enthalpy and entropy changes on complexation with β-CD could be estimated. From all these results it is concluded, that β-CD complexation of curcumin takes place in the hydrophobic cavity of β-CD. Such a complex formation changes curcumin into a water-soluble form. Superoxide scavenging ability of curcumin on complexation with β-CD increased as compared to uncomplexed curcumin.

Acknowledgements

The authors are thankful to Dr S. K. Sarkar, Head, Radiation & Photochemistry Division for encouragement and support.

References

1. Aggarwal, B. B., Sundaram, C., Malani, N. and I chikawa, H. (227) Curcumin: the Indian Solid Gold. in: The Molecular Targets and Therapeutic

Uses of Curcumin in Health and Disease (B.B. Aggarwal, S.Young-Joon, S. Shishodia, Eds),Springer, NY USA, pp. 1-76.

2. Baglole, K. N., Boland, P. G. and Wagner, B. D. (2005) *J. Photochem. Photobiol. A* **173**, 230.

3. Barik, A., Priyadarsini, K. I. and Mohan, H. (2003) *Photochem. Photobiol*. **77**, 597.

4. Li, S. and Purdy, W. C. (1992) *Chem. Rev*. **92**, 1457.

5. Singh, M. K., Pal, H.,Koti, A. S. R., and Sapre, A. V. (2004) *J. Phys. Chem.* A. **108**, 1465.

6. Hodges, G. R., Young, M. J., Paul, T. and Ingold, K. U. (2000) *Free Radic. Biol. Med.* **29**, 434.

About the Authors

Mr. Swaroop, S., received his M.Sc. from School of Chemical Sciences, Mahatma Gandhi University Kottayam, Kerala in 2005. During his M.Sc. he worked under the guidance of Dr. K. I. Priyadarsini on the project entitled "Photophysical and Radiation Chemical Studies on curcumin-â-cyclodextrin complexes", at Radiation and Photochemistry Division, Bhabha Atomic Research Center, (BARC). Currently he is working at School of Chemical Sciences, Mahatma Gandhi University, Kottayam on electron transfer reaction of polyphenols.

Dr B. Mishra received her M.Sc. degree in Inorganic Chemistry from Institute of Science, Mumbai, in 2001. She was a DAE research fellow working in Radiation and Photochemistry Division, BARC. She obtained her Ph.D. degree in chemistry from University of Mamba in 2007. She joined same division as a K. S. Krishnan Research Associate. Presently she is working on free radical and biochemical studies of organoselenium compounds.

Dr K. I. Priyadarsini joined Bhabha Atomic Research Centre in 1983. She is currently working on the elucidation of mechanisms of antioxidant action involving natural products and herbal extracts with potential application as radioprotectors, employing electron pulse radiolysis and *in vitro* biochemical studies. Dr Priyadarsini has co-authored more than 100 papers in peer reviewed international journals on radiation chemistry, photochemistry and radiation biology. She has been elected as the Fellow of the National Academy of Sciences, India and is a recipient of the Homi Bhabha Science & Technology Award.

ABSORPTION AND FLUORESCENCE STUDIES OF CURCUMIN BOUND TO LIPOSOME AND LIVING CELLS

A. Kunwar, A. Barik and K. I. Priyadarsini
Radiation & Photochemistry Division
Bhabha Atomic Research Centre

and

R. Pandey
Radiation Biology & Health Sciences Division
Bhabha Atomic Research Centre

This paper was adjudged as one of the Best Posters at the "Trombay Symposium on Radiation & Photochemistry (TSRP-2006)" held at BARC, Mumbai, during January 5-9, 2006

Abstract

The absorption and fluorescence properties of curcumin were used, to study its average binding constants with phosphatidylcholine (PC) liposomes. The liposomal vehicle was examined for the delivery of curcumin to spleen lymphocyte cells, EL4 lymphoma cells and compared with aqueous DMSO vehicles. From these studies it was found that liposomal vehicle is capable of loading more curcumin in to cells than aqueous-DMSO. Lymphoma cells show preferential uptake of curcumin as compared to lymphocytes. The fluorescence of curcumin in EL4 lymphoma cells was found to be significantly higher as compared to the lymphocytes.

Introduction

Curcumin, a natural polyphenol, found in the rhizomes of *Curcuma longa* (turmeric), exhibits anti-inflammatory, anti-neoplastic, anti-oxidant and chemopreventive activities and has been shown to be pharmacologically safe even at high doses [1-3]. It is a hydrophobic molecule and is practically insoluble in aqueous solutions. Because of this hydrophobic nature, its bioavailability is poor after oral administration and therefore it needs a carrier vehicle to transport it to the desired targets. Curcumin has preferential interaction with lipid membranes [4-5]. Liposome is one of the most commonly used transporting vehicles for drugs, proteins, hormones, diagnostic agents etc [6]. In this paper following absorption and fluorescence changes in curcumin in different systems, quantitative estimations were made on the loading of curcumin from phosphatidylcholine (PC) liposomes to cellular systems.

Materials and Method

Reagents and equipment

Curcumin, cholesterol, acrylamide, potassium iodide, cell culture medium and egg yolk phosphatidylcholine (PC) were procured from local dealers. Whenever necessary, spectro grade solvents were used. Solutions were freshly prepared in nanopure water from a Millipore Milli-Q system. Mouse spleen lymphocytes were freshly isolated and EL4 cell line (Lymphoma of T cell of mouse origin) was obtained from NCCS, India. Absorption spectra were recorded on a JASCO V-530 spectrophotometer and fluorescence spectra recorded on a Hitachi F-4010 fluorimeter. All the experiments were repeated twice and each experiment was performed in duplicate.

Preparation of curcumin containing liposome

Curcumin containing liposome was prepared by dissolving PC, cholesterol and a known amount of curcumin [7] in organic solvent followed by solvent evaporation. The curcumin-loaded liposome was separated from the unbound curcumin through centrifugation. For fluorescence quenching studies, the liposomal curcumin solutions were incubated in quartz cells at 30°C in the presence of iodide (I^-) and acrylamide as quenching agents in 10 mM phosphate buffer (pH 7) and the fluorescence intensity at 498 nm was monitored after excitation at 420 nm. The ionic strength of the solution was kept constant at 0.3 M using sodium chloride. This stock solution after appropriate dilution was used for cell uptake studies.

Estimation of binding constant

The process of binding of curcumin to the binding agent, BA (BA represents PC liposomes) can be shown by the equations given below.

$$\text{Curicumin} + \text{BA} \rightleftharpoons \text{Complex} \qquad (1)$$

The equilibrium constant K for the above equilibrium is given by equation

$$K = \frac{[\text{Complex}]}{[\text{BA}][\text{Curcumin}]} \qquad (2)$$

For the above equilibrium, assuming 1:1 complex formation, linear plot is made by following absorbance changes at a suitable wavelength, as a function of reciprocal concentration of PC or curcumin according to the equation (3) given below.

$$\frac{1}{\Delta A} = \frac{1}{K\Delta\varepsilon[\text{BA}]}\left[\frac{1}{\text{Curcumin}}\right] = \frac{1}{\Delta A[\text{BA}]} \qquad (3)$$

Here ΔA and Δε correspond to the change in the absorbance and the molar extinction coefficient at the wavelength of the study respectively. Using this equation, the values of K and De were estimated by following the absorbance changes in curcumin in the region 420 to 450 nm. The binding constants were estimated by following the fluorescence changes too. The changes in fluorescence intensity due to curcumin, were followed as a function of concentration of PC according to equation (4) to estimate the binding constant.

$$F = \frac{F_0 + F_{\text{complex}} K[\text{BA}]}{1 + K[\text{BA}]} \qquad (4)$$

Here F_0 and F are the respective fluorescence intensities from curcumin at a suitable wavelength in the range from 490 to 520 nm in the absence and presence of liposomes and F_{complex} is the saturation value.

Cell culture and uptake studies

For cell uptake studies, freshly isolated mouse spleen lymphocytes and EL4 cell line (T cell lymphoma of mouse origin) was used. Mouse spleen lymphocytes were isolated as described earlier [8]. For loading of curcumin, the cells were incubated with curcumin for 4 hours. After washing three times, the cells were suspended in Phosphate Buffered Saline (PBS) and subjected to fluorescence spectral studies. The actual concentration of curcumin loaded (uptake) into the cells was determined by extracting cell lysate into methanol. The cellular uptake was expressed in pmoles/million cells.

Results and Discussion

Binding of curcumin with PC liposomes

The absorption spectrum of curcumin is blue shifted from 425 nm to 420 nm in presence of liposomes (Fig.1a and 1b respectively for 1% aqueous-methanol and PC liposomes). The binding constant of curcumin to PC liposomes, was estimated to be (2.1±0.1) x 10^4 M^{-1}.

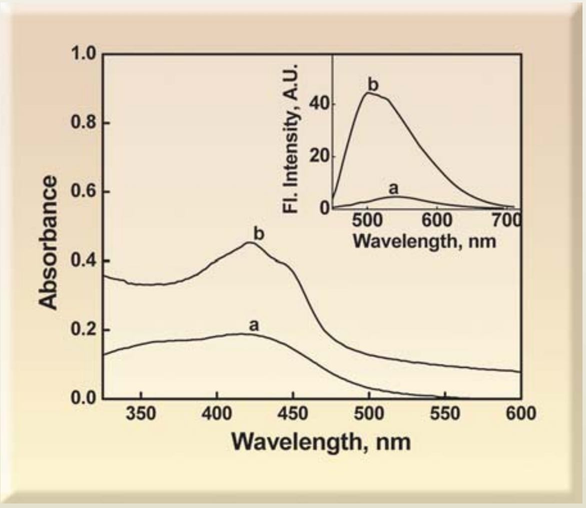

Fig. 1 : Absorption spectra of curcumin at pH 7.4 (a) in aqueous solution containing 1% methanol, (b) in the presence of PC liposome Inset shows fluorescence spectra of the same solutions, after excitation at 420 nm. For the reference spectra, corresponding blanks without curcumin were used.

Curcumin in aqueous buffer, exhibits weak fluorescence with featureless and broad maximum ~550 nm (Inset a of Fig.1). However with increasing addition of PC liposomes at a fixed amount of curcumin, the fluorescence intensity increased and there is a large blue shift (498 nm) in the fluorescence maximum on curcumin binding to PC liposomes (Inset b of Fig.1). The binding constant for the binding of curcumin with liposomes was also estimated by following fluorescence intensity changes at 498 nm, after excitation at 420 nm to be (2.9±1.1) x 10^4 M^{-1}. The blue shift in the fluorescence maximum and the increase in intensity with increasing liposome concentration suggest that curcumin in PC liposomes experiences nonpolar environment probably by binding to the hydrophobic regions of PC liposomes.

To know about the distribution of curcumin in different compartments of the PC liposome bilayer, experiments were carried out by following fluorescence quenching studies in the presence of different quenchers at pH 7. Following the quenching of fluorescence from liposomal curcumin by using iodide and acrylamide as quenchers, it is possible to evaluate the location of curcumin inside the membrane. Iodide is a hydrophilic quencher, which can access curcumin in the liposome surface, while acrylamide, being hydrophobic, can access curcumin only when inserted inside the liposome bilayer. The quencher concentrations were varied from 0 to 0.15 M keeping the ionic strength constant. The concentrations of the quenchers and salts were selected in such a way, that they do not induce changes in the bilayer structure of liposomes. The fluorescence data were analyzed according to the Stern-Volmer equation (5).

$$\frac{F_0}{F} = 1 + K_D[Q] \qquad (5)$$

Here F_0 and F are the intensities of the fluorophore (liposomal curcumin) in the absence and presence of the quencher Q, respectively and K_D is the Stern-Volmer collision constant. Insets of Figs. 2A and 2B show the fluorescence quenching data for iodide and acrylamide respectively and lines show fitting to equation (5). Here, deviation from linearity indicates presence of more than one class of fluorophore, which are not equally accessible to the quencher.

In order to understand the relative population of curcumin in different layers of PC liposome, the fluorescence intensity changes due to curcumin in presence of quenchers were treated with the modified Stern-Volmer equation (6) according to the procedure given in reference [9].

$$\frac{F_0}{\Delta F} = \left[\frac{1}{f_a K'_D [Q]}\right] + \left[\frac{1}{f_a}\right] \qquad (6)$$

Here ΔF is the difference between the fluorescence intensity from the fluorophore in the absence and presence of Q, f_a is the fraction of fluorophore that is accessible to the quencher and K'_D is the Stern Volmer constant. Figs. 2(A) and Fig. 2(B) show fitting of the data to equation (6) for iodide and acrylamide respectively. The fitted parameters were found to be $f_a = 0.22 \pm 0.01$ and $K'_D = 10.3 \pm 1.7$ M^{-1} for iodide quenching and $f_a = 0.40 \pm 0.01$ and $\text{K¢}_D = 31.6 \pm 2.1$ M^{-1} for acrylamide quenching. This confirms that curcumin is non-uniformly distributed into different compartments of the liposomal bilayer and is preferably located inside the hydrophobic interior, which is important for higher drug loading capacity of liposome formulation.

Cellular uptake studies

Liposomal formulations were subjected to cell uptake studies for their probable use as delivery vehicles of curcumin to cellular system. To address this, we compared the uptake of curcumin using two different cell systems, spleen lymphocytes and T lymphoma cell line EL4. The cells were incubated with different concentrations of curcumin. Fig. 3 (a-d) shows the representative absorption spectra of methanol extracted cell lysate from spleen cells, after treatment with different concentrations of free and liposomal curcumin. Fig. 3e corresponds to cells treated with DMSO vehicle controls. Other vehicle controls (liposome) showed similar spectra and therefore were not included in the figure. Inset of Fig. 3 shows the amount of curcumin delivered to spleen cells by different vehicles.

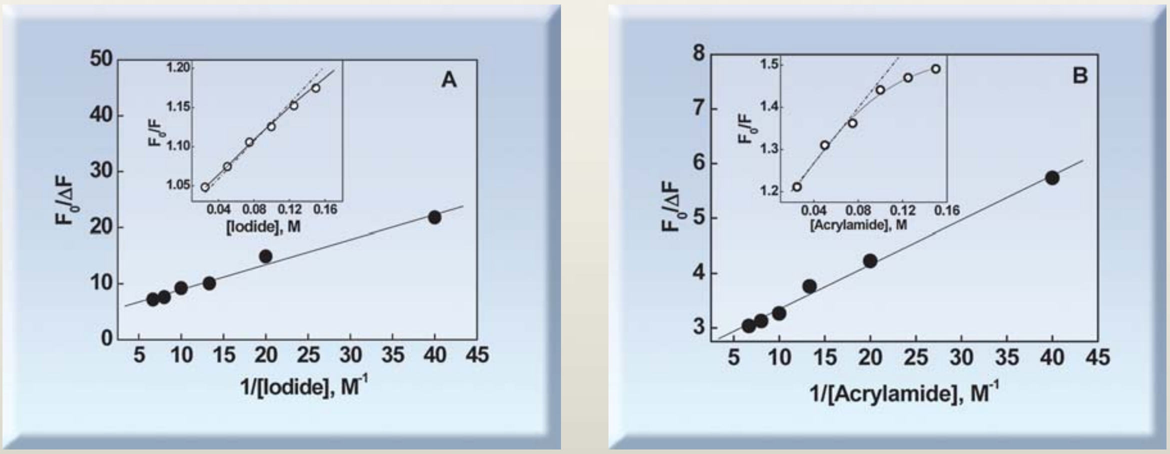

Fig. 2 : Plots showing the fluorescence quenching of liposomal formulation containing curcumin in phosphate buffer at pH 7 at constant ionic strength (0.3M) (A) iodide as quencher and (B) acrylamide as quencher. Line shows fitting to equation (6). Insets of Figs. 2 (A) and 2 (B) respectively show the data for the quenching of curcumin fluorescence by iodide and acrylamide fitting to equation (5), dotted lines show linear fits for equation (5).

The figure confirms concentration dependent uptake of curcumin by spleen cells. Similarly, absorption spectra of methanol extracted cell lysate from EL4 cells were also obtained and these confirmed the concentration dependent uptake of curcumin by EL4 cells. After normalization to one nmoles/ml/ million cells of curcumin treatment, the average cellular uptake was found to vary in the range of 20-40 pmoles/million cells for these cells. However, it was observed, that the uptake of curcumin is significantly higher with liposomal formulation in either cell type and at the same time cellular uptake of curcumin is significantly higher, in EL4 cells with all the vehicles as compared to spleenic lymphocytes. These results indicate that the liposomal formulation is better than aqueous DMSO vehicle for delivering curcumin to cellular system and tumor cells show preferential uptake of curcumin, which is in agreement with the literature reports [1,3]. Fluorescence spectra of curcumin in the above incubated spleenic lymphocytes and EL4 lymphoma cells were also recorded.

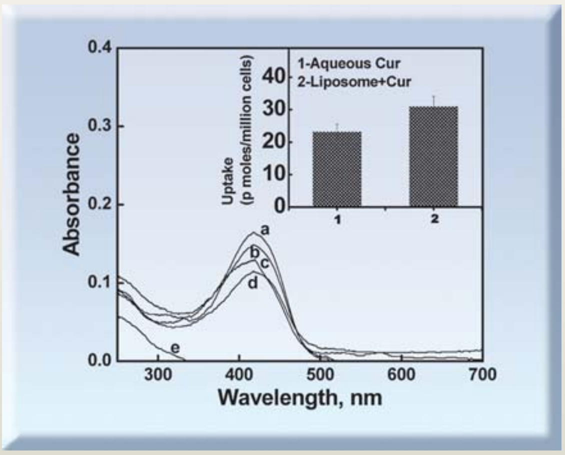

Fig. 3 : Overlapped absorption spectra of methanol lysates of spleen cells treated with different concentrations of free (c, d) and liposomal curcumin (a, b). Inset shows uptake/million cells per 1 nmole of substrate added/million cells/ml by different vehicles

For these studies, the cell suspensions were excited at 420 nm and fluorescence emission was followed in the wavelength range of 440 to 700 nm. Fig. 4a and 4b show fluorescence spectra of curcumin in spleenic lymphocytes treated with free and liposomal curcumin respectively.

Figs. 4c and 4d show corresponding spectra in EL4 cells. The fluorescence from cells treated with vehicle controls showed no detectable fluorescence. Inset of Fig. 4 gives the bar graph showing the comparative fluorescence intensity at fluorescence maximum at 498 nm in these systems.

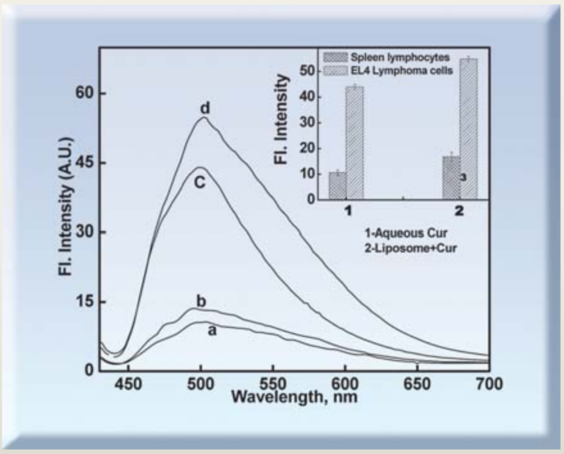

Fig. 4 : Fluorescence spectra of curcumin in lymphocytes (a, b) and EL4 cells (c, d) after treating with aqueous-DMSO solution of curcumin and liposomal bound curcumin respectively in the culture medium for 4 hours. The excitation wavelength was 420 nm. Inset shows bar graph representing comparative fluorescence intensities in EL4 cells and lymphocytes by different vehicles.

The results clearly support our previous observations that liposomal system could load more curcumin to both the cell types and EL4 cells show preferential uptake. Interestingly, for the same absorbance at the excitation wavelength, the relative fluorescence intensity was nearly three times more in EL4 cells as compared to lymphocytes suggesting higher fluorescence emission from curcumin in lymphoma cells. The enhanced uptake of curcumin by lymphoma cells could be either due to their high metabolic activity or larger size. The increase in fluorescence intensity in lymphoma cells indicates difference in microenvironment experienced by curcumin molecule inside these cells.

Conclusions

The present study demonstrates the use of absorption and fluorescence methods for quantitative estimation and identification of the loading capacity of curcumin by different vehicles to normal and tumor cells. The absorption method is best suited for the quantitative estimation, while fluorescence method is useful in identifying the site of location. The results confirm that the most efficient means of delivering curcumin to cells is via incorporation in to liposomes and also the lymphatic cancerous cells more readily adsorb curcumin, than normal lymphocytes. Our future experiments are therefore directed to follow this more in detail, to examine whether curcumin can be used for selective imaging of tumor cells.

Acknowledgements

The authors are thankful to Dr H. Pal for help in fluorescence studies and Dr S. K. Sarkar, Dr T. Mukherjee and Dr K. B. Sainis, for constant encouragement and support.

References

1. B. B. Aggarwal, A. Kumar, A. C. Bharti, *Anticancer Res.* 23 (2003) 363-398.
2. R. A. Sharma, A. J. Gescher, W. P. Steward, *Eur. J. Cancer* 41 (2005) 1955-1968
3. S. Shishodia, G. Sethi, B. B. Aggarwal, *Ann. N. Y. Acad. Sci.* 1056 (2005) 206-217
4. A. Barik, K. I. Priyadarsini, H. Mohan, *Photochem. Photobiol.* 77 (2003) 597-603.
5. G. Began, E. Sudharshan, K. Udaya Sankar, A.G. Appu Rao, *J. Agric. Food Chem.* 47 (1999) 4992-4997.
6. H. Brochu, A. Polidori, B. Pucci, P. Vermette, Curr. *Drug Deliv.* 1(3) (2004) 299-312.
7. N. L. Zalloum, D.N. Biloti, F.B.T. Pessine, *Applied Spectroscopy* 59 (2005) 1032-1036.
8. S. Santosh Kumar, B. Shankar, K. B. Sainis, *Biochim. Biophys.* Acta 1672 (2004) 100-111.
9. J. R. Lakowicz, Principles of Fluorescence Spectroscopy, Kluwer Academic/Plenum Publishers, New York, 1999.

About the Authors

Mr. A. Kunwar obtained his M.Sc degree in Biotechnology from Centre For Plant Molecular Biology, Tamil Nadu Agricultural University in 2003. After graduating from BARC Training School in 2005 (48th Batch, Bioscience discipline), he joined the Radiation & Photochemistry Division, BARC. Since then he is involved in free radical cellular biochemistry and evaluation of synthetic as well as natural molecules for their anti-oxidant and pro-oxidant activity employing spectroscopic and biochemical techniques.

Dr A. Barik obtained his M.Sc degree in Chemistry from Burdwan University (West Bengal) in 1999. After graduating from BARC Training School in 2000 (43rd Batch, Chemistry discipline), he joined the Radiation & Photochemistry Division, BARC. Since then he is actively involved in free radical chemistry and excited state properties of important biomolecules employing photochemical and radiation chemical techniques. He obtained Ph. D. degree in Chemistry from University of Mumbai in 2006.

Dr K. I. Priyadarsini joined Bhabha Atomic Research Centre in 1983. She is currently working on the elucidation of mechanisms of antioxidant action involving natural products and herbal extracts with potential application as radioprotectors, employing electron pulse radiolysis and *in vitro* biochemical studies. Dr Priyadarsini has co-authored more than 100 papers in peer reviewed international journals on radiation chemistry, photochemistry and radiation biology. She has been elected as the Fellow of the National Academy of Sciences, India and is a recipient of the Homi Bhabha Science & Technology Award.

After graduating from the 41st batch of BARC training school, **Dr R. Pandey** has been working at Radiation Biology & Health Sciences Division. She has made significant contribution towards the understanding of effects of low dose radiation on the immune system and has recently been awarded Ph. D. in Applied Biology from University of Mumbai for her work on the immunosuppressive activity of a novel tri-pyrrole pigment. Presently she is working on immunomodulation by natural products.

EFFECT OF pH ON ONE-ELECTRON OXIDATION OF SELENIUM AMINOACIDS

B. Mishra, K. I. Priyadarsini and H. Mohan
Radiation & Photo Chemistry Division,
Bhabha Atomic Research Centre

This paper was adjudged as one of the Best Posters in the "Trombay Symposium on Radiation & Photochemistry (TSRP-2006)" held at BARC, Mumbai, during January 5-9, 2006

Abstract

Pulse radiolysis has been employed to study one-electron oxidation of selenomethionine (SeM), selenocystine (SeCys), and methyl selenocysteine (MeSeCys) in aqueous solutions. Hydroxyl radicals ($^{\bullet}OH$) in the pH range from 1 to 7 and specific one-electron oxidants $Cl_2^{\bullet -}$(pH 1) and $Br_2^{\bullet -}$ (pH 7) have been used, to carry out the oxidation reactions. Reactions of oxidizing radicals with all these compounds, produced selenium centered radical cations. The structure and stability of the radical cation was found to depend mainly on the substituent and pH. From these studies it is concluded, that formation of monomer and dimer radical cations mainly depend on the substitution, pH and the heteroatom like N, O. Availability of lone pair on N or O atom at or g position, results in monomer radical cations having intra-molecular stabilization. When such lone pair is not available, the monomer radical cation is converted into a dimer radical cation, which acquires intermolecular stabilization by the other selenium atom.

Introduction

Selenium is an essential trace element and is found in prokaryotic and eukaryotic cells mainly in the form of selenocysteine [1]. It has also been reported that some enzyme catalyzed redox reactions e.g. glutathione peroxidase, require the participation of Se-containing proteins [1]. One of the reasons for the wide spread interest of selenium is its specific redox properties [2]. The radical species generated from organoselenium compounds play an important role in a number of chemical and biological processes and are considered to be possible intermediates in redox reactions of bio-molecules containing selenium [3]. Hence, characterization of the radicals formed on redox reactions of some important organoselenium compounds is necessary in understanding the role played by them in Chemistry and Biology. Pulse radiolysis is a clean method to generate the transients formed by redox reaction and to perform time resolved studies in short time scales ranging from nanoseconds to milliseconds [3,4]. In this paper, we report the one-electron oxidation reactions of selenium containing amino acids, selenomethionine, methylseleno-cysteine and selenocystine. These are present in plants and animals and act as selenium reservoirs in them [2].

Experimental Section

Materials

Selenomethionine, selenocystine, methyl selenocysteine were obtained from Sigma/Aldrich Chemicals and used without any further purification.

Pulse radiolysis studies

Pulse radiolysis experiments were carried out with high-energy electron pulses (7 MeV, 500 ns) obtained from a linear electron accelerator. The dose for the experiment was ~ 9-10Gy/pulse. Reaction of $^{\bullet}$OH radical was carried out in N_2O saturated aqueous solution and the reaction with specific one electron oxidant was generated by the procedure given in the reference [5]. The chemical structures of these selenium compounds are given in Scheme 1.

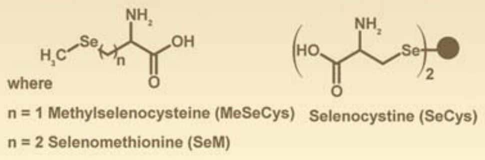

Scheme 1: Chemical structures of selenium compounds

Results

SeM and MeSeCys have two pK_a values at pH ~2 and the other at pH ~9 and corresponding to COOH and NH_3^+ groups respectively and an isoelectric point at 5.75. SeCys has four pK_a values two at pH ~2 and two ~ pH 8. These compounds are in the zwitterionic form, in the pH range 2–10.

Reactions of the organoselenium compounds with H atom

The contribution of $H^{\bullet}$ atom reaction with all the organoselenium compounds was found to be negligible, as confirmed by running independent experiments. Therefore, the present results are based on reaction of $^{\bullet}$OH radicals and specific one electron oxidant with the selenium amino acids.

Reactions with SeM

The reaction of SeM with $^{\bullet}$OH radicals at pH 7, produced a transient showing a broad absorption band with λ_{max} at 380 nm and a shoulder at 280 – 290 nm region (Fig. 1a). The transient at 380 nm decayed by first order kinetics with $k = 1.2 \pm 0.1 \times 10^4 \ s^{-1}$. Similar transient spectrum was obtained by the reaction of specific one-electron oxidant, $Br_2^{\bullet-}$ with SeM. Thus the transient absorption spectrum given in Fig. 1a is assigned to the one-electron oxidized species. The absorbance at 380 nm was found to remain independent of SeM concentration. The absorbance at 280-290 nm is due to carbon centered radical which is formed due to H-abstraction. At pH 1, the reaction of $^{\bullet}$OH radicals with SeM, generated transient having a strong and broad absorption band at 480 nm (Fig. 1b). The similarity in the spectrum obtained by specific one electron oxidant, $Cl_2^{\bullet-}$ confirmed that the reaction of $^{\bullet}$OH radicals with SeM at pH 1 produced one-electron oxidation. The absorbance at 480 nm was found to increase with increasing concentration of SeM in the range from 0.025 mM – 2.4 mM (inset c of Fig.1). This increase in the absorbance is due to the reaction of initially formed transient species with SeM, indicating the formation of a dimeric species. The transient absorption band at 480 nm decayed by second order kinetics with 2k value of $7.5 \pm 0.2 \times 10^8 \ M^{-1} \ s^{-1}$. Since the kinetic and spectroscopic properties of the transient species formed on reaction of $^{\bullet}$OH radicals with SeM at pH 1 were different from those observed at pH 7, the absorption changes at 380 nm and 480 nm were followed as a function of pH in the range 1 to 7. As the pH of the solution is decreased, the transient absorbance at 380 nm decreased with the appearance of a new band at 480 nm. The variation in the absorbance at 380 and 480 nm, formed at fixed SeM concentration of $\sim 5 \times 10^{-4}$ M, as a function of pH is given as inset e & d of

Fig. 1, which showed an inflection point at 2.2 ± 0.3. This point corresponds to the pK_a of the carboxylic group, indicating the role of functional group in the nature and formation of monomer and dimer radical cation. In addition to the increase in the absorbance of 480 nm band with decrease in pH, the rate of formation was also observed to increase with decrease in the pH.

Reactions with SeCys

The transient absorption spectrum obtained on reaction of %OH radicals with SeCys at pH 7, exhibits a broad absorption band with λ_{max} at 460 nm (Fig. 2a), which decayed by first order kinetics with k = 2.4 ± 0.3 x10^3 s^{-1}. Similar transient spectrum was observed with specific one electron oxidant. Due to limiting solubility of SeCys at pH 7, concentration dependent studies were not carried out. At pH 1, reaction of SeCys with $^{\bullet}$OH radical formed a transient absorbing at 560 nm (Fig. 2b). This transient was found to decay by first order kinetics with a rate constant of 1.1 ± 0.1 x 10^4 s^{-1}.

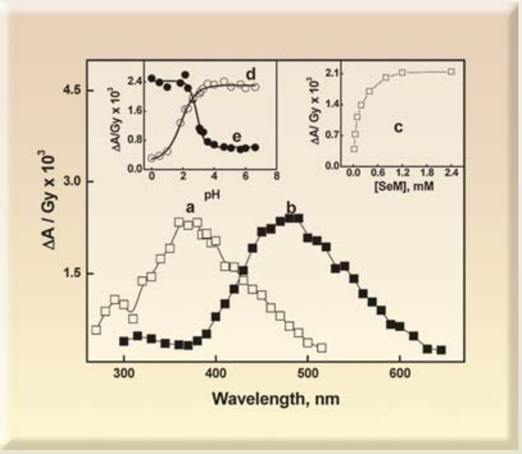

Fig.1 : Difference absorption spectrum of the transient obtained on pulse radiolysis of (a) N_2O saturated solution of SeM (0.5 mM) at pH 7 and (b) N_2-saturated aqueous solution of SeM (1mM) at pH 1. Inset (c) shows variation of absorbance at 480 nm as a function of SeM concentration at pH 1 and inset (d) and (e) show variation of absorbance at 380 and 480 nm respectively as a function of pH

Reaction with $Cl_2^{\bullet-}$ also gave the same transient absorbing at 560 nm, confirming formation of radical cation. This absorbance at 560 nm was found to be independent of the parent concentration, indicating absence of any dimer radical cation formation. Although a monomeric radical cation is formed at pH 1 and 7, there is a significant change in the absorption spectrum of the transient with pH, indicating the involvement of prototropic equilibrium. To understand the pH dependency, the variation of absorbance at 460 and 560 nm, formed on pulse radiolysis of N_2O-saturated aqueous solution of SeCys (5x10^{-4} M), as a function of pH was plotted as shown in the inset c of Fig. 2, to get an inflection point at 3.13 ± 0.01. This point corresponds to the pK_a of the carboxylic group, indicating the role of functional group in the nature and formation of the transient.

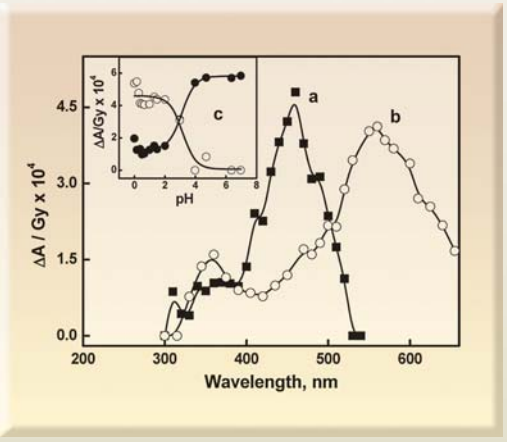

Fig. 2 : Difference absorption spectrum of the transient obtained on pulse radiolysis of N_2O saturated solution of SeCys (0.5 mM) at pH 7 (a) and pH 1 (b). The inset (fig. 1C) shows variation of absorbance at 560 nm (○) and 460 nm (●) as a function of pH.

Reactions with MeSeCys

$^{\bullet}$OH radical reaction of MeSeCys at pH 7, produced a transient absorbing at 350 nm (Fig. 3a). This transient is found to decay by first order kinetics with a rate constant of 4.3 ± 0.4 x 10^5 s^{-1}. The reaction with $^{\bullet}$OH radical at pH 1, also produced similar transient absorbing at 350 nm. Here the reactions of $Cl_2^{\bullet-}$ and $Br_2^{\bullet-}$ with MeSeCys at pH 1 and pH 7 also produced similar transient absorbing at 350 nm. This 350 nm absorbing transient at all pHs from 1 to 7 was found to be independent of the parent concentration. indicating formation of monomer radical cation. At pH 1, this transient was found to decay by first order kinetics with a rate constant of 1.1 ± 0.1 x 10^4 s^{-1}. When the pH was further decreased to 0 or less than that, a new transient absorption at 460 nm was observed (Fig. 3b) in addition to a broad peak with absorption maximum at 370 nm. While the transient absorbance in the 350 to 370 nm region was independent of the parent concentration (Inset c of Fig. 3), the transient absorbance at 460 nm was found to depend on the parent (Inset d of Fig. 3), indicating the formation of dimer radical cation at high acidic conditions.

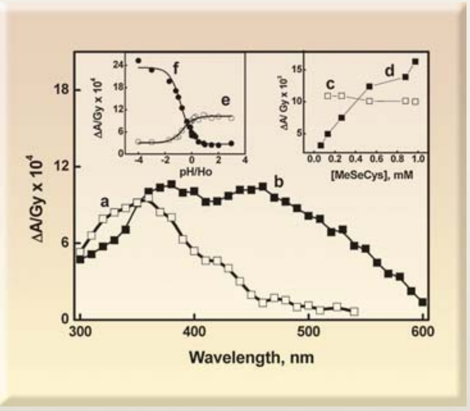

Fig. 3: Difference absorption spectrum of the transient obtained on pulse radiolysis of (a) N_2O saturated solution of MeSeCys (0.5 mM) at pH 7 and (b) N_2-saturated aqueous solution of MeSeCys (1mM at pH 0). Inset c and d show variation of absorbance at 350 nm and 460 nm respectively as a function of MeSeCys concentration at pH 0. Inset e and f show variation in the absorbance at 350 and 460 nm as a function of pH

At pH = 0, the band observed at 370 nm is due to a monomeric species as its absorbance remained independent of solute concentration. With increasing acid concentration, the absorbance due to the dimer radical cation at 460 nm increased, while that at 350 to 370 nm region decreased as seen in the inset of Fig. 3 (e & f), suggesting conversion of monomer radical cation to dimer radical cation.

The overall reactions of all these selenium compounds (SeC) with $^{\bullet}$OH, $Cl_2^{\bullet-}$ and $Br_2^{\bullet-}$ radicals are given in equation (3) and (4).

$$\begin{tikzcd} SeC \arrow[r, "^{\cdot}OH"] \arrow[rr, bend left, "Br_2^{\cdot-} / Cl_2^{\cdot-}"] & {[SeC\text{-}OH]^{\cdot}} \arrow[r, "-H_2O/OH^-"] & SeC^{\cdot+} \end{tikzcd} \qquad (3)$$

Under some favourable conditions, the monomer radical cation reacts with the parent molecule to form the dimer radical cation

$$(SeC)^{\bullet+} + SeC \leftrightharpoons (SeC)_2^{\bullet+} \qquad (4)$$

Discussion

Structures of monomer and dimer radical cations

In the above compounds, since selenium has high electron density and low ionization potential, the radical cations produced by the reaction of hydroxyl radicals and one-electron oxidants are mostly centered on the selenium atom [3,5]. Subsequent to oxidation, both monomer and dimer radical cations are observed depending on the pH and substitution. It is reported earlier that the selenium centered radical cation would be highly unstable and would have high tendency to stabilize on coordination with another selenium or heteroatom [3,5]. The monomer radical cation therefore has to attain stabilization through the intramolecular heteroatom. Such stabilization is possible either through the lone pair of electrons available on N or O atom [3-5]. In case of SeM, at pH 7, the radical cation on selenium can interact with the lone pair on either N atom of the amino group or the O atom of the carboxylic group, forming thermodynamically stable five and six membered rings respectively. However in the absence of conductivity studies and with limited data, it is not possible to assign the exact nature of the monomer radical cation structure of SeM, probably both the structures may be considered.

At pH 1, due to the protonation of the amino and carboxylic group, lone pair of electron is not available for stabilization of the radical cation, thus decreasing the stability of the monomer. Therefore at this pH, the stabilization can occur only intermolecularly through another selenium atom. Moreover, experimentally it is confirmed that the transient absorption band at 480 nm is due to a dimeric species. Thus the transient formed at pH 1 is assigned to dimer radical cation formed on p orbital overlap of oxidized Se with the Se atom of other SeM molecule. The dimer radical cation is stabilized by the intermolecular two-center three-electron (2c-3e) bond between two Se atoms, where the two valance p-orbitals are mixed head-on, resulting in a hemi bond of σ nature [4,5].

SeCys, being a diselenide, on oxidation by hydroxyl radicals and one-electron oxidants produced radical cation, which can be stabilized as a monomer radical cation due to the presence of intramolecular Se-Se bond. The radical cations of SeCys show significant spectral shift and by following the absorbance changes as a function of pH, an inflection point at 3.1 was observed. This indicates that the radical cation structure of such a diselenide too is influenced by the pK_a of the carboxylic acid group, therefore a different transient is formed, due to the participation of the heteroatom., i.e. Nor O atom.

MeSeCys is structurally similar to SeM, it is only a smaller analogue. Therefore, one would expect very similar oxidation chemistry. But its oxidation produced radical cations at all the pHs from 1 to 7 absorbing at 350 nm. The dimer radical cation formation was observed at < pH 0 only. Here the selenium centered radical cations can be stabilized only by the carboxylic oxygen and not through the amino group, as it involves only four membered ring formation, while the former gives a five membered ring stabilization. However due to the pK_a of the carboxylic acid group, the nature of the radical will be different at different pH, as seen by slightly different absorption spectra at pH 7 (350 nm) and pH 1 (350-370 nm).

On comparison with sulfur compounds[4,6] the above studies indicated that the oxidation chemistry of selenium compounds is comparable to their sulfur analogues. The nature of the transients is very similar. In both the cases, the radical cations are stabilized either by the lone pair available from intramolecular hetero atoms or by the intermolecular dimerization. Also the radical cations from selenium analogues show much longer lifetimes and the dimers are more stable. This similarity in the pH dependent transient behavior of selenium and sulfur compounds and the easier oxidation of selenium compounds, makes them better alternatives as antioxidants, radioprotectors and GPx mimics.

Acknowledgement

The authors are thankful to Dr. S. K. Sarkar, Head RPC Division, BARC for his support to this work.

References

1. Bock, A. In *Encyclopedia of Inorganic Chemistry*; Bruce-King, R., Ed., Wiley: New York, **1994**; Vol. 7, p 3700.
2. Mugesh, G.; du Mont, W.; Sies, H. *Chem. Rev*. **2001**, 101, 2125.
3. Badiello, R. In *Chemistry of Organic Selenium ad Tellurium Compounds*; Patai, S., Rappoport, Z., Eds.; Wiley: New York, 1986; Vol. 1. p 287.

4. Asmus, K. -D. *In Sulfur-Centered Reactive Intermediates as Studied by Radiation Chemical and Complementary Techniques, S-Centered Radicals*, Alfassi, Z. B. Ed.; John Wiley: New York, 1999, p 142.

5. Mishra, B.; Maity, D. K.; Priyadarsini, K. I.; Mohan, H.; Mittal, J. P. *J. Phys. Chem. A* **2004**, 108, 1552.

6. John Elliot, A.; McEachern, R. J.; Armstrong, D. A. *J. Phys. Chem*. **1981**, 85, 68.

About the Authors

Dr B. Mishra received her M.Sc. degree in Inorganic Chemistry from Institute of Science, Mumbai, in 2001. She was a DAE research fellow working in Radiation and Photochemistry Division, BARC. She obtained her Ph.D. degree in chemistry from University of Mamba in 2007. She joined the same division as a K. S. Krishnan Research Associate. Presently she is working on free radical and biochemical studies of organoselenium compounds.

Dr K. I. Priyadarsini joined Bhabha Atomic Research Centre in 1983. She is currently working on the elucidation of mechanisms of antioxidant action involving natural products and herbal extracts with potential application as radioprotectors, employing electron pulse radiolysis and *in vitro* biochemical studies. Dr Priyadarsini has co-authored more than 100 papers in peer reviewed international journals on radiation chemistry, photochemistry and radiation biology. She has been elected as the Fellow of the National Academy of Sciences, India, and is a recipient of the Homi Bhabha Science & Technology Award.

Dr Hari Mohan joined Bhabha Atomic Research Centre in 1967. Since then he is actively involved in the study of fast reaction kinetics using accelerators and lasers. His research interests include free radical reactions of halogenated and sulfur compounds and biomolecules of natural origin. He has co-authored more than 200 research papers in peer reviewed international journals. He retired in November 2004 as Head, Radiation Chemistry Section of Radiation Chemistry & Chemical Dynamics Division of Bhabha Atomic Research Centre, Mumbai.

बीएआरसी न्यूज़लैटर
BARC NEWSLETTER

INDUCTION OF SALT TOLERANCE FOR RADICLE GROWTH IN GROUNDNUT THROUGH GAMMA RAY MUTAGENESIS

Anand M. Badigannavar, Suvendu Mondal and G.S.S. Murty
Nuclear Agriculture and Biotechnology Division,
Bhabha Atomic Research Centre

This paper received the Best Poster award during
the BARC Golden Jubilee & DAE-BRNS Life Sciences Symposium held
at BARC, Mumbai, during December 18-20, 2006

Abstract

Groundnut is an important oilseed, food and feed crop of our country whose productivity is curtailed due to biotic and abiotic stresses. Salinity is one of the important abiotic stresses which affects all stages of groundnut growth and finally the yield. Soil amelioration against salinity is a costly and time-consuming procedure. Alternative strategy is to develop salinity-tolerant groundnut genotypes to overcome salinity problem, towards which, success has so far not been attained in groundnut, due to lack of efficient and simple screening protocol for salt tolerance. In the present study, we have developed a simple, cost effective and repeatable protocol for screening large number of mutant/segregating populations for radicle growth. Genetic variability for germination under 400mM NaCl stress was observed, among established TAG 24 mutants. Superior radicle growth in six of the TAG 24 mutants was noted by screening at 125mM and 150mM NaCl. Further, three mutants showed increased tolerance due to greater radicle length and lesser radicle reduction at 125mM and one mutant at 150mM NaCl. Induction of genetic variability for radicle growth under saline conditions in large seed groundnut variety TPG 41 was carried out, through gamma ray mutagenesis. By screening large number of seeds at 100mM NaCl during M_3 generation followed by screening plant wise during M_4 and M_5 generations, 91 true breeding mutants having salt tolerance for radicle growth were isolated. As a result, by screening from F3 to F5 generations, 114 true breeding lines were identified having salt tolerance for radicle growth.

These mutants and breeding lines will be evaluated in the salt-affected soils for their salinity tolerance and yield performance.

Introduction

In India, groundnut is an important oilseed, food and feed crop grown in an area of 6.45 million ha with a total production of 6.57 million tons based on an average of the last five years (FAO, 2005). This contributes to 26.6% of world's groundnut area and 18.5% of world's groundnut production. Groundnut occupies nearly 28.3% of the cultivated area and contributes 31.7% of the production of the total oilseeds in the country. It is widely used as cooking oil, digestible protein, minerals and vitamins in many countries and contributes significantly to food security and alleviating poverty. About 80% of India's groundnut production is crushed for oil, 12% for using as seed, 5% for food and 2% for export.

Among many reasons ascribed for the lower productivity of groundnut, salinity is an important abiotic stress which significantly affects seedling, vegetative and reproductive growth, seed quality and yield. Root zone salinity increases as a result of continuous use of saline water for irrigation because of limited or non-availability of good quality water in majority of groundnut growing areas. It can rapidly inhibit root growth and in turn their capacity to uptake water and essential mineral nutrients from the soil (Neumann 1995). Groundnut yields were severely affected with an increase in soil and water salinity (Singh and Abrol, 1985; Lauter and Meiri, 1990; Patel *et al*, 1993; Girdhar *et al*, 2005).

For many agricultural purposes and in arid lands, the cost and lack of water make reclamation of saline soils prohibitive. The alternative to reclamation is to breed for salinity tolerance. The first step towards breeding for salinity tolerance is to identify parent plants with traits which are heritable and contribute to salinity resistance. Promising traits can identified by: (a) screening for appropriate diversity in responses to salinity among modern cultivars or wild species; (b) treatment with mutagens in order to produce mutants which show hypersensitive or reduced responses to salinity as compared with the wild type; (c) engineering transgenic plants which express one or more foreign genes which are expected to increase cellular resistance to salinity.

Unfortunately, the most salt-tolerant species are generally not productive or desirable. Even though literature indicates variability for salinity tolerance in many crops, few salt-tolerant cultivars have been released (Flowers and Yeo, 1995). Sruvastave and Jana (1984) and Shannon (1984) attribute the lack of salt tolerant cultivars to inadequate means of detecting and measuring plant response to salinity and ineffective selection methods. Selection of salt-tolerant plants from saline fields seems a logical step for most plant breeders; however, this procedure has not produced consistent results (Shannon, 1984). Selection in the field is not efficient because soil salinity varies substantially with time, location, soil type and depth. In groundnut, studies on breeding for salt tolerance are rare. Further, systematic screening protocols for large populations in order to isolate salt-tolerant genotype are lacking. Our objective was to develop a protocol to screen large number of plants with simplicity, ease of use and consistent separation of genotypes, based on their tolerance to saline conditions. A second objective was to determine the genetic variability for salt tolerance among induced mutant/segregating populations.

Materials and Method

Standardization for salt screening

Development of salt-tolerant plant materials, will require selection at several stages of plant growth. Dewey (1962) proposed a breeding scheme to improve salinity tolerance in perennial grasses that included selection during germination with subsequent selection at later crop growth stages. Selection for salt tolerance in the field has proven to be very difficult and often not effective, because of lack of uniformity of most salt affected fields.

In order to develop simple screening methodology for salt tolerance, initially, dry seeds of two popular groundnut varieties TAG 24 (Patil et al, 1995) and TG

26 (Kale et al, 1997) were treated with 100 to 1000mM NaCl in laboratory at BARC, Mumbai (Fig. 1). Each treatment contained 20 seeds in petri plates lined with filter paper and moistened with 20mL NaCl solution in three replications and incubated at 28° ± 2°C. For control, 20 mL of distilled water was used. LD_{50} for germination was analyzed in TAG 24 and TG 26 by Probit analysis based on germination % at different NaCl concentrations. Seeds of both varieties were germinated up to 400mM NaCl and hence this concentration was taken for screening seed germination.

In another experiment, to determine effective lower NaCl concentration for screening large mutant/segregating populations so as to have radicle growth as a criterion in addition to germination %, TAG 24, JL 24, SB XI and Girnar-1 (40-50 g/100 seeds) and TPG 41 (70 g/100 seeds) were treated with 25, 50, 75, 100, 125 and 150 mM NaCl in two replications. Also, seeds of TPG 41 grown at Kolhapur, Solapur, Parbhani and Trombay were treated with these NaCl concentrations. Percent reduction in radicle growth was estimated by comparing with control grown in distilled water.

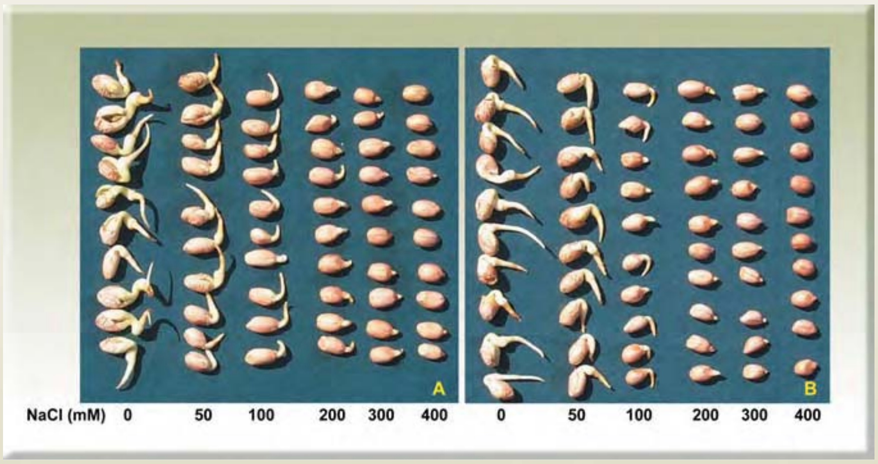

Fig. 1 : Germination of seeds of TAG 24 (A) and TG 26 (B) groundnut varieties under different concentrations of NaCl after four days

Induced mutagenesis

TAG 24 was irradiated with 150, 250 and 350 Gy gamma rays and 83 true breeding mutants for various morphological and biochemical traits were isolated (Badigannavar, 2007) and were studied for salt tolerance.

To induce genetic variability for salt tolerance, 500 seeds each of a large seed variety TPG 41 were irradiated with 200 and 300 Gy of gamma rays during rainy season (June-September), 2004. The M_2 generation was grown in summer, 2005 by advancing M_1 plants as plant to row progenies. M_2 plants were harvested individually to obtain M_3 seeds and were bulked dose-wise.

To incorporate salt tolerance in recently released varieties TG 37A (Kale et al, 2004a) and TPG 41 (Kale et al, 2004b) they were hybridized with salt-tolerant accessions, NRCG 2419 and NRCG 7548 (Rajgopal and Bandyopadhyay, 1999) during rainy season, 2004. F_1 plants were grown in summer, 2005 and crosswise harvested individually.

Screening mutant/segregating populations for salt tolerance

Using protocol for germination, 83 mutants of TAG 24 were screened with 400mM NaCl and germination % was recorded after 48 h based on radicle appearance. In another study under the same experimental settings, 20 seeds from 43 mutants of TAG 24 grown in summer and rainy seasons were treated with 20mL each of distilled water (control), 125 and 150mM NaCl in two replications for radicle growth. Radicle length from the collar region to radicle tip was measured from the germinated seeds after four days and mean radicle length was estimated. Percent reduction in radicle length from 125 and 150mM NaCl treatments in comparison with control was estimated.

M_3 seeds of TPG 41 from both 200 and 300 Gy treatments were subjected to NaCl treatment. In each plastic tray (54cm X 34cm X 5cm) lined with blotting paper, around 300g (~500 seeds) of M_3 seeds were put and 600 mL of 100mM NaCl was added. Similarly, 20 trays per day were treated with NaCl to cover ~ 10,000 seeds (Fig. 2). Two controls, one with 100 unirradiated seeds of TPG 41 and 200 mL distilled water and another one with 100 unirradiated seeds of TPG 41 and 200 mL 100mM NaCl were maintained at each time of testing. Treated seeds were incubated for four days at 30° ± 2°C and germination percent was taken. NaCl tolerant M_3 seeds were selected by comparing radicle growth with that of the distilled water control (Fig. 3). M_3 seeds having radicle growth similar to the radicle growth of the unirradiated seeds in distilled water were considered as tolerant ones. Such tolerant seeds were transferred to distilled water for 45 min and then to thermocol cups (9cm X 6cm) having soil and farm yard manure (3:1) mixture (Fig. 4). Established seedlings were transplanted in the field after 10 days. Similarly F_3 seeds (~13,000) from four crosses were screened for NaCl tolerance. M_3 and F_3 plants were harvested individually.

Fig. 2 : Large scale screening of M_3 seeds of TPG 41 groundnut variety at 100mM NaCl

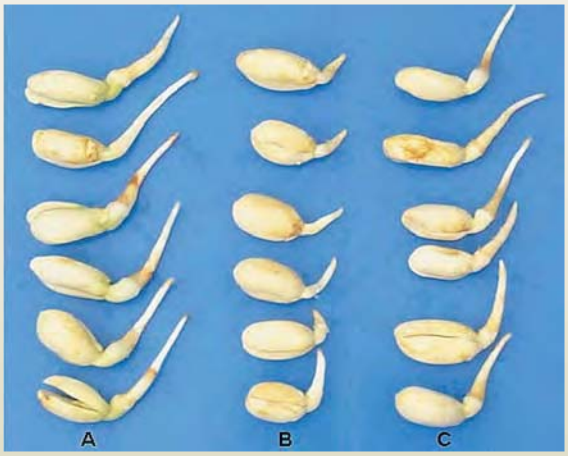

Fig. 3 : Comparison of tolerant M_3 germinated seeds under 100mM NaCl (C) with unirradiated germinated seeds under distilled water (A) and 100mM NaCl (B)

M_4 and F_4 seeds were screened for NaCl plant wise. In each plastic tray, plant wise M_4 and F_4 seeds from 15 plants were kept separately after adding 600mL NaCl. Through out the experimentation, two controls were maintained. Tolerant M_4 and F_4 progenies were selected based on 1) all the seeds in each plant should have been germinated in NaCl solution and 2) radicle growth of these seeds should be similar to radicle growth in distilled water (Fig. 5). Five such germinated seeds from each tolerant plant were directly sown in the field and maintained progeny-wise, through out the crop cycle. In each M_4 and F_4 progeny, one out of five plants having good pod setting was selected and harvested separately, dose-wise and cross-wise, respectively. Similarly, progeny screening for NaCl tolerance for M_5 and F_5 seeds was undertaken in the next season.

Fig. 4 : M_3 seedlings of TPG 41 groundnut variety which showed NaCl tolerance for radicle growth ready for transplanting in the field

Fig. 5 : Plantwise screening of M_4 seeds of TPG 41 groundnut variety at 100mM NaCl (Arrow indicates NaCl tolerant plant for radicle growth).

Results and discussion

Screening TAG 24 mutants for salt tolerance

Based on the germination %, LD_{50} for germination in TAG 24 and TG 26 was 416.9 mM and 331.1mM of NaCl, respectively when they were initially subjected to 100mM to 1000 mM NaCl under laboratory conditions. Percent reduction was arrived at by comparing radicle length in control. Further at 100, 200, 300, and 400mM NaCl, mean reduction in radicle growth was 40.4, 70.0, 84.4 and 93.3% for TAG 24 and 44.8, 68.4, 88.4 and 95.0% for TG 26, respectively.

For identifying salt-tolerant mutants, 83 TAG 24 mutants along with parents were screened at 400mM NaCl and germination % recorded (Fig. 6). Wide variability for germination % in the mutants was observed, indicating their differences in genotypic responses to salinity stress. Parent, TAG 24 itself exhibited considerable tolerance to NaCl by scoring 80% germination. Though, none of the mutants had significantly superior germination, TGM 22, TGM 25, TGM 28, TGM 32, TGM 35, TGM 51, TGM 52, TGM 75, TGM 79 and TGM 94 scored higher germination (82.5%-90.0%) as compared to TAG 24. Earlier varietal differences for germination and seedling growth due to salinity stress were noted in groundnut (Nautiyal et al, 1989; Girdhar, 2004; Girdhar et al, 2005; Vadez et al, 2005). Understanding genotypic variability would offer good scope for identifying tolerant types.

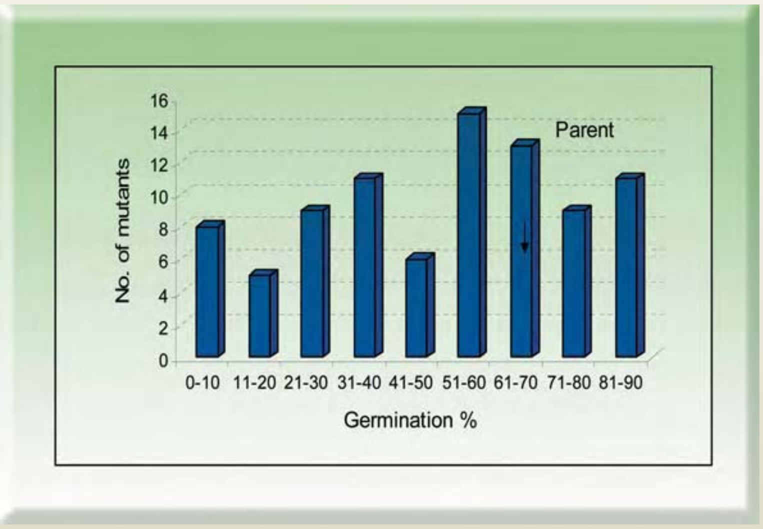

Fig. 6 : Frequency distribution of germination % of TAG 24 mutants when screened at 400 mM NaCl

In order to find out effective lower NaCl concentration for screening for radicle growth, TAG 24, JL 24, SB XI, Girnar 1 and TPG 41 were treated with 25, 50, 75, 100, 125 and 150mM NaCl. Pooled mean over the varieties indicated that there was a significant reduction in the radicle growth from 13.0% in 25mM to 76.3% in 150mM as compared to control (Fig. 7). Among the varieties screened, the least reduction of 57.4% was noticed in JL 24 at 150 mM and for the rest of the varieties it was over 80%. By 100mM NaCl concentration, radicle reduction was more than 60% in SB XI, Girnar-1 and TPG 41 while in TAG 24 and JL 24 it was around 35%. In order to ascertain the influence of environmental conditions on the response of the variety to NaCl treatment, seeds of TPG 41 grown at Kolhapur, Solapur, Parbhani and Trombay were treated with 25, 50, 75, 100, 125 and 150mM NaCl. There was a difference in the response to different locations, for lower NaCl concentration. However, higher concentration drastically affected the radicle growth of TPG 41 irrespective of the location (Fig. 8). Based on these studies, 100-150mM NaCl was found to be the ideal concentration for radicle growth. Vadez *et al* (2005) also showed that 100-125 mM range of NaCl treatment was suitable for salinity screening, based on biomass parameters in groundnut.

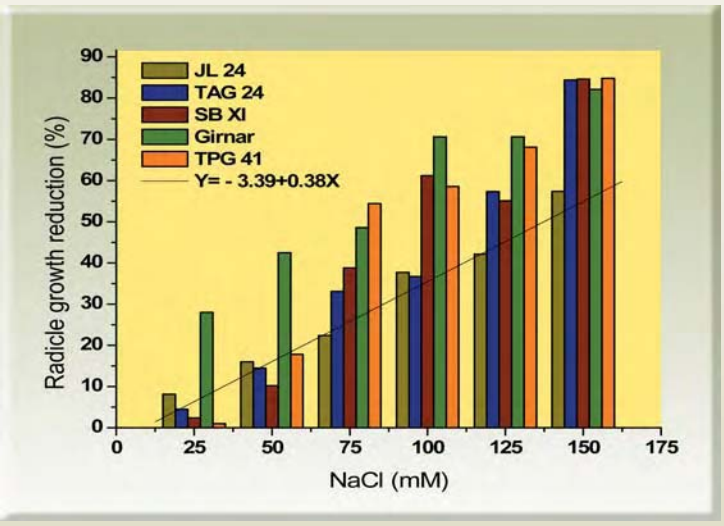

Fig. 7 : Screening of groundnut varieties for radicle growth with NaCl solution

Using radicle growth as the criteria for salt tolerance, 43 mutants and TAG 24, grown during both rainy and summer seasons were screened at 125 and 150 mM NaCl. In both the seasons, significant differences were observed among TAG 24 mutants for radicle growth. In summer, five mutants had longer radicle (2.7 – 3.0cm)

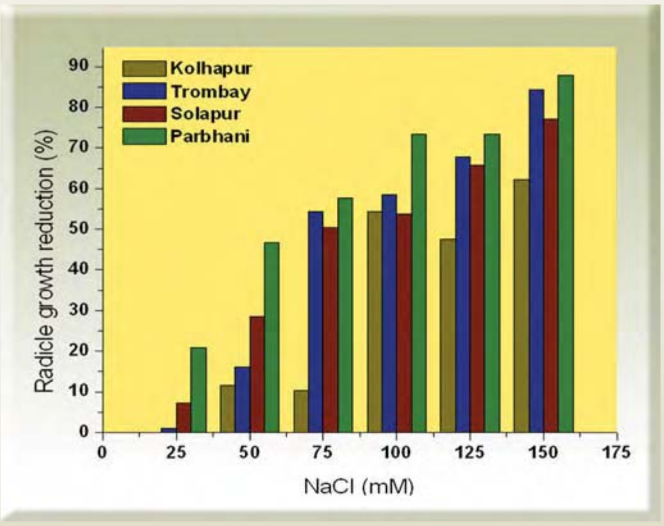

Fig. 8 : Screening of groundnut variety TPG 41 grown at different locations for radicle growth with NaCl solution

than TAG 24 (2.3cm) while, 13 mutants had reduced length (0.9 - 1.8cm) with 125mM NaCl treatment. In two mutants, the radicle reduction was comparatively less (22.1 to 24.1%) as compared to parent (40%), while in four mutants, it was more (54.2 to 70.6%). Following 150mM NaCl treatment, nine mutants recorded significantly superior radicle length (2.3 – 2.6cm) than TAG 24 (1.9cm) while in 17 mutants, it was reduced (0.6 – 1.5cm). Due to 150 mM NaCl treatment, the radicle reduction was relatively less (26.7 to 37.2%) in six mutants as compared to parent (50.6%) while in other six mutants, it was more (65.0 to 81.3%). TGM 64 and TGM 93 exhibited higher tolerance by having longer radicle both at 125 and 150mM NaCl levels than TAG 24. Further, TGM 2 and TGM 67 also showed increased tolerance due to greater radicle length and lesser radicle reduction at 125mM NaCl and TGM 77, TGM 79 and TGM 93 at 150mM NaCl.

During rainy season, following 125mM NaCl treatment, eight mutants recorded significantly greater radicle length (2.2 – 2.9cm) than TAG 24 (1.8cm) while, 19 mutants had reduced length (0.3 - 1.5cm). The radicle reduction in six mutants was comparatively less (13.0 to 32.1%) than parent (42.6%) while in 17 mutants, it was more (54.9% to 88.6%). With 150mM NaCl treatment, six mutants recorded superior radicle length (2.2 – 2.6cm) than TAG 24 (1.8cm) while, 27 mutants had reduced length (0.3 – 1.5cm). In four mutants, the radicle reduction was relatively less (23.5 to 37.0%) than parent (44.1%) while in 28 mutants, it was more (52.4 to 92.4%). TGM 16, TGM 53, TGM 64, TGM 81, TGM 82 and TGM 93 exhibited higher tolerance by having longer radicle both at 125 and 150mM NaCl levels than TAG 24. Further, TGM 53, TGM 64 and TGM 81 showed increased tolerance due to greater radicle length and lesser radicle reduction at 125mM NaCl and TGM 53 and TGM 81 at 150mM NaCl.

Pooled analysis over both the seasons indicated that TGM 16, TGM 53, TGM 64, TGM 81, TGM 82 and TGM 93 showed enhanced tolerance by having longer radicle than TAG 24 at both 125 and 150mM NaCl. The reduction in radicle length was relatively less in TGM 10, TGM 29, TGM 53, TGM 64 and TGM 81 as compared to TAG 24 due to 125mM NaCl treatment and in TGM 29, TGM 53 and TGM 77 due to 150mM NaCl treatment. Further, TGM 53, TGM 64 and TGM 81 showed increased tolerance due to greater radicle length and lesser radicle reduction at 125mM NaCl and TGM 53 at 150mM NaCl. Using sand culture experiments, Girdhar (2004) identified germplasm lines which are sensitive or tolerant to saline environments.

Screening mutant or segregating populations for salt tolerance

A large seeded variety, TPG 41 was irradiated with 200 and 300 Gy gamma rays to induce genetic variability for salinity tolerance. Around 45,775 M_3 seeds from 4,240 M_2 plants were screened with

100 mM NaCl during rainy season 2005. Of these, 55% of M_3 seeds germinated with NaCl treatment as compared to 60% in unirradiated NaCl control and 76% in unirradiated distilled water control (Table 1). Further, 1,790 seeds (1,155 seeds from 200Gy and 635 from 300 Gy) had radicle growth similar to unirradiated distilled water control and were considered as NaCl tolerant ones (Fig. 3). These germinated seeds were transplanted to thermocol cups and later to the field to ensure proper establishment of the seedlings. At the time of harvest, 631 plants from 200Gy and 390 from 300 Gy survived.

Plant-wise M_4 seeds from 631 plants from 200Gy and 390 from 300 Gy were screened without bulking with 100mM NaCl (Fig. 5). Using radicle growth criterion for all seeds from each plant, 181 M_4 plants from 200Gy (28.7%) and 390 from 300 Gy (31.0%) were identified as tolerant plants for radicle growth (Table 1). Since all the seeds in each of the tolerant plant were with radicle growth as that of unirradiated distilled water control, these plants were genetically true breeding for their response to NaCl treatment. In order to avoid escapes in these tolerant plants, plant wise M_5 seeds were screened with NaCl and 91 true breeding M_5 plants were isolated for radicle growth tolerance to NaCl (Table 1). As a consequence, only 0.2% of the M_3 seeds treated were true breeding tolerant mutants. In a preliminary yield trial of these 91 M_6 mutants during summer 2007 (Fig. 9), four mutants had significantly higher pod and seed yield and 10 mutants had larger seed size (> 88g/100 seeds) than parent TPG 41 (84g/100 seeds). Thus,

Table 1: Screening of mutant populations in groundnut for radicle growth tolerance to NaCl (100mM) treatment

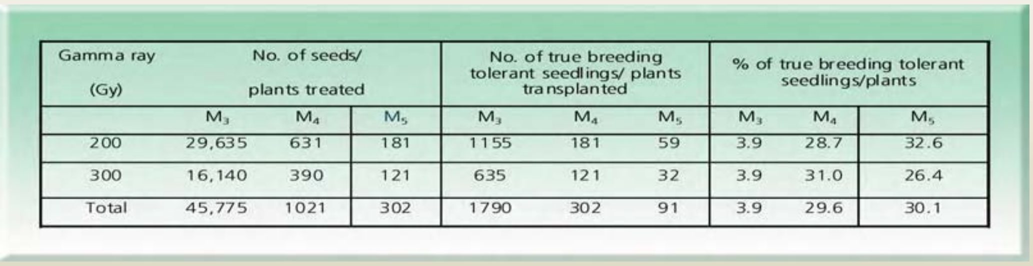

Gamma ray (Gy)	No. of seeds/ plants treated			No. of true breeding tolerant seedlings/ plants transplanted			% of true breeding tolerant seedlings/plants		
	M_3	M_4	M_5	M_3	M_4	M_5	M_3	M_4	M_5
200	29,635	631	181	1155	181	59	3.9	28.7	32.6
300	16,140	390	121	635	121	32	3.9	31.0	26.4
Total	45,775	1021	302	1790	302	91	3.9	29.6	30.1

Fig. 9 : Preliminary field evaluation of M_6 mutants of TPG 41 groundnut variety for yield performance at Trombay

following this simple screening technique, large seed groundnut mutants tolerant to salinity at radicle stage were identified. Salinity tolerance in these mutants at later plant phenophases is undergoing at salt affected soils, Agricultural Research Station, Digraj and Bheemarayanagudi.

F_3 seeds from the crosses involving TG 37A, TPG 41, NRCG 2419 and NRCG 7548 were screened with 100mM NaCl during summer 2005. The mean germination % over these crosses was 90% as compared to 100%, 98%, 95% and 97% in TG 37A, TPG 41, NRCG 2419 and NRCG 7548 in distilled water control, respectively (Table 2). Further from all the crosses, 795 F_3 seeds (6.1%) were found to be NaCl tolerant had radicle growth similar to distilled water control and one of these, 614 plants survived at harvest in the field (Table 2). Plant-wise F_4 seeds from all the crosses were screened with 100mM NaCl and 266 plants (43.3%) were found to be tolerant to NaCl based radicle growth. Following the same protocol, 246 F_5 plants were screened with NaCl and 114 true breeding F_5 plants were isolated for radicle growth tolerance to NaCl (Table 2). Thus, 0.8% of the F_3 seeds treated were true breeding tolerant genotypes and will be screened at salt affected soils to ascertain their salt tolerance.

Table 2: Screening of segregating populations in groundnut for radicle growth tolerance to NaCl (100mM) treatment

Cross	No. of seeds/ plants treated			No. of true breeding tolerant seedlings/ plants transplanted			% of true breeding tolerant seedlings/plants		
	F_3	F_4	F_5	F_3	F_4	F_5	F_3	F_4	F_5
TPG 41 X NRCG 2419	3,115	131	59	184	59	35	5.9	45.0	59.3
NRCG 2419 X TPG 41	1,322	15	-	30	7	-	2.2	46.7	-
TPG 41 X NRCG 7548	2,361	110	30	128	38	12	5.4	34.5	40.0
NRCG 7548 X TPG 41	2,186	104	45	129	45	14	5.9	43.3	31.1
NRCG 2419 X TG 37A	1,401	96	37	131	38	24	9.3	39.6	64.8
TG 37A X NRCG 7548	886	57	30	72	30	7	8.1	52.6	23.3
NRCG 7548 X TG 37A	1,674	101	45	121	49	22	7.2	48.5	48.9
Total	12,945	614	246	795	266	114	6.1	43.3	46.3

Conclusion

This protocol provides a simple method to effectively screen and identify, potential genotypes from large populations in groundnut, whose screening is difficult in salt affected soils due to its heterogeneous nature. Furthermore, this protocol will be helpful as a selection tool since virtually any level of selection intensity can be obtained. But final evaluation and selection for high yielding tolerant genotypes in groundnut will require field evaluation in the salt affected soils.

Acknowledgements

We thank Dr. S.F. D'Souza Associate Director (A), Biomedical Group and Head, Nuclear Agriculture and Biotechnology Division for support and encouragement. This work is part of the project, partially funded by the International Atomic Energy Agency, Vienna under the Coordinated Research Project No. 12818.

References

1. Badigannavar, A.M. 2007 Genetic improvement for agronomical and biochemical traits in groundnut (*Arachis hypogaea* L.). Ph D Thesis, University of Mumbai, Mumbai. Pp 1-121.
2. Dewey, D.R. 1962 Germination of crested wheatgrass in salinized soil. Agron. J. 54: 353-355.
3. FAO, 2005. http://www. faostat. org.
4. Flowers, T.J. and Yeo, A.R. 1995 Breeding for salinity resistance in crop plants: where next? *Aust. J. Plant Physiol.* 22: 875-884.
5. Girdhar, I.K. 2004. Management of soil and water salinity for groundnut production. In: Basu, M.S. and Singh, N.B. (eds.) Groundnut Research in India, NRCG, Junagadh pp 260-272.
6. Girdhar, I.K., Bhalodia, P.K., Misra, J.B., Girdhar, V. and Devi Dayal 2005. Performance of groundnut, *Arachis hypogaea* L. as influenced by soil salinity and saline water irrigation in black clay soils. *J. Oilseeds Res.* 22: 183-187.
7. Kale, D.M., Mouli, C., Murty, G.S.S. and Rao, M.V.P. 1997. Development of a new groundnut variety, TG-26 by using induced mutations in cross breeding. *Mutation Breeding Newsl.* 43: 25-27.
8. Kale, D.M., Murty, G.S.S. and Badigannavar, A.M. 2004a. A new Trombay groundnut variety with wide adaptation. *Int. Arachis Newslett.* 24: 19-20
9. Kale, D.M., Murty, G.S.S. and Badigannavar, A.M. 2004b. TPG 41 - A new large seeded groundnut variety released in India. *Int. Arachis Newslett.* 24: 21-22
10. Lauter, D.J. and Meiri, A. 1990 Peanut pod development in pegging and root zone salinized with sodium chloride. *Crop Sci.* 30: 660-664.
11. Nautiyal, P.C., Ravindra, V. and Joshi, Y.C. 1989. Germination and early seedling growth of some groundnut cultivars under salt stress. *Indian J. Plant Physiol.* 32:251-253.
12. Neumann P.M. 1995 Inhibition of root growth salinity stress: Toxicity or an adaptive biophysical response? In Structure and Function of Roots. Developments in Plant and Soil Sciences (eds F. Baluska, M. Ciamporova, O. Gasparikova & P.W. Barlow), pp. 299-304. Kluwer academic publishers, Dordrecht, Netherlands.
13. Patel, M.S., Gundalia, J.D., Polara, K.B. and Patel, A.G. 1993. Effect of depth and frequency of saline well water irrigation and FYM on yield of wheat-maize-groundnut/paddy cropping sequence on two calcareous sodic soils of coastal belt. *GAU Res.* J. 18: 40-48.
14. Patil, S.H., Kale, D.M., Deshmukh, S.N., Fulzele, G.R. and Weginwar, B.G. 1995. Semi-dwarf, early maturing and high yielding new groundnut variety, TAG-24. *J. Oilseed Res.* 12: 254-257.
15. Rajgopal K. and Bandyopadhyay A. 1999 Elite groundnut Germplasm- A ready Reference, Technical Bulletin, NRCG, Junagadh. p-8.
16. Shannon, M.C. 1984 Breeding, selection and the genetics of salt tolerance in plants. p. 231-254. In RC Staples and GH Toeniessen (ed) Salinity tolerance in plants. John Wiley & Sons, New York.

17. Singh, S.B. and Abrol, I.P. 1985. Effect of soil sodicity on growth, yield and chemical composition of groundnut. *Plant and Soil* 84: 123-127.
18. Sruvastave JP and Jana S. 1984 Screening wheat and barley germplasm for salt tolerance. p. 273-283. In RC Staples and GH Toeniessen (ed) Salinity tolerance in plants. John Wiley & Sons, New York.
19. Vadez, V., Srivastava, N., Krisnamurthy, L., Aruna, R. and Nigam, S.N. 2005. Standardization of a protocol to screen for salinity tolerance in groundnut. *Int. Arachis Newslett.* 25: 42-47.

About the Authors

Dr Anand M. Badigannavar, MSc (Agriculture) from University of Agricultural Sciences, Dharwad, joined BARC in 1997. He obtained his PhD (Botany) from University of Mumbai, Mumbai on the project "Genetic improvement for agronomical and biochemical traits in groundnut (*Arachis hypogaea* L.)". His field of interest is genetics, mutation and recombination breeding in groundnut leading to the development of improved groundnut varieties. Presently, he is involved in the pyramiding of disease resistant and salt-tolerant genes with largeseed trait in groundnut .

Mr. Suvendu Mondal, MSc (Microbiology) from Indian Agricultural Research Institute, New Delhi, joined BARC in 2003 through training school (46th batch, Bioscience) and is currently working in groundnut improvement group, Nuclear Agriculture and Biotechnology Division, BARC. He is currently pursuing his PhD on the project entitled "Induction of mutations and its morphological, biochemical and molecular characterization in groundnut." His major research interest is to develop molecular markers for the biotic stress tolerance and characterization of mutants/ mutations in groundnut. Besides he is involved in developing Trombay groundnut varieties and their dissemination.

Dr G.S.S. Murty, M.Sc. (Botany) from Andhra University, Waltair, joined BARC in 1971 and served up to January 2007. His interest was in mutation research of sesame and groundnut for which he received international acclaim. His significant contributions include inducing variability and discovering inter-mutant hybrid heterosis in sesame, leading Trombay Groundnut (TG) project for nearly two decades. Relentless efforts put in by him and his team, made TG project to attain a top position in India from the point of view of breeders as well as farmers, which increased BARC's reputation. During his career in BARC, he produced more than 50 research papers; he is a co-breeder for 7 out of 12 TG varieties; he registered three sesame mutants with NBPGR; he was associated with many IAEA projects including undertaking Expert Mission.

INDUCTION OF GENETIC VARIABILITY IN A DISEASE-RESISTANT GROUNDNUT BREEDING LINE

Suvendu Mondal, A.M. Badigannavar, D.M. Kale and G.S.S. Murty
Nuclear Agriculture & Biotechnology Division
Bhabha Atomic Research Centre

This paper was adjudged as the Best Poster presentation at
the Second National Plant Breeding Congress 2006 held at
Tamil Nadu Agriculture University, Coimbatore, during March 1-3, 2006

Abstract

Due to narrow genetic base of groundnut (Arachis hypogaea L.), induction of genetic variability was undertaken by treating seeds of TFDRG 5 with 200 and 300 Gy of gamma rays and with 1, 2 and 3 mM of sodium azide (NaN_3) singly and in combination. The combination of 200 Gy and 3 mM of NaN_3 induced maximum number of mutants with a frequency of 2.48% in M_2 generation. In all, 63 true breeding mutants were induced, affecting various morphological traits. Among them, the fused terminal leaflet was unique. In newly formed leaves of disease lesion mimic mutant, catalase activity was reduced as compared to the parent. In large seed mutants, seed size ranged from 52 to 69g/100 seeds as compared to 45g in parent, with 15 to 53% superiority along with resistance to rust. Dominant rose testa mutants were also induced. Cluster analysis revealed considerable genetic variability, among induced mutants.

Introduction

Groundnut (*Arachis hypogaea* L.) is an important food, feed and oilseed crop. It is grown in nearly 100 countries. Major groundnut producers in the world are: China, India, Nigeria, USA, Indonesia and Sudan. In recent times, groundnut is gaining importance as a food crop, due to its high content of digestable proteins, vitamins, minerals, phytosterols and due to increased consumer preference after value addition. Though the groundnut crop has morphological, biochemical, physiological variability, it has narrow genetic base because of its monophyletic origin, lack of gene flow due to ploidy barrier and self-pollination.

The most popular method employed for creating genetic variability, is induced mutagenesis through gamma irradiation (Reddy 1977). Besides gamma irradiation, chemical mutagens like ethyl-nitroso-urea, methyl-nitroso-urea, ethyl-methane-sulphonate (EMS) and sodium azide (SA) are also used for mutation-assisted breeding. Among all these SA is considered as safe and has capability of producing high frequency of mutation. Gregory (1956) was able to produce useful mutation in

Virginia bunch varieties of groundnut by irradiation with X rays. Different spectra of leaf mutants were isolated through gamma irradiation in dormant seeds of TG 2 (Patil and Mouli 1975). Mutagenesis through EMS yielded a very high frequency of mutants for intraspecific differentiation in groundnut (Gowda *et al,* 1996). Branch (2002) detected large variability among advanced gamma-irradiation induced large-seeded mutant breeding lines in the 'Georgia Browne' peanut cultivar. Both the direct and indirect utilization of mutants in groundnut resulted in the release of commercial varieties in India (Murty *et al,* 2004).

The present study was conducted to induce genetic variability by employing gamma ray and sodium azide in a disease resistant breeding line as parent. In this context we were able to assess different types of mutants and variability among them.

Materials and Method

Plant material : TFDRG 5, a recombinant line from the cross between VG 9514 (Varman 1999) and TAG 24 (Patil *et al*, 1995) has a red seed coat, highly resistant to rust and moderately to late leaf spot (Badigannavar *et al.,* 2005). VG 9514 and TAG 24 have red and rose testa respectively.

Mutagenesis : Seeds of TFDRG 5 (200 each) treated with gamma rays (200 & 300 Gy) or sodium azide (NaN_3 1, 2 & 3 mM) or combination of both. For NaN_3 treatment, seeds were initially soaked in distilled water for 4 h and then treated with NaN_3 at 1mM, 2mM and 3 mM for 17 h at pH 7.0. After treatment, seeds were washed properly under running tap water and then dried under blotting sheets to remove excess water. M_1 generation was grown in experimental field station at Trombay during summer 2004.

Isolation of mutants: In M_2 generation, mutants were selected from 1177 progenies consisting 20,619 plants. Breeding behavior of the mutants was confirmed in M_3 and M_4 by growing progeny to row method.

Morphometric observation: Observations on plant height, number of branches, pod and seed weight/plant, shelling %, Hundred-Kernel Weight (HKW) and reaction to rust and Late Leaf Spot (LLS) were recorded on ten plants from each mutant at M_3 and M_4. Besides, observations on length, breadth and area of terminal leaflets, length of rachis, stipule and leaflet fusion and dry weight of whole leaf were recorded at 70 DAS from five plants on fused leaflet mutants. Breadth of terminal leaflets was recorded from 1 cm above the leaflet base. Leaflet fusion length was measured by taking the length of terminal connation. The mutants were evaluated for rust and LLS resistance in the field using modified 1-9 point scale (Subrahmanyam et al 1995).

Enzyme assay: Newly formed upper leaves at the third node from the terminal bud and the lower leaves at the third node from the base from disease lesion mimic, mosaic leaf mutants and TFDRG 5 at 60, 67 and 86 DAS were used to extract and assay catalase, guiacol peroxidase and superoxide dismutase (Kim *et al*, 2005).

Statistical analysis: Parent and mutants were compared for different traits by Student t' test using OriginPro 7.5 software. Mutants were subjected to cluster analysis based on complete linkage and Two-way joining (Hartigan, 1975) methods using Euclidean distances performed by Statistica software (Statistica 1996).

Results and Discussion

Mutants and mutagen

A total of 215 variants were isolated from an M_2 population consisting of 20,619 plants. Out of 11 different treatment, the combination of '200 Gy + 3 mM NaN_3' was ideal with the highest mutation frequency (2.48%) in the M_2 (Table 1). The highest frequency obtained in this combination, can be due to the mode of action of two different mutagens. The gamma rays damaged the DNA by directly heating the DNA (direct action) or through water effect by indirect way of action, whereas the chemical mutagen (NaN_3)

Table 1: Effect of different treatment of mutagen (gamma ray and NaN_3) on groundnut

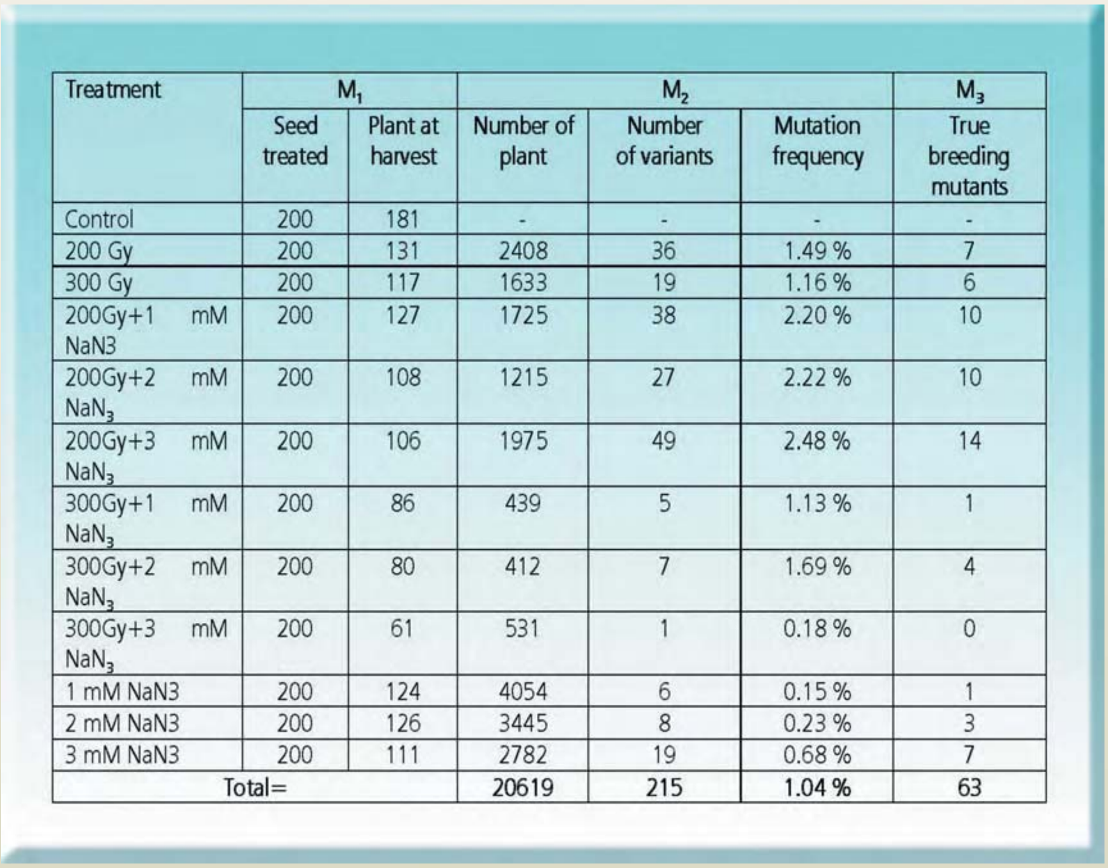

Treatment	M_1		M_2			M_3
	Seed treated	Plant at harvest	Number of plant	Number of variants	Mutation frequency	True breeding mutants
Control	200	181	-	-	-	-
200 Gy	200	131	2408	36	1.49 %	7
300 Gy	200	117	1633	19	1.16 %	6
200Gy+1 mM NaN3	200	127	1725	38	2.20 %	10
200Gy+2 mM NaN_3	200	108	1215	27	2.22 %	10
200Gy+3 mM NaN_3	200	106	1975	49	2.48 %	14
300Gy+1 mM NaN_3	200	86	439	5	1.13 %	1
300Gy+2 mM NaN_3	200	80	412	7	1.69 %	4
300Gy+3 mM NaN_3	200	61	531	1	0.18 %	0
1 mM NaN3	200	124	4054	6	0.15 %	1
2 mM NaN3	200	126	3445	8	0.23 %	3
3 mM NaN3	200	111	2782	19	0.68 %	7
Total=			**20619**	**215**	**1.04 %**	**63**

normally acts as a base substitution agent. It means when the damaged DNA in the embryo undergoes repair during germination (metabolic active stage) the presence of NaN_3 hinders repair process and thus accumulation of mutation and mis-incorporation of bases occur at a high frequency. But combination of '300 Gy + 3 mM NaN_3' gave highest mortality as it tends to LD_{50} in groundnut.

Among 215 variants in the M_2, 63 true breeding mutants for plant height, plant habit, leaf related traits, flower colour, pod-traits, seed size and testa colour were identified in M_3. Maximum numbers of mutants were obtained for the leaf related traits. Among leaf related mutants, mutant phenotype like light green, small leaf, narrow leaf, disease mimic leaf, mosaic leaf, virescent leaf, twisted leaf and Fused Terminal Leaflet (FTL) were isolated. Among plant height mutants seven dwarf mutants were isolated (Fig. 1). Besides, ten rose seed coat colour mutant, 21 large pod mutant, one for hard kernel and two mutants for plant habit were identified in the M_2. The mutants M 95 and M 101 were Virginia bunch (VB) and they are mutants for intraspecific differentiation (Gowda et al., 1996). Probably, these VB mutants arose due to reversion as one of the progenitors of the TFDRG 5 is VG 9514, which is a Virginia bunch, red seed coat and immune to both rust and Late Leaf Spot (LLS) (Varman 1999). Between these two VB mutants M 95 was susceptible to rust but resistant to LLS whereas M 101 was resistant to both the diseases. Thus it showed, that even in the mutation for a specific trait (like VB plant type), the mutants were diverse in respect of other characters.

Fig 1: Dwarf mutants in groundnut

Fused leaflet mutants

Arachis hypogaea is a member of papilionaceae. It produces pinnately compound leaves with four to five leaflets. The Fused Top Leaflet (FTL) mutants (Fig. 2) in our study, produced three leaflets and the top leaflet is a result of fusion between top two leaflets in the parent. Besides, the rachis between two pairs of leaflets is completely absent in these FTL mutants. Thus, the whole leaf appears as a trifoliate. In this connection the mutant can be considered as a missing link/ transition state between compound pinnate leaves and compound foliate leaves. These new FTL mutants with their fused top leaflets are novel in nature because they show 100% expressivity between the plants and the rachis between the pair of leaflets is completely absent. Earlier fused leaflets were identified in groundnut through X ray irradiation but the expressivity was only from 20-50% between the plants (Patil S.H., 1966). Though the top fused leaflets in our mutants showed the same

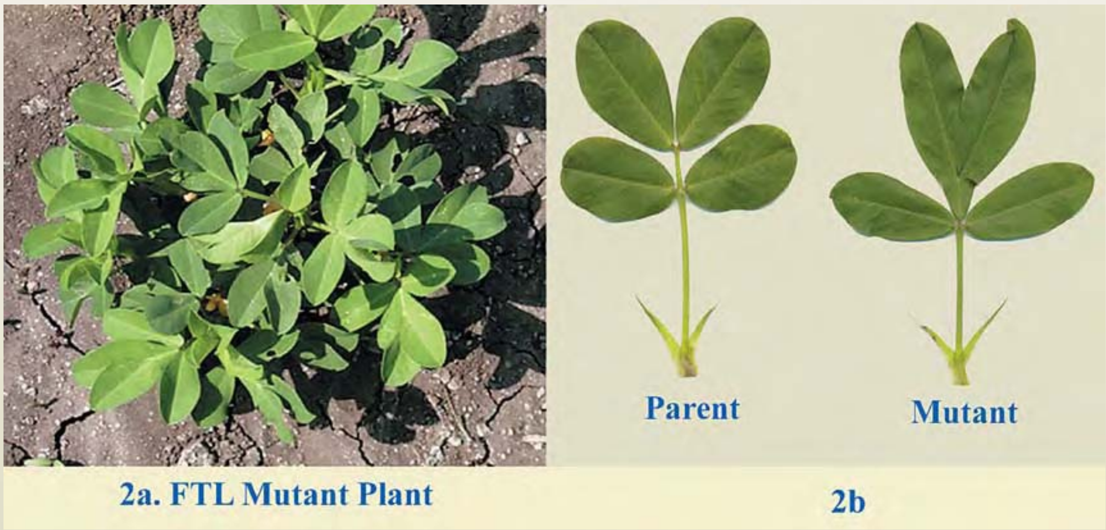

2a. FTL Mutant Plant

2b

Fig 2a & b: Novel Fused Top Leaflet (FTL) mutant plant (a) and leaf (b) in groundnut

Table 2: Morphometric observation on FTL mutants and parent

Characters	Parent	FTL mutant
Leaflet Length (cm)	5.28	5.32
Petiole Length (cm)	5.24	3.32**
BTTL (cm)	3.0	1.32**
Stipule Length (cm)	2.22	2.02
TTLA (sq. cm)	18.68	12.72**
Fusion length (cm)	0	2.26**
Leaf dry weight (g)	0.184	0.14**
Plant height (cm)	42	43.2
Number of branches	9.4	6.9
Shelling %	73.50	70.13
Hundred Kernel Weight(HKW)	48.75	37.80**

*Note : **indicates significance at 1% based on paired 't' test*

morphology as in bifurcated leaflets (Mouli C., 1984) the bifurcated leaflets are not the result of fusion between top pair of leaflets like in our mutants. The number of leaflets in the bifurcated ones is 4-6 per leaf but in fused leaflet mutants, the total number of leaflets is only 3 per leaf. In other cases, the bifurcated leaf character is closely linked to small leaf (sl). But the fused leaflets that appear in our study are not with small leaf. Thus it is distinct and novel in nature. The morphometric observations in the FTL mutant were compared with the parent TFDRG 5 (Table 2). The rachis length in the mutant was significantly reduced. This reduction in rachis length was due to the complete absence of rachis between the two pairs of leaflets. Fusion between top two leaflets brought about changes in Top Two-Leaflets Area (TTLA) in this mutant (Table 2). This significant reduction in TTLA was due to the overlap area between interior margins of top two leaflets as an effect of fusion. Besides the uniform shelling% in mutant and parent, FTL mutant showed significant reduction in seed size (expressed as HKW) (Table 2). The reduction in HKW in the mutant could be explained by the reduction of TTLA and leaf dry weight, which leads to less photosynthate accumulation. This pleiotropic phenomenon was also reported in imparipinnate and small leaf mutant in groundnut (Patil and Mouli, 1984).

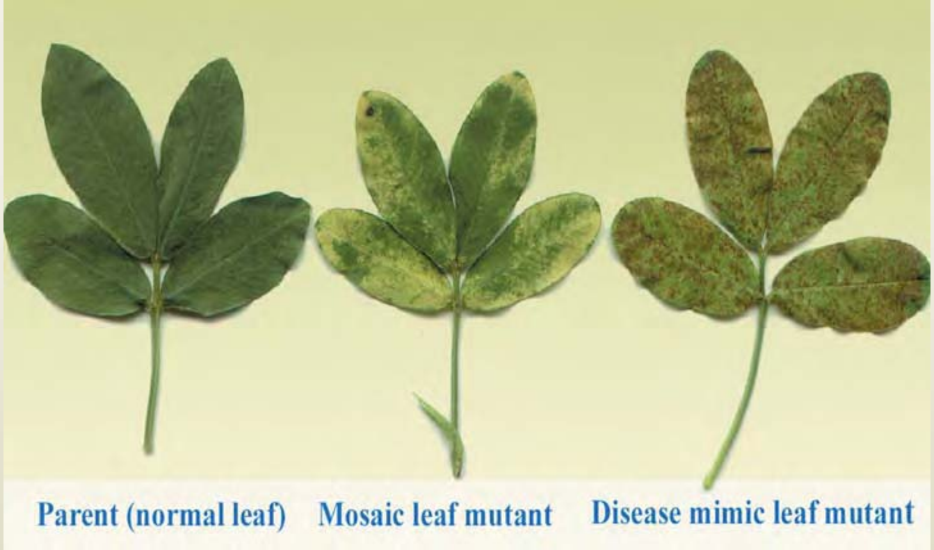

Fig. 3: Disease mimic leaf mutant and Mosaic leaf mutant in groundnut

Enzyme assay

In newly formed leaves of disease lesion mimic mutant (Fig. 3), catalase activity was reduced (Fig. 4) as compared to the parent. Whereas activity of catalase was similar to parent in mosaic leaf mutant. The probable reason behind the reduction of catalase activity is due to inthe sufficiency of 'heme' group as it is a prosthetic group for catalase. Hu et al (1998), reported impairment of porphyrin pathway responsible, for the phenotype of a dominant disease lesion mimic mutant, in maize. As the heme group in plant is synthesized in the same pathway as porphyrin, the present mutation could be due to impairment of porphyrin pathway.

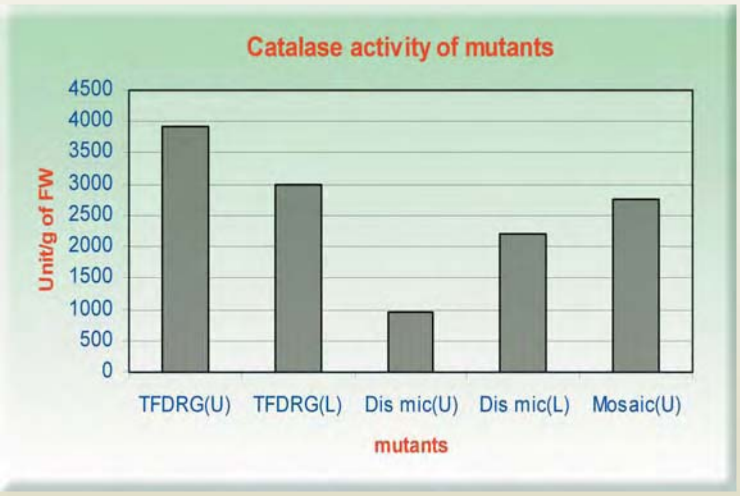

Note: U = upper leaves, L = lower leaves

Fig. 4: Catalase activity in disease lesion mimic mutant in groundnut

Large Seed Mutants

In 21 large seed mutants (Fig. 5), seed size increased by 15 to 53% as compared to the parent. Of these, 18 are with red testa like parent and 3 are with rose testa. Three of these large seed mutants showed superior pod and seed weights by 15.7 to 46.3% in comparison to parent (Table 3) at M_4. Among these three, two mutants namely M59 and M78 showed consistent pod yield performances at both M_3 and M_4. Variability among the mutants was also observed in terms of their disease resistance and the agronomic characteristic like Hundred Kernel Weight (HKW). All the large seed mutants retained their resistance against rust but, M59, M60, M66, M74, M78 and M79 showed moderate susceptibility to LLS like the parent. Whereas M13, M58, M61, M63, M64 and M69 showed resistance against LLS. A similar phenomenon was also noted in

Fig. 5 : Large pod mutant in groundnut

Table 3 : Agronomic performance of large seed mutants in groundnut

Mutant	Pod wt (g/plant)		Seed wt (g/plant		100 seed wt (g)		LLS Rust (1-9 scale	
	M_3	M_4	M_3	M_4	M_3	M_4	M_3	M_4
M 13	19.5	30.0*	11.3	20.3*	56.3**	58.8*	1	1
M 58	25.3*	22.7	16.0	16.0	64.1**	57.6*	1	1
M 59	38.5**	31.6*	25.2**	22.4*	62.8**	58.8*	4	1
M 60	38.2*	26.1	24.3**	17.6	61.6**	49.4*	6	1
M 61	30.6**	22.7	20.4**	16.0	57.0**	49.5*	1	1
M 63	21.8	21.9	15.0	14.7	59.9**	55.1*	1	1
M 64	14.3	16.7	9.8	11.2	60.1**	51.2*	1	1
M 66	23.7	25.0	17.9	16.7	69.4**	56.8*	6	1
M 69	30.0**	22.3	21.6*	14.9	60.2**	50.6*	1	1
M 74	24.5*	25.1	18.0**	16.3	60.2**	52.8*	6	1
M 78	30.8*	27.9*	21.4*	19.1	63.2**	52.3*	7	1
M 79	29.7**	21.4	21.4**	15.0	63.8**	50.6*	7	1
TFDRG 5 (Parent	19.1	21.6	13.6	15.5	52.0	45.0	6	1

* *Indicates significant difference from parent at 5% level of significance*
** *Indicates significant difference from parent at 1% level of significance*

induced large-seeded mutant breeding lines in the 'Georgia Browne' peanut cultivar (Branch W.D., 2002).

Seed coat colour segregation

Ten rose testa mutants were identified in the M_2. M_3 segregation gave 3 plants with rose testa and 1 with red (Fig. 6). Further, M_4 segregation into 1 (all rose): 2 (3 rose: 1 red): 1 (all red) confirmed single gene dominant mutation for rose testa. This occurrence of rose testa mutants from red testa parent (TFDRG 5) where one of the parents had rose testa (TAG 24) is an example of revertants. Earlier, Smart (1960) noted reversion of the red testa to parental variegated type in a red-seeded selection from groundnut variety Mani Pintar (variegated testa).

Fig. 6: Rose seed coat colour mutant in groundnut

Diversity among Mutants

Cluster analysis created two genetically diverse clusters with 29 (cluster A) and 9 (cluster B) mutants each at a linkage distance (based on Euclidean distance) of 73. The cluster B also accommodated TAG 24, one of the progenitors of TFDRG 5 (Fig. 7). All the nine mutants in cluster B were with bold pod like TAG 24 and semi dwarf with dark green foliage. Further at a linkage distance of 50, cluster 'A' sub-divided into two clusters 'C' and 'D'. In Cluster 'C' all the individuals are grouped with their immediate parent TFDRG 5 and as well as with one progenitor VG 9514. Whereas cluster 'D' did not contain any of the parents. Cluster D accommodated only six mutants (M37, M40, M41, M49, M54 and M55), which are low yielders and with various types of leaf-related macro-mutations. Interestingly the VB mutant M 95 was very closer to VG 9514, which is VB type and one of the progenitors of TFDRG 5 (Badigannavar et al., 2005). Thus the cluster analysis clearly showed the genetic variability among the mutants and divergence towards their progenitors. Two ways joining graph analysis (Fig. 8) showed that greater genetic variability for plant height and seed size (HKW) than other traits among the mutants. The mutant M95 showed high variation in respect of number of branches. This variation in respect of number of branches was due to the mutation in plant type as M95 was mutated

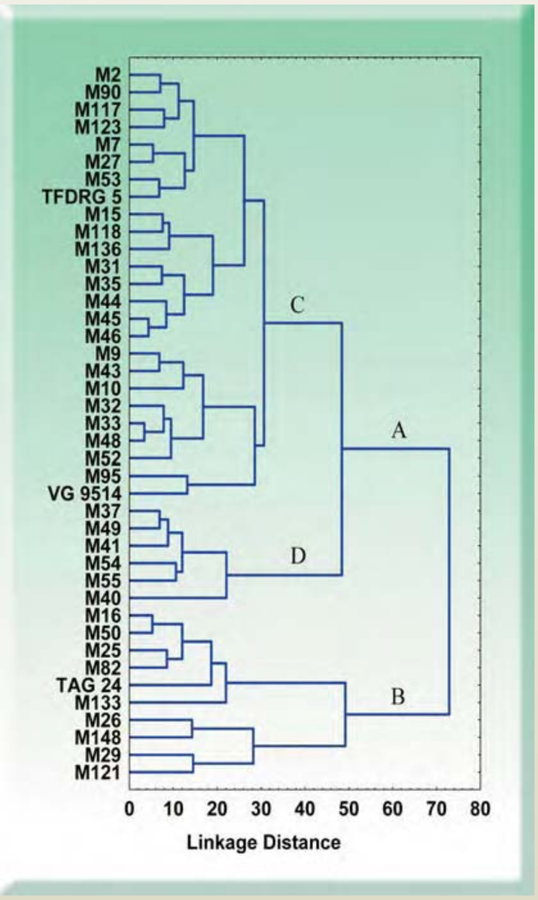

Fig. 7: Dendrogram showing relationship among groundnut mutants

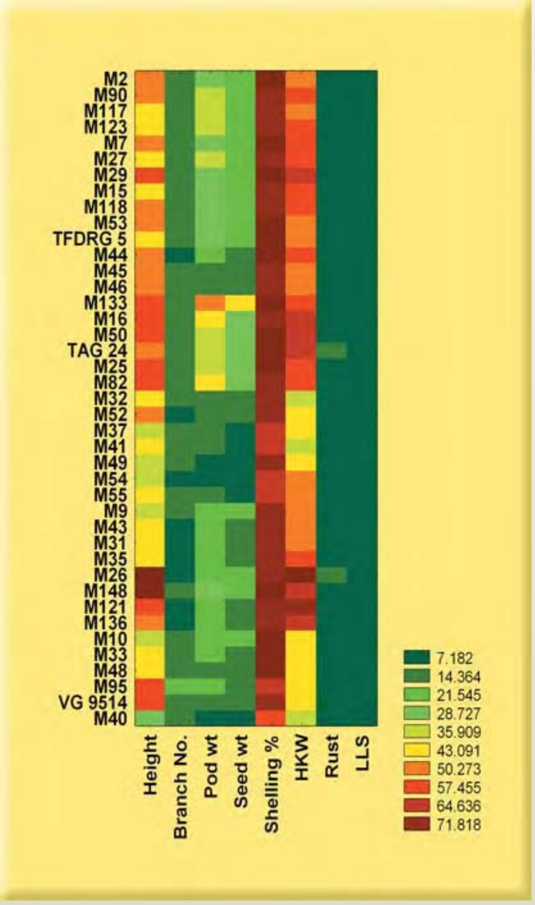

Fig. 8: Two-way graph showing contribution of each trait towards the variability

to VB type. Regarding LLS score (1-9 scale, Subrahmanyam et al, 1995) there was no variation among the mutants. But, M26 and M95 showed variation in respect to rust resistance (1-9 scale, Subrahmanyam et al, 1995) and they were susceptible to rust.

Conclusion

Induced mutagenesis particularly through combination of gamma rays and sodium azide was successful for creating mutants in groundnut with wide genetic variability. The identified high yielding large seed mutant will be tested in replicated yield trial along with the check varieties and parent for channeling them to All India Coordinate yield trial conducted by the Indian Council for Agricultural Research. The present research has generated lot of material for mutant characterization and isolation of mutated genes in groundnut. Future work will be directed towards the biochemical and molecular characterization of these induced mutants and mutations.

Acknowledgements

We thank Dr S.F. D'Souza Associate Director (A), Biomedical Group and Head, Nuclear Agriculture and Biotechnology Division for support and encouragement. This work is part of the project, partially funded by the International Atomic Energy Agency, Vienna under the Coordinated Research Project No. 12818.

References

1. Badigannavar A.M., Kale D.M., Mondal S. and Murty G.S.S. 2005. Trombay groundnut recombinants resistant to foliar diseases. *Mutation Breeding Newsletter and Reviews* 1:11-12.
2. Branch W.D. 2002. Variability among advanced gamma-irradiation induced large-seeded mutant breeding lines in the 'Georgia Browne' peanut cultivar. *Plant Breeding*.121: 275.
3. Gowda M.V.C., Nadaf H.L. and Sheshagiri R. 1996. The role of mutations in intraspecific differentiation of groundnut (*Arachis hypogaea* L.). *Euphytica*. 90: 105-113.
4. Gregory W.C. 1956. Induction of useful mutants in the peanut. *Brookenhaven symp. Biol* 9: 117-190.
5. Hartigan, J.A. 1975. Clustering algorithm, NewYork: Wiley.
6. Hu G., Yalpani N., Briggs S.P. and Johal G.S. 1998. A porphyrin pathway impairment is responsible for the phenotype of adominant disease lesion mimic mutant of maize. *Cell*. 10: 1095-1105.
7. Kim D.S., Lee I.S., Jang C.S., Kang S.Y., Park I.S., Song H.S. and Seo Y. W. 2004. High amino acid accumulating 5-methyltryptophan-resistant rice mutants may include an increased antioxidative response system. *Physiologia Plantarum* 123: 302-313.
8. Mouli C., Kale D.M. and Patil S.H. 1984. Bifurcated leaflets in groundnut. *Oleagineux* 39 (7): 375-377.
9. Murty G.S.S., Badigannavar A.M., Mondal S. and Kale D.M. 2004. Research and impact of groundnut mutation breeding in India. In " Groundnut Research in India" (Eds. Basu M.S. and Singh N.B.), NRCG, Junagadh, India pp. 57-69.
10. Patil S.H. 1966. Mutation induced in groundnut by X-rays. *Indian journal of genetics* 26A (symposium number): 334-348.
11. Patil S.H. and Mouli C. 1975. Radiation induced instability at the virescent locus in groundnut. *Indian journal of genetics and plant breeding* 35 (3): 356-363.
12. Patil S.H. and Mouli C. 1984. Preferential segregation of two allelic mutations for small leaf character in groundnut. *Theoretical Applied Genetics* 67: 327-332.
13. Patil S.H., Kale D.M., Deshmukh S.N., Fulzele G.R. and Weginwar B.G. 1995. Semi-dwarf, early maturing and high yielding new groundnut variety, TAG-24. *Journal of Oilseed Research* 12: 254-257.

14. Reddy P.S, Reddi M.V, Raju B.T, Ali S.M. 1977. Creation of genetic variability by recourse to irradiation in groundnut (*Arachis hypogaea* L.). *Oleagineux* 32 (2): 59-62.
15. Smartt J. 1960. Genetic instability and outcrossing in the groundnut variety Mani Pintar. *Nature*. 186: 1070-1071.
16. Statistica 1996. STATISTICA, version 6.0. Statsoft Inc., Tulsa, USA.
17. Subrahmanyam P, McDonald D, Waliyar F, Reddy LJ, Nigam SN, Gibbons RW, Rao VR, Singh AK, Pande S, Reddy PM, Subba Rao PV (1995) Screening methods and sources of resistance to rust and late leaf spot of groundnut. In: Information bulletin no. 47. ICRISAT, Patancheru India.
18. Varman P.V. 1999. A foliar disease resistant line developed through interspecific hybridization in groundnut (*Arachis hypogaea*). *Indian journal of Agricultural science*. 69 (1):67-68.

About the Authors

Mr. Suvendu Mondal, MSc (Microbiology) from Indian Agricultural Research Institute, New Delhi, joined BARC in 2003 through training school (46th batch, Bioscience) and is currently working in groundnut improvement group, Nuclear Agriculture and Biotechnology Division, BARC. He is currently pursuing PhD on the project entitled "Induction of mutations and its morphological, biochemical and molecular characterization in groundnut." His major research interest is to develop molecular markers for the biotic stress tolerance and characterization of mutants/ mutations in groundnut. Besides he is involving in developing Trombay groundnut varieties and its dissemination.

Dr Anand M. Badigannavar, MSc (Agriculture) from University of Agricultural Sciences, Dharwad, joined BARC in 1997. He obtained his PhD (Botany) from University of Mumbai, Mumbai on the project "Genetic improvement for agronomical and biochemical traits in groundnut (*Arachis hypogaea* L.)". His field of interest is genetics, mutation and recombination breeding in groundnut leading to the development of improved groundnut varieties. Presently, he is involved in the pyramiding of disease resistant and salt tolerant genes with large seed trait in groundnut.

Mr. D.M. Kale joined BARC in 1965 and served upto March 2006. Since joining, he was actively involved in groundnut improvement programme at Nuclear Agriculture and Biotechnology Division. He was actively involved in the mutation and recombination breeding of groundnut leading to the development of 12 Trombay Groundnut (TG) varieties, and more than 100 breeding/mutant lines in groundnut. Besides he has published 30 scientific papers and registered five groundnut mutant lines with NBPGR, New Delhi. He was also involved in the dissemination and popularization of TG varieties among farmers across the country.

Dr G.S.S. Murty, M.Sc. (Botany) from Andhra University, Waltair, joined BARC in 1971 and served up to January 2007. His interest was in mutation research of sesame and groundnut for which he could get international acclaim. His significant contributions include inducing variability and discovering inter-mutant hybrid heterosis in sesame, leading Trombay Groundnut (TG) project for nearly two decades. Relentless efforts put in by him and his team, made TG project to attain a top position in India from the point of view of breeders as well as farmers, which brought reputation to BARC. During his career in BARC, he produced more than 50 research papers; he is a co-breeder for 7 out of 12 TG varieties; he registered three sesame mutants with NBPGR; he was associated with many IAEA projects including undertaking Expert Mission.

AUTHOR INDEX

Edited & Published by :
Dr. Vijai Kumar,
Associate Director,Knowledge Management Group &
Head, Scientific Information Resource Division,
Bhabha Atomic Research Centre, Trombay, Mumbai 400 085, India.
Editorial Management : Ms. S.C. Deokattey,
Computer Graphics & Layout : P.A.S. Warrier, SIRD, BARC
BARC Newsletter is also available at URL: http://www.barc.gov.in
(for private circulation only)